An atomic scale study of strain, chirality, topology and domain wall networks in antiferromagnetic multilayers of Mn on Ir(111)

Dissertation

zur Erlangung des Doktorgrades
An der Fakultät für Mathematik, Informatik
und Naturwissenschaften

Fachbereich Physik der Universität Hamburg

vorgelegt von

Vishesh Saxena

- Hamburg, 2025 -

GUTACHTER DER DISSERTATION:

PD Dr. Kirsten von Bergmann
Prof. Dr. Roland Wiesendanger

MITGLIEDER DER PRÜFUNGSKOMMISSION:

PD Dr. Kirsten von Bergmann
Prof. Dr. Roland Wiesendanger
Prof. Dr. Stefan Heinze
Dr. Aurore Finco
Prof. Dr. Michael Potthoff

DATUM DER DISPUTATION:

16.07.2025

VORSITZENDER DER PRÜFUNGSKOMMISSION:

Prof. Dr. Michael Potthoff

VORSITZENDER DES PROMOTIONSAUSSCHUSSES:

Dr. Wolfgang J. Parak

DEKAN DER MIN-FAKULTÄT:

Prof. Dr.-Ing. Norbert Ritter

"When there is righteousness in the heart, there is harmony in the home; when there is harmony in the home, there is order in the nation; when there is order in the nation, there is peace in the world."

– Dr. APJ Abdul Kalam

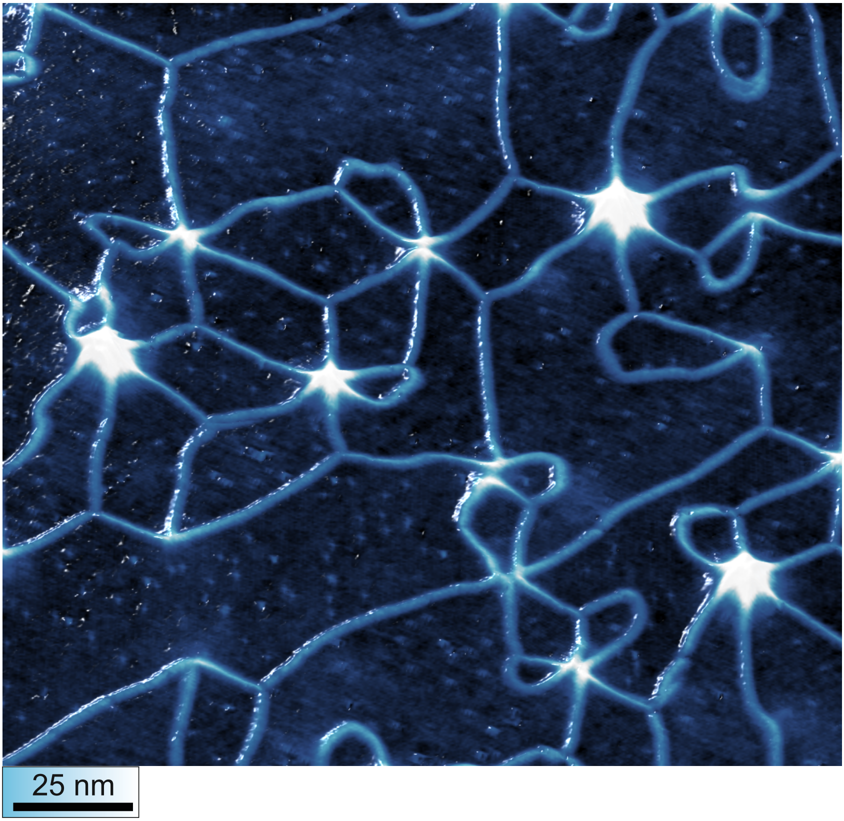

A magnetic domain wall network in the bilayer of Mn on Ir(111), reminiscent of a neural network.

Abstract

Antiferromagnetic spin textures are rapidly emerging as key building blocks for next-generation spintronic devices. Their inherent lack of stray fields, robustness against external perturbations, and ultra-fast spin dynamics in the terahertz regime make them especially attractive for high-density, low-power memory technologies such as racetrack memory. Beyond their potential for device applications, antiferromagnetic systems also host a rich landscape of topological phenomena, including emergent orbital magnetism and exotic Hall effects, offering a fertile ground for fundamental research at the intersection of topology, spintronics, and materials design.

In this thesis, a model type system of a few atomic layers of Manganese (Mn) deposited on a hexagonal lattice of Ir(111) has been investigated with spin-polarized scanning tunneling microscopy (SP-STM) for antiferromagnetic spin textures and domain walls. By introducing localized strain via embedded argon bubbles, magnetic imaging of domain wall networks has been shown. The elements of the domain wall networks, i.e. triple magnetic domain wall junctions and hexa-junctions have been studied down to the atomic scale.

A systematic study of the double, triple, and quadruple Manganese layers on Ir(111), reveals a strong correlation between structural relaxation and magnetic behavior. In particular, stress-relief-induced reconstruction patterns in the triple and quadruple layers significantly influence the orientation of surrounding magnetic domain walls. The double layer has been characterized to have the row-wise antiferromagnetic (1Q) state. Moreover, multi-Q states such as the 2Q and 3Q have also been observed in the different layers, suggesting the presence of higher-order exchange interactions.

Across all the layers, structurally chiral domain wall junctions have been observed, which reflect the broken symmetries inherent to the system. Notably, a lateral shift of the double layer relative to the monolayer has been observed. This has been attributed to an enhanced inter-layer antiferromagnetic coupling and symmetry reduction arising from the onset of the row-wise antiferromagnetic (RW-AFM) order.

Furthermore, the thesis reports the presence of the non-trivial topological 3Q state, appearing as localized spin textures in the double layer and as extended magnetic domains and domain walls in the thicker layers. A collaborative density functional theory (DFT) analysis reveals a topological orbital moment associated with the 3Q state in the double layer of Manganese on Ir(111).

These findings open new pathways for incorporating antiferromagnetic textures into future device architectures. The ability to induce domain walls in an antiferromagnet through localized strain highlights a viable route for strain-engineered control of magnetic states, with potential implications for ultra-fast domain wall dynamics. Moreover, the emergence of the topological 3Q state and its associated orbital moment lays the groundwork for transport experiments and computational studies exploring exotic Hall effects — including the recently proposed topological orbital Hall effect. Together, this work offers a foundation for both experimental and theoretical investigations into topologically driven spin phenomena in antiferromagnetic systems.

Zusammenfassung

Antiferromagnetische Spin-Texturen entwickeln sich rasant zu vielversprechenden Bausteinen für zukünftige spintronische Bauelemente. Ihre inhärente Freiheit von Streufeldern, die Robustheit gegenüber äußeren Störungen und die ultraschnelle Spin-Dynamik im Terahertz-Bereich machen sie besonders attraktiv für hochdichte, energieeffiziente Speichertechnologien wie das Racetrack-Memory. Insbesondere die Möglichkeit, Domänenwände und topologische Spin-Texturen in Antiferromagneten gezielt zu erzeugen und zu manipulieren, eröffnet neue Perspektiven zur Informationsspeicherung und -übertragung mit bislang unerreichter Geschwindigkeit. Über ihre mögliche Anwendung in Bauelementen hinaus bieten antiferromagnetische Systeme ein reichhaltiges Spektrum topologischer Phänomene, einschließlich emergenter orbitaler Magnetisierung und exotischer Hall-Effekte. Sie bilden damit ein fruchtbares Umfeld für grundlegende Forschung an der Schnittstelle von Topologie, Spintronik und Materialdesign.

In dieser Arbeit wird ein Modellsystem aus wenigen atomaren Schichten Mangan (Mn) auf dem hexagonalen Gitter von Ir(111) mittels spinpolarisierter Rastertunnelmikroskopie (SP-STM) im Hinblick auf antiferromagnetische Spin-Texturen und Domänenwände untersucht. Durch das gezielte Einbringen lokaler Spannungen mittels eingeschlossener Argonblasen konnte die kontrollierte Nukleation und Ausbreitung von Domänenwandnetzwerken demonstriert werden. Die Elemente dieser Netzwerke – insbesondere magnetische Dreifach-Domänenwände und Hexa-Verzweigungen – wurden bis auf atomare Skalen untersucht.

Eine systematische Untersuchung der doppelten, dreifachen und vierfachen Mangan-Schichten auf Ir(111) zeigt eine starke Korrelation zwischen struktureller Relaxation und magnetischem Verhalten. Insbesondere beeinflussen spannungsbedingte Rekonstruktionsmuster in

der Dreifach- und Vierfachschicht die Orientierung benachbarter magnetischer Domänenwände signifikant. Die Doppelschicht zeigt einen zeilenweisen antiferromagnetischen (1Q) Zustand, wobei auch Multi-Q-Zustände wie 2Q und 3Q in den Domänenwänden beobachtet wurden.

Über alle Schichten hinweg wurden strukturell chirale Domänenwände identifiziert, die die durch Symmetriebrechung bedingten Eigenschaften des Systems widerspiegeln. Besonders hervorzuheben ist eine laterale Verschiebung der Doppelschicht relativ zur Monoschicht, die auf eine verstärkte zwischenchichtliche antiferromagnetische Kopplung und eine durch den RW-AFM-Zustand hervorgerufene Symmetriereduktion zurückgeführt werden kann.

Darüber hinaus wird das Auftreten eines nicht-trivialen topologischen 3Q-Zustands berichtet, der sich in der Doppelschicht als lokalisierte Spin-Texturen und in den dickeren Schichten als ausgedehnte magnetische Domänen und Domänenwände manifestiert. Eine kollaborative Dichtefunktionaltheorie (DFT)-Analyse zeigt ein damit verbundenes topologisches orbitales Moment in der Doppelschicht von Mangan auf Ir(111).

Diese Ergebnisse eröffnen neue Perspektiven zur Integration antiferromagnetischer Texturen in zukünftige Bauelementarchitekturen. Die Möglichkeit, Domänenwände in Antiferromagneten durch lokal induzierte Spannungen zu erzeugen, zeigt einen vielversprechenden Weg zur spannungsbasierten Kontrolle magnetischer Zustände mit potenziellen Anwendungen in ultraschneller Domänenwanddynamik. Darüber hinaus bildet das Auftreten des topologischen 3Q-Zustands und seines assoziierten orbitalen Moments die Grundlage für Transportexperimente und numerische Studien zu exotischen Hall-Effekten – einschließlich des kürzlich vorgeschlagenen topologischen orbitalen Hall-Effekts. Insgesamt liefert diese Arbeit eine Grundlage für zukünftige experimentelle und theoretische Untersuchungen topologisch getriebener

---

Spin-Phänomene in antiferromagnetischen Systemen.

Contents

Acronyms

ML	monolayer
DL	double layer
TL	triple layer
QL	quadruple layer
AL	atomic layer
AFM	antiferromagnet
RW-AFM	row wise antiferromagnet
STM	scanning tunneling microscopy
SP-STM	spin polarized scanning tunneling microscopy
TOM	topological orbital moment
DFT	density functional theory
fcc	face-centered cubic
hcp	hexagonal close-packed
LDOS	local density of states
FFT	fast Fourier transform
PSDF	power spectral density function
SOC	spin-orbit coupling
UHV	ultra-high vacuum

1 Introduction

1.1 Magnetism for energy saving

Energy consumption has emerged as a critical global issue in recent years. A significant portion of this challenge stems from the growing demand from personal electronics and smartphones to high-performance computers and supercomputers. The recent surge in artificial intelligence, machine learning, and cryptocurrency technologies has dramatically increased the computational load on large-scale systems, resulting in substantial energy costs [1, 2]. Targeting electronics in general, which we require everyday for a smooth functioning of our lives, the scientific community has been in pursuit of finding potential solutions for making them energy efficient. At the base of some potential solutions in the scientific community, lies the field of magnetism. In magnetism, the two main promising areas of research close to being commercialized in the near future are Magnonics and Spintronics.

1.2 Magnetism close to applications

Magnonics is the field of research where magnons, which are collective excitations of the spin degree of freedom of electrons, are being studied to be used in transporting spin based information across distances of micrometers in devices. The most promising material to employ magnon based devices is Yttrium Iron Garnet (YIG) which is a ferrimagnetic insulator. In this scenario, there is no charge transport involved and hence saves on Joule heating which benefits energy consumption. With the recent surge in magnonics, it appears to be the closest and most promising field of magnetism that can be realized commercially in the near future [3].

Spintronics on the other hand is the field of research where the spin of electrons is used for data storage and transport in devices, instead of their charge. This is a very old field of research and some products of it have also been implemented in industrial applications [4]. For example, the Giant magneto-resistance effect is being used for memory storage in devices since 1997, which was first discovered by Albert Fert [5] and Peter Grünberg [6] individually in different studies, for which they were both awarded the Nobel prize in 2007. Concepts such as the spin Hall effect [7], spin transfer torque (STT) [8], spin-orbit torque (SOT) [9, 10], spin Seebeck effect [11] are some of the very important phenomena that are under intensive research for device physics applications. Lately, efforts are being focused towards the development of SOT based magnetic random access memories (MRAMs) which are more energy efficient than STT based MRAMS [12].

1.3 Magnetic nanostructures

Since there is a persistent desire for advancement in the field of magnetism, researchers are looking for magnetic spin textures which if realized in devices, can be used for memory storage with very low operational currents that are in the order of nano-Amperes [13]. Some examples of such spin textures are magnetic domain walls and skyrmions. These two classes of spin textures are being widely studied with respect to their realization and interaction with spin and charge currents in devices to be used commercially in the near future.

A prominent application of the aforementioned spin textures is the proposed concept of racetrack memory. Unlike conventional hard drives that rely on mechanical motion of a read/write head over a spinning magnetic disk, racetrack memory eliminates moving parts by shifting spin textures (domain walls or skyrmions) along nanowires using spin-polarized currents. The position of each spin texture is read by a fixed magnetic read head, enabling binary information to be encoded through the presence or absence of a domain wall or skyrmion—corresponding to logical ′1′ and ′0′, respectively [14, 15]. This design promises significantly faster access times, higher endurance, and lower energy consumption. Significant progress has been made in this direction, with recent experimental studies demonstrating spin texture velocities that are approaching values suitable for real-world device performance [16].

In order to employ antiferromagnetic spin textures in functional devices, it is essential to develop a fundamental understanding of the mechanisms that stabilize these textures in antiferromagnetic materials, as well as to establish methods for characterizing them at the atomic scale. This thesis employs the technique of spin-polarized scanning tunnelling microscopy (SP-STM) down to the atomic scale and hence we will now shift the focus of the discussion to fundamental magnetism.

1.4 In this thesis

In this thesis, the material under investigation is an antiferromagnet — a class of magnetic materials that presents significant challenges in both fundamental understanding and practical application.

Antiferromagnets offer negligible to zero stray field which make them attractive materials. They operate in the THz regime which is three orders of magnitude larger than for ferromagnets. Hence, ultra-fast techniques are also being used to study the spin dynamics in antiferromagnets in a time-resolved fashion [17].

In this thesis, a few atomic layers of Manganese (Mn) on Iridium (Ir(111)) have been studied by SP-STM. The layers investigated in this thesis are from the double layer up-to the quadruple layer, with a brief mention about the monolayer. Every layer has an antiferromagnetic state which has been imaged using the SP-STM technique. The antiferromagnetic states observed in this material system range from collinear to non-collinear and non-coplanar.

Beyond its magnetic properties, the Mn/Ir(111) material system also hosts topologically non-trivial states. The field of topology has become a central topic in condensed matter physics, with implications spanning a broad range of phenomena - from magnetic textures to potential applications in quantum computing [18]. Topology has emerged as a key area of interest in magnetism due to the concept of topological protection. For instance, magnetic skyrmions are topological spin textures that are particularly attractive for use in racetrack memory devices, owing to their robustness against external electromagnetic perturbations. In addition to skyrmions, other topological magnetic states also exist, such as the 3Q state. The 3Q state is an antiferromagnetic configuration where the spin arrangement within a magnetic unit cell can be visualized as a tetrahedron, with spins oriented at mutual angles of approximately 109.4°.

The 3Q state has been experimentally observed in real-space using spin-polarized scanning tunneling microscopy [19], and its presence has also been inferred in transport measurements through the observation of a spontaneous topological Hall effect [20]. In this thesis, both localized and extended realizations of 3Q states have been identified. Furthermore, the topological orbital moment associated with the 3Q state in the Mn double-layer on Ir(111) is also discussed in Chapter 4.

Although antiferromagnets are highly attractive for spintronic applications due to their ultra-fast dynamics and insensitivity to external magnetic fields, the realization of magnetic structures such as domain walls or skyrmions in these materials remains challenging. This difficulty primarily arises from the absence of a net magnetization, and consequently, the lack of stray fields that typically drive such textures in ferromagnets.

Therefore, unconventional or indirect approaches are required to stabilize and manipulate these magnetic structures in antiferromagnetic systems. In this thesis, it has been shown that by trapping Argon bubbles in the Ir(111) cyrstal, antiferromagnetic domain wall networks on the nanometer scale can be generated with interconnected junctions. The junctions and domain walls have been characterized for their magnetic state down to the atomic scale using SP-STM.

Besides the above mentioned novel findings in this material system, there is an observed magneto-elastic coupling at zero applied magnetic field. The bilayer system of Mn/Ir(111) has been shown experimentally and theoretically to undergo a structural shift due to a gain in the magnetic energy.

The effect of this structural shift has been seen in the formation of chiral domain wall junctions that constitute the large domain wall networks. The domain wall network exhibits a unique connectivity of the junctions in a specific manner, that is influenced by the requirement of dominant 120° domain walls in the system.

Moving to higher thicknesses, the triple and quadruple layers reveal intriguing structural behavior, particularly in the form of exotic reconstruction patterns. Such reconstructions have previously been observed in a limited number of material systems, including Ag/Pt(111)[21], Au(111) [22], and Cu/Ru(111) [23]. In the case of Mn/Ir(111), a temperature-dependent stress-relief reconstruction pattern is observed in the QL, while no such transition is clearly evident in the TL. This contrast highlights the sensitivity of surface reconstructions to both thickness and thermal effects. These reconstruction patterns dictate the behaviour of magnetic domain walls around them and this intricate relationship has been investigated in detail by SP-STM.

Since the concepts of topology, strain, chirality, and antiferromagnetism are present across all layers of the Mn/Ir(111) system—but manifest differently in each case—this thesis has been structured as follows:

- **Chapter 2** discusses the theoretical framework relevant for this thesis that includes concepts of antiferromagnetism, structural chirality, scalar spin chirality, and the topological orbital moment.
- **Chapter 3** contains information regarding the experimental and sample preparation methods. I will discuss about the technique of SP-STM and the possible mechanisms giving rise to magnetic contrast observed experimentally.
- **Chapter 4**, **5**, and **6** will be about the DL, TL, and the QL of Mn/Ir(111) respectively. The antiferromagnetic ground states, presence of strain, topologically non-trivial states and domain walls constituting a large network will be discussed for every layer.
- **Chapter 7** will provide a summary of all the Mn layers investigated in this thesis. The similarity and differences between the layers with respect to the topology, domain walls, growth and magnetic states will be discussed. An outlook will also be presented with respect to the novel findings.

Bibliography

1. Himeur, Y., Ghanem, K., Alsalemi, A., Bensaali, F. & Amira, A. Artificial intelligence based anomaly detection of energy consumption in buildings: A review, current trends and new perspectives. *Applied Energy* **287,** 116601 (2021).
2. Wendl, M., Doan, M. H. & Sassen, R. The environmental impact of cryptocurrencies using proof of work and proof of stake consensus algorithms: A systematic review. *Journal of Environmental Management* **326,** 116530 (2023).
3. Flebus, B. *et al.* The 2024 magnonics roadmap. *Journal of Physics: Condensed Matter* **36,** 363501 (2024).
4. Guo, Z. *et al.* Spintronics for energy-efficient computing: An overview and outlook. *Proceedings of the IEEE* **109,** 1398–1417 (2021).
5. Baibich, M. N. *et al.* Giant magnetoresistance of (001) Fe/(001) Cr magnetic superlattices. *Physical review letters* **61,** 2472 (1988).
6. Binasch, G., Grünberg, P., Saurenbach, F. & Zinn, W. Enhanced magnetoresistance in layered magnetic structures with antiferromagnetic interlayer exchange. *Physical review B* **39,** 4828 (1989).
7. Hirsch, J. Spin hall effect. *Physical review letters* **83,** 1834 (1999).
8. Slonczewski, J. C. Current-driven excitation of magnetic multilayers. *Journal of Magnetism and Magnetic Materials* **159,** L1–L7 (1996).
9. Chernyshov, A. *et al.* Evidence for reversible control of magnetization in a ferromagnetic material by means of spin–orbit magnetic field. *Nature Physics* **5,** 656–659 (2009).
10. Mihai Miron, I. *et al.* Current-driven spin torque induced by the Rashba effect in a ferromagnetic metal layer. *Nature materials* **9,** 230–234 (2010).
11. Uchida, K.-I. *et al.* Observation of the spin Seebeck effect. *Nature* **455,** 778–781 (2008).

12. Shao, Q. *et al.* Roadmap of spin–orbit torques. *IEEE transactions on magnetics* **57,** 1–39 (2021).
13. Barla, P., Joshi, V. K. & Bhat, S. Spintronic devices: a promising alternative to CMOS devices. *Journal of Computational Electronics* **20,** 805–837 (2021).
14. Parkin, S. S., Hayashi, M. & Thomas, L. Magnetic domain-wall racetrack memory. *Science* **320,** 190–194 (2008).
15. Kang, W. *et al.* A comparative cross-layer study on racetrack memories: Domain wall vs skyrmion. *ACM Journal on Emerging Technologies in Computing Systems (JETC)* **16,** 1–17 (2019).
16. Pham, V. T. *et al.* Fast current-induced skyrmion motion in synthetic antiferromagnets. *Science* **384,** 307–312 (2024).
17. Dal Din, A., Amin, O., Wadley, P. & Edmonds, K. Antiferromagnetic spintronics and beyond. *npj Spintronics* **2,** 25 (2024).
18. Bernevig, B. A., Felser, C. & Beidenkopf, H. Progress and prospects in magnetic topological materials. *Nature* **603,** 41–51 (2022).
19. Spethmann, J. *et al.* Discovery of magnetic single-and triple-q states in Mn/Re (0001). *Physical review letters* **124,** 227203 (2020).
20. Takagi, H. *et al.* Spontaneous topological Hall effect induced by non-coplanar antiferromagnetic order in intercalated van der Waals materials. *Nature Physics* **19,** 961–968 (2023).
21. Brune, H., Röder, H., Boragno, C. & Kern, K. Strain relief at hexagonal-close-packed interfaces. *Physical Review B* **49,** 2997 (1994).
22. Li, P. & Ding, F. Origin of the herringbone reconstruction of Au (111) surface at the atomic scale. *Science advances* **8,** eabq2900 (2022).
23. Hamilton, J. C. & Foiles, S. M. Misfit Dislocation Structure for Close-Packed Metal-Metal Interfaces. *Phys. Rev. Lett.* **75,** 882–885 (5 1995).

2 Theoretical foundations

2.1 Magnetism

Magnetic materials are widely studied, having played a role in human civilization for centuries and now integrated into countless modern technologies—ranging from refrigerators and car engines to magnetic resonance imaging (MRI) machines and headphones. A common type of magnet used in these applications is the NdFeB (neodymium iron boron) magnet, first developed by Masato Sagawa in 1984 [1]. Despite the long-standing use of magnetic materials, research in magnetism remains highly active. As discussed in the introductory chapter, the demand for more energy-efficient technologies continues to grow, and magnetic structures are increasingly seen as promising candidates for next-generation low-power electronic and spintronic devices.

2.1.1 Ferromagnetism and domain walls

We will first discuss about the simplest class of magnets, namely ferromagnets. Ferromagnets are materials where the magnetic moments are aligned parallel to each other. The advantage ferromagnets offer is that they possess a net magnetization which can be tapped into - for example - fridge magnets.

What keeps the neighbouring magnetic moments aligned in a parallel fashion is the nearest neighbour exchange interaction. The formalism developed by Heisenberg to understand magnetic interactions at the atomic scale is shown below in Eqn. 2.1 [2].

$$\hat{H}_{\text{Heisenberg}} = -J \sum_{\langle i,j \rangle} \hat{\mathbf{S}}_i \cdot \hat{\mathbf{S}}_j \tag{2.1}$$

In the above equation, J corresponds to the Heisenberg exchange constant, the sign of which determines the coupling between neighbouring spins, $\mathbf{S}_i$ and $\mathbf{S}_j$ to be ferro ($J > 0$) or antiferromagnetic ($J < 0$).

The origin of the Heisenberg exchange interaction lies in the interplay between the Coulomb repulsion and the Pauli exclusion principle. In quantum mechanics, the total wave function of two identical fermions — such as electrons must be antisymmetric under particle exchange. This anti-symmetry applies to the combined product of their spin and spatial components. As a result, the spatial overlap of electron wave functions, constrained by the requirement of anti-symmetry, gives rise to an effective interaction that favors either parallel or antiparallel spin alignment [3].

In itinerant magnets, like Fe, Co and Ni, the magnetic interactions are mediated by conduction electrons. These delocalized itinerant electrons scatter off magnetic ions, thus getting spin polarized. This exchange is thus indirect as it is mediated by conduction electrons in the system and is often as called as the RKKY interaction named after four physicists, Ruderman-Kittel-Kasuya-Yosida [4].

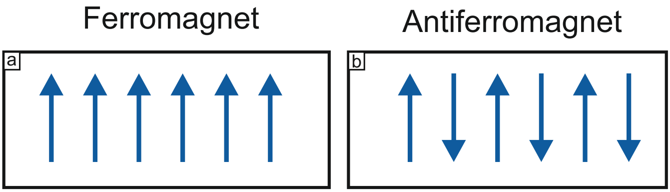

Figure 2.1: A schematic of magnetic ordering types. (a) Ferromagnetic ordering, where all spins are aligned parallel to each other, **(b)** Antiferromagnetic ordering, where neighboring spins are aligned antiparallel, resulting in no net magnetization.

An illustration of the atomic-scale magnetic structure of a ferromagnet is shown in Fig. 2.2(a), where all magnetic moments are aligned in the same direction. In contrast, Fig. 2.2(b) depicts a configuration in which neighboring magnetic moments are aligned antiparallel to one another — characteristic of an antiferromagnet.

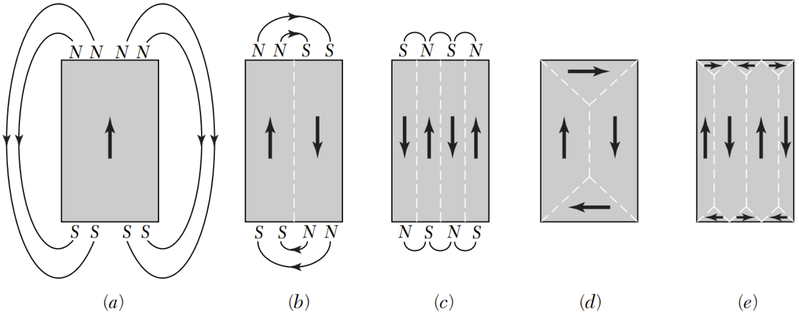

Figure 2.2: Magnetic domain configurations to reduce stray field energy. (a) A uniformly magnetized single magnetic domain exhibiting stray fields. **(b)** A two-domain configuration with opposite magnetization reducing the stray field. **(c)** Multidomain structure with alternating domains and minimized stray fields. **(d)** Closure domains forming along the edges to further reduce magnetic energy. **(e)** Ideal flux-closure configuration with minimal external stray field and reduced magnetostatic energy. Extracted from the solid state physics book of Charles Kittel [5]

Having introduced ferromagnetism, we now proceed to discuss the formation and significance of magnetic domains within ferromagnetic materials. We start with Fig. 2.2(a), where a single magnetic domain exists. The stray field emanating from the sample due to a net magnetization is depicted by the curved lines. The ferromagnet tries to reduce the stray field energy, which results in the formation of domains, oriented in opposite directions. This can be seen in Fig. 2.2 (b), where a reduced stray field is observed by the formation of oppositely oriented ferromagnetic domains resulting in a 180° domain wall. A further reduction in stray field energy is seen in panel (c), where multiple domains are formed. Fig. 2.2(d, e) show the formation of closure domains that give rise to 90° domain walls resulting in a complete reduction of the stray field. In ultra-thin films, i.e., a few atomic layers, the domain orientations can be determined largely by the underlying lattice symmetry of the substrate upon which the magnetic material is deposited.

2.1.2 Spin-orbit coupling and magnetic anisotropies

Following the introduction of the preceding concepts, we now turn to the topic of magnetic anisotropy. Magnetic anisotropy refers to the directional dependence of magnetic moment orientation within a material—i.e., the tendency of magnetic moments to preferentially align along certain crystallographic directions. This behavior is governed by various types of anisotropies, which can be intrinsic or externally controlled.

Magneto-crystalline anisotropy is the energy required to orient the magnetization away from its preferred direction. This phenomenon arises from spin-orbit coupling (SOC), a relativistic effect that couples the electron's spin and its orbital motion.

Before discussing SOC in detail, it is important to recognize that an electron's magnetic properties have two contributions: one from its intrinsic spin and one from its orbital motion. The electron's orbital angular momentum is defined as:

$$\vec{L} = \vec{r} \times \vec{p},$$

where $\vec{L}$ is the angular momentum, $\vec{r}$ is the position vector of the particle relative to the origin, and $\vec{p}$ is the linear momentum of the particle. This gives rise to the orbital magnetic moment:

$$\vec{\mu}_L = -\frac{e}{2m}\vec{L}, \tag{2.2}$$

where e is the elementary charge and m is the electron mass. SOC arises when a moving electron in a crystal with a periodic potential experiences a potential gradient. In systems with broken inversion symmetry, this gradient results in an electric field $\vec{E}$ which, according to special relativity, appears in the electron's rest frame as an effective magnetic field:

$$\vec{B}_{\mathrm{SO}} = \frac{\vec{E} \times \vec{v}}{c^2}, \tag{2.3}$$

where $\vec{v}$ is the electron velocity and c is the speed of light.

The corresponding interaction energy is given by:

$$H_{\mathrm{SO}} = -\vec{\mu}_S \cdot \vec{B}_{\mathrm{SO}}. \tag{2.4}$$

Substituting the expressions for $\vec{\mu}_S$ and $\vec{B}_{\mathrm{SO}}$ into Eq. (2.4), we obtain:

$$H_{\mathrm{SO}} = -\vec{\mu}_S \cdot \vec{B}_{\mathrm{SO}} = -\left(\frac{e}{2m}\vec{S}\right) \cdot \left(\frac{\vec{E} \times \vec{v}}{c^2}\right),$$

which highlights the dependence of the interaction energy on the electron's velocity and the electric field. Since the velocity is related to orbital motion, this expression can be rewritten in terms of the orbital angular momentum:

$$H_{\mathrm{SO}} = \lambda\left(\vec{L} \cdot \vec{S}\right),$$

where λ is the spin-orbit coupling strength.

$$H_{\mathrm{SO}} = \frac{Z^4 e^2 \hbar^2 \langle \mathbf{S} \cdot \mathbf{L} \rangle}{4\pi\epsilon_0 a_0^3 n^3 l \left(l + \frac{1}{2}\right)(l+1)} \tag{2.5}$$

Eqn. 2.5 shows that the SOC strength depends on the atomic number Z, orbital quantum number l, and the expectation value $\langle \mathbf{S} \cdot \mathbf{L} \rangle$, as well as on the Bohr radius a_0, the principal quantum number n, and the vacuum permittivity ϵ_0 [6].

The total angular momentum **J** is given by:

$$\mathbf{J} = \mathbf{L} + \mathbf{S} \tag{2.6}$$

In materials with strong spin-orbit coupling (SOC), rotating the spins away from a preferred crystallographic direction requires additional energy. This is because spin and orbital moments are coupled, meaning that changing the spin orientation affects the electronic orbital states. The interplay between spin and orbital moments leads to **magnetocrystalline anisotropy**, where certain spin orientations are energetically preferred due to the SOC effect [2].

For hexagonal systems, we can have a look at the anisotropy energy density terms in the equation below:

$$E = K_1 \sin^2\theta + K_2 \sin^4\theta + K_3 \sin^6\theta + ... \tag{2.7}$$

In the above Eqn. 2.7, θ is the angle between the magnetization vector and the hexagonal c-axis. For example, in cobalt which is hexagonal, the easy axis is along the c-axis [7] which refers to the favourable axis of the magnetization vector. In the above equation, K_1, K_2, and K_3 are anisotropy constants, the units of which are in J cm^{-3} [6].

We can now have a look at the **surface anisotropy**. This is prevalent in thin films and ultra-thin film systems where there is an interface involved. The surface breaks symmetry and there is a slight difference in the number of nearest neighbour atoms. This creates a different magnetic interaction on the surface compared to the bulk. This plays an important role when the film thickness is very low or when there is an abrupt change in the magnetic properties across the interface in cases when two different magnetic materials are proximitized. An important type of surface anisotropy is the perpendicular magnetic anisotropy (PMA) that causes the equilibrium magnetization to be perpendicular to the surface of a ferromagnet, rather than in-plane. PMA is often advantageous over in-plane anisotropy for data storage applications, as it can support smaller and more stable magnetic domains, which allows for higher storage densities [8].

Lastly, it is important to mention the **shape anisotropy**. As the name suggests, this form of magnetic anisotropy arises from the geometric shape of the material which is related to the stray field energy. Shape anisotropy plays a significant role in systems such as magnetic nanoparticles, thin films, and nanostructured devices where the magnetic material is confined to specific geometries. In such cases, the magnetic easy axis is typically aligned along the longest physical dimension of the structure. For instance, in magnetic nanowires, the easy axis tends to lie along the cylindrical axis of the wire [9]. Shape anisotropy will be revisited in the context of sample preparation in a later section.

A notable example of magnetic domain formation is the emergence of the well-known Landau patterns in rectangular or square-shaped ferromagnetic geometries. In the case of a square-shaped ferromagnet, the system can minimize its total magnetic energy by forming alternating domains separated by domain walls, resulting in the characteristic Landau pattern shown in Fig. 2.3. These configurations arise due to the combined effects of magneto-static energy minimization (stray field re-

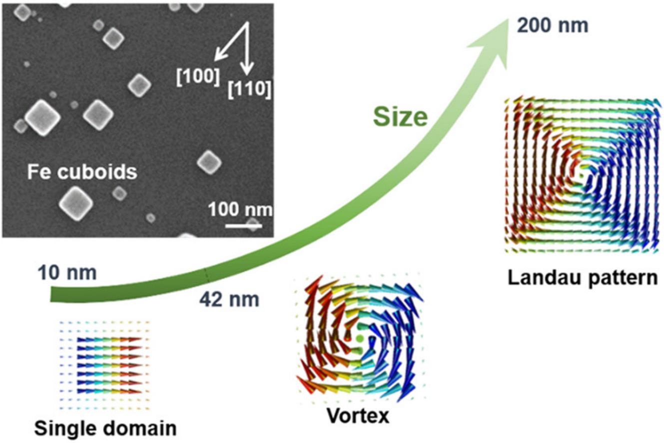

Figure 2.3: Size-Dependent Magnetic Domains in Fe nano-cuboids. Scanning electron microscopy (SEM) image of fabricated Fe nano-cuboids. Schematics showing the evolution of magnetic domain structures in Fe nano-cuboids as a function of their size. For small sizes (around 10 nm), the cuboids exhibit a single-domain state. As the size increases (around 42 nm), a magnetic vortex state becomes energetically favorable. For even larger sizes (around 200 nm), a Landau pattern with multiple domains is observed to minimize the magnetostatic energy. The arrows within each schematic represent the direction of the magnetization. Reprinted with permission from [10], copyright 2022 by the American Chemical Society.

duction) and shape anisotropy. The central junction point of the domain walls, often forming a vortex-like structure, can be manipulated by applying external magnetic fields in opposite in-plane directions, [11]. Experimental evidence of such patterns has been obtained through magnetic force microscopy and electron holography imaging of Fe nano-cuboids [10]. Fig. 2.3 presents simulated spin configurations illustrating a single-domain state, a vortex state, and a Landau domain pattern in Fe nano-cuboids.

2.1.3 Antiferromagnets

We now turn to a more complex class of magnetic materials - antiferromagnets (AFMs). AFMs are characterized by a zero net magnetization over their magnetic unit cell, achieved through the antiparallel alignment of neighboring spins. The constraint of zero net magnetization allows for a variety of spin arrangements, depending on the underlying crystal symmetry. For instance, in cubic lattices, four distinct types of AFM ordering are possible [4]. In hexagonal systems, several antiferromagnetic configurations can emerge, including the row-wise (RW) AFM, Néel state, 2Q state, and 3Q state - all of which are explored in this thesis.

In this thesis, a few atomic layers of Mn have been studied on a hexagonal (111) surface of an Ir crystal. As different antiferromagnetic states have been found in different layers of Mn/Ir(111), I will discuss the terms involved in the Hamiltonian that give rise to these AFM states.

First, I will discuss the Néel and RW-AFM states. Mn atoms and extended layers deposited on heavy metals have been shown to exhibit an antiferromagnetic behaviour [12–15]. Hence, to understand the AFM states that can occur, let us first understand what happens when atoms with an AFM coupling are placed on a triangle. It can be seen that in the

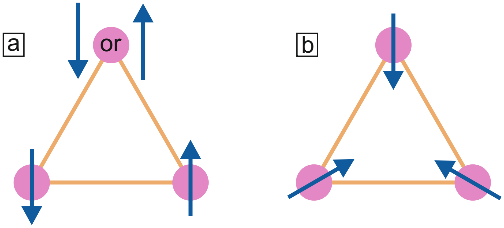

Figure 2.4: Antiferromagnetic spin configurations on a triangular lattice. (a) To achieve an AFM configuration on a triangular lattice, the spins cannot be collinear. Hence, the resultant configuration in **(b)** is where the spins are oriented at 120 degrees relative to each other resulting in a net zero magnetization in a non-collinear fashion.

first scenario in Fig. 2.4(a), the spins cannot be placed all in a collinear fashion due to geometric frustration. In Fig. 2.4(b), the ground state is shown, where neighbouring spins are aligned at 120 degrees to each other, where the vector sum of the magnetic moments is zero. In this case the nearest neighbour exchange interaction (J_1) plays the defining role in producing the non-collinear Néel state [16].

Additionally, if the J_2 also has a considerable size along with the J_1, the resulting AFM state is the collinear RW-AFM state [15, 18]. In this magnetic state, every row is ferromagnetic, but coupled antiferromagnetically to the next one which can be seen in the sketch shown in Fig. 2.5. There are two possible scenarios for the RW-AFM state shown in Figs. 2.5(a, b) respectively. The difference in the alignment of the spins for cases in (a,b) can be accounted for, by an energy term called anisotropic symmetric exchange (ASE) [15].

The RW-AFM state is also commonly referred to as the 1Q state, a terminology that originates from density functional theory (DFT) calculations. The designation "1Q" arises because the RW-AFM state can be described using a single spin-spiral vector **Q**, which defines the periodicity of the

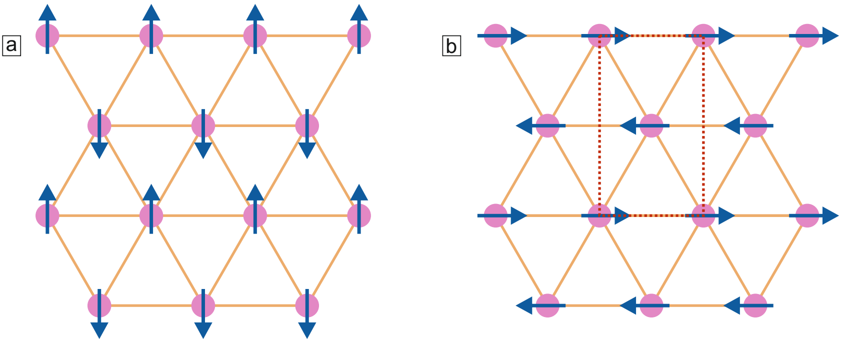

Figure 2.5: Two possible orientations of the RW-AFM state dependent on the anisotropic symmetric exchange constant. (a) The spins are oriented orthogonal to the close packed rows. **(b)** The spins are oriented parallel to the close packed rows

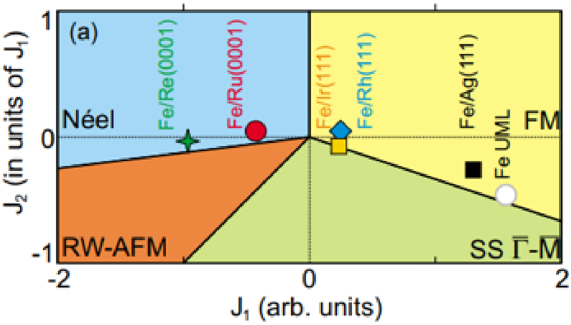

Figure 2.6: Magnetic phase diagram as a function of exchange interactions. A theoretical magnetic phase diagram plotted as a function of the first (J_1) and second (J_2) nearest-neighbor exchange interactions. Different colored regions indicate distinct magnetic phases. Experimental data points for various Fe based thin films on hexagonal lattices are superimposed on the phase diagram. Reprinted with permission from [17], copyright 2009 by the American Physical Society.

magnetic modulation. Here, the **Q** vector corresponds to a specific **k**-point in reciprocal space [19].

The interplay of J_1 and J_2 as shown in Fig. 2.6 can lead to different magnetic configurations. This has been exemplified in a study where the ratio of J_1 and J_2 has been shown to induce different magnetic states ranging from ferromagnetism to spin spirals in ultra-thin film systems for Fe monolayers on different hexagonal substrates [17].

Another recently identified class of magnetism is that of *altermagnets* - materials with zero net magnetization like AFMs, but which exhibit spin-split electronic bands due to specific crystalline symmetries. Unlike conventional AFMs, altermagnets can produce spin-polarized transport even in the absence of net moment, owing to their unique symmetry properties. This makes them particularly relevant in spintronics applications [20].

Spin glasses form a separate category, defined by a disordered and frozen spin configuration with no long-range magnetic order [21]. These systems display zero net magnetization on average but lack the coherent spatial modulation of spins found in AFMs or ferrimagnets.

In this thesis, magnetic states are classified as antiferromagnetic if the net magnetization averages to zero over the magnetic unit cell. This definition will be revisited in the context of the 3Q state discussed later.

2.2 Beyond the Heisenberg exchange

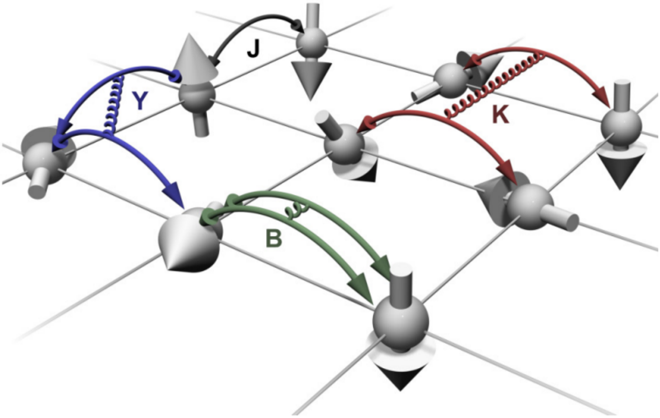

Figure 2.7: Schematic representation of higher-order magnetic interactions on a lattice. This schematic illustrates various higher-order magnetic interactions on a two-dimensional lattice. The spheres with arrows represent localized magnetic moments. The labeled curved arrows depict various exchange interaction mechanisms. *'J'* represents the Heisenberg exchange, whereas *'Y'*, *'K'* and *'B'* represent the different higher-order exchange interactions. Reprinted with permission from [22], copyright 2020 by the American Physical Society.

More complex non-collinear antiferromagnetic (AFM) states can arise due to the presence of higher-order interactions (HOIs) [15, 18], which go beyond the conventional pairwise Heisenberg exchange interactions. The theoretical foundation for these HOIs originates from quantum field theory [23], and they can also be understood as emerging from the Hubbard model, which describes electrons hopping between atomic sites in a crystal. Beyond the usual exchange interaction, additional interaction terms appear when one considers more complex hopping paths involving multiple spins. These give rise to higher-order effects such as biquadratic and ring exchange interactions [22]. Consider an electron entering a region containing four localized spins. The electron may scatter off one spin, hop to a neighboring spin, and then return to the original site. This process, an extension of the standard Heisenberg mechanism, leads to what is known as the biquadratic exchange interaction, often denoted by **B**, and is also referred to as the two-site four-spin interaction.

The Hamiltonian corresponding to the biquadratic exchange interaction is presented in Eqn. 2.8. In addition to this two-site four-spin interaction, more complex higher-order interactions are possible, wherein an electron undergoes successive scattering events involving three or four distinct atomic sites. These multi-site exchange processes are denoted by Y and K, referring to the three-site and four-site interactions respectively [22].

$$H = -\sum_{ij} B_{ij} (\mathbf{S}_i \cdot \mathbf{S}_j)^2 \tag{2.8}$$

2.3 Topological magnetic state: 3Q

Antiferromagnets (AFMs) are characterized by a complete cancellation of magnetic moments due to antiparallel alignment of equivalent spins, resulting in zero net magnetization over the magnetic unit cell. While canonical AFMs such as MnO or NiO exhibit collinear spin arrangements, more complex antiferromagnetic states exist. These include non-collinear and non-coplanar configurations such as the 3Q state, where the spin structure arises from the superposition of multiple spin modulation vectors. Despite their complex textures, such states also satisfy the condition of zero net magnetization and the absence of long-range ferromagnetic order, and are thus treated as generalized forms of antiferromagnetism in this work.

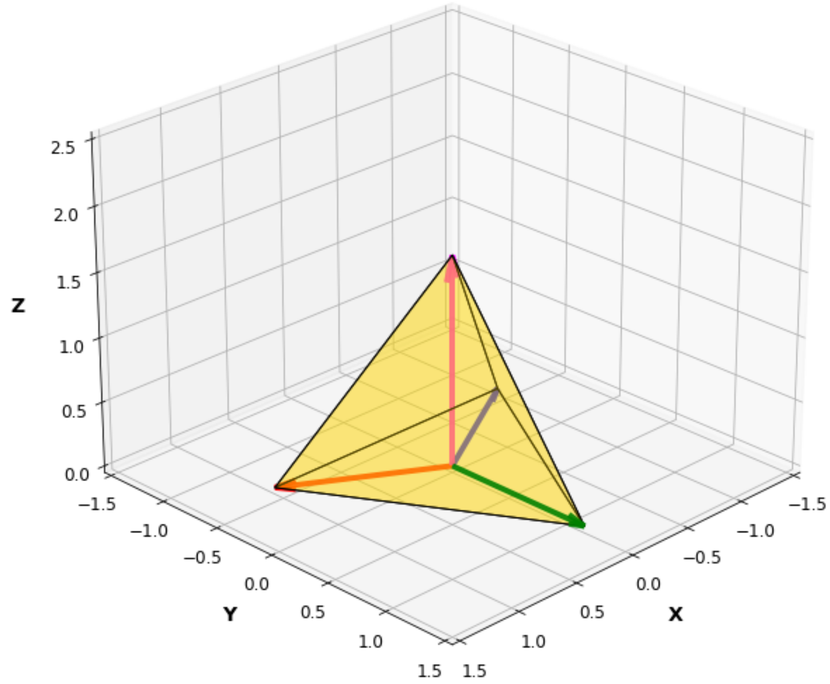

Figure 2.8: The 3Q non-coplanar antiferromagnetic state on a tetrahedral unit cell. The yellow tetrahedron has four spins located at its vertices such that the angle between any two spins is 109.45 degrees, corresponding to the angle between chemical bonds in a regular tetrahedron. The non-coplanar arrangement signifies that the spin vectors do not lie within a single plane, leading to a complex three-dimensional magnetic structure.

In this thesis, the magnetic structures observed in multilayer Mn/Ir(111) films—such as the 3Q state—are classified as antiferromagnetic due to their vanishing net moment in the magnetic unit cell and ordered, albeit non-collinear, non-coplanar spin arrangements.

The 3Q state is characterized by a non-coplanar, non-collinear configuration. The 3Q state has neighbouring spins at angles of 109.45° and hence is often represented by a tetrahedron as shown in Fig. 2.8. The magnetic unit cell of the 3Q state gives a zero net magnetization. This spin texture carries a topological charge of 2 per magnetic unit cell and was first directly imaged in an hcp-stacked monolayer Mn/Re(0001) system in 2020 [15].

In ultra-thin films, the 3Q state was first predicted for a monolayer of Mn on Cu(111) in 2001 [19]. However, experimental indications of the 3Q state date back to as early as 1978, where neutron diffraction studies of the γ-phase FeMn alloy suggested its presence [24]. This early observation was later supported by theoretical band structure calculations in 2000 [25].

The first real space imaging was reported for the system of hcp-stacked monolayer of Mn/Re(0001) [15]. The 3Q state arises due to the presence of higher-order interactions (HOIs). It is interesting to note that the 1Q and 2Q states were discovered in the fcc-stacked Mn/Re(0001) [18], whereas the 3Q state was found in the hcp-stacked Mn/Re(0001) [15], indicating a clear dependence of the magnetic state on the electronic structure of the system. With regards to this thesis, the DL has the RW-AFM as the ground state with 2Q state domain walls, whereas the TL and QL have the 3Q state as their magnetic ground states.

There can be three types of the 3Q state - $3Q^1$, $3Q^2$ and the $3Q^3$. These different states arise from the different orientation of the tetrahedron with respect to the 2D surface or the XY plane in Fig. 2.8.

The three types of $3Q$ states arise from different orientations of the magnetic tetrahedron with respect to the surface. The $3Q^1$ state corresponds to a tetrahedron resting on a face parallel to the XY plane, producing a hexagonal SP-STM contrast with an out-of-plane (OOP) magnetized tip. The $3Q^2$ state results from the tetrahedron lying on an edge, yielding a stripy pattern. The $3Q^3$ state occurs when the tetrahedron rests on a single vertex, producing a mixed stripy-hexagonal pattern. In all cases, the contrast reverses with opposite OOP tip magnetization. The simulated spin textures and corresponding SP-STM images are shown in Fig. 2.9, adapted from Spethmann et al. [15].

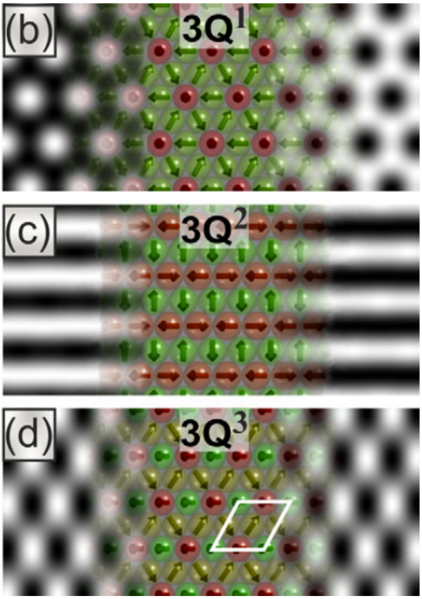

Figure 2.9: SP-STM simulations of the different kinds of the 3Q state measured with an out-of-plane magnetized tip superimposed with spin models. Different orientations of the tetrahedron with respect to the XY plane result in different magnetic contrast. **(b)** represents the magnetic contrast when the tetrahedron's face is parallel to the XY plane. **(c)** occurs when an edge of the tetrahedron is parallel to the XY plane and **(d)** occurs when the tetrahedron's vertex sits on the XY plane. Reprinted with permission from [15], copyright 2020 by the American Physical Society.

2.4 Topological orbital moment

In conventional solid-state systems, the contribution of orbital angular momentum is often assumed to be quenched due to the presence of the crystal field. However, a study published in 2005 demonstrated that this assumption is not universally valid. In particular, the orbital angular momentum contribution plays a crucial role in explaining the spin Hall effect, indicating that orbital effects must be taken into account when describing spin–orbit-coupled phenomena [26]. This did not attract attention at that time but recently the spintronics community has started to consider the orbital angular momentum contribution to explain the Hall effects [27–29].

In this section, I discuss the concept of the *topological orbital moment* (TOM), which has recently attracted significant attention within the orbitronics community [29–33]. Unlike the recently reported orbital angular momentum (OAM) contribution observed in transport phenomena such as the orbital Hall effect [34], the TOM arises from the nontrivial real-space topology of magnetic textures and is therefore fundamentally different in origin and behavior. To develop an understanding of the TOM, it is helpful to begin with a brief overview of the basic principles of angular momentum in quantum systems.

The net angular momentum of electrons in a solid arises from the combination of two components: the spin and orbital angular momenta. The orbital angular momentum originates from the electron's motion around the nucleus, and this motion gives rise to a magnetic moment. Classically, this can be visualized as a circulating electric current in a closed loop, which generates a magnetic field according to Ampère's law.

In addition to this, electrons possess an intrinsic form of angular momentum known as spin. The spin quantum number for an electron is $s = \frac{1}{2}$, and the corresponding spin angular momentum takes on quantized values of $+\frac{\hbar}{2}$ and $-\frac{\hbar}{2}$, where $\hbar$ is the reduced Planck constant.

2.4.1 Scalar spin chirality

Now that we have had a look at some basics of angular momentum, our next topic of discussion is the scalar spin chirality (SSC), denoted as χ. This is important to understand the TOM. SSC is a box product in vector mathematics given by the following equation, where **a**, **b** and **c** are vectors: $\mathbf{a} \cdot (\mathbf{b} \times \mathbf{c})$

$$\chi = \mathbf{S}_i \cdot (\mathbf{S}_j \times \mathbf{S}_k) \tag{2.9}$$

The above equation defines the scalar spin chirality (SSC) χ in terms of the spin vectors at three atomic sites: i, j, and k. For non-coplanar spin textures, the scalar spin chirality becomes finite. In order to obtain a non-zero value of χ, the combined PT symmetry must be broken—that is, the spin texture must not remain invariant under simultaneous spatial inversion and time reversal [30].

In ferromagnetic systems, time-reversal symmetry is inherently broken due to the net magnetization. In contrast, collinear antiferromagnets often preserve a combined symmetry operation consisting of time reversal and lattice translation. This symmetry prohibits the emergence of anomalous Hall conductivity (AHC), which is a key signature of the anomalous Hall effect (AHE) [35].

However, in non-collinear coplanar antiferromagnets, the inclusion of spin–orbit coupling (SOC) lowers the overall symmetry of the system, thereby allowing for a finite anomalous Hall conductivity (AHC).

In non-coplanar antiferromagnets (AFMs), a non-zero anomalous Hall conductivity (AHC) is allowed and originates from a finite scalar spin chirality χ [35], even in the absence of spin–orbit coupling. It has to be made clear that in the case of non-collinear coplanar AFMs, the AHE owes its contribution to the Berry phase in the reciprocal space, while for non-coplanar AFMS, the AHE originates from the Berry phase accumulation in the real space [35].

To have a non-zero topological orbital moment (TOM), the orbital degeneracy needs to be lifted by some mechanism. The lifting of orbital and spin degeneracies can be lifted by other factors besides the spin-orbit coupling [31]. The beauty of the TOM lies in the fact of not requiring spin-orbit coupling. If the spin texture is non-coplanar, i.e. for $\chi \neq 0$, the orbital degeneracy can be lifted by higher order exchange interactions. As an additional note, it is worthy to mention that the concept of SSC in condensed matter physics gained attention with the discovery of high T_c cuprates which are strongly correlated superconductors [36–38].

A relevant AFM for the emergence of TOM is the 3Q state. The 3Q state as discussed before is a non-coplanar AFM state having a non-zero SSC. In the real space, an electron hopping amongst the non-coplanar spins of the 3Q state allows for an accumulation of a Berry phase, analogous to the acquiring of a geometrical phase in the Ahranov-Bohm effect [39]. This lifts the orbital degeneracy and favours a certain orbital current direction. The resultant orbital current gives rise to a magnetic moment analogous to a current in a circular wire giving rise to a magnetic field in classical electromagnetism (see Fig. 2.10).

This can also be explained via the fictitious or emergent magnetic field which is the magnetic field that would cause the electron to orbit amongst the three non-coplanar magnetic moments. The presence of a TOM can be detected via the spontaneous topological Hall effect (THE) shown recently, in the van der Waals magnets $CoTa_3S_6$ and $CoNb_3S_6$ [40]. A spontaneous THE corresponds to the accumulation of a Berry phase in the real space due to the intrinsic non-coplanar spin texture, unlike in the conventional THE, where an external magnetic field is applied to stabilize non-coplanar spin textures. A comprehensive review can be found where the different Hall effects and the confusion in terminologies in the community has been discussed [41].

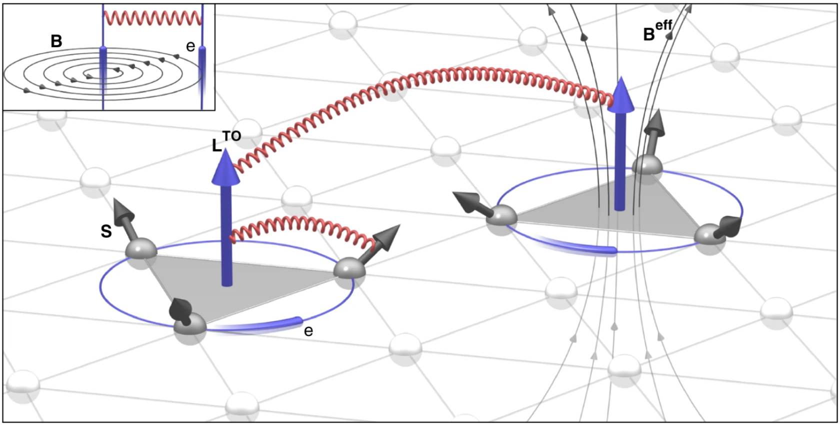

Figure 2.10: Non-coplanar spin structures inducing topological orbital moment via orbital currents. This schematic illustrates the mechanism for topological orbital moments (TOM) which give rise to topological chiral magnetic interactions. The gray circles represent atoms on a lattice. The black arrows labeled 'S' depict the intrinsic spin magnetic moments. The large blue arrows labeled 'L^{TO}' represent the TOM. The orbital motion of electrons amongst non-coplanar spins gives rise to a Berry phase in the real space. The emergent magnetic field (B^{eff}) gives rise to the local TOM on each triangular plaquette. The inset on the top left shows the classical analogue of a current in a circular loop giving rise to a magnetic field (B). Reprinted with permission from [32], copyright 2019 by Springer Nature.

$$\mathbf{L}_i^{\mathrm{TO}} = \sum_{(jk)} \kappa_{ijk}^{\mathrm{TO}} \chi_{ijk} \tau_{ijk} \tag{2.10}$$

The way the TOM couples to the scalar spin chirality is shown in Eqn. 2.10. In this equation, i, j, and k denote neighboring lattice sites, while the summation is over all pairs of neighboring lattice sites (jk) with respect to site i. $\kappa_{ijk}^{\mathrm{TO}}$ is the topological orbital susceptibility, which depends on the electronic structure. The vector $\boldsymbol{\tau}_{ijk} \propto (\mathbf{R}_j - \mathbf{R}_i) \times (\mathbf{R}_k - \mathbf{R}_i)$ represents the surface normal of the triangle spanned by the position vectors $\mathbf{R}_i$, $\mathbf{R}_j$, and $\mathbf{R}_k$ of the lattice sites i, j, and k, respectively [42]. Hence, the direction of the TOM is perpendicular to the plane defined by the non-coplanar spins.

Additionally, two springs colored in red are shown in Fig. 2.10. The long spring connects the localized TOMs of the two triangular plaquettes. The shorter spring corresponds to the interaction between the localized TOM and the spin of the corresponding plaquette. These two interactions are types of topological-chiral interactions where the former is the chiral-chiral interaction and the latter is called spin-chiral interaction.

2.5 Distorted 3Q state

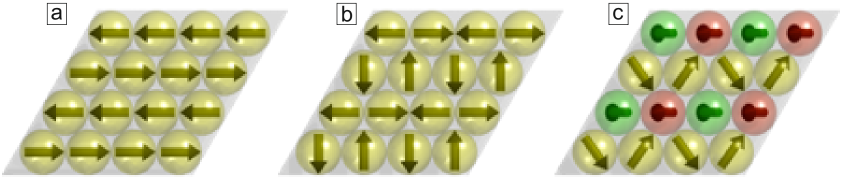

Figure 2.11: Schematic representation of antiferromagnetic states on a hexagonal lattice. **(a)** RW-AFM state or the 1Q state. **(b)** 2Q state which is a superposition of two 1Q states. **(c)** non-coplanar 3Q state that arises with the superposition of three 1Q states. Extracted from [43] and [44].

Fig. 2.11 illustrates the 1Q, 2Q, and 3Q magnetic states on a hexagonal lattice. The 1Q and 2Q configurations are coplanar (yellow spins), while the 3Q state is a non-coplanar antiferromagnetic configuration, as indicated in the figure by the red and green arrows representing the out-of-plane components of the spin vectors.

Distorted 3Q states, which deviate from the ideal tetrahedral spin arrangement, have been theoretically explored by Haldar et al. [43] using the Rodriguez rotation formalism. These intermediate states bridge the perfect 3Q configuration with other Q states (1Q and 2Q) through controlled spin rotations. This progression is demonstrated in Fig. 2.12, where the transformation from a 2Q state to a 1Q state occurs via a perfect 3Q state at $\alpha = 35^\circ$. Distorted 3Q configurations also emerge along this transition path, as seen for $\alpha = 50^\circ$ and $\alpha = 20^\circ$, highlighting the continuous tunability of the spin texture through angular modulation.

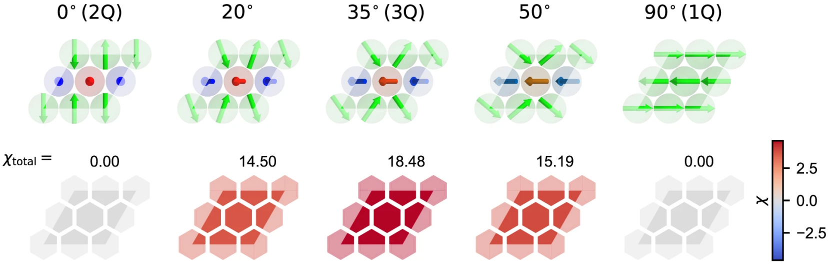

Figure 2.12: Evolution of scalar spin chirality and topological charge with the different Q states. Top row: Representative spin textures for varying spin configuration angles from 0° (2Q) to 90° (1Q). The 35° configuration corresponds to a non-coplanar 3Q state with significant scalar spin chirality. Bottom row: Corresponding maps of local scalar spin chirality χ, with red indicating positive and blue negative values. The total scalar chirality χ_{total} peaks at 35°, confirming maximal non-coplanarity in the 3Q regime, while collinear (1Q) and coplanar (2Q) states yield vanishing chirality. This figure is extracted from Ref. [45], copyright of Nature Springer 2025.

The distorted 3Q states have the angles between the neighbouring spins slightly deviating from the perfect 109.45 degrees. This distortion comes into effect due to the topological-chiral interaction as shown in Fig. 2.10

defined by the sixth order interaction term [43]. The bottom panel of Fig. 2.12 shows that the scalar spin chirality scales with the non-coplanarity of the spin structure and is reported to be the highest for the 3Q state and zero for the coplanar 1Q and 2Q states [45].

Bibliography

1. Sagawa, M., Fujimura, S., Togawa, N., Yamamoto, H. & Matsuura, Y. New material for permanent magnets on a base of Nd and Fe. *Journal of applied physics* **55,** 2083–2087 (1984).
2. Spaldin, N. A. *Magnetic materials: fundamentals and applications* (Cambridge university press, 2010).
3. Griffiths, D. J. & Schroeter, D. F. *Introduction to quantum mechanics* (Cambridge university press, 2018).
4. Blundell, S. *Magnetism in condensed matter* (OUP Oxford, 2001).
5. Kittel, C. & McEuen, P. *Introduction to solid state physics* (John Wiley & Sons, 2018).
6. Dupas, C. & Lahmani, M. *Nanoscience: Nanotechnologies and nanophysics* (Springer Science & Business Media, 2007).
7. Sucksmith, W. & Thompson, J. E. The magnetic anisotropy of cobalt. *Proceedings of the Royal Society of London. Series A. Mathematical and Physical Sciences* **225,** 362–375 (1954).
8. Tudu, B. & Tiwari, A. Recent developments in perpendicular magnetic anisotropy thin films for data storage applications. *Vacuum* **146,** 329–341 (2017).
9. Dubowik, J. Shape anisotropy of magnetic heterostructures. *Physical Review B* **54,** 1088 (1996).
10. Guo, S. *et al.* Size-specific magnetic configurations in electrodeposited epitaxial iron nanocuboids: from Landau pattern to vortex and single domain states. *Nano Letters* **22,** 4006–4012 (2022).
11. Lau, J. W., Beleggia, M. & Zhu, Y. Common reversal mechanisms and correlation between transient domain states and field sweep rate in patterned Permalloy structures. *Journal of Applied Physics* **102** (2007).

12. Lo Conte, R. *et al.* Coexistence of antiferromagnetism and superconductivity in Mn/Nb (110). *Physical Review B* **105,** L100406 (2022).
13. Beck, P., Schneider, L., Wiesendanger, R. & Wiebe, J. Systematic study of Mn atoms, artificial dimers, and chains on superconducting Ta (110). *Physical Review B* **107,** 024426 (2023).
14. Bode, M. *et al.* Structural, electronic, and magnetic properties of a Mn monolayer on W (110). *Physical Review B* **66,** 014425 (2002).
15. Spethmann, J. *et al.* Discovery of magnetic single-and triple-q states in Mn/Re (0001). *Physical review letters* **124,** 227203 (2020).
16. Rodríguez-Sota, A. *et al.* Phase Coexistence of Mn Trimer Clusters and Antiferromagnetic Mn Islands on Ir (111). *ACS nano* **18,** 3699–3706 (2024).
17. Hardrat, B. *et al.* Complex magnetism of iron monolayers on hexagonal transition metal surfaces from first principles. *Physical Review B—Condensed Matter and Materials Physics* **79,** 094411 (2009).
18. Spethmann, J., Grünebohm, M., Wiesendanger, R., von Bergmann, K. & Kubetzka, A. Discovery and characterization of a new type of domain wall in a row-wise antiferromagnet. *Nature Communications* **12,** 3488 (2021).
19. Kurz, P., Bihlmayer, G., Hirai, K. & Blügel, S. Three-dimensional spin structure on a two-dimensional lattice: Mn/Cu (111). *Physical review letters* **86,** 1106 (2001).
20. Song, C. *et al.* Altermagnets as a new class of functional materials. *Nature Reviews Materials,* 1–13 (2025).
21. Binder, K. & Young, A. P. Spin glasses: Experimental facts, theoretical concepts, and open questions. *Reviews of Modern physics* **58,** 801 (1986).
22. Hoffmann, M. & Blügel, S. Systematic derivation of realistic spin models for beyond-Heisenberg solids. *Physical Review B* **101,** 024418 (2020).

23. Cabra, D. C. & Pujol, P. Field-theoretical methods in quantum magnetism. *Quantum Magnetism,* 253–305 (2008).
24. Endoh, Y. & Ishikawa, Y. Antiferromagnetism of γ iron manganes alloys. *Journal of the Physical Society of Japan* **30,** 1614–1627 (1971).
25. Sakuma, A. First-principles study on the non-collinear magnetic structures of disordered alloys. *Journal of the Physical Society of Japan* **69,** 3072–3083 (2000).
26. Zhang, S. & Yang, Z. Intrinsic spin and orbital angular momentum Hall effect. *Physical review letters* **94,** 066602 (2005).
27. Wang, H. *et al.* Orbital Pumping in Ferrimagnetic Insulators. *Physical Review Letters* **134,** 126701 (2025).
28. El Hamdi, A. *et al.* Observation of the orbital inverse Rashba–Edelstein effect. *Nature Physics* **19,** 1855–1860 (2023).
29. Jo, D., Go, D., Choi, G.-M. & Lee, H.-W. Spintronics meets orbitronics: Emergence of orbital angular momentum in solids. *npj Spintronics* **2,** 19 (2024).
30. Martin, I. & Batista, C. Itinerant Electron-Driven Chiral Magnetic Ordering and Spontaneous Quantum Hall Effect<? format?> in Triangular Lattice Models. *Physical review letters* **101,** 156402 (2008).
31. Dos Santos Dias, M., Bouaziz, J., Bouhassoune, M., Blügel, S. & Lounis, S. Chirality-driven orbital magnetic moments as a new probe for topological magnetic structures. *Nature Communications* **7,** 13613 (2016).
32. Grytsiuk, S. *et al.* Topological–chiral magnetic interactions driven by emergent orbital magnetism. *Nature communications* **11,** 511 (2020).
33. Nickel, F. *et al.* Antiferromagnetic order of topological orbital moments in atomic-scale skyrmion lattices. *npj Spintronics* **3,** 7 (2025).

34. Mendoza-Rodarte, J., Cosset-Chéneau, M., Van Wees, B. & Guimarães, M. Efficient magnon injection and detection via the orbital rashba-edelstein effect. *Physical Review Letters* **132,** 226704 (2024).
35. Zang, J., Cros, V. & Hoffmann, A. *Topology in magnetism* (Springer, 2018).
36. Kalmeyer, V. & Laughlin, R. Equivalence of the resonating-valence-bond and fractional quantum Hall states. *Physical review letters* **59,** 2095 (1987).
37. Wen, X.-G., Wilczek, F. & Zee, A. Chiral spin states and superconductivity. *Physical Review B* **39,** 11413 (1989).
38. Lee, P. A. & Nagaosa, N. Gauge theory of the normal state of high-T c superconductors. *Physical Review B* **46,** 5621 (1992).
39. Peshkin, M. The aharonov-bohm effect part one: Theory. *The Aharonov-Bohm Effect,* 1–34 (2005).
40. Takagi, H. *et al.* Spontaneous topological Hall effect induced by non-coplanar antiferromagnetic order in intercalated van der Waals materials. *Nature Physics* **19,** 961–968 (2023).
41. Kimbell, G., Kim, C., Wu, W., Cuoco, M. & Robinson, J. W. Challenges in identifying chiral spin textures via the topological Hall effect. *Communications Materials* **3,** 19 (2022).
42. Saxena, V. *et al.* Strain-driven domain wall network with chiral junctions in an antiferromagnet. *arXiv preprint arXiv:2408.12580* (2024).
43. Haldar, S., Meyer, S., Kubetzka, A. & Heinze, S. Distorted 3 Q state driven by topological-chiral magnetic interactions. *Physical Review B* **104,** L180404 (2021).
44. Nickel, F. *et al.* Coupling of the triple-q state to the atomic lattice by anisotropic symmetric exchange. *Physical Review B* **108,** L180411 (2023).

45. Nickel, F. & Heinze, S. Topological properties of magnet-superconductor hybrid systems due to atomic-scale non-coplanar spin textures. *npj Spintronics* **3,** 13 (2025).

3 Experimental methods and setup

In this chapter, I introduce the techniques of scanning tunnelling microscopy (STM) and spin-polarized STM (SP-STM), along with the underlying mechanisms responsible for generating electronic and magnetic contrast in the acquired images. In addition, the sample preparation protocols employed for fabricating the systems studied in this thesis are described in detail.

3.1 Scanning tunneling microscopy

Optical microscopes were invented in the 17th century. As humanity progressed, so did science and engineering which led to the creation of the electron microscope. This was built by Ernst Ruska in around 1933 where he used magnetic coils to deflect a beam of electrons. The invention of the scanning tunnelling microscope (STM) took place in 1981 by Gerd Binnig and Heinrich Rohrer at IBM, Zurich.

Before the invention of the scanning tunnelling microscope, researchers were already studying the tunnelling effect [1]. Classically, objects cannot overcome an energy barrier without providing the required energy. However, in quantum mechanics, particles can pass through a barrier even without the required energy as shown in the sketch below in Fig. 3.1. This phenomenon arises from the wave-like nature of particles, whose probability amplitude decays exponentially within the barrier. The Nobel prize in 1973 for physics was awarded partly to Leo Esaki and Ivar Giaver for their tunnelling experiments with semiconductors and superconductors, respectively. The other half was awarded to Brian Josephson for the development of the theoretical framework of

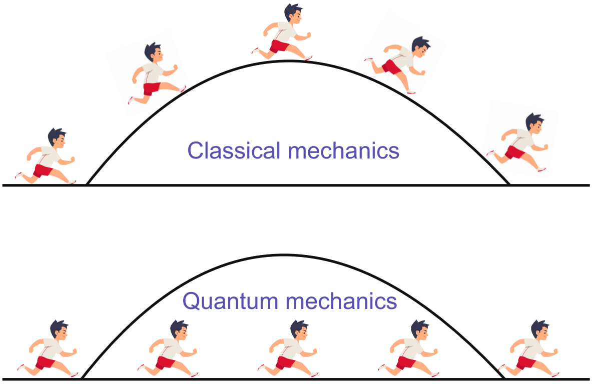

Figure 3.1: Classical vs. Quantum Tunneling Analogy. The top panel illustrates a scenario governed by classical mechanics, where a runner attempting to overcome a potential energy barrier (represented by the curved hill) must possess sufficient kinetic energy to reach the peak and then descend on the other side. In contrast, the bottom panel depicts a similar scenario under quantum mechanics. Here, there is a non-zero probability for the runner (representing a quantum particle) to "tunnel" through the potential energy barrier, even if their energy is lower than the barrier height. The multiple runners shown suggest the probabilistic nature of quantum mechanics, where there's a chance of finding the particle on the other side of the barrier without classically having enough energy to overcome it.

the tunneling effect across superconductors, which are now known as Josephson junctions [2].

This idea was put into play by Gerd Binnig and Heinrich Rohrer to develop the scanning tunnelling microscope in 1981 for which they shared the Nobel prize in 1986 with Ernst Ruska for the development of the electron microscope [2]. The technique of STM relies on the concept of quantum tunneling where an atomically sharp metallic tip is employed as the probe. This probe is at a distance of a few Angstroms from the metallic surface under investigation. Upon applying a voltage bias, electrons tunnel from the metallic tip to the conducting sample or vice versa. A schematic can be seen below in Fig. 3.2(a). This tunneling occurs even when the applied bias voltage is smaller than the height of the tunnelling barrier. These experiments can be performed at room temperature or even at very low temperatures down to 30mK using a dilution refrigerator [3].

A crucial engineering part of the STM are the piezoelectric actuators. These motors help the STM metallic tip to move very small distances while scanning, that are in the Angstrom scales. This precise control is what enables the STM to image samples with atomic resolution. The two main types of piezoelectric actuators used in STM are the tube scanners and the stick-slip types. When the tip is far away from the sample, i.e. in the range of milli- or centi-meters, the stick-slip actuators are used to provide for a coarse approach. When the tip is within a few atomic distances to the sample surface, the piezotube actuators are used for the lateral movement of the tip in the X and Y directions providing sub-Angstrom level precision. Fig. 3.2(b) shows a schematic of a piezotube scanner which has two electrodes for the X and Y directions, each for the lateral movement, and one electrode for the Z direction.

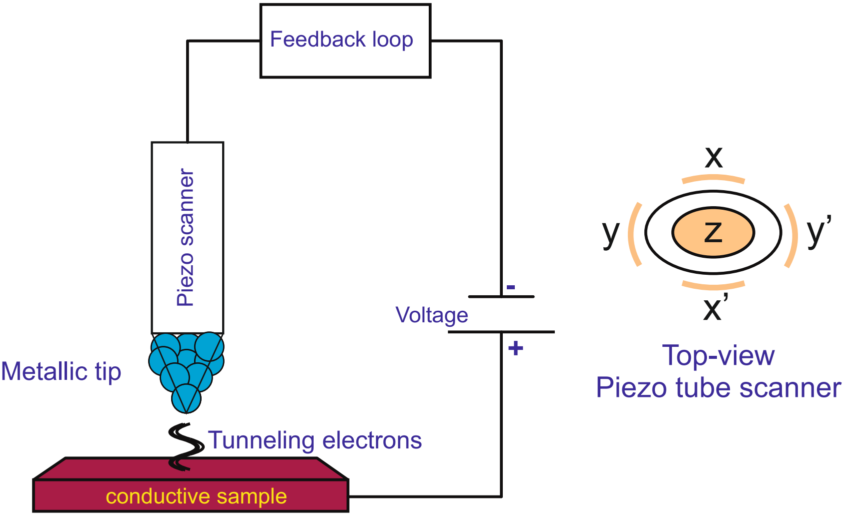

Figure 3.2: Schematic of a Scanning Tunneling Microscope (STM). A sharp metallic tip is brought close to a conductive sample, allowing electrons to tunnel across the vacuum barrier when a bias voltage is applied. The resulting tunneling current is kept constant by a feedback loop that adjusts the vertical position (z) of the tip via a piezoelectric scanner. The top-view diagram of the piezo tube scanner illustrates the segmented electrodes (x, y, x', y') responsible for lateral and vertical tip motion.

3.1.1 STM tunnelling current

The tunneling current in a scanning tunneling microscope (STM) originates from electrons quantum mechanically tunneling between the sample and the tip when a bias voltage V is applied. The total current is computed by summing over all energetically allowed electron states that can tunnel from the filled states of one electrode to the empty states of the other. This is formally expressed as:

$$\begin{aligned} I = \int_{-\infty}^{\infty} & [\rho_s(\epsilon)\, \rho_t(\epsilon - eV)\, f(\epsilon)\, (1 - f(\epsilon - eV)) \\ & +\rho_t(\epsilon)\, \rho_s(\epsilon - eV)\, f(\epsilon)\, (1 - f(\epsilon - eV))]\, |M|^2\, d\epsilon \end{aligned} \tag{3.1}$$

Here, $\rho_s(\epsilon)$ and $\rho_t(\epsilon)$ are the energy-dependent densities of states (DOS) of the sample and tip, respectively; $f(\epsilon)$ is the Fermi–Dirac distribution, and $|M|$ is the tunneling matrix element. The integration is carried out over all energies ϵ from $-\infty$ to ∞, accounting for all possible initial and final states involved in the tunneling process.

The two terms in Eq. (3.1) correspond to electrons tunneling from the sample to the tip and vice versa. The expressions $f(\epsilon)[1 - f(\epsilon - eV)]$ and $f(\epsilon)[1 - f(\epsilon + eV)]$ represent the occupation probabilities that ensure electrons only tunnel from filled to empty states.

At low temperatures (typically $\sim 4\,\mathrm{K}$), the Fermi–Dirac distribution can be approximated by a step function, and thermal broadening becomes negligible. In this limit, only states within an energy window defined by the applied bias eV contribute to tunneling. If the Fermi level of the tip is defined as the reference energy $\epsilon = 0$, then the Fermi level of the sample shifts by eV under applied bias. The tunneling current thus simplifies to:

$$I \propto \int_0^{eV} |M|^2 \, \rho_s(\epsilon) \, \rho_t(\epsilon - eV) \, d\epsilon \tag{3.2}$$

The integration limits from 0 to eV reflect the energy window over which occupied states in one electrode (e.g., the sample) align with unoccupied states in the other (e.g., the tip). The point $\epsilon = 0$ corresponds to the Fermi level of the tip (assumed grounded), and $\epsilon = eV$ corresponds to the Fermi level of the biased sample.

Assuming the tip DOS is nearly constant near the Fermi energy, i.e., $\rho_t(\epsilon - eV) \approx \rho_t(0)$, and if the matrix element $|M|$ is also approximately energy-independent, they can be pulled out of the integral. The current expression then becomes:

$$I \propto |M|^2 \, \rho_t(0) \int_0^{eV} \rho_s(\epsilon) \, d\epsilon \tag{3.3}$$

This equation reveals that the tunneling current is directly proportional to the integrated local density of states (LDOS) of the sample over the bias window, making STM a powerful probe of the sample's electronic structure.

To evaluate the matrix element $|M|$, we model the vacuum barrier between the tip and sample as a rectangular potential barrier. Using the WKB approximation, the matrix element takes the form:

$$|M|^2 \propto e^{-2\kappa d} \quad \text{with} \quad \kappa = \frac{\sqrt{2m\phi}}{\hbar} \tag{3.4}$$

Here, d is the tip–sample distance, m is the electron mass, and ϕ is the effective barrier height, typically taken as the average of the tip and sample work functions.

Combining Eqs. (3.3) and (3.4), the final form of the tunneling current becomes:

$$I \propto \rho_t(0)\, e^{-2\kappa d} \int_0^{eV} \rho_s(\epsilon)\, d\epsilon \tag{3.5}$$

This expression shows that the STM current depends exponentially on the tip–sample distance and linearly on the integrated LDOS of the sample over the applied bias window. It forms the basis for interpreting STM topographic and spectroscopic measurements.

3.1.2 Measurement modes

- **Constant-current mode**: This is the most commonly used measurement mode in STM experiments. In this approach, the tunneling current between the tip and the sample is pre-defined by the user. While scanning, any deviation in the tunneling current is corrected by a feedback loop that dynamically adjusts the vertical position (z) of the tip to maintain a constant current. The resulting z-position signal of the tip, recorded as a function of lateral position, is used to generate the topographic image of the surface.
- **Constant-height mode:** In this mode, the vertical distance between the tip and the sample is kept fixed during scanning, and the feedback loop is disabled. As a result, the tunneling current varies depending on the local surface topography and electronic structure. This mode is particularly useful for studying fast dynamic processes such as atom diffusion or molecular interactions, where maintaining feedback control could interfere with the measurement [4, 5]. However, it is typically used only on atomically flat surfaces to avoid the risk of tip crashes due to sudden height variations.

- **Differential conductance**: Differential conductance, or dI/dU, represents the variation of the tunneling current arising from a small modulation in the applied bias voltage. This signal is typically measured using a lock-in amplifier, which detects the current response to a sinusoidal voltage modulation superimposed on the DC bias. Eqn. 3.5 shows that the STM tunneling current is sensitive to the integrated local density of states (LDOS) of the sample from the Fermi level up to the applied bias voltage V. In differential conductance (dI/dV) measurements, commonly used in scanning tunneling spectroscopy (STS), the signal is proportional to the LDOS at the energy $E = E_F + eV$:

  $$\frac{dI}{dV}(r, V) \propto \rho_s(r, E_F + eV)$$

  The dI/dU imaging mode is important because it provides spatially resolved information about the local density of states (LDOS) of the sample. This allows access to the electronic structure with both energy and spatial resolution, making it a powerful tool for studying surface states, electronic inhomogeneities, and quasi-particle interference patterns [6].

3.2 Spin-polarized scanning tunneling microscopy

After introducing the working principle and measurement modes of STM, we can now move to a magnetic version of it, called spin-polarized scanning tunnelling microscopy (SP-STM). In SP-STM, the tip is magnetic which then allows for spin-polarized tunnelling of electrons into a magnetic sample, shown in the schematic below.

In this scenario, the magnetic contrast is obtained via the tunnelling

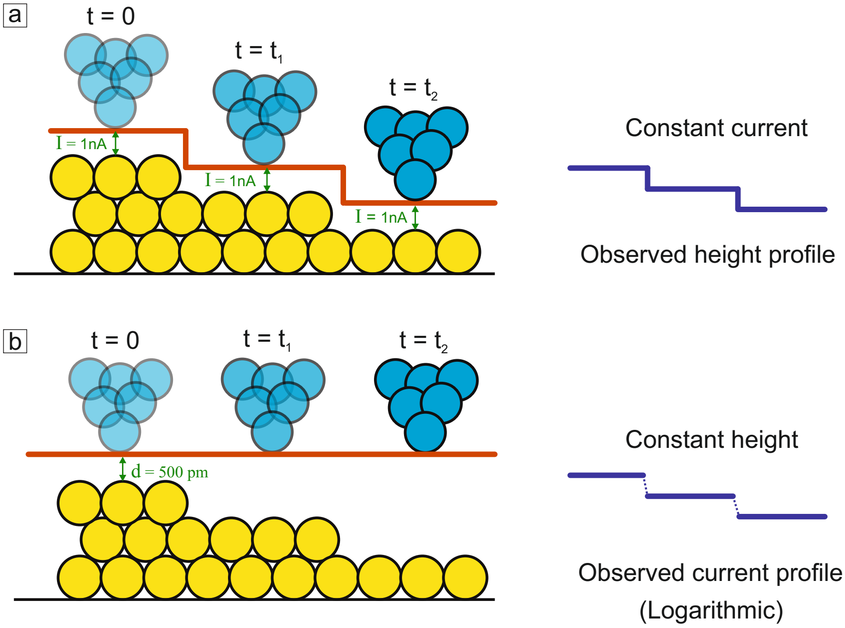

Figure 3.3: Scanning tunneling microscopy imaging modes. **(a)** Illustration of the constant-current mode in STM. As the sharp metallic tip (blue spheres) scans over a stepped surface of the conductive sample (yellow spheres), the vertical position of the tip is adjusted by the feedback loop to maintain a constant tunneling current ($I = 1\,\mathrm{nA}$ in this example). The trace of the tip's vertical movement over time ($t = 0, t_1, t_2$) reflects the topography of the sample surface, resulting in the observed profile shown on the right. **(b)** Illustration of the constant-height mode in STM. In this mode, the vertical position of the tip is kept constant (at a distance $d = 500\,\mathrm{pm}$ from a reference plane). As the tip scans over the stepped surface, the tunneling current varies depending on the tip-sample distance. The changes in the tunneling current over time ($t = 0, t_1, t_2$) are then recorded to generate the topographical image of the sample surface, resulting in the observed profile shown on the right. A step-like appearance emerges when the current is plotted on a logarithmic scale, reflecting its exponential dependence on the surface topography.

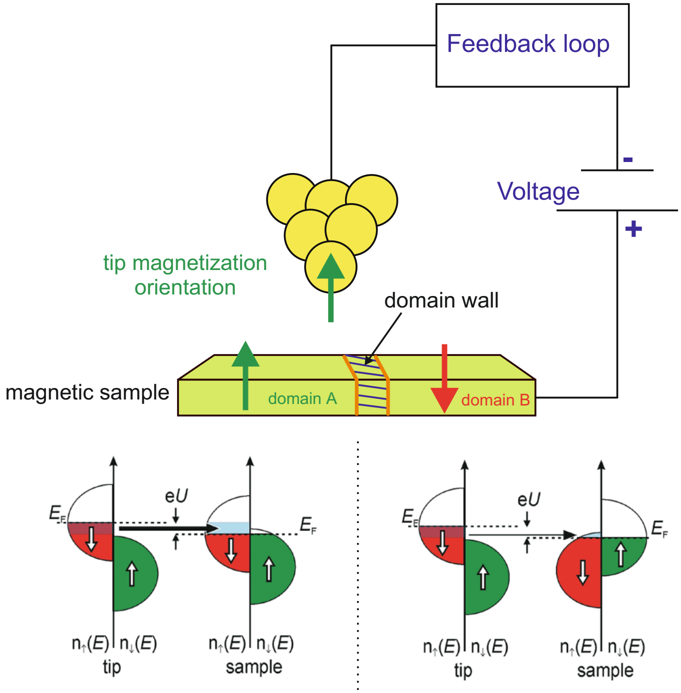

Figure 3.4: Spin-polarized scanning tunneling microscopy (SP-STM). A schematic depicts a scenario where the STM tip's magnetization orientation is parallel to domain A and antiparallel to domain B. When scanning with such a ti and sample, the topography would appear higher for domain A and lower for domain B. The tunneling process happening in these two cases is shown by the LDOS schematic on the left and right side based on the tunneling magnetoresistance effect. The LDOS schematic shown in the figure is reprinted with permission from [7], copyright 2009 by the American Physical Society.

magneto-resistance (TMR) effect [8]. In the TMR effect, the tunnelling current is maximum when the magnetization of the tip and sample are parallel and is minimum when they are antiparallel. When the tip and sample's magnetization are orthogonal, there is no spin-dependent tunnelling current. This can be understood from the following equation, where the dependence of the tunnelling current on the tip and sample's spin polarization and the angle θ between the their magnetization orientations is shown.

$$I \propto \rho_s \rho_t (1 + P_s P_t \cos\theta) \tag{3.6}$$

In the above equation, P_s and P_t are the spin polarizations of the sample and tip respectively. θ is the relative angle between the magnetization orientations of the tip and the sample. The TMR effect can be understood by the spin-resolved LDOS of the tip and sample. If the majority LDOS of the tip and sample have the same (opposite) spin polarization, the tunnelling current will be high (low). This can be seen from the equation below:

$$I \propto \int_{E_F}^{E_F+eV} \left[\rho_s^{\uparrow}(E) \rho_t^{\uparrow}(E - eV) + \rho_s^{\downarrow}(E) \rho_t^{\downarrow}(E - eV) \right] dE \tag{3.7}$$

In the above equation, $\rho_s^{\uparrow}(E)$ and $\rho_s^{\downarrow}(E)$ denote the spin-resolved local density of states (LDOS) of the sample, while $\rho_t^{\uparrow}(E)$ and $\rho_t^{\downarrow}(E)$ are the spin-resolved LDOS of the tip apex. The applied bias voltage is denoted by eV [9].

The spin polarization P is defined as:

$$P = \frac{\rho^{\uparrow} - \rho^{\downarrow}}{\rho^{\uparrow} + \rho^{\downarrow}} \tag{3.8}$$

where $\rho^{\uparrow}$ and $\rho^{\downarrow}$ refer to the spin-up and spin-down LDOS, respectively. The spin polarization can be defined separately for the tip (P_t) and the sample (P_s), and is crucial in determining the magnetic contrast observed in spin-polarized STM measurements.

Fig. 3.5 shows a sketch where spin-polarized tunnelling has been shown for both scenarios of the tip and sample: parallel and anti-parallel magnetization of the tip and sample. As the tunnelling is happening from the tip in this case, the magnetization of the tip is fixed. In the parallel (antiparallel) configuration of the sample magnetization, a high (low) spin-polarized tunneling current is observed giving rise to magnetic contrast down to the atomic scale. Some important discoveries using SP-STM can be found in references [10–14].

3.2.1 Electronic contrast mechanisms

As discussed above, the tunneling magnetoresistance (TMR) effect is the primary mechanism responsible for obtaining magnetic contrast in spin-polarized scanning tunneling microscopy (SP-STM) when both the tip and the sample are magnetic. However, even in the absence of a magnetic tip, a conventional metallic STM tip can still provide information related to the magnetic properties of the sample. This is possible due to the presence of additional magnetoresistive effects, beyond TMR, that can yield contrast sensitive to local magnetic configurations. In the following, a few of these mechanisms are briefly discussed.

- **Tunneling anisotropic magneto-resistance**: Tunneling Anisotropic Magnetoresistance (TAMR) is a phenomenon observed in spin-polarized scanning tunneling microscopy (SP-STM), where the tunneling conductance depends on the orientation of the magnetization with respect to the crystallographic axes, even when the tip itself is non-magnetic. Unlike

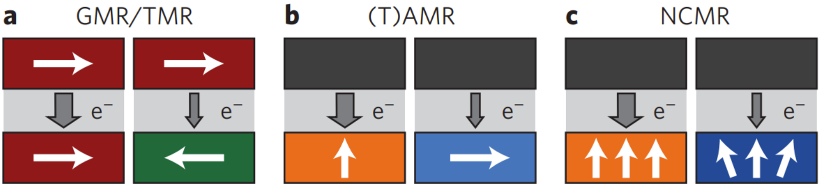

Figure 3.5: Schematic illustrations of different magneto-resistive effects. This figure presents simplified diagrams illustrating the underlying principles of three magnetoresistive phenomena: **(a)** Giant magnetoresistance (GMR) or Tunnel magnetoresistance (TMR), **(b)** (Tunneling) anisotropic magnetoresistance ((T)AMR), and **(c)** Non-collinear magnetoresistance (NCMR). Reprinted with permission from [15], copyright 2015 of Springer Nature.

conventional SP-STM contrast, which arises from the relative spin polarization between tip and sample, TAMR originates from spin–orbit coupling in the sample, which modulates the local density of states (LDOS) depending on the magnetization direction.

In SP-STM experiments, TAMR manifests as a change in the tunneling current (or dI/dU signal) when the sample magnetization is rotated, for example by applying an external magnetic field, even if the spin polarization of the tip remains fixed or is zero. TAMR allows for imaging magnetic domain structures without the need for a spin-polarized tip and provides access to magneto-crystalline anisotropy at the atomic scale.

- **Non-collinear magneto-resistance**: This effect was discovered in 2015 to play a role in providing electronic contrast for the imaging of skyrmions with a non-magnetic STM tip in the ultra-thin film system of Pd/Fe/Ir(111) [15]. This magneto-resistance arises in non-collinear spin textures present in a collinear background, for example having skyrmions in a ferromagnet. When spins become non-collinear, the relative orientation of neighboring spins affects the spin-dependent hybridization and mixing of electronic states, which in turn modifies the local density of states (LDOS). This is then reflected as a variation in the dI/dU signal. In this thesis, the non-collinear magnetic domain walls are visible in almost all images due to a small contribution from the NCMR contrast. Other effects contributing to the domain wall contrast will be mentioned later.

3.3 Sample and tip preparation

Here, I will present the preparation methods used for the samples in this thesis and for the spin-polarized tips.

3.3.1 Sample preparation

The samples prepared in this thesis were deposited using molecular beam epitaxy (MBE), a technique in which material is evaporated slowly onto a substrate under ultra-high vacuum (UHV) conditions, typically in the range of 10^{-9} to 10^{-11} mbar. The source material is evaporated either using a Knudsen cell or an electron-beam (e-beam) evaporator. A Knudsen cell consists of a resistively heated crucible that allows thermal evaporation of the material, providing stable and low flux rates suitable for volatile elements. In contrast, an e-beam evaporator uses a focused electron beam to heat and sublime high-melting-point materials, such as refractory metals, from a rod or a crucible.

MBE allows for highly controlled layer-by-layer growth, resulting in atomically flat surfaces. Under UHV conditions, the mean free path of the evaporated atoms typically exceeds several meters, which is significantly longer than the distance between the evaporator and the substrate (usually on the order of tens of centimeters). This ensures a ballistic trajectory of atoms toward the substrate, minimizing scattering and enabling precise film growth. The mean free path depends on both the residual gas pressure and the kinetic energy (or temperature) of the evaporated atoms. MBE remains the method of choice for achieving atomically smooth and high-purity thin films [16].

In this thesis, Mn layers on Ir(111) have been deposited which range from one to four layers of Mn. Two kinds of growth protocols have been used in this thesis. Before proceeding to the two kinds of protocols, I would like to mention the general steps followed during the sample preparations.

The cleaning of the Ir(111) crystal is carried out to remove any magnetic overlayers that may remain from previous sample preparations. This is achieved by bombarding the surface with a beam of ionized argon (Ar) atoms. Argon gas is ionized by generating a plasma within the chamber using a high-voltage electric field. To direct the Ar^+ ions toward the crystal surface, the sample is held at a negative bias voltage. This creates an electrostatic potential difference that accelerates the positively charged ions toward the substrate, enabling them to sputter off surface contaminants through momentum transfer.

During ion bombardment, the chamber pressure is maintained in the range of 10^{-5} to 10^{-6} mbar. At this stage, only the turbo-molecular pump is engaged, while the ion-getter pump remains off. This is because ion-getter pumps are sensitive to contamination from inert gases such as argon, which are commonly used during sputtering. Operating the ion-getter pump in the presence of high partial pressures of argon can lead to implantation or degradation of the pump elements. Once ion sputtering is complete and the chamber is evacuated to lower pressures, typically below 10^{-6} mbar, the ion-getter pump is activated to further reduce the pressure to ultra-high vacuum levels around 10^{-11} mbar.

Following Ar ion bombardment, the Ir(111) crystal is annealed at high temperatures of around 1500 K for 1 minute. This annealing step is performed twice, with a 30-second interval in between. The ion bombardment process introduces vacancies and defects at the surface and within the near-surface layers of the crystal. During annealing, increased atomic mobility enables surface diffusion of Ir atoms, which helps to reorganize and smooth the surface by filling in vacancies and minimizing surface energy. This process results in the formation of atomically flat Ir(111) terraces [17].

Now we can have a look at the two approaches used for the samples grown in this thesis:

- **Near room temperature samples**: In this approach, the samples were prepared without any substrate annealing involved. The Mn evaporator was pre-heated to 690°C before deposition. The duration of deposition was typically in the range of 5 to 20 minutes to get a coverage of around 1.5 to 3.5 MLs.
- **Beyond room temperature samples**: In this approach, we anneal the substrate during the deposition of Mn via resistive heating. The substrate is pre-heated to a fixed temperature and then this temperature is maintained during the deposition of Mn. The annealing temperatures used in this thesis range from 250°C to 350°C.
- **Island growth**: In this approach, the samples were prepared without any substrate annealing involved. The Mn evaporator was preheated to 690°C before deposition. The duration of deposition was for 9.5 minutes to achieve a coverage of around 1.2 MLs. To get island growth, Mn was deposited for around 90 minutes after the Ir crystal was flashed (at 50W) to have a clean surface.

Following the growth, the sample is then transferred to the STM chamber. It is to be noted that all the sample preparation steps are done in UHV and all the growth chambers are connected to the STM chambers. Hence, the sample always experiences UHV conditions and is never exposed to higher pressures or air.

3.3.2 Tip preparation

To get an atomically sharp metallic tip, the general method is to use electro-chemical etching. The STM tips used in this thesis were made of Cr and W. W is a non-magnetic metallic tip, while Cr is a bulk antiferromagnetic metallic tip.

To perform SP-STM measurements with a controlled magnetization of the tip using external magnetic fields, the 8K STM setup is used (see Fig. 3.6). In this setup, the lowest temperature that can be achieved is 8K. The STM is operated in a standard low temperature cryostat with an outer casing of liquid Nitrogen and an inner casing of liquid Helium. In this setup, to carry out controlled SP-STM measurements, the W-tip is made magnetic by coating it with Fe. Fe is deposited on the W tip via MBE by heating an Fe rod. Approximately, 40 to 50 monolayers of Fe are deposited on the W-tip. This thickness of Fe results in an in-plane magnetic anisotropy at zero external magnetic field due to the shape anisotropy [18]. At an applied field of 2.5T, the Fe/W tip's magnetization is nearly OOP. This helps us to image in-plane and OOP components of a sample's spin texture. A maximum of 3T can be applied in this setup.

An alternative approach for getting a magnetic tip is to simply poke the STM tip into the magnetic surface of the sample. This is a trial and error method, where the parameters such as poking depth and bias voltage during poking are varied. After every attempt, the magnetic surface is

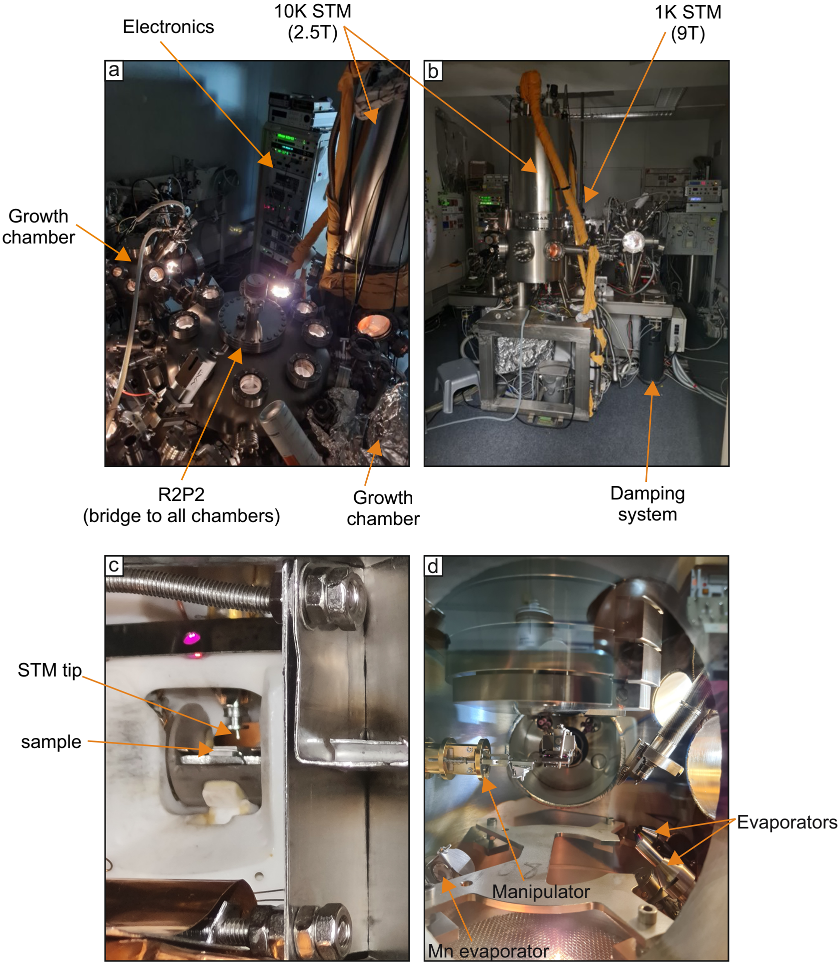

Figure 3.6: UHV chambers for sample growth and low-temperature STM. (a, b) Overview of the measurement lab showing the growth chamber and the 8K STM, operable at 2.5T. The "R2P2" system enables sample transfer across the setup. **(c)** Close-up of the STM stage with the tip positioned near the sample in UHV. **(d)** Detailed view of the growth chamber, showing material evaporators and the sample manipulator for precise positioning and heating.

scanned to verify if the tip is magnetic or not.

The 1K - STM setup (see Fig. 3.6) uses a bulk Cr antiferromagnetic tip. Being AFM, it helps to not influence the sample's magnetization while scanning. Most of the SP-STM images shown in this thesis are measured in the 1K - STM setup at 4 K. A maximum of 9T OOP magnetic field can be applied in this setup.

Bibliography

1. Merzbacher, E. The early history of quantum tunneling. *Physics Today* **55,** 44–49 (2002).
2. Robinson, A. L. Electron Microscope Inventors Share Nobel Physics Prize: Ernst Ruska built the first electron microscope in 1931; Gerd Binnig and Heinrich Rohrer developed the scanning tunneling microscope 50 years later. *Science* **234,** 821–822 (1986).
3. Marz, M., Goll, G. & Löhneysen, H. v. A scanning tunneling microscope for a dilution refrigerator. *Review of Scientific Instruments* **81** (2010).
4. Moresco, F. *et al.* Low temperature manipulation of big molecules in constant height mode. *Applied Physics Letters* **78,** 306–308 (2001).
5. Siegert, B., Donarini, A. & Grifoni, M. The role of the tip symmetry on the STM topography of-conjugated molecules. *physica status solidi (b)* **250,** 2444–2451 (2013).
6. Stroscio, J. A. & Kaiser, W. J. *Scanning tunneling microscopy* (Academic press, 1993).
7. Wiesendanger, R. Mapping spin structures on the atomic scale. *Europhysics News* **38,** 16–21 (2007).
8. Parkin, S. S. *et al.* Giant tunnelling magnetoresistance at room temperature with MgO (100) tunnel barriers. *Nature materials* **3,** 862–867 (2004).
9. Wiesendanger, R. & Güntherodt, H.-J. *Scanning tunneling microscopy III: theory of STM and related scanning probe methods* (Springer Science & Business Media, 2013).
10. Wiesendanger, R., Güntherodt, H.-J., Güntherodt, G., Gambino, R. & Ruf, R. Observation of vacuum tunneling of spin-polarized electrons with the scanning tunneling microscope. *Physical Review Letters* **65,** 247 (1990).

11. Heinze, S. *et al.* Spontaneous atomic-scale magnetic skyrmion lattice in two dimensions. *Nature physics* **7,** 713–718 (2011).
12. Romming, N. *et al.* Writing and deleting single magnetic skyrmions. *Science* **341,** 636–639 (2013).
13. Von Bergmann, K., Kubetzka, A., Pietzsch, O. & Wiesendanger, R. Interface-induced chiral domain walls, spin spirals and skyrmions revealed by spin-polarized scanning tunneling microscopy. *Journal of Physics: Condensed Matter* **26,** 394002 (2014).
14. Wulfhekel, W. & Kirschner, J. Spin-polarized scanning tunneling microscopy of magnetic structures and antiferromagnetic thin films. *Annu. Rev. Mater. Res.* **37,** 69–91 (2007).
15. Hanneken, C. *et al.* Electrical detection of magnetic skyrmions by tunnelling non-collinear magnetoresistance. *Nature nanotechnology* **10,** 1039–1042 (2015).
16. Arthur, J. R. Molecular beam epitaxy. *Surface science* **500,** 189–217 (2002).
17. Kurnosikov, O., Kulikov, D., Kharlamov, V., Swagten, H. & Trushin, Y. V. Temperature-induced evolution of subsurface nanocavities in argon-implanted copper. *Physical Review B—Condensed Matter and Materials Physics* **84,** 054109 (2011).
18. Pietzsch, O. *Magnetic imaging by spin-polarized scanning tunneling spectroscopy applied to ultrathin Fe/W (110) films* PhD thesis (Staats- und Universitätsbibliothek Hamburg Carl von Ossietzky, 2001).

4 Double layer of Mn on Ir(111)

Abstract

This chapter presents novel findings for the Mn bilayer grown on Ir(111). This atomic-scale system exhibits a row-wise antiferromagnetic (AFM) state with distinct rotational domains. Domain walls have the coplanar 2Q state, which have been imaged with high electronic and magnetic contrast down to the atomic scale. It has been demonstrated, that trapping Argon bubbles intentionally in the Ir substrate helps to generate a large domain wall network with interconnected junctions. Different kinds of junctions have been imaged in this network which comprise of triple domain wall junctions and hexa-junctions. These junctions have been shown to host the 3Q AFM state and an associated topological orbital moment. Additionally, the system undergoes a large structural shift due to the magnetic order, where the 2^{nd} *ML shifts by almost 40 percent of the lattice constant with respect to the* 1^{st} *ML at zero applied magnetic field.*

4.1 Introduction

The bilayer system of Mn/Ir(111) was selected for the investigation of antiferromagnetic (AFM) spin textures, primarily due to the geometric frustration induced by the hexagonal symmetry of the Ir(111) substrate. A related system, namely a monolayer of Mn on Re(0001), has previously demonstrated that different stacking sequences—fcc and hcp, stabilize distinct magnetic ground states: the row-wise antiferromagnetic (RW-AFM or 1Q) state and the 3Q state, respectively [1]. Furthermore, magnetic domain walls exhibiting 2Q type spin configurations have been observed in the fcc-stacked Mn/Re(0001) [2].

This chapter addresses the challenge of inducing magnetic domain walls in an AFM, as introduced in Chapter 2. It is demonstrated that by appropriately tuning external parameters during the growth process, AFM domain walls can be reliably induced in the Mn bilayer on Ir(111). The methodology and findings presented here are expected to be broadly applicable to a wider class of AFM materials.

An intriguing aspect of the Mn bilayer system is the occurrence of a structural shift occurring due to the onset of magnetic order. This phenomenon has been investigated at the atomic scale, with insights obtained from density functional theory (DFT) calculations.

From a topological perspective, the Mn bilayer system hosts localized non-coplanar AFM states carrying a finite topological charge. These states are associated with a non-zero topological orbital moment, the origin and implications of which are discussed in conjunction with DFT results.

4.2 Growth of the Mn bilayer on Ir(111)

This section examines the growth of the Mn bilayer on Ir(111) under different conditions, i.e., near room temperature and at elevated temperatures involving in-situ annealing with Argon ion implantation. While the focus here is on the bilayer, it is worth noting that the Mn monolayer has been studied previously [3] and is known to grow as isolated clusters at sub-monolayer coverage, eventually forming a pseudomorphic layer as it approaches a closed monolayer. Magnetic domain walls in the Mn bilayer appear with pronounced contrast, making them readily observable in nearly every image, regardless of the specific growth conditions. Hence, this chapter is structured strategically to provide a clear understanding of both the magnetic and growth properties of the Mn bilayer on Ir(111).

4.2.1 Near room-temperature growth

Fig. 4.1 gives an overview of the sample growth near room temperatures. A step-flow growth is observed where regions of the ML and the DL can be seen. Fig. 4.1(a) shows a partially differentiated topography image whose simultaneous differential conductance (dI/dU) map is shown in panel (b). In Fig. 4.1(c), it can be seen that amongst the structural features, zig-zag shaped dislocation lines and reconstruction lines occur on the DL in an otherwise largely pseudomorphic area. The zig-zag dislocation lines exist on the DL just next to the buried step edge to the ML. The reconstruction line marked in panel (c) occurs in the $[11\bar{2}]$ direction perpendicular to the close packed rows. Also, one can see islands having a dark contrast that corresponds to impurities present in the STM chamber, most probably being hydrogen. These aspects will be shown in detail in the following sections with respect to their interplay with magnetism.

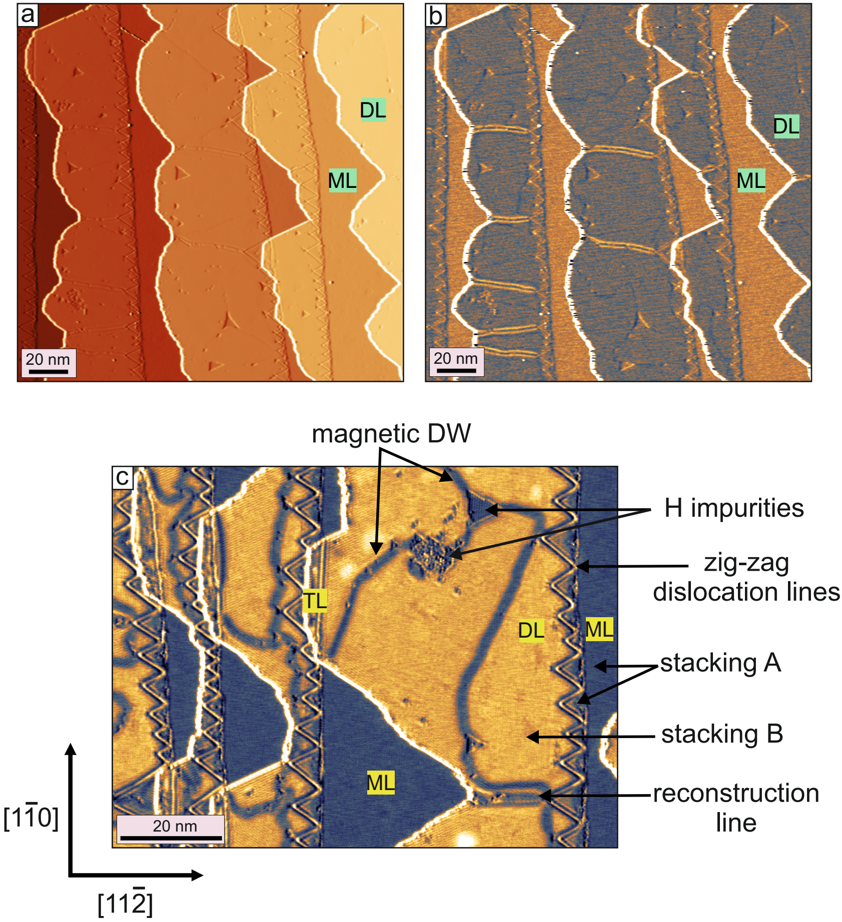

Figure 4.1: Overview of the DL growth at near room temperatures. (a,b) constant-current topography and dI/dU images of a sample area with a coverage of 1.7 atomic layers (ALs). **(c)** A dI/dU image showing areas of the ML and DL revealing various surface defects and structural features. These include zig-zag dislocation lines, H impurities (appearing as dark spots), regions with different stacking (stacking A and stacking B), and a reconstruction line. The ML and DL regions are also labeled. The crystallographic directions [11$\bar{2}$] and [111] are indicated by arrows. (Measurement parameters: $U = +100\,\text{mV}$, $I = 1\,\text{nA}$; c: $U = +10\,\text{mV}$, $I = 1\,\text{nA}$; c: $U = +10\,\text{mV}$, $I = 1\,\text{nA}$; all: $T = 4\,\text{K}$).

4.3 Magnetism of the Mn bilayer on Ir(111)

In this section, we will discuss the magnetic ground state, domains and domain walls observed for the DL system. We will see in section 4.9, how tuning the growth parameters helps us to induce large domain wall networks in the bilayer system.

4.3.1 Magnetic ground state of the ML and DL

Fig. 4.2 presents spin-polarized STM (SP-STM) measurements of the Mn double layer (DL) on Ir(111). Panels (a) and (b) show regions exhibiting a stripe-like magnetic contrast, which corresponds to the row-wise antiferromagnetic (RW-AFM) spin texture. Owing to the hexagonal symmetry of the Ir(111) substrate, the Mn bilayer accommodates three rotational magnetic domains, indicated by schematic overlays in Fig. 4.2(a). In panel (b), both the monolayer (ML) and DL regions of Mn/Ir(111) are visible. The ML displays a hexagonal contrast pattern consistent with the Néel-type antiferromagnetic order [3], while the DL maintains the RW-AFM structure [4]. A buried step edge, indicated by a dotted line, separates the two regions; a zigzag-shaped dislocation line is observed at this interface within the DL. If one follows the solid line on the ML, it can be seen that there is an inversion of the magnetic contrast. This most probably corresponds to the existence of two domains in the Néel state with a domain wall somewhere in between. This would be interesting to investigate further and more details on the Mn monolayer on Ir(111) with respect to the growth and magnetism have been reported by Rodríguez-Sota et al. [3].

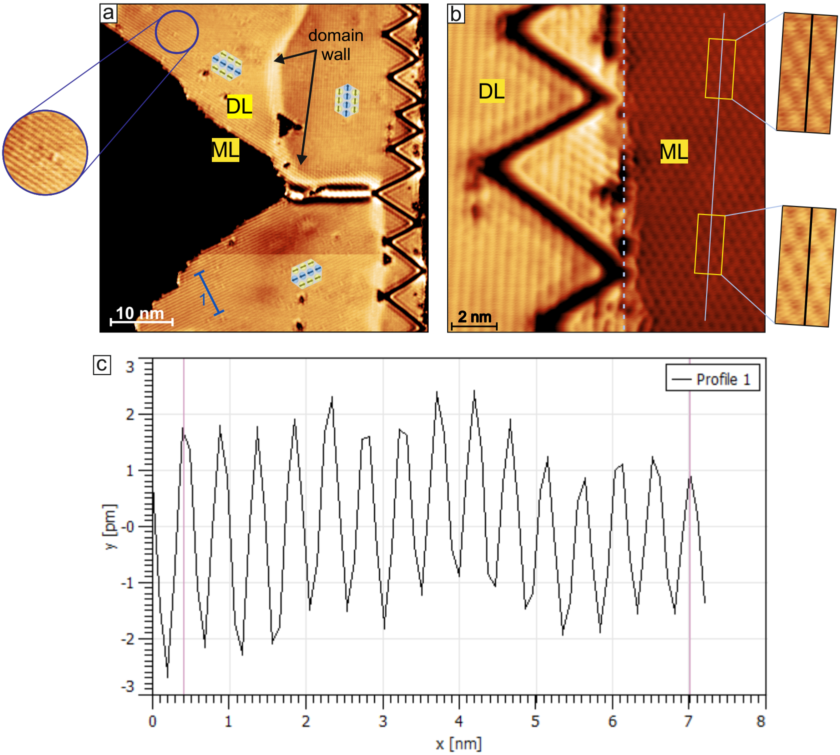

Figure 4.2: SP-STM images showing the magnetic ground states of the ML and DL. (a) constant-current topography image displaying ML and DL regions. A magnetic domain wall (labelled), separates rotational domains exhibiting the RW-AFM state. The blue schematics illustrate the orientation of the RW-AFM domains. **(b)** A constant-current topography image showing the antiferromagnetic ground states of the ML (Néel) and DL (RW-AFM) region across a buried step edge (white dotted line). Zoomed-in sections on the right reveal an inversion of the magnetic contrast in the ML suggesting the occurrence of a domain wall in between. **(c)** Line profile taken on an area of the DL marked in panel (a). The vertical red lines drawn in the graph correspond to a distance of 6.6 nm, which averaged over 14 peaks amounts to 471 pm being equal to $\sqrt{3}a$, where a is the Ir lattice constant of 271pm.(Measurement parameters: a: $U = +10\,\text{mV}$, $I = 1\,\text{nA}$; b: $U = 2\,\text{mV}$, $I = 9\,\text{nA}$; all: $T = 4\,\text{K}$).

4.3.2 Magnetism induced structural shift

Magnetostriction - the change in shape or length of a material in response to an applied magnetic field, has been a subject of scientific interest since the pioneering experiment by Joule in 1842 [5]. In his study on an iron rod, Joule observed that sections of the rod aligned parallel to the applied magnetic field expanded, while those perpendicular to the field contracted. Despite the significance of these findings, the small magnitude of the observed dimensional changes led to limited attention at that time.

Interest in magnetostriction was revived in 1873 following the experiments by Mayer [6], who discovered that steel initially expands along the axis of magnetization under weak magnetic fields, but subsequently contracts to lengths shorter than its original size under stronger fields. These findings laid the foundation for modern hysteresis measurements in bulk magnetic samples [7] in 1926.

Over time, the field has expanded to include various forms of magnetostrictive effects. A recent development is the observation of *spin-current striction*, where the injection of a spin current into a ferromagnet, typically via the spin Hall effect—induces a measurable change in the material's volume [8]. Despite their diversity, these effects fundamentally originate from the dependence of material strain on the orientation of magnetic moments at the atomic scale.

In the Mn bilayer on Ir(111), a structurally significant lateral shift of atomic positions is observed, induced not by an external magnetic field but by a strong interlayer antiferromagnetic (AFM) coupling. This magnetism-driven shift highlights a unique form of magnetostriction, where the energy gain from the AFM alignment leads to a relaxation of the atomic lattice. The row-wise antiferromagnetic (RW-AFM) spin configuration further lowers the symmetry of the system, enabling lateral displacements only in directions perpendicular to the domain orientation.

Initial hints of this structural relaxation arose from a discrepancy between experiment and theory: while the RW-AFM state was clearly observed experimentally, early density functional theory (DFT) calculations predicted a 3Q spin state as the ground state. Around the same time, a similar lateral shift (15 pm) was also predicted for a monolayer of Mn/Re(0001) [9], prompting theorists to revisit the Mn/Ir(111) system. When a lateral atomic relaxation was incorporated into DFT, the RW-AFM state emerged as the energetically favored ground state with an incorporated lateral structural shift. In this relaxed configuration, atoms in the second Mn layer shift away from ideal hollow sites toward positions closer to bridge sites with respect to the Mn monolayer on the Ir(111) surface.

Fig. 4.3 presents the DFT-calculated interlayer magnetic configurations for the Mn bilayer on Ir(111). Panels (a) and (b) show the unshifted RW-AFM states with ferromagnetic (FM) and antiferromagnetic (AFM) inter-layer couplings. To understand the inter-layer coupling, a blue triangle is drawn in panels (a,b). In the blue triangle, the inter-layer nearest neighbouring exchange coupling can be seen to have a net AFM and FM coupling for (a) and (b) respectively. The FM configuration is found to be approximately 20 meV/atom higher in energy compared to the AFM state.

Panels (c) and (d) display the corresponding structures after allowing for lateral relaxation. In the AFM case, a significant lateral shift of approximately 1 Å is observed, which corresponds to nearly 40% of the lattice constant. This shifted AFM structure constitutes the true energetic ground state, exhibiting an energy gain of nearly 60 meV compared to the unshifted AFM configuration. Notably, the direction of the atomic shift is perpendicular to the orientation of the RW-AFM domain.

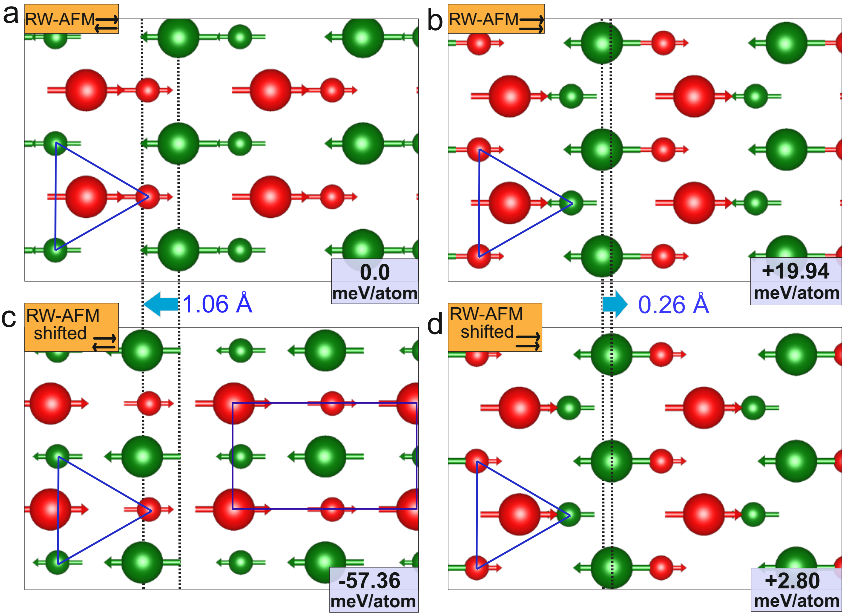

Figure 4.3: Antiferromagnetic inter-layer coupling induced structural shift. (a,b) Top view of the RW-AFM states with an inter-layer AFM and FM coupling respectively. **(c,d)** Top view of a laterally shifted 2nd ML with respect to the ML, where the lateral displacement of the Mn atoms in the top layer relative to the hollow sites is indicated by cyan arrows. Blue triangles indicate the triangular lattice of the lower Mn layer. The total DFT energy of each magnetic state is given with respect to the RW-AFM$_{\rightleftarrows}$ state. The presented DFT results are taken from [4].

The lateral shift illustrated in Fig. 4.3 is calculated for a bilayer stacking configuration of hcpMn/hcpMn/Ir(111). Notably, a comparable magnitude of lateral shift is also observed for the fccMn/hcpMn/Ir(111) stacking. This indicates that the observed shift arises primarily from the inter-layer antiferromagnetic coupling, rather than being solely a consequence of the specific stacking sequence of the Mn bilayers on Ir(111).

The experimental verification of the structural shift is shown in Section 4.3.4 and a precise calculation of the lateral shift is shown in Section 4.4 with respect to the zig-zag dislocation lines.

4.3.3 Magnetic domain walls in the DL

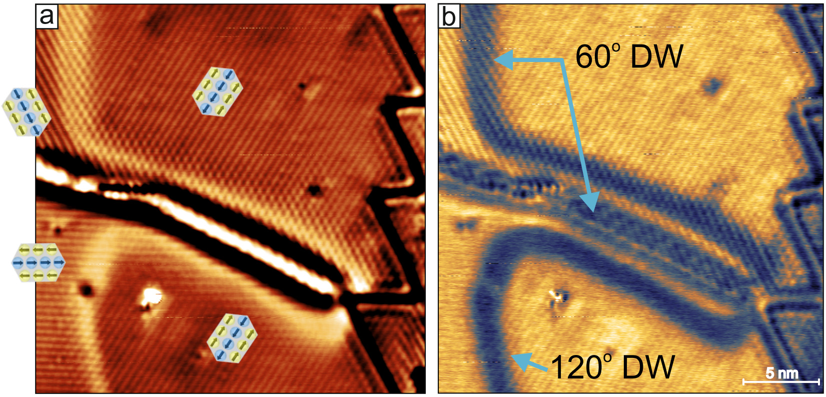

Figure 4.4: Observation of 60° and 120° magnetic domain walls. (a) constant-current topography and **(b)** dI/dU images showing the 60° and 120° magnetic domain walls with a hexagonal magnetic structure corresponding to the 2Q state. Overlaid schematics illustrate the different orientational RW-AFM domains. (Measurement parameters:: $U = +10\,\text{mV}$, $I = 3\,\text{nA}$, $T = 4\,\text{K}$).

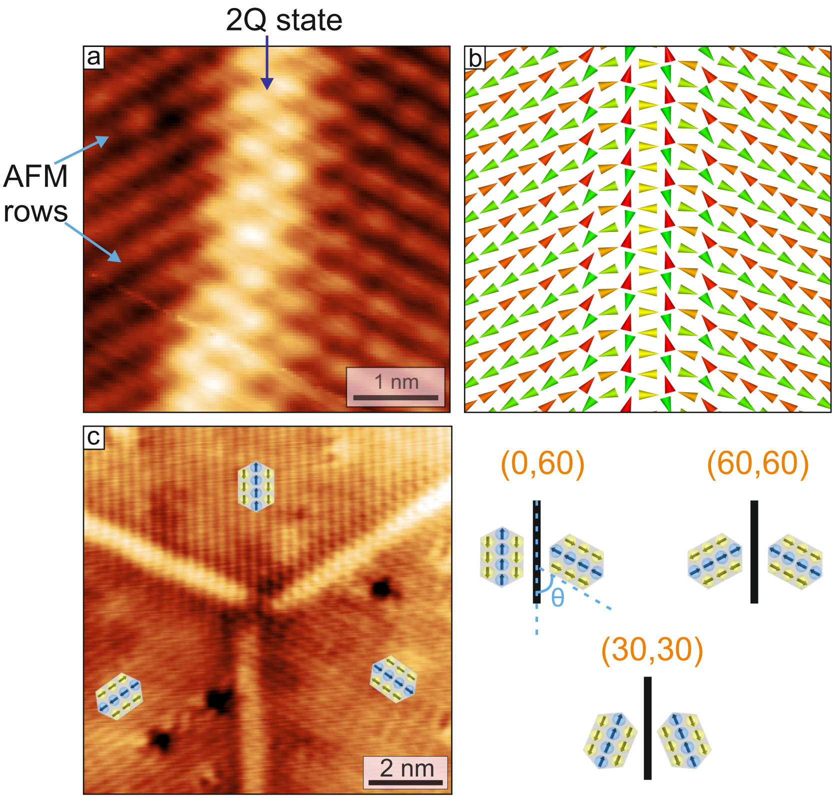

Figure 4.5: The dominant magnetic domain wall: 120° DW (a) constant-current topography SP-STM image showing the 120° DW with the 2Q state visible having a hexagonal magnetic pattern. **(b)** Sketch of a 120° DW corresponding to (a). *(c)* constant-current topography SP-STM image showing three magnetic domain walls meeting at a point resulting in a Y shaped junction. The three rotational domains with the RW-AFM contrast can be seen with overlaid schematics. (Measurement parameters: a: $U = +10\,\mathrm{mV}$, $I = 3\,\mathrm{nA}$; a: $U = +10\,\mathrm{mV}$, $I = 5\,\mathrm{nA}$ all: $T = 4\,\mathrm{K}$).

In the Mn double-layer system, the two types of magnetic domain walls observed are the 60° and the 120° types. Both of these domain walls can be seen in Fig. 4.4. Figs. 4.4(a,b) show the constant-current STM topography and *dI/dU* images with the domain walls labelled in the *dI/dU* image. The domain walls can be seen with high contrast in the topography and *dI/dU* images due to an additional contribution arising from strain effects besides the NCMR contrast [2] which will be discussed in Section 4.3.2. An additional 60° domain wall is marked in the reconstruction line.

The most frequently observed type of magnetic domain wall is the 120° domain wall, which forms between two adjacent rotational domains enclosing an angle of 120° which is shown in Fig. 4.5. A high resolution SP-STM image (Fig. 4.5(a)) shows the hexagonal magnetic pattern that results from the 2Q state in the domain wall. The corresponding spin model is presented in Fig. 4.5(b). Fig. 4.5(c) shows a domain wall configuration where three domain walls meet, resulting in a Y shaped junction. The three orientational domains of the RW-AFM state can be seen with magnetic contrast in panel (c) with overlaid schematics. Ideally, each domain forms an angle of 60° with respect to the domain wall. However, in practice, deviations from this ideal configuration are commonly observed, with the angles formed between each domain and the domain wall differing significantly from 60°. Despite these variations, the total angular separation between the two rotational domains consistently remains close to 120°.

4.3.4 Experimental verification of the structural shift

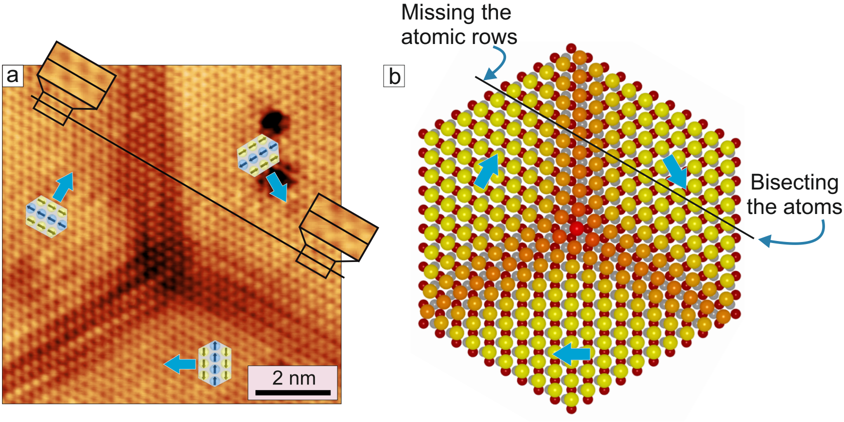

Figure 4.6: Experimental verification of the structural shift at the atomic scale. **(a)** Atomic resolution constant-current topography image of an inverted Y-magnetic domain wall junction; the black line is placed across an atomic row (dark spots) in the right domain, and extrapolation to the top domain confirms the different relative shifts for the top Mn layer, as indicated by cyan arrows ($U = +10$ mV, $I = 5$ nA, $T = 4$ K). **(b)** Atomistic model of an inverted Y- magnetic domain wall junction where the atom positions vary from hollow-site in the center (3Q) to bridge site in the RW-AFM domains; the color code illustrates the size of the shift.

The lateral structural shift predicted is perpendicular to the RW-AFM domain orientation as shown in Fig. 4.3. This corresponds to different shift directions for different rotational domains of the 1Q state. Due to this anisotropic shift direction, a suitable method to probe this experimentally is across a domain wall.

For this reason, a domain wall configuration, where three domain walls meet, has been chosen to check for the structural shift. This DW configuration will be referred to as a triple junction throughout this thesis. The DWs constituting this triple junction are the 120° types. Hence, the

RW-AFM orientation in the domains forming these domain walls can be deduced from Fig. 4.4.

Fig. 4.6(b) represents an atomistic model simulated by André Kubetzka, where an inverted Y shaped triple domain wall junction (called as Y* later in this thesis) is shown. The small grey colored atoms correspond to the Ir(111) surface. The red and yellow atoms in the domains correspond to the ML and DL, respectively.

The DL atoms are shifted from the perfect hollow sites by approx. 40% of the lattice constant. In this scenario, the black solid line drawn in the schematic bisects the atoms in the right domain (labelled), and is then extended to the left domain. This has been done also in the atomically resolved STM topography image in panel (a) and a similar misalignment of the atomic rows is observed. This misalignment would not happen in a non-shifted case, where the DL atoms would occupy the perfect hollow sites. It is noteworthy that Fig. 4.6(a) presents an atomic-resolution topographic image in which the magnetic domain wall is also discernible. While the domain wall contrast in the topography includes a minor contribution from non-collinear magnetoresistance (NCMR) [2], the dominant contribution arises from strain localized along the domain wall, induced by the lateral structural shift. A detailed discussion of these strain effects is provided in the subsequent sections.

This is a clear experimental verification of the presence of a structural shift in the bilayer system. The lateral shift directions for the different rotational domains are marked by blue arrows.

4.4 Why do magnetic domain walls exist in this system?

In principle, due to the lack of stray field, there should be no formation of domain walls in an antiferromagnet. To understand why we observe magnetic domain walls in this simplistic Mn bilayer on Ir(111) system, I will show the factors inducing them in the following sub - sections.

4.4.1 Reconstruction and zig-zag dislocation lines

The reconstruction and the zig-zag dislocation lines observed in the DL showcase a preference for the orientation of the RW-AFM domains. This is made clear in Fig. 4.7. In the following Fig. 4.7, in panel (a), an overview *dI/dU* image shows a sample grown at near RT with a coverage of around 1.5 MLs. One can see that the DL areas exhibit a frequent occurrence of the reconstruction lines and the zig-zag dislocation lines, marked by blue arrows.

A zoom-in of one of the reconstruction lines is shown in (b) with SP-STM contrast. In the vicinity of the reconstruction line, two rotational domains can be seen in a “>” shape. The magnetic domain wall has always been seen to occur near the reconstruction line. This is the case because of the proximity of the reconstruction line to the step edges and the zig-zag dislocations. The different preferences of the RW-AFM domain orientations for the step-edges, zig-zag dislocation line, and the reconstruction lines, forces the existence of a domain wall near the reconstruction line. The orientational preference for the RW-AFM domains for the step edges, zig-zag dislocation lines, and the hydrogen islands will be shown in the following sub-sections below.

This behavior is examined more closely in Fig. 4.7(c), where a magnetic domain wall originating from the top of the image is seen to pass di-

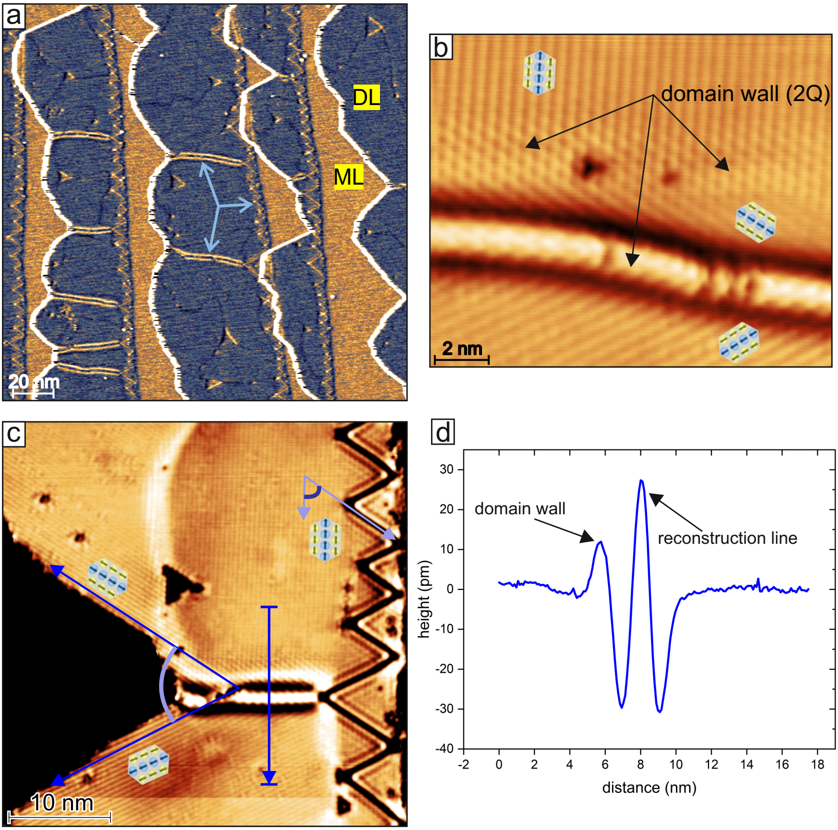

Figure 4.7: Influence of the DL reconstruction line on magnetic domain walls. **(a)** An overview *dI/dU* image showing a step-flow growth with regions of the ML and DL. The characteristic reconstruction lines of the DL have been marked by blue arrows. **(b)** A constant-current topography SP-STM image showing a magnetic domain wall around a reconstruction line. **(d)** A line profile taken across the DL reconstruction line (from top to bottom), as indicated by the blue line in panel **(c)**, showing the height variation in picometers (pm) as a function of distance in nanometers (nm). (Measurement parameters: a: $U = +100\,\mathrm{mV}$, $I = 1\,\mathrm{nA}$; b: $U = +2\,\mathrm{mV}$, $I = 9\,\mathrm{nA}$; c: $U = +10\,\mathrm{mV}$, $I = 1\,\mathrm{nA}$; all: $T = 4\,\mathrm{K}$).

rectly across a reconstruction line. A line profile drawn across this region, shown in Fig. 4.7(d), highlights both the magnetic domain wall and the underlying reconstruction line. While the exact origin of the enhanced electronic contrast observed at the reconstruction line has not been fully investigated, it is likely related to variations in the local atomic arrangement in the reconstruction line. The arrows drawn in Fig. 4.7(c) indicate the angle of the RW-AFM domain with respect to the zig-zag dislocation line and the reconstruction line. The reconstruction line can be seen to have the RW-AFM domains at a total angle of 60 degrees with a domain wall in the centre.

Regarding the zig-zag dislocation lines, in the SP-STM image in (c), one can see the AFM rows are always at an angle of 60 degrees to the zig-zag dislocation lines. This selection is further exemplified in the bottom of this image where the magnetic domain wall, after passing along the reconstruction lines, comes down vertically just touching the vertices of the zig-zag dislocation lines.

Fig. 4.8 illustrates a growth model for the reconstruction line with the particular orientational RW-AFM domain.

A key feature influencing RW-AFM domain selection in the double layer (DL) is the presence of a structural reconstruction line running along the $[1\bar{1}2]$ crystallographic direction. This reconstruction is composed of a line of atoms (shown in purple) embedded between extended magnetic domains on either side. Above the Néel temperature (T_N) in Fig. 4.8 (a), the DL remains pseudomorphic, with atoms (pink) occupying ideal hollow sites. The reconstruction line atoms also occupy alternate hollow sites, maintaining the overall symmetry. Between these two hollow-site configurations lies a transition region formed by a row of atoms (blue) that span from one hollow site to the other, effectively passing through the bridge sites.

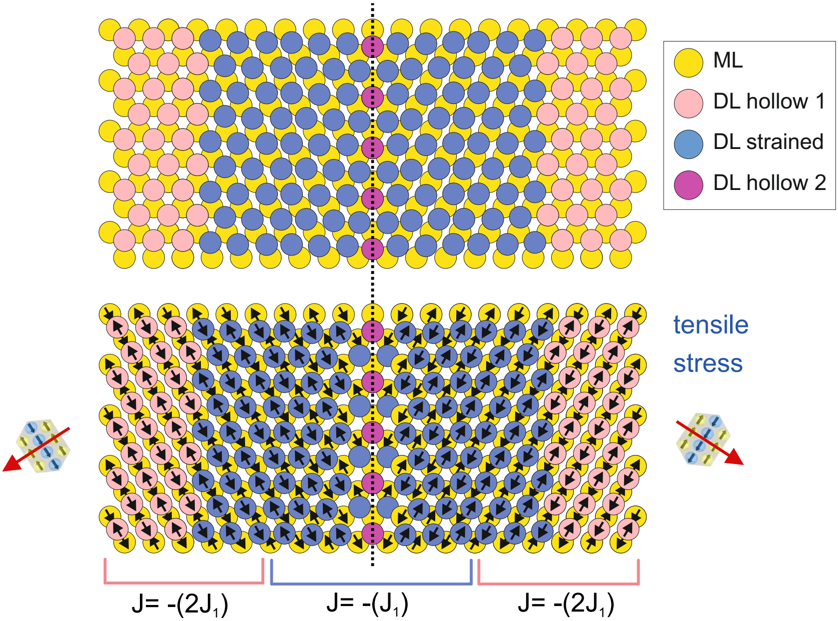

Figure 4.8: RW-AFM domain selection by the reconstruction line in the DL. Structure model of the reconstruction line (purple atoms) with extended domains on either side. **(a)** shows the configuration above T_N, where the pseudomorphic DL atoms (pink) occupy perfect hollow sites, and the purple atoms sit in the alternate hollow sites. The blue DL atoms form the transition region between the pink and purple atoms, effectively passing through the bridge site as they move from one hollow site to the other. **(b)** shows the configuration below T_N, where the onset of RW-AFM order induces a lateral shift of the atoms orthogonal to the RW-AFM domain orientation, generating tensile stress along the reconstruction line. The inter-layer nearest-neighbour exchange constant is $-J_1$ for the blue atoms positioned near the hollow sites, while it becomes $-2J_1$ for atoms located at the bridge sites.

In Fig. 4.8 (b), below T_N, the onset of RW-AFM order drives a lateral shift of atoms in the DL, orthogonal to the domain orientation. The pseudomorphic DL region shifts toward the bridge site, and the reconstructed region (blue atoms) appears to undergo the same shift. Since no DFT calculations are available for the lateral displacement in the reconstructed DL areas, the same magnitude of shift as that of the pseudomorphic DL has been assumed. This overall lateral shift introduces tensile stress along the reconstruction line. The magnetic coupling across the interface reflects this structural asymmetry: the inter-layer nearest-neighbour exchange constant is $-J_1$ for blue atoms located near hollow sites, but increases in magnitude to $-2J_1$ for atoms at bridge positions. This spatial modulation in exchange interaction underscores the role of atomic registry in stabilizing distinct RW-AFM domains across the reconstruction, thereby facilitating domain selection.

Another possible configuration involves compressive strain along the reconstruction line. However, this scenario would lead to significant atomic crowding, as the reconstructed DL atoms would be forced into close proximity, resulting in a highly strained state that is likely energetically unfavorable.

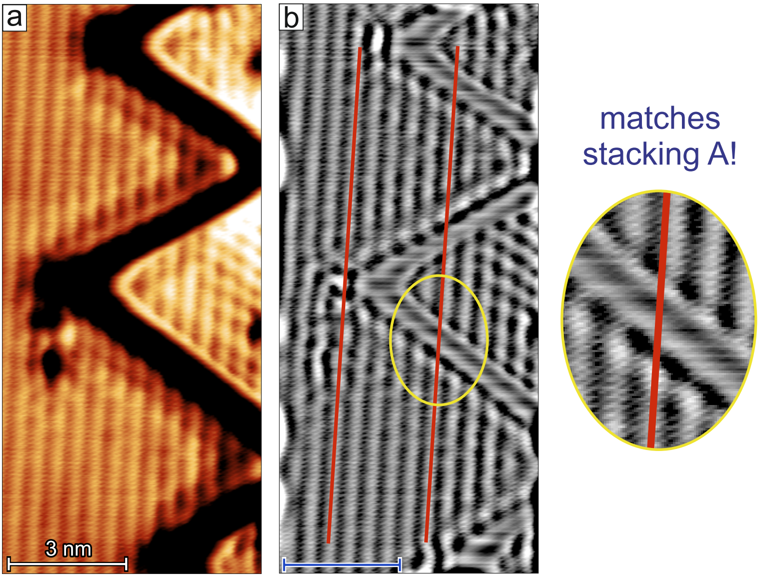

Figure 4.9: Experimental evidence of the lateral shift by the AFM rows in the DL. (a) constant-current SP-STM topography image showing a vertically oriented RW-AFM domain with respect to the zig-zag dislocation lines. **(b)** A frequency split of (a), done to reduce the intensity of the dislocation line so as to allow for a better visibility of the AFM rows in its vicinity. The $2 \times x$ magnified inset shows that the red line, overlaid on the AFM row in the region outside the dislocation line, intersects the AFM row inside the dislocation area on the left.

We now examine the orientational preference of the row-wise antiferromagnetic (RW-AFM) domains induced by the zig-zag dislocation lines in the DL. As shown in Fig. 4.9 (a), the AFM rows intersect the zig-zag dislocation lines at an angle of 60°. In panel (b), a frequency-filtered version of (a) is presented, which suppresses the intensity of the zig-zag dislocation lines, thereby enhancing the visibility of the AFM rows in their vicinity. A red guideline is drawn along one of the AFM rows and replicated across another equivalent row. Notably, this line also aligns with the AFM rows located within the region enclosed by the zig-zag dislocation lines.

To interpret this configuration, we refer to the structural models shown in Fig. 4.10. In panels (a) and (b), the DL atoms (purple) are positioned on a specific hollow site of the ML (yellow atoms), referred to as stacking A. In contrast, panels (c) and (d) depict DL atoms occupying the alternative hollow site, referred to as stacking B. Panels (a) and (c) represent the high-temperature phase above T_{N}, where all DL atoms sit perfectly atop the chosen hollow sites. Panels (b) and (d) depict the situation where the majority of DL atoms undergo a lateral shift to bridge sites (pink atoms), while a subset of atoms remain unshifted (purple), possibly pinned by the ML adjacent to it across a buried step edge. This local pinning is assumed to prevent a uniform shift from propagating into the DL. It should be noted that the zig-zag dislocation line always occurs near a buried step edge between the DL and ML.

The 2× magnified insets illustrate how a black solid line, when drawn along an AFM row outside the zig-zag region, maps onto the spin rows inside the dislocation lines. For stacking A, the projected line touches the left portion of the AFM row enclosed by the zig-zag structure. This corresponds to the experimental observation in Fig. 4.9(b), and thus confirms that the DL in this region adopts stacking A. Additionally, the direction of the lateral shift in the RW-AFM domain is found to be away from the dislocation lines. This provides a useful criterion for identi-

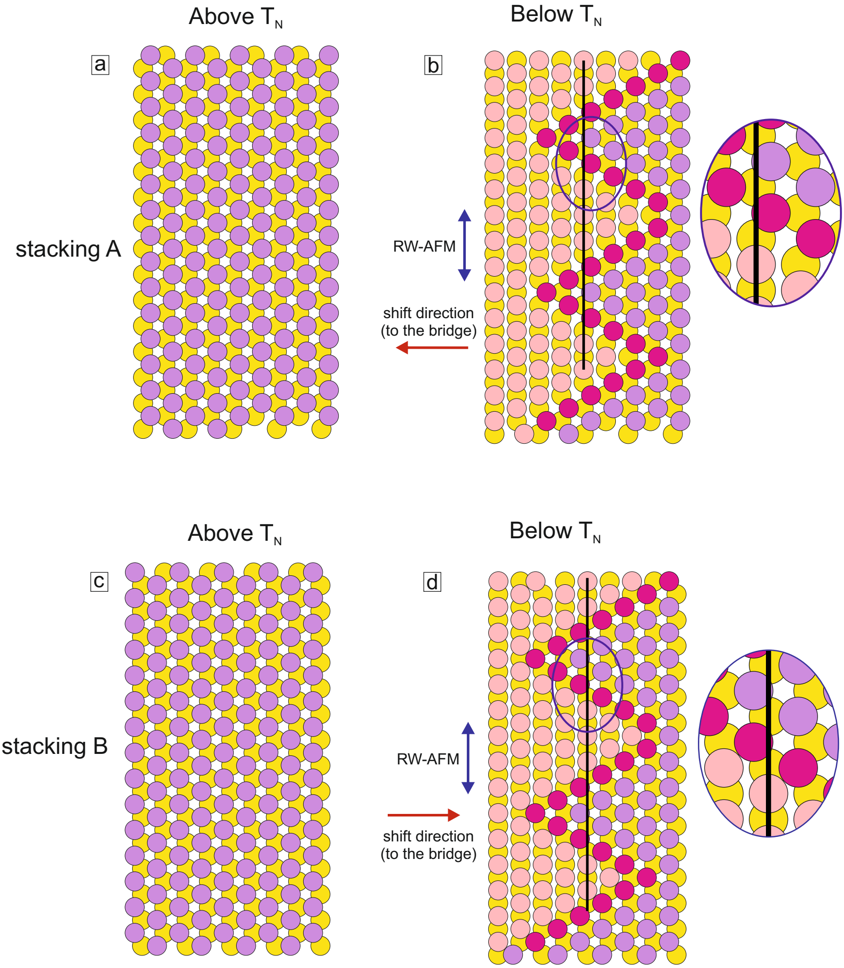

Figure 4.10: Structure model for the zig-zag dislocation line in the DL. (a) Above the T_N, the two stackings have the 2nd ML atoms sitting in the perfect hollow sites separated by the zig-zag dislocation line. The $2 \times x$ magnified inset shows that a black solid line, overlaid onto the AFM row on the pink atoms, touches the purple atoms on the left. **(b)** Below the T_N, the two stackings have the 2nd ML atoms shifted to the bridge sites in opposite directions, while a small amount of the DL atoms (purple) are left in the initial stacking position as that above the T_N. The $2 \times x$ magnified inset shows that a black solid line, overlaid onto the AFM row on the pink atoms, touches the purple atoms on the right.

fying the shift direction in DL regions where magnetic contrast is not directly observed.

According to density functional theory (DFT) calculations (see Supporting Information in Ref. [4]), the magnitude of the lateral shift is found to be the same for both stacking configurations. This value has been incorporated into the structural models presented here.

An insightful calculation enabled by the zig-zag dislocation line is the determination of the precise lateral shift in the DL. By measuring the horizontal displacement between the AFM rows inside and outside the zig-zag dislocation line (see Fig. 4.9(b)), and using the RW-AFM periodicity of 470 pm, the lateral shift is found to be approximately 110 pm. This value aligns remarkably well with the DFT-predicted shift of 1.06 Å [4]. Theoretically, the horizontal distance between a hollow site and a bridge site is 78 pm. Therefore, both the DFT prediction and the experimentally measured value of 110 pm indicate that the lateral shift moves the atoms beyond the bridge site, starting from a hollow site.

4.4.2 Step edges

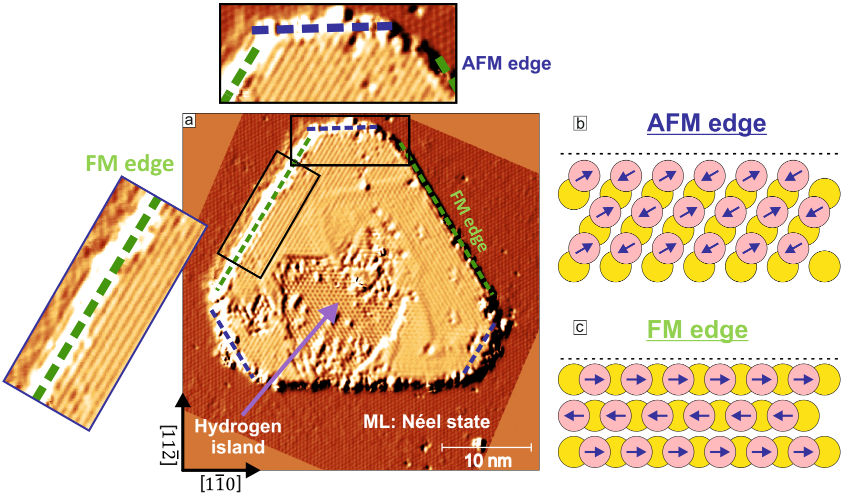

Figure 4.11: The existence of ferro- and antiferromagnetic edges in Mn double-layer islands. (a) Partially differentiated SP-STM image showing the AFM and FM edge where the rows of the RW-AFM domains are parallel and not parallel respectively. These are exemplified by the magnified insets. Schematic representations of the AFM (**(b)**) and FM **(c)** edges with respect to a RW-AFM state in the laterally shifted configuration, where the DL atoms (pink) occupy the bridge sites of the ML (yellow). (Measurement parameters: a: $U = +10\,\mathrm{mV}$, $I = 1\,\mathrm{nA}$, $T = 4\,\mathrm{K}$).

A third factor contributing to the formation of magnetic domain walls is the presence of step edges that traverse the monolayer (ML) and bilayer (DL). These step edges have been observed to exhibit a ferromagnetic (FM) alignment, such that the antiferromagnetic (AFM) rows run parallel to the step direction as shown in Fig. 4.11(a). The different kind of edges with respect to the spin orientation are shown in the schematics in Fig. 4.11(b,c). Such edges were observed also for the fcc-stacked Mn ML on Re(0001) [2].

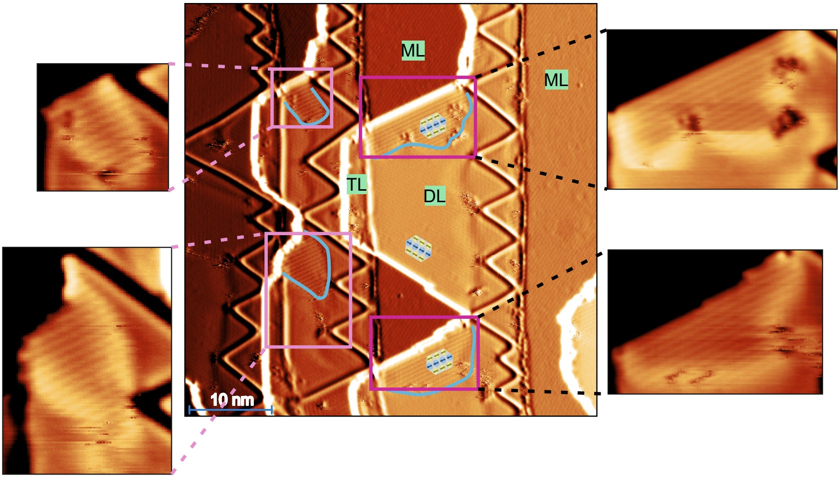

Figure 4.12: Preference of a FM edge by the ML-DL step edges in DL terraces. constant-current SP-STM topography overview image (in centre) showing regions of the ML and DL. The rotational domains near the ML-DL step edge can be seen to be parallel to the step edge directions. This FM edge requirement forces the formation of magnetic domain walls (marked with blue lines). Magnified insets show the AFM rows and the magnetic domain walls for areas marked by pink rectangles. (Measurement parameters: $U = -100\,\text{mV}$, $I = 1\,\text{nA}$, $T = 4\,\text{K}$).

As we begin to explore the role of step edges, it is instructive to first consider the behavior of step edges in a simpler configuration of the same material system - namely, Mn double-layer (DL) islands on a monolayer (ML) background. Fig. 4.12 shows such a Mn DL island embedded in a ML background that exhibits the well-known Néel antiferromagnetic state.

In the case of the Mn DL island, both ferromagnetic (FM) and antiferromagnetic (AFM) edge configurations are observed and have been marked accordingly in the figure. The FM edges are the long edges running along the $[1\bar{1}0]$ directions, while the AFM edges are along the $[11\bar{2}]$

directions. The schematics shown are constructed taking into account the lateral structural shift orthogonal to the orientation of the RW-AFM domain. The yellow and pink atoms represent the ML and DL atoms respectively.

Having discussed the magnetic behavior at the edges of Mn double-layer islands, we now turn to the more extended case where Mn grows in continuous two-dimensional terraces.

As shown in Fig. 4.12, the step edges at the boundary between ML and DL regions exhibit a distinct alignment of the RW-AFM domains, with the domain orientation running parallel to the step edges. This alignment implies a preferential stabilization of ferromagnetic (FM) edge configurations along the step edges.

The magnified insets in the figure further emphasize this behavior: magnetic domain walls emerge specifically to accommodate the FM alignment along these narrow step-edge regions. This suggests that even small step-edge segments exert sufficient influence to locally alter the magnetic configuration, introducing domain walls where necessary to maintain the energetically favorable FM edge condition.

4.4.3 Hydrogen islands

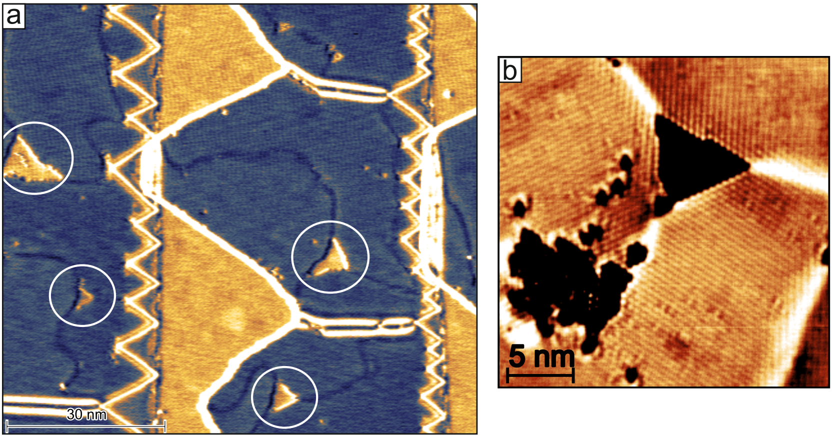

Figure 4.13: (a) Differential conductance (dI/dU) map showing triangular hydrogen islands (circled) embedded within a network of magnetic domain walls on Mn/Ir(111). **(b)** Constant-current STM topography of a single hydrogen island reveals that the island edges preferentially adopt an antiferromagnetic (AFM) alignment, leading to the formation of three distinct magnetic domain walls at the vertices of the island. (Measurement parameters: a: $U = +100\,\text{mV}$, $I = 1\,\text{nA}$; b: $U = +10\,\text{mV}$, $I = 1\,\text{nA}$; all: $T = 4\,\text{K}$).

Hydrogen, being the lightest element, is notoriously difficult to remove from ultra-high vacuum environments, as it cannot be efficiently pumped out by standard vacuum pumps. As a result, its presence is difficult to avoid during STM measurements. In the Mn bilayer system on Ir(111), hydrogen impurities likely appear to exhibit a strong affinity for the surface, particularly in the DL regions. Interestingly, hydrogen-induced superlattices in the form of ordered islands have not been observed in the ML areas, suggesting a possible stacking-dependent affinity of the hydrogen in this system.

These hydrogen islands have a pronounced impact on the magnetic configuration. Their presence is often associated with the formation of magnetic domain walls. In Fig. 4.13(a), white circles highlight several hydrogen islands, each surrounded by domain walls. A zoomed-in SP-STM image of the area surrounding one such hydrogen island in panel (b), reveals magnetic contrast across all three rotational domains. This observation suggests that the edges of the hydrogen islands tend to favor an antiferromagnetic (AFM) alignment. Also in (a), the edges of the hydrogen islands can be seen to be oriented along the $[11\bar{2}]$ directions, thus resulting in AFM edges.

4.4.4 Triple layer boundary

The fourth factor contributing to the formation of magnetic domain walls in the Mn/Ir(111) system is the presence of buried step edges at the boundary between the DL and TL. These transitions tend to favor an antiferromagnetic (AFM) edge configuration of the RW-AFM state in the DL.

As shown in Fig. 4.14, a magnetic domain wall is clearly observed near the buried step edge separating the DL from the TL. In the dI/dU image in Fig. 4.14(a), the domain wall is seen to reside on the DL side, just before the buried step edge. This observation is consistent with the fact that the DL and TL possess fundamentally different magnetic ground states. While the DL hosts the collinear and coplanar row-wise antiferromagnetic (RW-AFM) state, the TL stabilizes a non-coplanar $3Q$ antiferromagnetic state, which will be discussed in detail in the following chapter. Hence, this domain is different in nature as compared to the domain walls shown previously in the chapter, which separated two adjacent rotational domains.

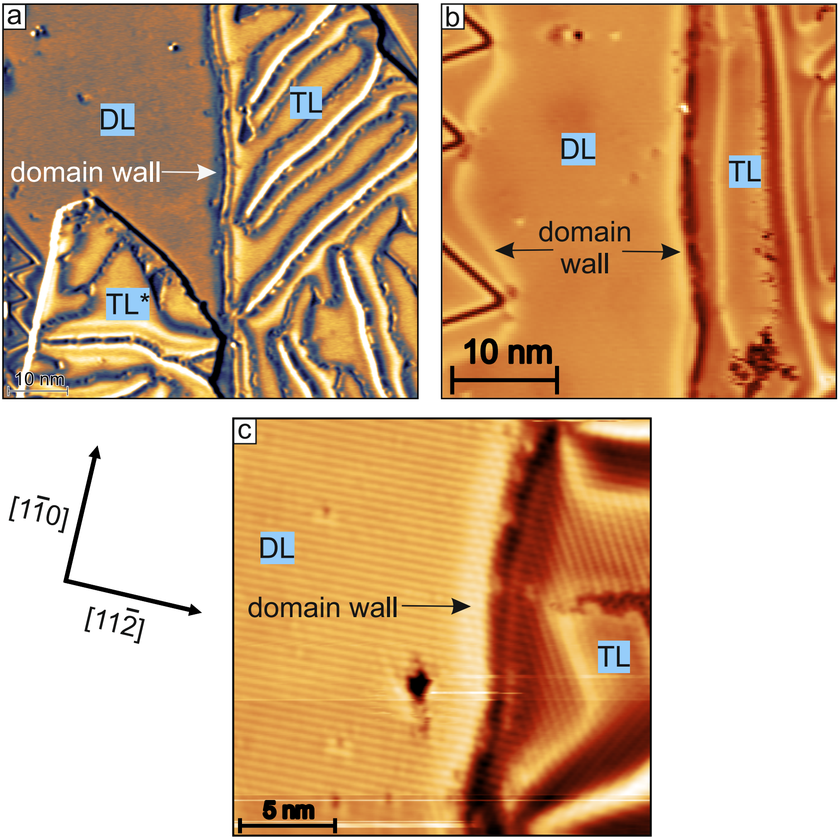

Figure 4.14: Magnetic domain wall at the buried step edge between the DL and TL. The TL has a requirement for a certain domain orientation and hence a magnetic domain wall lining the TL can be seen in the dI/dU (**a**) and constant-current topography images in **(b)** and **(c)**. (Measurement parameters: a: $U = +30\,\mathrm{mV}$, $I = 1\,\mathrm{nA}$; b: $U = -70\,\mathrm{mV}$, $I = 1\,\mathrm{nA}$; c: $U = -10\,\mathrm{mV}$, $I = 6\,\mathrm{nA}$; all: $T = 4\,\mathrm{K}$).

Further insight is provided by the SP-STM image shown in Fig. 4.14(c), where magnetic contrast reveals a hexagonal pattern within the domain wall region on the DL. Although the precise magnetic configuration of this domain wall has not been studied theoretically, the observed pattern could suggest the possibility of a $2Q$ state in the domain wall. Notably, a recent theoretical study demonstrated a continuous transformation from the $1Q$ to the $3Q$ state via an intermediate $2Q$ configuration using the Rodriguez rotation formalism [10].

4.5 Stress induced effects by the shift

The lateral structural shift present in the Mn bilayer system is expected to influence both structural and magnetic features, including the formation and orientation of dislocation lines as well as the configuration of magnetic domain walls. To understand these effects in detail, it is essential to accurately determine the directions of the structural shift.

If the direction of the shift can be correlated with the surrounding magnetic domains in the vicinity of a characteristic feature, such as a dislocation line, this information can then serve as a reference framework to identify shift directions in other regions of the DL. Consequently, in the following subsections, we aim at determining the structural shift directions associated with the domains enclosed by zig-zag dislocation lines - a characteristic feature observed in DL samples grown at both near-room-temperature and elevated temperatures.

4.5.1 Identifying the direction of the structural shift

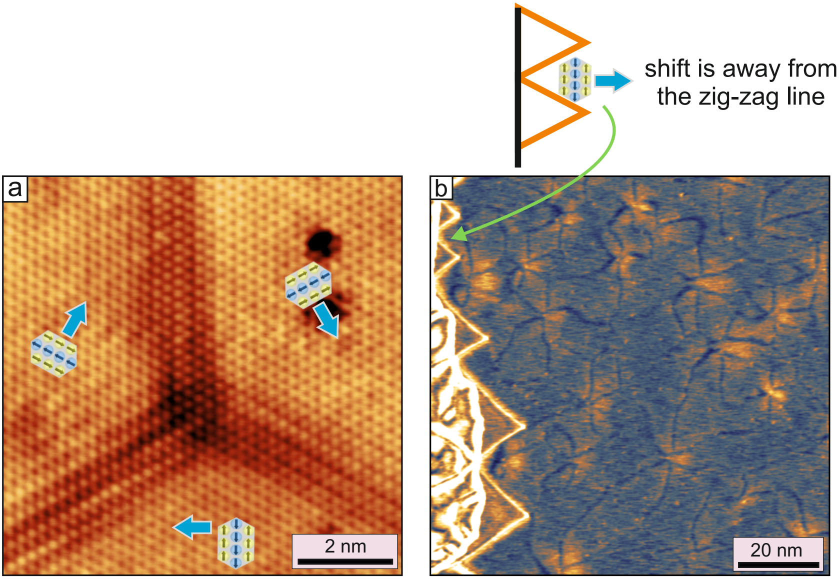

Figure 4.15: Identifying the lateral shift direction for a characteristic structural feature on the DL. (a) Constant-current topography image with atomic resolution of a magnetic domain wall triple junction with blue arrows corresponding to the lateral shift directions for each rotational domain. **(b)** Identifying the lateral shift direction for the rotational domain near the zig-zag dislocation line in the same sample as in (a). (Measurement parameters: c: $U = +10\,\text{mV}$, $I = 5\,\text{nA}$, $T = 4\,\text{K}$).

With the correct stacking configuration identified, we are now in a position to determine the lateral shift directions for different orientational domains in a given Mn bilayer sample on Ir(111). Fig. 4.15 focuses on deducing the shift direction of domains adjacent to zig-zag dislocation lines, a hallmark feature of the DL system.

In Fig. 4.15(b), a schematic is for the top-left region to indicate the domain orientation (see Fig. 4.7). The *dI/dU* image was acquired from the same area as shown in Fig. 4.15(a), allowing for a direct comparison. Based on this, it can be inferred that the lateral shift direction of the domains surrounding the zig-zag lines points away from the dislocation line. This insight can now be used as a reference for identifying the shift directions for magnetic and structural features in the DL.

4.5.2 Stress on magnetic domain walls

Now that the structural shift has been qualitatively verified through experimental observation at a triple domain wall junction, it becomes compelling to explore how this shift influences the magnetic domain walls themselves. While triple domain wall junctions will be a central focus later in this chapter, here we begin by considering a simpler configuration: a single 120° domain wall in the DL system.

The schematic shown below in Fig. 4.16 illustrates such a 120° domain wall, with the atoms of the second Mn layer (2^{nd} ML) laterally shifted from their ideal hollow sites to bridge sites, following the theoretical predictions and experimental observations discussed above. Since the direction of structural shift is perpendicular to the RW-AFM domain orientation, each magnetic domain exhibits a different shift direction. For the magnetic domain wall, the domain dependent shift directions induces a compressive stress in the left domain and tensile stress in the right domain resulting in an asymmetric stress on the domain wall.

The slightly transparent red atoms in Fig. 4.16 depicted in both domains represent the original atomic positions at the perfect hollow sites. Arrows drawn on these atoms indicate the direction of the lateral shift. As highlighted in the magnified insets, the atoms in the left domain move towards the domain wall, while those in the right domain move away from it. It should be noted that, in this model, the atoms within the domain wall itself have not been laterally shifted and remain in the perfect hollow sites. In reality, however, the atomic positions within the domain wall are also expected to deviate, particularly because of the $2Q$ magnetic state present in the domain walls. The $2Q$ is biaxial and thus is potentially subject to a lateral shift similar to the uniaxial RW-AFM state. For simplicity, no shift has been applied to the DW atoms in the current structural model.

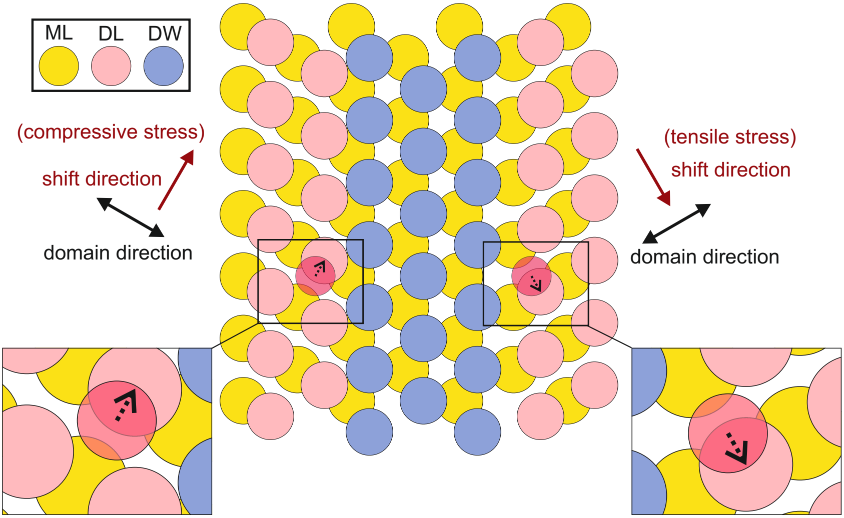

Figure 4.16: Stress effects on a 120° magnetic domain wall. The red and black arrows indicate the lateral shift directions and the orientation of the RW-AFM domains, respectively. On the left, a shift toward the magnetic domain wall (blue atoms) results in a compressive stress, while on the right, the outward shift leads to tensile stress. Insets show magnified views of the local stacking environment around the shift vectors. This schematic illustrates the presence of an asymmetric stress profile across a 120° magnetic domain wall.

This asymmetry in stress results in a strained domain wall. It is reasonable to expect that such a domain wall would tend to relieve some of this strain, either through slight positional shifts or local rearrangement of atomic configurations, in order to minimize the total energy, which includes both the domain wall energy and the additional strain energy.

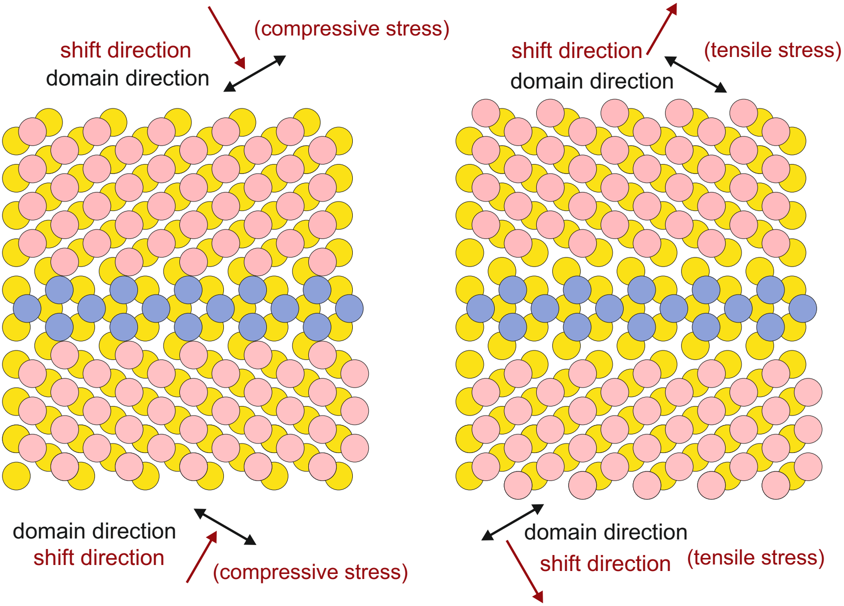

Figure 4.17: Symmetric stress profiles across 60° magnetic domain walls. 60° magnetic domain walls (blue atoms) are oriented along the $[11\bar{2}]$ direction. This allows for only symmetric stress profiles for the 60° magnetic domain walls. The two cases of compressive and tensile stress are shown in the left and right panels, respectively.

We have seen that a 120° domain wall has an asymmetric stress, where one domain provides compressive and the other domain provides a tensile stress. An interesting point to note is that for a 60° domain wall, the stress on both sides of the domain wall is the same. For the stacking used in the models in Fig. 4.17, the stress turns out to be tensile on both sides of the 60° domain wall. But for the opposite stacking, the structural shift direction will be opposite and hence the resulting net stress will be compressive.

4.5.3 Magnetic domain walls v/s dislocation lines

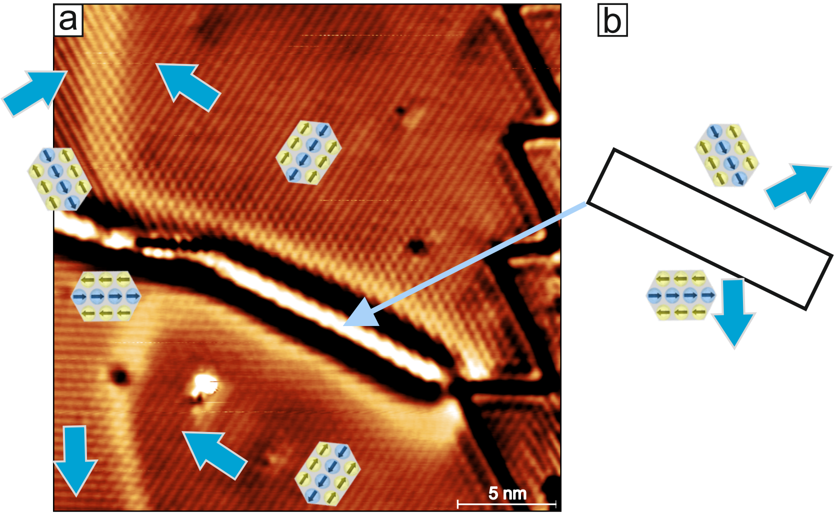

Figure 4.18: Experimental verification of the stress profiles for the magnetic and structural features on the DL. (a) A constant-current topography SP-STM image shows a magnetic domain wall running from the top to the bottom image transitioning from a 120° to a 60° domain wall. The characteristic reconstruction and zig-zag dislocation lines are also seen. By knowing the lateral shift direction for the zig-zag dislocation lines from Fig. 4.15(b), the shift directions for the magnetic and structural features are shown in blue arrows. **(b)** The reconstruction line is associated with a symmetric tensile stress. (Measurement parameters: $U = +10\,\mathrm{mV}$, $I = 3\,\mathrm{nA}$, $T = 4\,\mathrm{K}$).

In this subsection, we examine experimental data to compare the stress induced by the lateral structural shift on dislocation lines and magnetic domain walls. From previous analysis in this chapter, the shift direction for the zig-zag dislocation lines is known to point away from the dislocation line. Additionally, it is established that the stress configuration for 60° domain walls (see Fig. 4.17) and reconstruction lines (see Fig.4.10) is symmetric.

Using this information, the shift directions for the other two rotational domains in the figure can be inferred. The 120° domain wall can be seen to have an asymmetric stress. On the other hand, the 60° domain wall exhibits compressive stress, while the reconstruction line is under tensile stress on both sides - see schematic in Fig. 4.18(b).

4.6 Observation of magnetic loops

Closed magnetic domain wall structures have long captivated the interest of the magnetism community. This fascination dates back to the discovery of magnetic bubble domains - cylindrical spin textures typically observed at the micrometer scale. These bubbles were first reported in rare-earth garnet films of the general form $MFeO_3$, where M denotes a rare-earth metal [11]. The technological relevance of magnetic bubbles became evident when Texas Instruments introduced a commercial product in 1977 that utilized them for data storage [12]. This early concept, akin to the modern racetrack memory, exploited the controlled movement of magnetic bubbles along patterned stripes using external magnetic fields [13].

However, the magnetic bubble memory was short-lived [14], as new generations of nano-scale magnetic data storage media with greater efficiency became available.

Nowadays, the spintronics research community continues to look for robust nano-scale magnetic objects. Among these, magnetic domain walls and skyrmions have emerged as promising candidates, offering operational demands in the nano-Ampere range which is orders of magnitude lower than those required by conventional micro-Ampere scale technologies [15]. Significant progress has been made in identifying material systems capable of stabilizing these nanoscale spin textures [16].

Recently, there has been renewed interest in closed domain wall structures, including magnetic bubbles and skyrmion-like configurations [17–19]. Whether skyrmionic or topologically trivial, the existence of such magnetic loops makes them particularly intriguing.

In the Mn bilayer on Ir(111) system studied here, we observe closed-loop magnetic structures at the nanoscale. These features may have relevance for future spintronic applications.

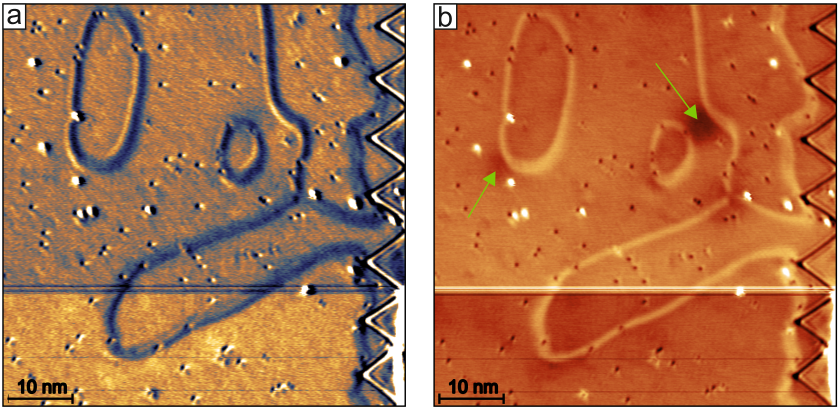

Figure 4.19: Magnetic loops in the DL. constant-current dI/dU and topography images of a sample grown at elevated temperatures shown in **(a)** and **(b)** respectively. The magnetic loops are seen to be pinned by some defects marked by green arrows. (Measurement parameters: $U = +5\,\mathrm{mV}$, $I = 2\,\mathrm{nA}$, $T = 4\,\mathrm{K}$).

Fig. 4.19 shows the dI/dU and the topographic images of a sample area of the bilayer, where closed loop domain wall structures are observed. These loops are isolated ones and not connected to any other magnetic domain wall structure. However, some dark contrast features which have been marked by green arrows are pinning sites for the magnetic loops. Potentially, the pinning sites help the loops to exist, because in an ideal case, the loops should in principle collapse to the RW-AFM state, as the loop has no topological character, due to the planar 2Q state in the wall.

Although it is not clear as to why the loops exist in this sample, an interesting aspect to note is the orientation of these loops. It can be seen that the loops are not circular, but rather elliptical. To understand this elliptical formation and also the orientation of the long axis of the ellipse, a schematic is displayed in the next figure.

The schematic is motivated by the following: If the background RW-AFM domain is defined, what is the favourable loop orientation in that given RW-AFM domain.

As can be seen in the above schematic, option (b) and (c) are not allowed. The reason is that in (b), the AFM rows of the external domain are parallel to the long axis domain walls of the loop. And in (c), the AFM rows of the internal domain will be parallel to the long axis domain walls of the loop. The domain selected in these options needs to take into account the strict requirement of 120° domain walls. In both these cases, the AFM rows are parallel to the long axis directional domain walls. In such a scenario, the domain wall would no longer be a 120° one and will transition into a 60° one, specifically being a (0°, 60°) type domain wall. This is the less observed domain wall type in this system.

In the end, option (d) is the favourable scenario, where the long axis directional domain walls are at angles of 60° to the adjacent domains, thus forming ideal (60°, 60°) domain wall types. Such an experimental exam-

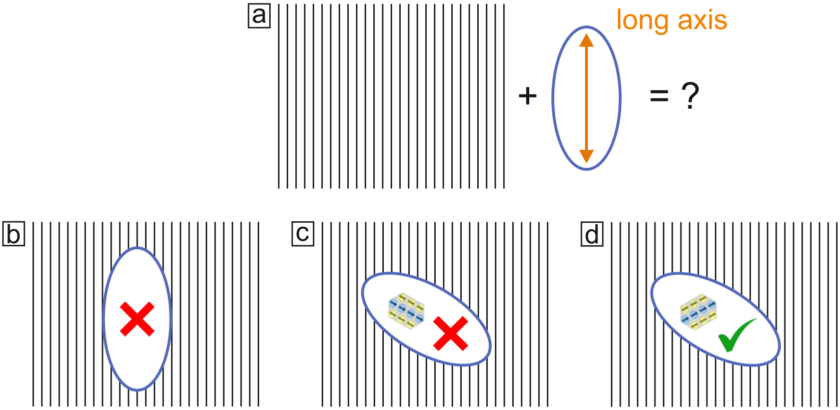

Figure 4.20: Preferred orientation of an elliptical loop in a RW-AFM background. (a) Schematic related question posed: which orientation of an elliptical loop is favoured within a uniform RW-AFM domain? The long axes of the ellipses cannot be parallel to the RW-AFM domain orientation as shown in **(b)** and **(c)**. (d) In this scenario, the long axes of the elliptical loop are not parallel to the AFM rows and hence this is the preferred orientation of the loop.

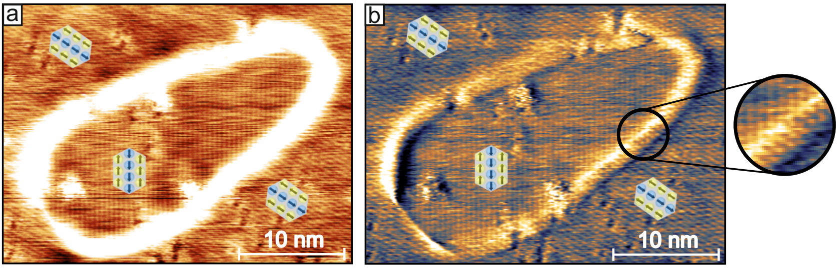

Figure 4.21: SP-STM imaging of an isolated magnetic loop in the DL. (a) Constant-current topography and **(b)** dI/dU SP-STM images of an isolated loop in the DL. The overlaid schematics show the orientation of the RW-AFM domains in and around the loop. The contrast in (a) has been adjusted to show the magnetic contrast of the RW-AFM domains and in (b) to show the 2Q state magnetic contrast. (Measurement parameters: $U = -5\,\mathrm{mV}$, $I = 1\,\mathrm{nA}$, $T = 4\,\mathrm{K}$).

ple can be seen in the SP-STM images shown in Fig. 4.21. The rotational domains with magnetic contrast can be seen and the schematics have also been placed for the reader's convenience.

The domain walls can be seen to have the hexagonal magnetic pattern which would correspond to the earlier described 2Q state. What happens at the short axes of the elliptical loops is unclear topologically, but it is not a skyrmion. There is no change in magnetic contrast at these points, which one would expect for a twist in the domain wall texture where the spins would be non-coplanar. These closed magnetic loops are planar loops having a collinear domain and a non-collinear domain wall.

4.7 Manipulation of magnetic loops

As we have now got an understanding of the magnetic loops observed in this sample system and also the rotational domain orientation requirements for their existence, we will now have a look at some STM induced manipulation.

The image series shown in Fig. 4.22 is a continuous scanning series where some rearrangement of domain walls can be observed. Two areas of interest are marked in Fig. 4.22, one to the left of the image and one in the middle of the terrace. A significant number of interconnected loops are found in this image, which can be attributed to surface impurities introduced during the resistive heating of the sample in the annealing process. These impurities likely act as pinning or nucleation centers, leading to the formation of irregular loop-like features within the domain wall network.

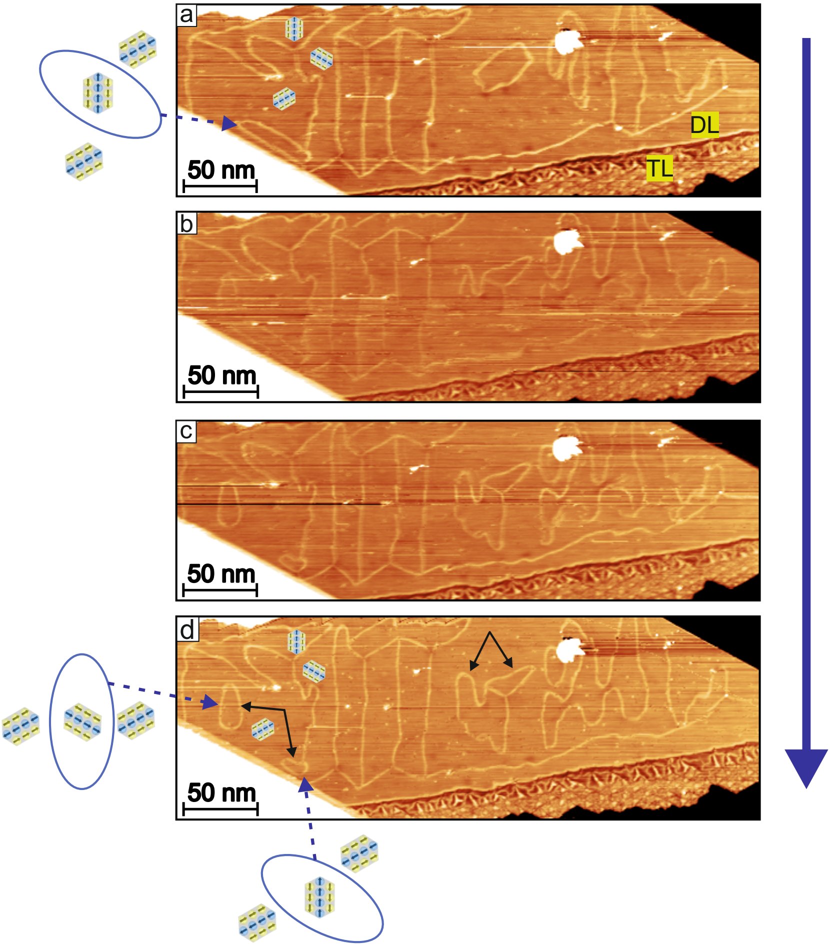

Figure 4.22: Re-arrangement of domain walls and loops in a scanning series. The sample area of the DL area shown in this figure was scanned for some time and the resultant consecutive constant-current topography images are shown from (a-d). The visible changes in the loops and domain wall configurations are marked by black arrows in the final (d) and initial (a) images. The orientation of the RW-AFM domain for the three elliptical loops are explained by schematics marked by blue dotted arrows. The images have been subjected to line average corrections during image processing for better visibility of the loops. (Measurement parameters: all: $U = -5\,\mathrm{mV}$, $I = 1\,\mathrm{nA}$, $T = 4\,\mathrm{K}$).

It can be seen that the elliptical loop marked in panel (a) is merged with the domain wall network. This elliptical loop holds the possibility of breaking into two parts which can be seen in (d). Alternatively, the vertically oriented loop seen in panel (d) may have formed as a result of scanning-induced perturbations from the STM tip. In this scenario, a portion of the original loop remains connected to the domain wall network, while the rest re-forms with its major axis reoriented vertically, potentially due to localized tip-induced restructuring during imaging.

This has been represented in the schematics provided aside the panels. The schematics follow the domain selection rule established in Fig. 4.22(d). This observation tells us that the rotational domain inside the loop has changed; it could only happen because the different rotational domains are degenerate in energy. This shows that the domain walls are vulnerable to the manipulation by the STM tip while scanning.

The other isolated loop marked in the centre of the terrace in Fig. 4.22(a), transforms into a new structure, that now has two loops as seen in Fig. 4.22(d).

In the course of my literature review, I was unable to find reports of similar loop or bubble dynamics in antiferromagnetic systems. However, an intriguing analogy can be drawn from fluid dynamics. In that field, simulations have shown that when two circular bubble rings in water intersect, they reorganize to form one larger and one smaller elliptical loop [20]. This restructuring arises from the surface tension acting on the walls of the bubbles - an effect that is visually analogous to the dynamics of domain wall restructuring shown in Fig. 4.22.

In the context of the Mn bilayer on Ir(111), the formation and stability of nanoscale magnetic loops appear to follow similar energy minimization principles. The analogy between surface tension in fluids and domain wall energy in magnetism provides a compelling framework for understanding the observed geometries. These closed-loop structures could offer exciting opportunities for further investigation, particularly through atomistic simulations aimed at exploring their stability and interaction dynamics.

4.8 Domain wall properties in islands

We will now have a look at how the domain walls behave in Mn double layer islands. The behaviour of domain walls can be different in the islands, because of geometrical effects arising from the triangular shapes of islands. In the island form, Mn grows in hexagonal/truncated hexagonal shapes due to the underlying (111) symmetry of the substrate [21]. To achieve island growth, Mn was deposited 90 minutes after flashing the Ir crystal. Additional preparation details of this sample can be read in Section 3.3.1.

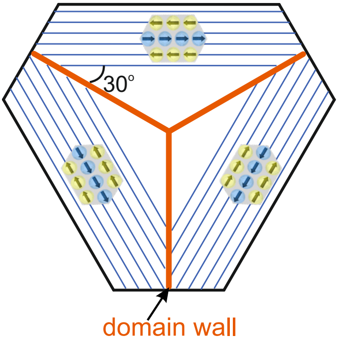

Figure 4.23: Existence of 60° domain walls in the DL islands. The sketch shows the ideal shape of an island on a hexagonal lattice with long and short edges. The AFM rows are parallel to the long edges and hence the domain walls are of the 60° type.

Now that we know what factors induce domain walls in the bilayer system, we can think and guess what the domain walls would do in such islands. We have seen a SP-STM image of an island in Fig. 4.11 where the long edges of the truncated hexagonal island require the RW-AFM domain to be parallel, thus demanding a FM edge. Due to the three long edges preferring a FM order, three domain walls will exist that meet in the centre ideally, to allow for the existence of the three RW-AFM domains. Hence, in contrast to the extended DL terraces, the domain walls that form in the DL islands are 60° domain walls and not the prominent 120° domain walls in extended layers of the DL.

In Fig. 4.24, an STM topography overview image of a sample with islands of the DL is shown. From (b) to (e), a series of STM measurements has been shown on a DL island (not present in (a)). What we see initially in panel (b), is the existence of three domain walls having connecting points at the corners of the island and meeting in the centre. But their formation is hindered by the presence of small triangular-shaped hydrogen islands. As we have seen before in Fig. 4.11, hydrogen islands like to have an AFM edge. And so the competition between a FM edge and an AFM edge requirement by the step edges and hydrogen islands, respectively, distorts the otherwise ideal triple junction formation of the domain walls in the island.

Hence, in the quest for remocing the hydrogen impurities, the islands were scanned at slightly higher voltages. As can be seen from (c-d), the hydrogen impurities try to move and accumulate roughly in the centre of the island, allowing for the ideal Y shaped triple junction formation of the domain walls. In panel (e), one can see that scanning at lower bias voltage of 10mV, brings back the hydrogen island, but now more agglomerated compared to the formation in panel (b).

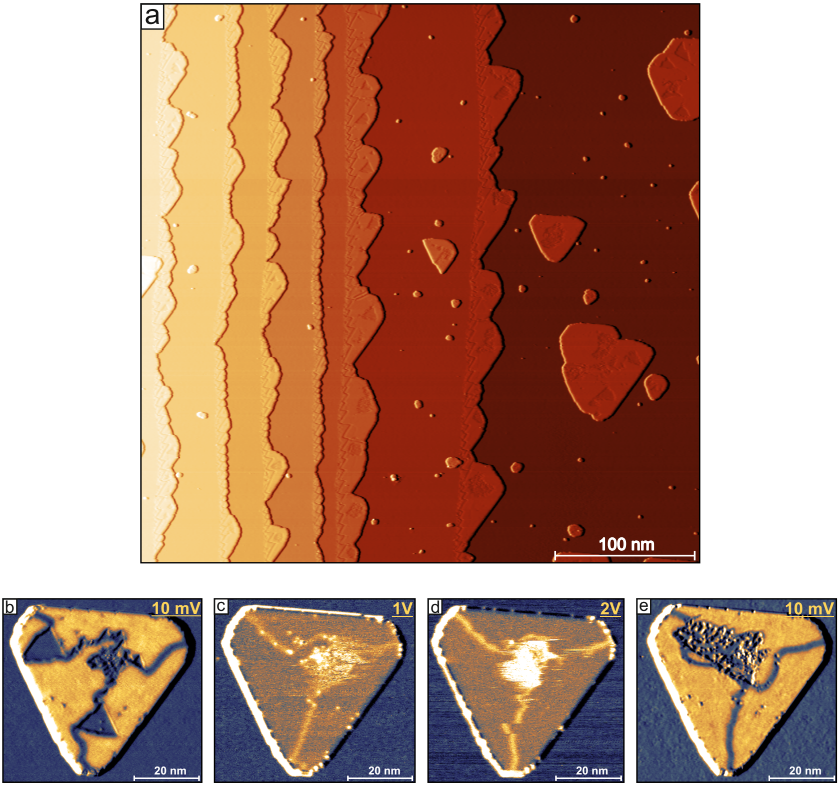

Figure 4.24: Magnetic domain wall triple junction in DL islands. **(a)** A constant-current topography image showing an overview of a sample coverage of 1.2 MLs and with DL islands. An attempt of imaging the nature of magnetic domain walls in the DL islands was made. Hydrogen impurities occupied a few patches on the islands which were tried to be removed by scanning at high voltages. **(b)-(e)** dI/dU images scanned in succession. A triple domain wall junction is seen in (c,d) which was obtained by scanning at 1V and 2V respectively. **(e)** dI/dU map obtained after scanning the island at 5V (not shown here). (Measurement parameters: a: $U = +10\,\text{mV}$, $I = 1\,\text{nA}$; b: $U = 10\,\text{mV}$, $I = 1\,\text{nA}$; c: $U = 1\,\text{V}$, $I = 1\,\text{nA}$; d: $U = 2\,\text{V}$, $I = 1\,\text{nA}$; e: $U = 10\,\text{mV}$, $I = 1\,\text{nA}$; all: $T = 4\,\text{K}$).

4.9 Generating magnetic domain wall networks

The formation of domain walls in ferromagnets is primarily driven by the need to reduce stray field energy. This phenomenon has been extensively documented in both thin films and bulk materials [22]. Depending on the geometry of the system, domain walls can adopt intricate configurations, such as the well-known Landau domain patterns [23].

Antiferromagnetic (AFM) domain walls have received significant interest in recent years, largely due to their lack of stray fields and potential for terahertz (THz) operation speeds. However, one of the key challenges in utilizing AFM domain walls lies in the difficulty of generating them in the first place.

In this chapter, the demonstration of the generation of extended domain wall networks in the Mn bilayer on Ir(111) using Argon ion (Ar^+) sputtering has been shown. Ion bombardment has long been employed in the magnetism community as a tool for creating domain walls, skyrmions, and for tuning the local magnetic properties by modifying the anisotropy of the magnetic moments near the implanted ion regions [24–28]. To the best of my knowledge, at the time of writing this thesis, there are no reported instances of domain wall networks being generated in non-synthetic antiferromagnetic systems. However, in one study published in 2024, authors report on a controlled creating and annihilation of domain walls and domain wall junctions, with specific tunneling conditions of bias and current. This is different to what is demonstrated in this chapter. No manipulation of domain wall structures has been carried out in this work [29].

The use of Ar ion bombardment is a standard practice for the surface preparation of ultra-thin films. Typically, high-energy Ar^+ ions are used to clean the crystal surface, but this process also creates vacancies and defects up to several layers beneath the surface. Subsequent annealing is employed to heal the surface. During this step, Ar atoms tend to form clusters or bubbles, and eventually escape from the crystal at sufficiently high annealing temperatures.

This mechanism has been thoroughly investigated by Kurnosikov et al. [30], as illustrated in Fig. 4.25. In our experimental protocol, the process was deliberately halted at the stage corresponding to panel (c). This is where the Ar ions form subsurface clusters or bubbles. Unlike conventional surface preparation routines, we did not anneal the Ir(111) crystal to the full recovery temperatures typically required to remove the implanted Ar. As a result, the crystal retains trapped Argon bubbles, which manifest as bright protrusions in STM topographic images. One of the earliest observations of such trapped Ar bubbles was reported by Gsell et al. for the Ru(0001) surface [31].

Fig. 4.26 above shows the topographic and dI/dU images of a large-scale magnetic domain wall network in the Mn bilayer on Ir(111) in panels (a) and (b) respectively. This particular sample was prepared by annealing the substrate to 470 K during Mn deposition, which facilitated the formation of large pseudomorphic areas. In the topographic image, the bright spots correspond to trapped Argon bubbles, with lateral dimensions in the range of 5–10 nm and apparent heights between 15–130 pm.

The bright and dark lines visible in the topography and dI/dU images, respectively, represent magnetic domain walls-predominantly 120° domain walls that align along the close-packed row directions. This stunning configuration visually resembles a neural network. In the dI/dU image, four triple domain wall junctions have been labeled as Y, Y*, T, and T*. These serve as the fundamental building blocks of the domain wall network and will be analyzed in greater detail in the subsequent section. It is worth emphasizing that these triple junctions host the non-coplanar, topologically non-trivial 3Q antiferromagnetic state. This feature adds a unique character to the observed network: it can be interpreted as a

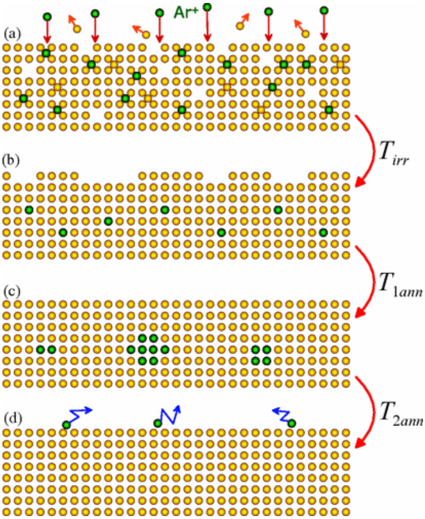

Figure 4.25: Schematic of Argon bubble formation and dynamics with respect to annealing temperature. **(a)** Ar^+ ion irradiation introduces a variety of point defects and lattice disorder in the near-surface region. **(b)** Upon annealing at T_{irr}, partial Ar^+ ion recombination occurs and some healing at the surface is observed. **(c)** Further annealing at $T_{1\mathrm{ann}}$ promotes Ar^+ ion diffusion and clustering resulting in Ar bubble formation. **(d)** At a higher annealing temperature $T_{2\mathrm{ann}}$, Ar bubbles escape the surface. Extracted with permission from [30], copyright 2011 by the American Physical Society.

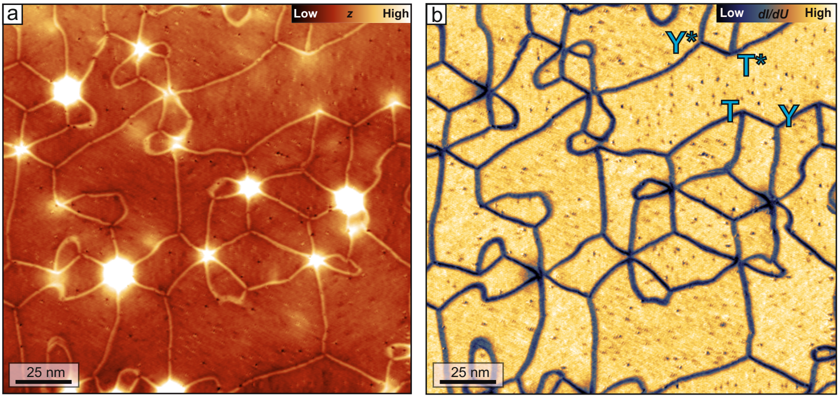

Figure 4.26: Strain-induced domain wall network in a collinear antiferromagnet. (a) Constant-current STM image of a Mn double-layer film on Ir(111); the bright spots correspond to Ar bubbles below the Ir surface; bright lines indicate domain walls between orientational antiferromagnetic domains. **(b)** dI/dU map acquired simultaneously with (a); labels refer to the types of triple-junctions. (Measurement parameters: $U = +10\,\text{mV}$, $I = 5\,\text{nA}$, $T = 4\,\text{K}$).

domain wall network in an otherwise collinear AFM background, interconnected by localized regions exhibiting topological 3Q order. This hybrid structure holds potential significance for future explorations in antiferromagnetic spintronics.

The influence of Argon bubbles can be seen in Fig. 4.27. In (a), the bare Ir(111) surface can be seen with trapped Argon bubbles. After deposition of Mn, (Fig. 4.27(b)), the Mn DL area exhbits a few domain walls running almost parallel to each other. In (c), one can observe the large domain wall network interconnected with junctions. It is worth mentioning that these images are all of very similar sizes and hence they have been used for comparison.

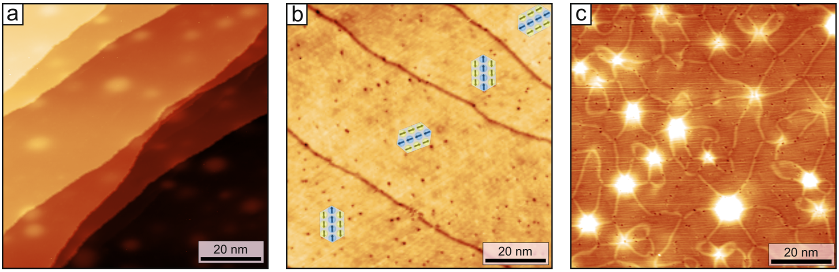

Figure 4.27: Impact of Ar bubbles on domain wall density. **(a)**, Constant-current STM image of Ar bubbles in the uncovered Ir(111) surface ($\Delta z = 1.2$ nm). After the final Ar-ion etching step, the Ir crystal was annealed twice at a temperature of $T \approx 1300$ K twice for 40 seconds. (Measurement parameters: $U = +250$ mV, $I = 0.5$ nA; $T = 300$ K). **(b)**, Constant-current STM image of the Mn double-layer on a broad Ir(111) terrace ($\Delta z = 25$ pm). In contrast to the other samples with Ar bubbles, in this preparation the Ir(111) substrate was annealed at a higher temperature of $T \approx 1600$ K before the deposition of Mn. Dark lines indicate domain walls between orientational domains of the RW-AFM state; note that due to a different sample bias voltage the domain walls appear dark in this measurement. (Measurement parameters: $U = +500$ mV, $I = 1$ nA; $T = 10$ K). **(c)**, Constant-current STM image of the Mn double-layer on an Ir(111) surface with Ar bubbles ($\Delta z = 144$ pm); bright lines indicate domain walls between orientational domains of the RW-AFM state, which form a network induced by the strain around the Ar bubbles. (Measurement parameters: $U = +10$ mV, $I = 1$ nA; $T = 4$ K).

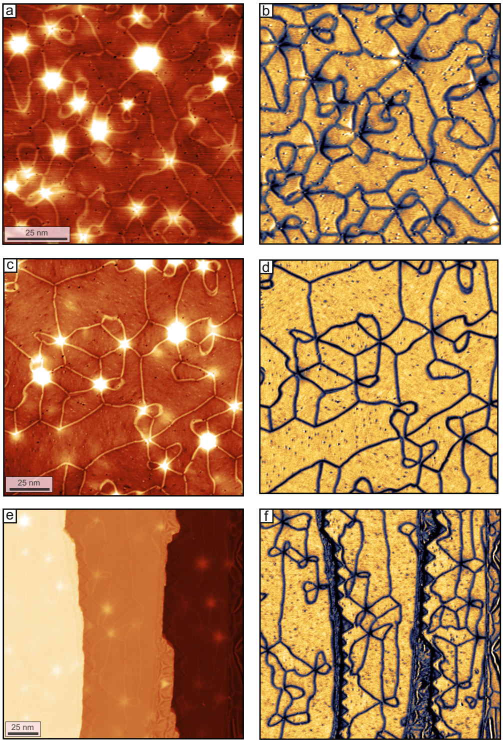

Figure 4.28: Correlation of domain wall network density with Argon bubbles. This figure illustrates the relationship between the density of argon bubbles trapped beneath the surface and the resulting magnetic domain wall network. **(a, c, e)** STM images showing surfaces with varying densities and distributions of argon bubbles (bright spots). The bubble density appears to decrease from (a) to (e). **(b, d, f)** Corresponding $\mathrm{d}I/\mathrm{d}U$ maps derived from the STM images in (a), (c), and (e), respectively. The dark blue lines represent magnetic domain walls. A clear correlation can be observed: higher argon bubble density corresponds to a denser domain wall network. This suggests that the strain fields induced by the argon bubbles play a significant role in the nucleation and stabilization of magnetic domain walls. (Measurement parameters: a,b: $U = +10\,\mathrm{mV}$, $I = 1\,\mathrm{nA}$, $T = 4\,\mathrm{K}$; c,d: $U = 110\,\mathrm{mV}$, $I = 5\,\mathrm{nA}$, $T = 4\,\mathrm{K}$; e,f: $U = 10\,\mathrm{mV}$, $I = 0.6\,\mathrm{nA}$, $T = 8\,\mathrm{K}$).

The domain wall network observed in the DL of Mn/Ir(111) has been successfully reproduced in another sample, as shown in Fig. 4.28(a, b). Figs. 4.28(c, e) further display domain wall networks captured from different regions of the same sample, demonstrating the robustness and reproducibility of the network formation. The domain wall density appears to correlate with the density of argon bubbles. However, it should be noted that the region shown in panel (c) contains Mn terraces, making direct comparison with the large, flat terrace areas in panels (a) and (e) less straightforward.

4.9.1 Building blocks of the network: Triple junctions

Fig. 4.29 shows a $\mathrm{d}I/\mathrm{d}U$ image with magnetic contrast of the Mn bilayer where a part of the domain wall network can be seen. All the three rotational domains as well as the magnetic state of the domain walls can clearly be recognized. As mentioned before, the triple junctions are the basic building blocks of this network which have been marked in this figure too. Red arrows are drawn to show the connectivity between the junctions.

This connection sequence is unique in the sense that a Y junction is always followed by a T/T* and never by a Y/Y*. This adds to the uniqueness of the domain wall network where the junctions do not form randomly, but are dictated by domain wall energies. To understand this, we will have a look at some schematics for these junctions.

In Fig. 4.30(a), we can see that a Y junction is connected by it's mirror image Y* junction. This is not allowed as the RW-AFM domain is parallel to the domain wall in the Y* junction which is not favourable as we have seen for the long axis directional domain walls in the elliptical loops in section 4.6

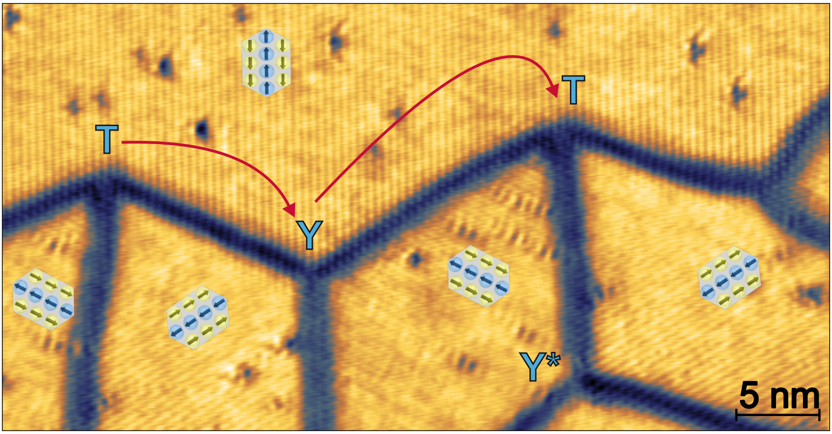

Figure 4.29: Building blocks of the network: Triple junctions. Constant-current dI/dU image showing a network of magnetic domain walls in the Mn double-layer, highlighting the formation of triple junctions. The junctions are categorized as T, Y, and Y^* types, based on the orientation of the surrounding RW-AFM domains and the connectivity of domain walls. Red arrows indicate the transformation from one junction type to another via domain wall reconfiguration. The junctions act as fundamental topological elements governing the morphology and connectivity of the domain wall network. (Measurement parameters: a,b: $U = +10\,\mathrm{mV}$, $I = 1\,\mathrm{nA}$, $T = 4\,\mathrm{K}$).

An analysis of the stress distribution in the Y* junction shown in Fig. 4.30(a) reveals symmetric stress characteristics across its branches, as indicated by the blue arrows. The upper branch of the Y* junction exhibits symmetric tensile stress, while the lower branch experiences symmetric compressive stress. In contrast, the dominant 120° domain walls typically exhibit asymmetric stress-one side tensile and the other compressive—as previously illustrated in Fig. 4.16, and also seen for the Y junction in Fig. 4.30(a).

Fig. 4.29(b) shows a schematic of an allowed connectivity pattern, where a Y junction is connected to a T* junction. In this configuration, none

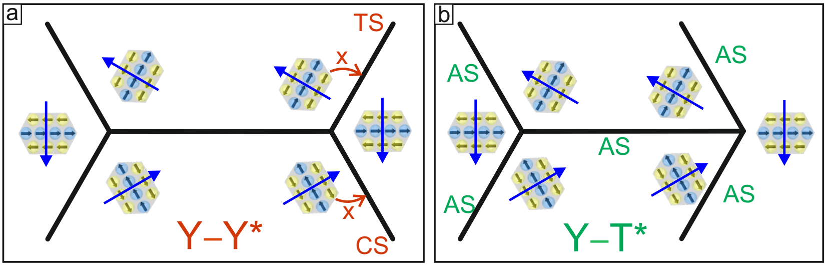

Figure 4.30: Stress configurations at triple junctions in the domain wall network. **(a)** Schematic of a Y–Y^* junction pair configuration under mixed stress conditions. Compressive stress (CS) and tensile stress (TS) are indicated by red arrows, corresponding to inward and outward shifts of the magnetic domains, respectively. **(b)** Schematic of a Y–T^* junction pair, showing a configuration under uniform asymmetric stress (AS). This corresponds to the experimentally observed situation of a Y–T^* connection.

of the RW-AFM domains are aligned parallel to the domain wall, and every domain wall segment experiences an asymmetric stress. This is consistent with the patterns observed experimentally.

4.9.2 Building blocks of the network: Hexa-junctions

Going beyond triple junctions, the domain wall network hosts more complex junctions where six magnetic domain walls meet. This again has a similarity to the existence of hexa-junctions in cosmological domain wall networks [32].

Fig. 4.31 shows an overview of a domain wall network in a sample area different to the one shown in Fig. 4.26. A zoom-in SP-STM topography image is shown in (b) where a Y junction can be seen connected to a hexa-junction. The hexa-junction has six domains and every pair of opposite domain has the same RW-AFM orientation.

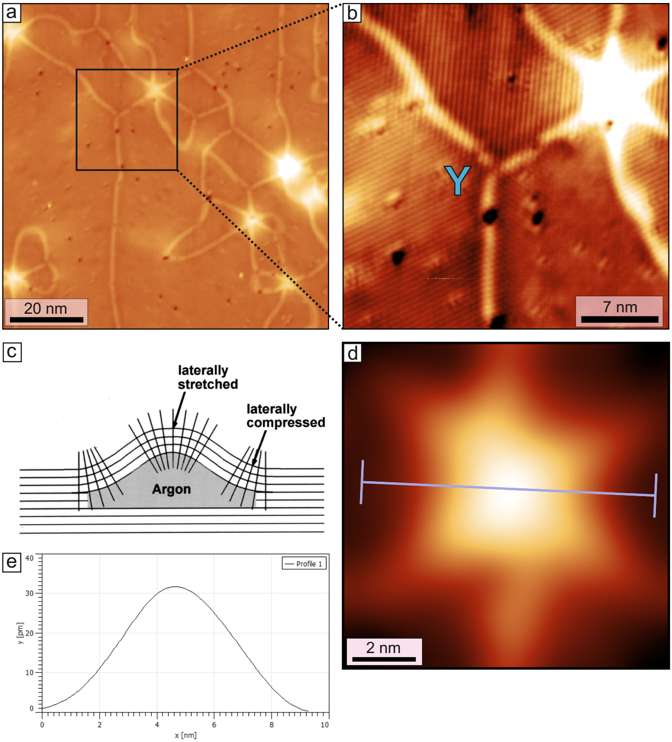

Figure 4.31: Formation of magnetic domain wall networks driven by strain from Argon bubbles. **(a)** Constant-current topography STM image revealing a domain wall network. **(b)** A higher magnification STM image shows a hexa-junction connecting to a Y junction. **(c)** A schematic illustration of the proposed mechanism for domain wall network formation. An argon bubble trapped beneath the surface induces a strain field in the overlying magnetic film. This strain field leads to regions of lateral stretching and compression on the surface, thereby facilitating the nucleation and propagation of magnetic domains and resulting in a domain wall network. **(d)** Hexa-junction in **(b)**after a high pass filtering with a cut-off wavelength of 3.706 nm shown. The line profile across the underlying Argon bubble shown in **(e)** has a Gaussian profile similar to the sketch in (c). (c) was reprinted with permission from [31], copyright 1998 of the American Association for the Advancement of Science. (Measurement parameters: a: $U = +10\,\mathrm{mV}$, $I = 0.6\,\mathrm{nA}$; b,c: $U = +10\,\mathrm{mV}$, $I = 1\,\mathrm{nA}$; all: $T = 8\,\mathrm{K}$).

Fig. 4.31(c) presents a sketch adapted from the study of sub-surface Argon bubbles in Ru(0001) by Gsell et al. [33]. In their work, Argon ions were implanted beneath the Ru surface, and the effect of the resulting subsurface strain fields on adsorbates such as O_2 and CO_2 was investigated using STM. The schematic in (c) showcases the presence of lateral tensile and compressive strain at the centre and slopes of the Argon bubble, respectively. It was observed that the adsorbates organized themselves into specific orientations, strongly influenced by the strain fields radiating from the trapped Argon bubbles.

A similar mechanism may be at play in the present case of hexa-junction formation in the Mn bilayer on Ir(111). At these junctions, the local C_3 symmetry is broken by the slope of the Argon bubble, even before the onset of magnetism. This symmetry breaking occurs during the sample preparation process and is therefore independent of the measurement temperature. When the sample is subsequently cooled below its Néel temperature (T_N), magnetic ordering sets in, and the RW-AFM orientational domains begin to form. These domains are guided by the local strain field induced by the Argon bubble at the hexa-junction, which acts as a symmetry-breaking seed.

The emergence of an orientational domain configuration at the hexa-junction then necessitates the formation of a triple domain wall junction to accommodate the resulting magnetic textures. This triple junction, in turn, must be connected to another compatible junction-such as a Y or T junction-to preserve continuity. Through this cascading process, an extended domain wall network is established. Fig. 4.31(c) presents a high-pass filtered image of the hexa-junction in panel (b). The filtering is applied to only retain the contrast arising from the Argon bubble in the topography. A line profile of the Argon bubble is presented in Fig. 4.31(e) where a Gaussian shaped profile is seen similar to panel (c).

It should be emphasized that this is a proposed mechanism, based on analogy and experimental observation. At present, no theoretical or atomistic simulations have been conducted to confirm the formation dynamics or energetics of domain wall networks in this system.

4.9.3 Magnetic state: Triple junctions

The triple junctions discussed in the preceding sections represent points where the three rotational domains of the row-wise antiferromagnetic (RW-AFM) state converge. In principle, such junctions should locally stabilize a $3Q$ magnetic state, as they constitute a superposition of three $1Q$ domains.

To investigate whether such a spin texture is realized at the junctions, SP-STM measurements were carried out, and the results are shown in Fig. 4.32. The experiment was performed using an iron-coated tungsten (Fe/W) tip. As discussed in Chapter 3, this tip exhibits in-plane magnetization at zero external field (0 T), and transitions to a predominantly out-of-plane (OOP) magnetization at an applied field of 2.5 T, thereby enabling OOP-sensitive magnetic contrast.

In the images shown in Fig. 4.32, clear RW-AFM contrast is observed at 0 T, with the expected domain pattern across the terrace. At 2.5 T, the RW-AFM contrast diminishes, while the magnetic contrast at the junction is enhanced. Notably, a hexagonal magnetic pattern emerges at the junction, suggestive of a localized $3Q_1$ state (see Fig. 2.9 for comparison). Due to a slight drift induced by the applied magnetic field, an identical sample area could not be imaged at both field strengths; however, the region imaged at 2.5 T remains spatially close to the one at 0 T (see defect marked in a square).

Figures 4.32(c) and (d) present zoomed-in images of a T and Y junction, respectively, imaged at 0T in a different sample. In both cases, a hexagonal magnetic contrast is observed, further supporting the hypothesis that triple junctions in this system locally host a non-coplanar $3Q$ magnetic state. Figures 4.32(e) and (f) present spin models of a T and Y junction respectively, where the emergence of a $3Q^1$ state can be seen at the junctions.

4.9.4 Magnetic state: Hexa-junctions and more

Fig. 4.33(a) displays two hexa-junctions, with the one on the right representing a pair of closely spaced T-T* junctions. Further insight is gained from the corresponding SP-STM current map shown in Fig. 4.33(b), which reveals the magnetic contrast with greater clarity than the topographic image.

In the current channel, a distinct hexagonal magnetic pattern is visible at the hexa-junction, strongly suggestive of a localized $3Q$ state. Given the symmetry and structure of the observed pattern, it is most likely indicative of a $3Q_1$ configuration, which is characterized by its regular hexagonal symmetry. The junction pair on the right also presents a hexagonal magnetic pattern similar to the hexa-junction. This is discussed in depth based on Fig. 4.34.

4.9.5 Phase-dependent magnetic state at the hexa-junction

Understanding the magnetic textures at complex domain wall junctions requires insight not only from experimental imaging but also from theoretical modeling. In particular, the role of phase relationships between adjacent magnetic domains plays a crucial role in shaping the local spin structure at these junctions. To explore this, spin simulations were car-

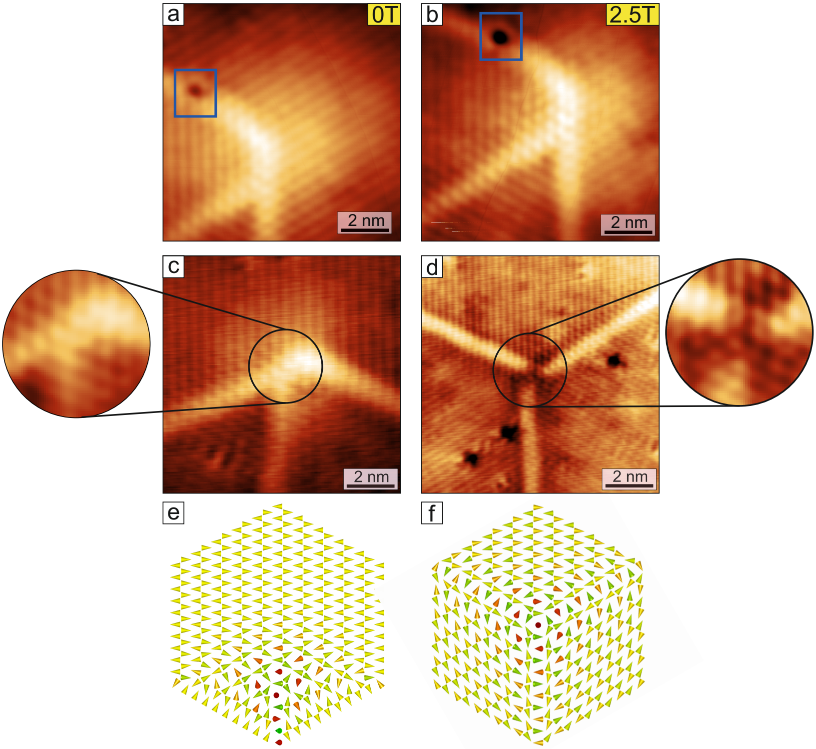

Figure 4.32: Probing the 3Q antiferromagnetic state at the junctions (a) and **(b)** show a constant-current SP-STM topography image of a T^* junction at 0T and 2.5T, respectively. At 2.5T, a hexagonal pattern at the junction can be seen which is not visible at 0T. This hints towards the presence of the 3Q state at the junction imaged with a supposedly out-of-plane magnetized tip in (b). **(c)** and **(d)** show constant-current SP-STM topography images of a T and Y junction, respectively measured at 0T with the tip having an arbitrary magnetization direction. The hexagonal magnetic pattern at the junctions shown in magnified insets also hints towards the 3Q state at the junctions. **(e,f)** Spin models of the T and Y junction, respectively. (Measurement parameters: a,b: $U = +10\,\text{mV}$, $I = 7\,\text{nA}$, $T = 80\,\text{K}$; c,d: $U = +10\,\text{mV}$, $I = 5\,\text{nA}$, $T = 4\,\text{K}$).

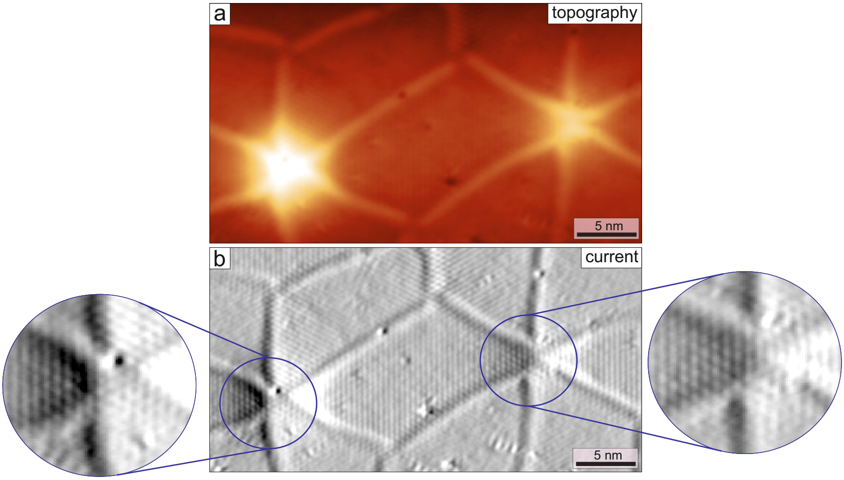

Figure 4.33: Magnetic contrast in the hexa-junction. **(a)** constant-current STM topography image of the DL showing two hexa-junctions as part of a domain wall network. **(b)**, Current map obtained simultaneously to the SP-STM image of (a), in which the hexagonal magnetic pattern in the center of the hexa-junctions can be seen. Magnified insets of the hexa-junction magnetic state are shown for clarity. (Measurement parameters: $U = +10$ mV, $I = 1$ nA, $T = 4$ K, Cr-bulk tip).

ried out using a monolayer hexagonal lattice-an approximation that captures the essential symmetry of the system while allowing for the analysis of spin textures in constrained geometries.

Fig. 4.34(a) presents a constant-current SP-STM topography image, processed with a filter to suppress the Argon bubble contrast at the hexa-junction. This zoom-in corresponds to the junction shown earlier in Fig. 4.31. The evenly spaced black segmented line across an opposing domain pair indicates that these domains are in-phase. The corresponding spin model in Fig. 4.34(b) confirms the emergence of a $3Q^1$ configuration at the junction, consistent with the SP-STM observations.

Fig. 4.34(c) shows a pair of T/T* junctions at a finite separation, where the resultant spin texture between the junction is a $1Q$ state. A reduced junction spacing is expected to enhance this distortion due to increased interaction between local spin environments. Figures 4.34(d) and (e) explore cases where pairs of opposing domains are out-of-phase. The resulting magnetic textures deviate from the ideal $3Q^1$ configuration, underscoring the influence of phase mismatches on local spin symmetry. These results highlight that domain wall networks are constrained not only by geometry but also by the phase relationships between domains.

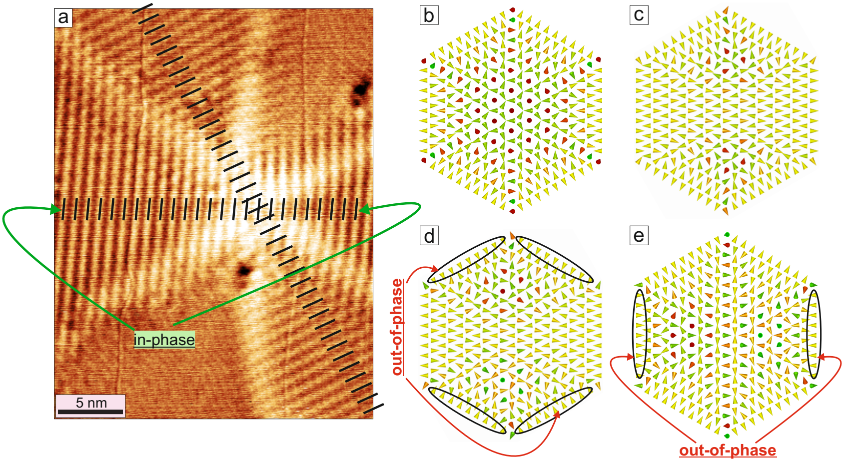

Figure 4.34: SP-STM image and spin model analysis of a hexa-junction and related magnetic textures. **(a)**, SP-STM constant-current image of a hexa-junction, after a high-pass filter with a cut-off frequency corresponding to 0.55 nm was applied to the raw data in order to remove the height variation of the Ar bubble and enhance the visibility of the magnetic state. Equally spaced black lines indicate the maxima of magnetic contrast of the RW-AFM and demonstrate that two pairs of RW-AFM domains across the Ar bubble are in-phase; no magnetic contrast was obtained for the third orientational domain. (Measurement parameters: $U = +10$ mV, $I = 1$ nA, $T = 8$ K, Fe-coated W tip.) **(b)**, Spin model with six RW-AFM domains, with the constraint that three pairs of RW-AFM domains across the center are in-phase, resulting in a perfect $3Q$ state in the center of the hexa-junction; the hexagonal magnetic pattern of the hexa-junction in (a) and the spatial distribution thereof are in good agreement with this spin model. **(c)**, Spin model with six RW-AFM domains, with the constraint that again three pairs of RW-AFM domains are in phase, resulting in a different spin texture in the center of the hexa-junction, which can be better described as a pair of T-/T*-triple-junctions; a T-/T*-triple-junction is present at the right side of the measurement in Fig. 4.33, but it has not been possible to identify the spin texture at its center. **(d,e)**, Spin models with six RW-AFM domains, with the constraint that some pairs of RW-AFM domains are out-of-phase, resulting in pairs of T-/T*-triple-junctions with complex spin textures in their centers.

4.9.6 Chirality of the junctions

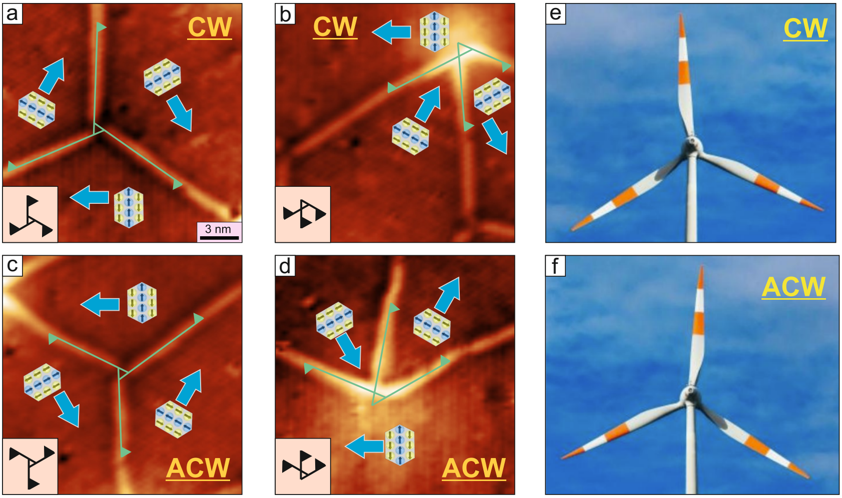

Figure 4.35: Deducing the handedness of structurally chiral junctions. The different triple junctions have been analyzed for their handedness which include the Y (**(a)**), Y^* (**(b)**), T (**(c)**) and T^* (**(d)**) junctions. Lines drawn along the domain walls do not meet at a point, but instead span a triangle, suggesting asymmetric junctions. Thick blue arrows represent the lateral shift directions for each rotational domain. Insets in each panel from (a-d) show the three armed fan schematic for clarity. The handedness of the junctions can be better visualized by the windmill pictures shown in **(e,f)** for clockwise (Y^*, T^*) and anti-clockwise handedness (Y, T). (Measurement parameters: all: $U = +10\,\mathrm{mV}$, $I = 5\,\mathrm{nA}$, $T = 4\,\mathrm{K}$).

The final aspect of the unique domain wall junctions to be discussed is their chirality. It is important to emphasize that the chirality referred to here is *structural chirality*, not the chirality induced by the Dzyaloshinskii–Moriya interaction (DMI). While the Ir(111) substrate is known to induce DMI, density functional theory (DFT) calculations have shown that the DMI contribution in this system is negligible.

Focusing on structural chirality, the triple junctions exhibit a distinct handedness. Rather than converging symmetrically at a central point, like the blades of a Mercedes-Benz logo, the domain walls exhibit a clear asymmetry at the junction. This asymmetry arises from the lateral atomic shift in the bilayer, which acts in different directions for each of the three rotational domains. It is this interplay that imparts chirality to the junction, making each one structurally unique.

To determine the handedness of a junction, lines are drawn along the three domain walls and extended towards the junction. When extended, these lines form a triangle whose geometry reflects the underlying asymmetry. Each line, when considered in relation to the triangle it forms, exhibits a preferred rotational sense. By associating small directional triangles at the ends of the extended domain wall lines, one can visualize the overall rotational character of the junction-analogous to the motion of a three-bladed windmill.

In the case of T and T* junctions, chirality is deduced by analyzing the net handedness of the three extended domain wall segments. This analysis is illustrated with four representative examples shown in Fig. 4.35, where the triangle construction and the corresponding sense of rotation are clearly marked.

Fig. 4.35 also highlights the lateral structural shift directions associated with each rotational domain around the junctions (blue arrows). An intriguing observation is that the structural shift directions themselves exhibit chirality, and this chirality appears to correlate with the handedness of the corresponding junctions. Specifically, the Y and Y* junctions shown in the figure display anti-clockwise handedness, and the associated structural shift directions follow the same rotational sense.

Although the handedness of the structural shift directions for the T and T* junctions is more difficult to deduce directly from the geometry, it is reasonable to assume that they follow the same correlation as observed for the Y/Y* junctions. This alignment between magnetic and structural chirality may point toward a deeper coupling mechanism in the formation and stabilization of these topological junctions within the domain wall network.

To summarize, the triple junctions discussed in this work are structurally chiral and exhibit a distinct handedness. Each junction type can exist in multiple orientations, obtained through 120° rotations due to the underlying hexagonal symmetry. In Fig. 4.36, all possible orientations for each kind of triple junction are illustrated using colored triangles. These triangles serve as indicators of the domain wall connection points. When constructing a domain wall network, the color-coded triangles provide a visual guide for determining which junctions are connectable and in what type of configuration.

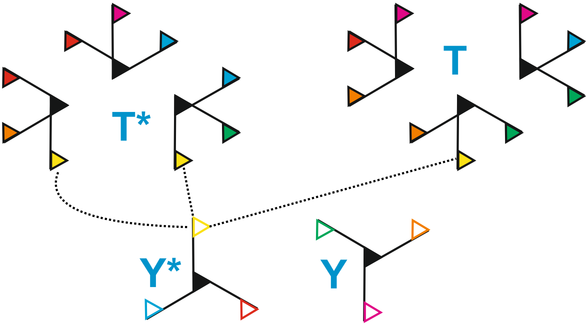

Figure 4.36: Sketches of all possible triple-junctions occurring with 120° domain walls. The T/T*-junctions occur in three orientations. To form a network, a pair of empty (Y/Y*-junction) and filled triangles (T/T*-junction) of the same color need to be connected, i.e., any straight wall must have a Y/Y*-junction at one end and a T/T*-junction at the other end, respectively, which is the only possible way of forming the network. An example has been shown for connecting the Y* junction to a T* and T junction via the yellow triangles - see black dotted lines.

4.10 Topological orbital moment

Moving to emergent magnetism in the DL, we will now discuss the topological orbital moment (TOM) which arises due to the presence of a non-coplanar spin texture with non-zero scalar spin chirality.

To start with the TOM, some DFT calculations by the theory collaborators from the group of Prof. Stefan Heinze, Univeristy of Kiel, Germany, will first be presented. In the sketches shown in Fig. 4.37, 3Q states in both the layers of Mn are shown. Hence, there is a 3Q state within the layers and also between the layers. The inter-layer coupling can be AFM or FM. Both cases have been calculated and it can be seen that the AFM case has a higher net TOM value. Importantly, only in the inter-layer AFM case does the 3Q state exhibit tetrahedral spin angles both within and between the layers. In contrast, for the inter-layer FM case, the tetrahedral angles appear only within the individual layers.

This behavior is consistent with the inter-layer AFM coupling of the RW-AFM magnetic state, which was previously shown—see Fig. 4.3—to be energetically more favorable than the FM case. This is in agreement with an inter-layer AFM coupling of the RW-AFM magnetic states which was shown to have lower energy than the FM case in Fig. 4.3. A point to be noted here is that when the 3Q inter-layer coupling is FM (AFM), the inter-layer TOM coupling is AFM (FM).

The TOM cannot be probed directly but there are indirect ways to probe it. In transport experiments, the spontaneous topological Hall effect is the hint for the presence of a non-zero TOM in the sample system as shown in the 2D vdW material [34]. In STM experiments, an indirect means of probing the TOM is to look for any effect of an externally applied magnetic field on the domains/domain walls. As the TOM has a non-zero magnetic moment, it should in principle react to an externally applied magnetic field. This could result in the movement of domain

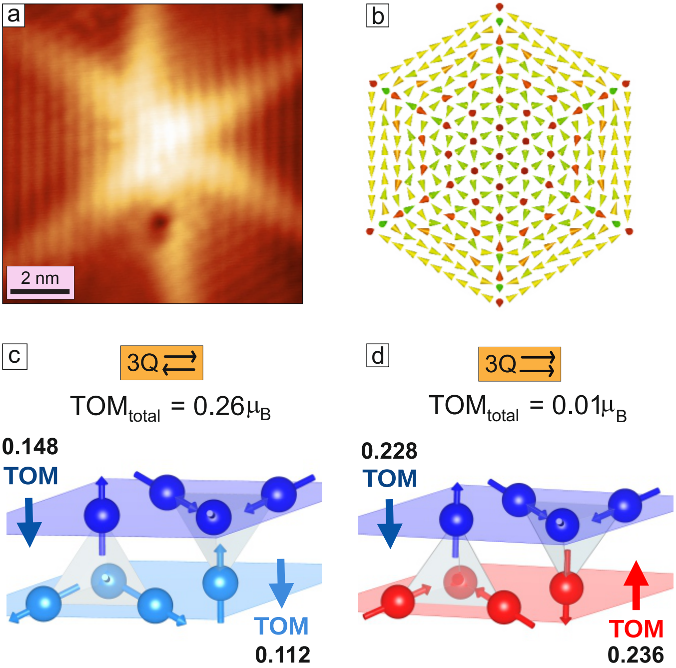

Figure 4.37: Calculation of the TOM for the double layer Mn/Ir(111) system assuming a 3Q state in both the layers with different inter-layer couplings. **(a)** Constant-current SP-STM topography image of a hexa-junction whose spin model has been shown in **(b)** with a 3Q state in the centre of the hexa-junction. **(c)** A 3Q state in both the layers with an inter-layer AFM coupling results in FM coupling of the TOM which amounts to 0.26 μ_B. **(d)** 3Q state in both the layers with an AFM inter-layer coupling resulting in a cancellation of the TOM contributions, and a vanishing total TOM of 0.01 μ_B per magnetic unit cell. (Measurement parameters: a: $U = +10\,\text{mV}$, $I = 1\,\text{nA}$, $T = 8\,\text{K}$).

walls which could be an effect of the TOM on the domains themselves.

A magnetic field-dependent experiment was performed on the domain wall network in the DL of Mn/Ir(111), as shown in Fig. 4.38. Panels (a) and (b) display SP-STM images acquired at 0 T and 9 T, respectively. The images are nearly identical, indicating that the topological orbital moment (TOM) does not exhibit any noticeable response to the applied magnetic field under the given conditions.

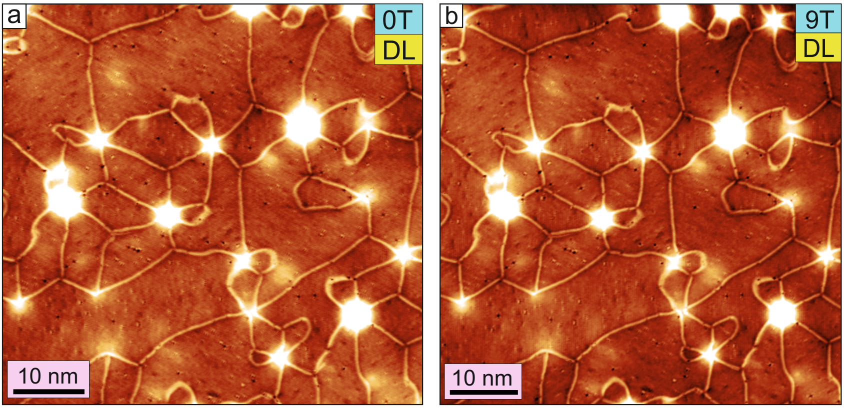

Figure 4.38: Field dependent measurement of the domain wall network in the DL. (a,b) Constant-current STM topography images of the domain wall network in the DL measured at applied external magnetic fields of 0T and 9T. Due to the presence of a TOM at the junctions, an effect of the external magnetic field on the junctions was expected, but not observed. (Measurement parameters: all: $U = +10\,\mathrm{mV}$, $I = 5\,\mathrm{nA}$, $T = 4\,\mathrm{K}$).

There are three plausible explanations for this observation. First, the magnitude of the TOM may be too small to interact measurably with an external magnetic field of this strength. Second, the orientation of the applied field could play a critical role. Since the experimental direction of the TOM in this system is unknown, it is possible that the chosen field direction does not couple effectively to it. The magnetic field in this experiment was applied only in one direction, up to 9 T; it remains to be tested whether applying the field in the opposite direction would produce a detectable effect. Third, it is conceivable that the trapped Argon bubbles act as strong pinning centers for the domain wall junctions, rendering the domain wall network exceptionally stable and resistant to magnetic field-induced reconfiguration. This pinning could mask any intrinsic response of the TOM to the external field.

It is important to note that no magnetic field-dependent measurements have yet been conducted on a DL system without trapped Argon bubbles. Therefore, the role of pinning and TOM response in such a system remains an open and intriguing question for future investigations.

Now that we have studied the building blocks of the domain wall network, I would like to discuss some analogies of domain wall networks in other areas of physics.

To begin this section, it is useful to draw on an analogy commonly encountered in everyday life. While walking along city streets or pavements composed of rectangular or square stone tiles, one often notices the formation of cracks. These cracks typically appear in Y-shaped junctions when they are small, and evolve into complex networks composed of Y- and T-shaped junctions as they grow larger.

4.11 From cosmology to condensed matter based domain wall networks

Interestingly, magnetic domain walls can be interpreted as topological defects within a system, particularly when analyzed through the lens of homotopy theory [35–37]. A similar classification applies to skyrmions, which are widely recognized as topological quasi-particles in condensed matter systems. This offers an intriguing perspective: a magnetic domain wall network can be regarded as a network of topological defects-conceptually analogous to crack networks in fractured stone - observed frequently on roads.

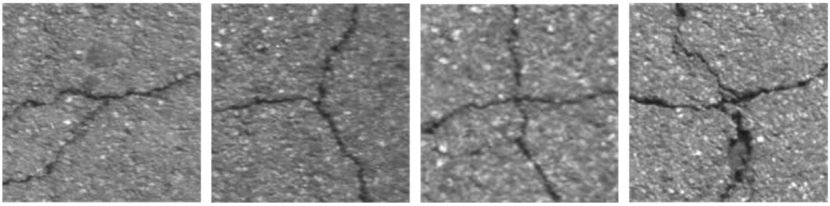

Figure 4.39: Cracks in stone commonly observed on the road. Images from left to right show the different types of junctions, including Y type, T type and X type junctions observed in cracks on roads. Reprinted with permission from [38], copyright 2019 by IEEE.

A more surprising and profound analogy arises from the field of cosmology. In the context of string theory and early universe models, domain walls are considered as fundamental topological defects that emerged as the universe expanded and cooled through successive phase transitions [39, 40]. These defects, much like their magnetic counterparts, originate from spontaneous symmetry breaking and can be classified using homotopy theory. Recent work in astrophysics has even simulated the dynamics of cosmological domain wall networks, highlighting the presence of Y- and X-shaped junctions strikingly similar to those observed in magnetic systems [32, 41].

This analogy not only underscores the universality of topological phenomena across vastly different scales-from cosmological distances to atomic lattices-but also invites cross-disciplinary insight into the behavior, dynamics, and stability of domain wall networks.

In the study by Avelino et al. [42], numerical simulations of domain wall networks arising from spontaneous symmetry breaking in the early universe illustrate how the long-time evolution of such networks is highly sensitive to the initial conditions and the underlying symmetry-breaking potential. As shown in Fig. 4.40, these simulations model the formation and coarsening of domain walls-boundaries separating different vacuum states-using coupled scalar field equations that describe how distinct regions of space settle into different stable configurations.

Depending on the parameters chosen, the system can evolve into late-time configurations dominated by Y-type junctions (three-wall intersections), X-type junctions (four-wall intersections), or a mixture of both. The sequence of panels, moving from top left to bottom right, shows the system evolving from a highly disordered initial state into a more regular, coarse-grained structure as the simulated "universe" expands. The survival of both Y- and X-type junctions is especially noteworthy, as it reflects a balance in the network's topology that is not always guaranteed in other theoretical models.

While domain wall junctions arise from vastly different physical contexts in cosmology and magnetic materials, they play conceptually parallel roles in governing the structure and evolution of the underlying field configurations. In cosmology, junctions form where three or more vacuum domains meet, and their type and stability—such as Y-type or X-type are determined by the topology of the vacuum manifold and the energetics of the scalar field. These junctions influence how the domain wall network coarsens during the universe's expansion and can leave

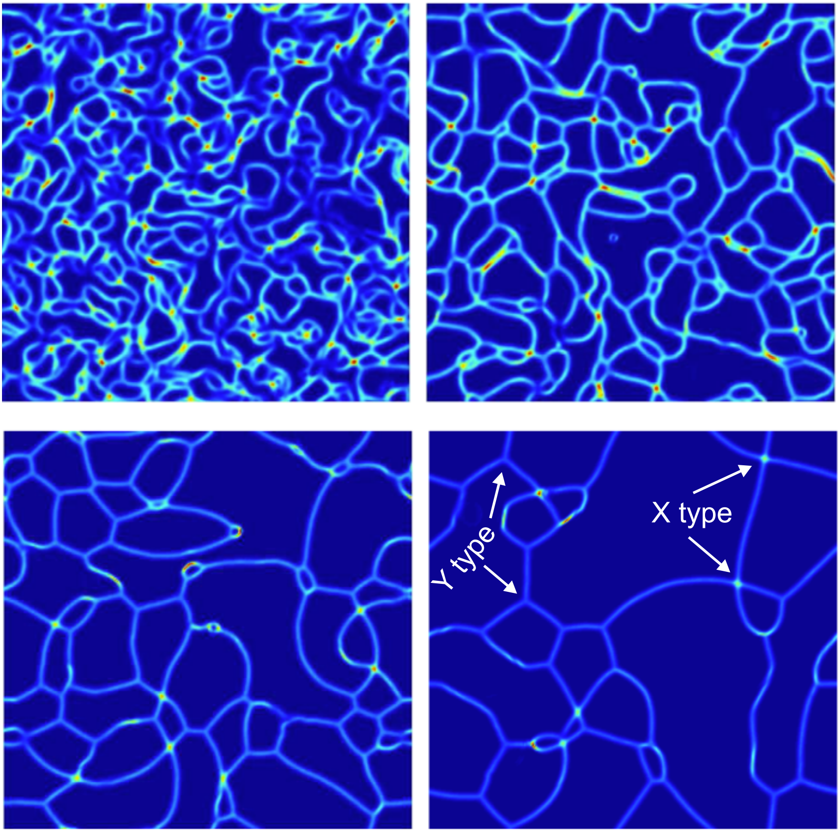

Figure 4.40: Cosmological domain wall network evolution. Matter-era evolution of a cosmological domain wall network, adapted from a Kubotani-type field theory model [42]. The four panels show snapshots at increasing times (top-left to bottom-right), as the horizon scale grows from approximately 1/16 to 1/2 of the simulation box size. As the universe expands, the initially dense and disordered wall structure coarsens into a more regular polygonal network. The walls separate different vacuum domains of the scalar field, and meet at junctions-both Y-type (three-wall) and X-type (four-wall) configurations-which remain stable in the late-time structure. This evolution bears a striking resemblance to the coarsening and junction formation observed in the magnetic domain wall networks in this chapter.

lasting imprints on large-scale structure or cosmological observables. In contrast, in our magnetic system, domain wall junctions emerge from strain-relief patterns and competing exchange interactions in a multilayer antiferromagnet. Here too, junctions are crucial: they define the connectivity of the domain network, mediate local strain and can stabilize non-trivial magnetic textures such as the 3Q states. Thus, while differing in scale and mechanism, domain wall junctions in both systems act as key structural and energetic nodes that dictate the long-range organization and stability of the network.

4.12 Summary

In the DL system, antiferromagnetic domain walls were observed in samples grown at room temperature, arising from various structural features such as hydrogen islands, buried DL–TL and ML–DL step edges, as well as reconstruction and zig-zag dislocation lines. A DFT-predicted lateral structural shift of 1.06 Å was experimentally confirmed, showing excellent agreement. Nanoscale domain wall networks were generated through Argon ion implantation, and their fundamental building blocks were characterized with respect to their magnetic states. Both triple- and hexa-junctions were analyzed: the former serve as localized regions hosting the topological 3*Q* state, while the latter are proposed as potential nucleation sites for domain wall network propagation. The emergence of a topological orbital moment, revealed through DFT calculations, adds further richness to the magnetic and topological landscape of the system. Additionally, the domain wall network has been proposed as a platform for reservoir computing, drawing intriguing parallels with cosmological domain wall networks and highlighting the universality of these structures across different areas of physics.

Bibliography

1. Spethmann, J. *et al.* Discovery of magnetic single-and triple-q states in Mn/Re (0001). *Physical review letters* **124,** 227203 (2020).
2. Spethmann, J., Grünebohm, M., Wiesendanger, R., von Bergmann, K. & Kubetzka, A. Discovery and characterization of a new type of domain wall in a row-wise antiferromagnet. *Nature Communications* **12,** 3488 (2021).
3. Rodríguez-Sota, A. *et al.* Phase Coexistence of Mn Trimer Clusters and Antiferromagnetic Mn Islands on Ir (111). *ACS nano* **18,** 3699–3706 (2024).
4. Saxena, V. *et al.* Strain-driven domain wall network with chiral junctions in an antiferromagnet. *arXiv preprint arXiv:2408.12580* (2024).
5. Joule, J. P. XVII. On the effects of magnetism upon the dimensions of iron and steel bars. *The London, Edinburgh, and Dublin Philosophical Magazine and Journal of Science* **30,** 76–87 (1847).
6. Mayer, A. M. XLIII. On the effects of magnetization in changing the dimensions of iron, steel, and bismuth bars, and in increasing the interior capacity of hollow iron cylinders.—Part I. *The London, Edinburgh, and Dublin Philosophical Magazine and Journal of Science* **45,** 350–359 (1873).
7. McKeehan, L. Magnetostriction. *Journal of the Franklin Institute* **202,** 737–773 (1926).
8. Arisawa, H. *et al.* Observation of spin-current striction in a magnet. *Nature Communications* **13,** 2440 (2022).
9. Zahner, F. *et al.* Kicking Co and Rh atoms on a row-wise antiferromagnet. *arXiv preprint arXiv:2405.20472* (2024).

10. Haldar, S., Meyer, S., Kubetzka, A. & Heinze, S. Distorted 3 Q state driven by topological-chiral magnetic interactions. *Physical Review B* **104,** L180404 (2021).
11. Kooy, C. Experimental and theoretical study of the domain configuration in thin layers of BaFe_< 12> O_< 19. *Philips Res. Repts* **15** (1960).
12. Baker, K. A review of magnetic bubble memories and their applications. *Radio and Electronic Engineer* **51,** 105–115 (1981).
13. O'Dell, T. Magnetic bubble domain devices. *Reports on Progress in Physics* **49,** 589 (1986).
14. Malozemoff, A. P. & Slonczewski, J. C. *Magnetic domain walls in bubble materials: advances in materials and device research* (Academic press, 2013).
15. Kang, W. *et al. A comparative study on racetrack memories: Domain wall vs. skyrmion* in *2018 IEEE 7th Non-Volatile Memory Systems and Applications Symposium (NVMSA)* (2018), 7–12.
16. Fert, A., Reyren, N. & Cros, V. Magnetic skyrmions: advances in physics and potential applications. *Nature Reviews Materials* **2,** 1–15 (2017).
17. Krizek, F. *et al.* Atomically sharp domain walls in an antiferromagnet. *Science advances* **8,** eabn3535 (2022).
18. Savchenko, A. S., Kuchkin, V. M., Rybakov, F. N. & Kiselev, N. S. Magnetic bubbles with alternating chirality in domain walls. *Frontiers in Physics* **11,** 1223609 (2023).
19. He, Y. *et al.* Nanoscale magnetic bubbles in Nd 2 Fe 14 B at room temperature. *Physical Review B* **105,** 064426 (2022).
20. Cheng, M., Lou, J. & Lim, T. Collision and reconnection of viscous elliptic vortex rings. *Physics of Fluids* **31** (2019).

21. Barreteau, C., Raouafi, F., Desjonquères, M.-C. & Spanjaard, D. Modelling of transition and noble metal vicinal surfaces: energetics, vibrations and stability. *Journal of Physics: Condensed Matter* **15,** S3171 (2003).
22. Kumar, D. *et al.* Domain wall memory: Physics, materials, and devices. *Physics Reports* **958,** 1–35 (2022).
23. Schäfer, R. *Magnetic domains* (Springer, 2020).
24. Fassbender, J. & McCord, J. *Magnetic patterning by means of ion irradiation and implantation* 2008.
25. Litvinov, D. *et al.* Ion implantation of magnetic thin films and nanostructures. *Journal of magnetism and magnetic materials* **283,** 128–132 (2004).
26. De Jong, M. C. *et al.* Local control of magnetic interface effects in chiral Ir∣ Co∣ Pt multilayers using Ga+ ion irradiation. *Physical Review B* **105,** 064429 (2022).
27. Zhao, Y. *et al.* Local manipulation of skyrmion nucleation in microscale areas of a thin film with nitrogen-ion implantation. *ACS Applied Materials & Interfaces* **15,** 15004–15013 (2023).
28. Mendisch, S. *et al.* Controlling domain-wall nucleation in Ta/Co-Fe-B/Mg O nanomagnets via local Ga+ ion irradiation. *Physical Review Applied* **16,** 014039 (2021).
29. Lee, J. *et al.* Topological Complex Charge Conservation in Nontrivial Z2× Z2 Domain Walls. *Advanced Materials* **36,** 2313803 (2024).
30. Kurnosikov, O., Kulikov, D., Kharlamov, V., Swagten, H. & Trushin, Y. V. Temperature-induced evolution of subsurface nanocavities in argon-implanted copper. *Physical Review B—Condensed Matter and Materials Physics* **84,** 054109 (2011).
31. Gsell, M., Jakob, P. & Menzel, D. Effect of substrate strain on adsorption. *Science* **280,** 717–720 (1998).

32. Avelino, P., Martins, C., Menezes, J., Menezes, R. & Oliveira, J. Dynamics of domain wall networks with junctions. *Physical Review D—Particles, Fields, Gravitation, and Cosmology* **78,** 103508 (2008).
33. Jakob, P., Gsell, M. & Menzel, D. Interactions of adsorbates with locally strained substrate lattices. *The Journal of Chemical Physics* **114,** 10075–10085 (2001).
34. Takagi, H. *et al.* Spontaneous topological Hall effect induced by non-coplanar antiferromagnetic order in intercalated van der Waals materials. *Nature Physics* **19,** 961–968 (2023).
35. Zang, J., Cros, V. & Hoffmann, A. *Topology in magnetism* (Springer, 2018).
36. Nagase, T. *et al.* Observation of domain wall bimerons in chiral magnets. *Nature Communications* **12,** 3490 (2021).
37. Seidel, J. Scanning Probe Microscopy Investigation of Topological Defects. *Symmetry* **14,** 1098 (2022).
38. Wang, Y., Huang, Y. & Huang, W. Crack junction detection in pavement image using correlation structure analysis and iterative tensor voting. *IEEE Access* **7,** 138094–138109 (2019).
39. Russell, J. S. Topological Defects. *A New Generation of Cosmic Superstring Simulations,* 15 (2023).
40. Mukhopadhyay, M., Pujolas, O. & Zahariade, G. Cosmological scaling of precursor domain walls. *Physical Review D* **110,** 063548 (2024).
41. Blanco-Pillado, J. J., Jiménez-Aguilar, D., Queiruga, J. M. & Urrestilla, J. The dynamics of domain wall strings. *Journal of Cosmology and Astroparticle Physics* **2023,** 011 (2023).
42. Avelino, P. P., Martins, C., Menezes, J., Menezes, R. & Oliveira, J. Defect junctions and domain wall dynamics. *Physical Review D—Particles, Fields, Gravitation, and Cosmology* **73,** 123520 (2006).

5 Triple layer of Mn on Ir(111)

Abstract

Moving on from the bilayer system, we now will focus on the triple layer of Mn/Ir(111). The TL is shown to host the topologically non-trivial 3Q antiferromagnetic ground state. The TL system has been studied with and without annealing. A well defined stress relief pattern has been observed in this system which then influences the occurrence and behaviour of magnetic domain walls. Domain walls in this system are proposed to have topological character. The triple-layer system also shows the ability to host a large domain wall network upon Ar ion implantation.

5.1 Introduction

In the STM community, monolayer and bilayer systems have been investigated extensively, while thicker layers have received comparatively less attention, particularly with respect to their magnetic properties. A key reason for this gap is the increasing complexity involved in modeling such systems magnetically using first-principles calculations. A well-studied example is the Mn/W(001) system, which has been explored with regards to magnetism up to the trilayer limit. In this system, the monolayer, bilayer, and trilayer were found to host a spin spiral [1], a $c(2 \times 2)$ antiferromagnetic state [2], and a conical spin spiral [3], respectively.

Experimentally, probing the magnetic coupling between layers remains challenging by spin-polarized STM, especially regarding how the buried layers interact with the topmost magnetic layer. Density functional theory (DFT) calculations of the bilayer Mn/W(001) system revealed that the Mn monolayer interfaced with the W substrate becomes a magnetically dead layer, with magnetic moments present only in the upper Mn layer(s) [3].

Another notable study involving three atomic layers was carried out by Finco et al. [4], who investigated an Fe trilayer on Ir(111) and reported a strain dependent period of spin spirals. Notably, this system was also used to demonstrate the electric field induced switching of skyrmions using STM [5].

Despite significant advances, spin-polarized STM studies remain scarce for systems comprising more than two atomic layers of the same magnetic material on a substrate, and are even rarer for trilayer and thicker films. In this context, Mn/Ir(111) stands out due to its unique combination of structural and magnetic properties, which are unparalleled among other magnetic systems. The only meaningful parallel can be drawn with multilayer graphene—albeit in a fundamentally different physical regime—where systematic investigations up to five layers have revealed a wealth of novel phenomena [6–9]. Similar to graphene, where each additional layer introduces qualitatively new physics, the progression from double to triple and quadruple Mn layers reveals emergent magnetic behavior not present in thinner films.

The exotic antiferromagnetic (AFM) states discussed so far in this thesis are believed to originate from significant higher-order interactions (HOIs). Spin textures such as skyrmions [10], spin spirals, and multi-Q states like the 2Q [11] and 3Q [12] configurations have been previously studied using SP-STM, with theoretical work suggesting the presence of HOIs. However, these studies have largely been confined to monolayer and bilayer systems, leaving their manifestation in thicker layers largely unexplored.

In this chapter, alongside the exploration of exotic magnetic states, we will also investigate the reconstruction patterns exhibited by the triple-layer (TL) system, as these patterns significantly influence the magnetic domain wall behavior.

In samples grown near room temperature, a well-defined reconstruction pattern is observed over the entire TL surface. This suggests that the TL is no longer pseudomorphic with respect to the underlying layers and would be subject to considerable strain if it attempted to remain so. To alleviate this strain, the TL undergoes structural reconstruction. Similar isotropic stress-relief reconstructions have been reported in a variety of other systems [13–15]. Of particular relevance for this work, is the bilayer Ag/Pt(111) system, which exhibits a reconstruction pattern closely resembling that of the TL. This system has been under continuous investigation since 1994 [15], with further studies as recent as 2014 [16]. Their work focused on understanding the growth mechanisms and atomic-scale structure of the reconstruction, including its potential use as a template for adatom growth [17]. Interestingly, a definitive growth model for the bilayer Ag/Pt(111) reconstruction remains elusive. As such, a detailed investigation into the growth and reconstruction behavior of the TL of Mn/Ir(111) could make a meaningful contribution to this field.

Unlike the double layer (DL) system, where localized regions such as triple and hexa-junctions hosted the 3Q state, the TL system likely stabilizes the 3Q state as its magnetic ground state. Remarkably, the TL also exhibits an extended domain wall network when Ar ion implantation is used to intentionally trap Ar bubbles. However, the domain walls and triple junctions comprising this network are magnetically and potentially topologically distinct from those in the DL system.

Very few recent studies have demonstrated material systems that host the 3Q state as the magnetic ground state [12, 18, 19]. However, to the best of my knowledge, direct imaging of a magnetic domain wall network composed of 3Q domains and domain walls has not been reported before. In addition to these features, this chapter will also discuss magnetic loops observed in the TL system in various orientations. These magnetic structures resemble those observed in the DL but are likely different in their topological character.

5.2 Growth of the triple layer system of Mn on Ir(111)

This section examines the growth of the triple layer Mn/Ir(111) system in different conditions, i.e. near room temperature and at higher temperatures assisted by in-situ post annealing.

5.2.1 Near room-temperature growth

Fig. 5.1 provides an overview of TL growth at near room temperature. Panel (a) displays a dI/dU image of a sample with a coverage of approximately 2.4 MLs. The contrast in the image, acquired at a bias voltage of -100 mV, allows for the clear distinction between the double-layer (DL), triple-layer (TL), and quadruple-layer (QL) regions. The TL and QL can be seen to have reconstruction lines. Although the contrast difference between the TL and QL can be subtle, a useful distinguishing feature is the relative thickness of the reconstruction lines: those in the TL are consistently thicker than those in the QL.

These reconstruction lines run along the $[11\bar{2}]$ high-symmetry direction, which-while not the close-packed row direction-is nonetheless one of the principal crystallographic axes in the system. Panel (b) in Fig. 5.1 shows a different sample grown under similar conditions, where dislocation lines are visible in all three rotationally equivalent $[11\bar{2}]$ directions, further confirming the symmetry of the reconstruction pattern.

Fig. 5.1(c) shows a zoomed-in view of a region from Fig. 5.1(a), where the TL is seen to grow in two distinct regions on the DL. These regions have been labeled as TL(A) and TL(B). TL(A) preferentially grows in the area bounded between the zig-zag dislocation lines and the buried step-edge separating the DL and ML. In contrast, TL(B) grows on the opposite side of the zig-zag dislocation lines, corresponding to the majority stacking

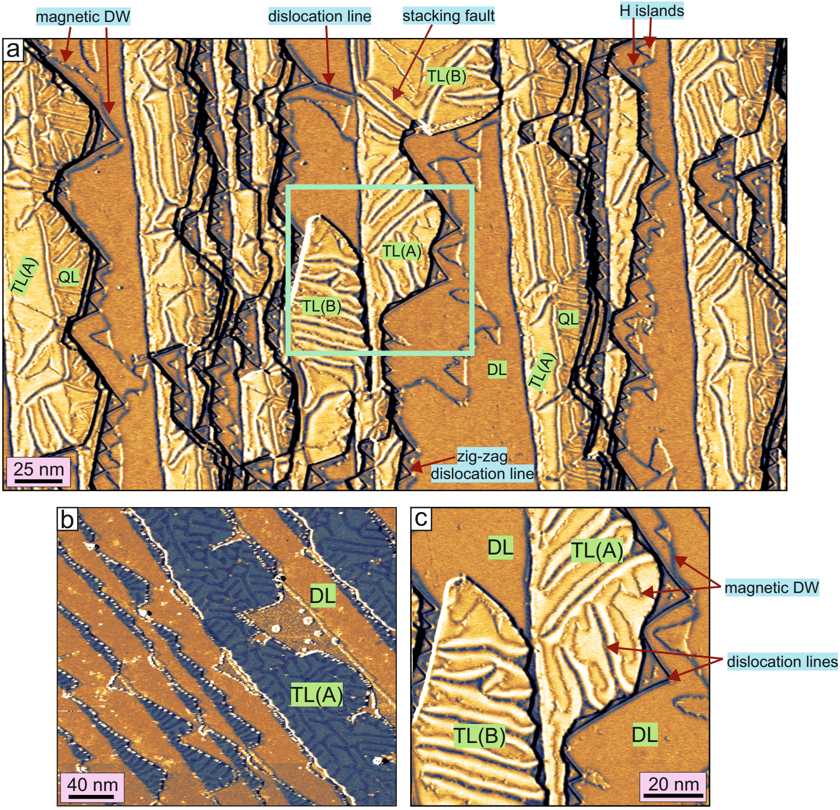

Figure 5.1: Growth overview of TL samples grown near RT. (a) An overview dI/dU STM image revealing a complex surface morphology with regions of double layer (DL), triple layer (TL) and quadruple layers (QL). TL regions exist in two distinct stacking variants (TL(A) and TL(B)). **(b)** A dI/dU image of a different sample shows the reconstruction lines of the TL occurring in the three rotational equivalent directions. **(c)** A magnified dI/dU image showing the interplay between magnetic domain walls and dislocation lines in the two different stackings of the TL. The dislocation lines appear to influence the propagation and structure of the magnetic domain walls. (Measurement parameters: a: $U = -100\,\text{mV}$, $I = 1\,\text{nA}$, $T = 4\,\text{K}$; b: $U = 650\,\text{mV}$, $I = 1\,\text{nA}$, $T = 300\,\text{K}$; c: $U = -100\,\text{mV}$, $I = 1\,\text{nA}$, $T = 4\,\text{K}$).

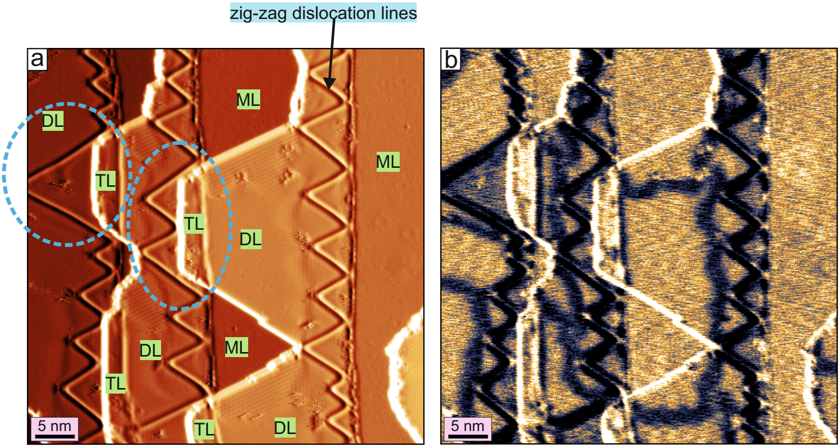

Figure 5.2: Visualizing the TL(A) growth on the DL. (a) Constant-current topography image showing a sample with ML, DL and little TL(A) regions. The TL(A) regions can be seen to grown in the stacking enclosed by the zig-zag dislocation lines in the DL, which appear extended in those regions. **(b)** dI/dU image of (a) showing a slight electronic contrast difference between the TL(A) and the DL regions. The domain wall contrast is also enhanced in this image compared to the topography in (a). (Measurement parameters: $U = -100\,\mathrm{mV}$, $I = 1\,\mathrm{nA}$; $T = 4\,\mathrm{K}$).

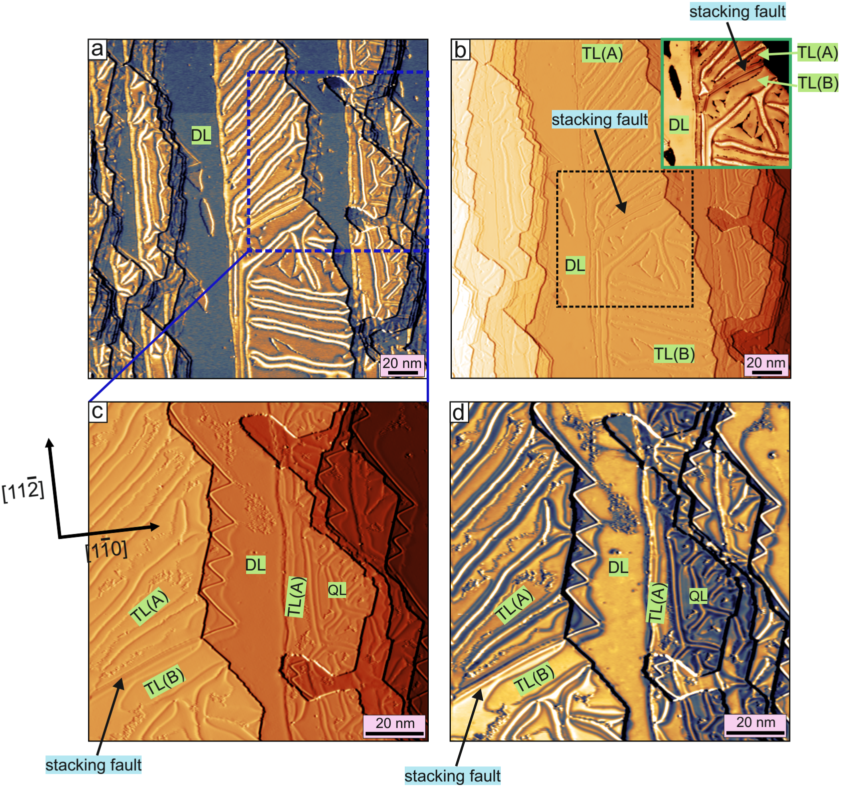

Figure 5.3: Examining the TL(A) and TL(B) stackings. (a) Regions of the TL(A) and TL(B) are seen in the STM image separated by stacking fault lines. These stacking fault lines are marked in **(b, c, d)**. In **(d)**, the dI/dU image shows a contrast between the TL(A) and TL(B) stackings. (Measurement parameters: a,b: $U = 50\,\text{mV}$, $I = 1\,\text{nA}$; c,d: $U = -50\,\text{mV}$, $I = 1\,\text{nA}$; all: $T = 4\,\text{K}$).

region of the DL. Among near-room-temperature-grown samples, TL(A) is observed far more frequently than TL(B).

It can be seen in Fig. 5.2(a), that in all the regions where the TL(A) grows, the zig-zag lines are larger in size and have their base shifted to the surrounding zig-zag lines where there is no TL. This helps to visualize that the TL(A) stacking grows on the stacking hosted by the region contained by the zig-zag lines.

To highlight the differences between these two stacking configurations, Fig. 5.3 is presented. Fig. 5.3(b) shows a partially differentiated image from a different sample area than that shown in Fig. 5.1(a). The inset in Fig. 5.3(b) highlights a cropped region in the topography channel, clearly illustrating the coexistence of TL(A) and TL(B) across a stacking fault line. A similar stacking fault line is also marked in Fig. 5.1(a). Figures 5.3(c,d) present a selected region where both stacking types are simultaneously observed. In the dI/dU image shown in Fig. 5.3(d), a notable electronic contrast difference is evident between TL(B) and TL(A), arising from their distinct stacking configurations. A visible difference between these two stackings is given by the directions of the reconstruction line pattern. The majority of the reconstruction lines in TL(A) are at an angle of 120 degrees to the majority of the reconstruction lines in TL(B).

Developing a growth model for the reconstruction lines on the TL is challenging, primarily due to the potential presence of a lateral structural shift, similar to that observed in the DL system. In the absence of theoretical calculations for the TL, it remains unclear whether such a shift exists and, if so, whether it is intrinsic to the TL or influenced by the underlying DL. The possibility of a structural shift in the TL is further explored later in this chapter through atomic-resolution imaging and the identification of asymmetric triple domain wall junctions, analogous to those observed in the DL.

5.2.2 High temperature growth

As seen in the previous subsection, the TL Mn/Ir(111) system grown at near room temperature offers a periodic reconstructed surface with very small pseudomorphic areas. In order to get rid of the reconstruction and to better investigate the magnetism in large pseudomorphic areas, substrate annealing during the deposition of Mn adatoms was tried, similar to the DL system. During Mn deposition, the substrate is annealed in situ by resistive heating, maintained at a fixed temperature between 250°C and 350°C.

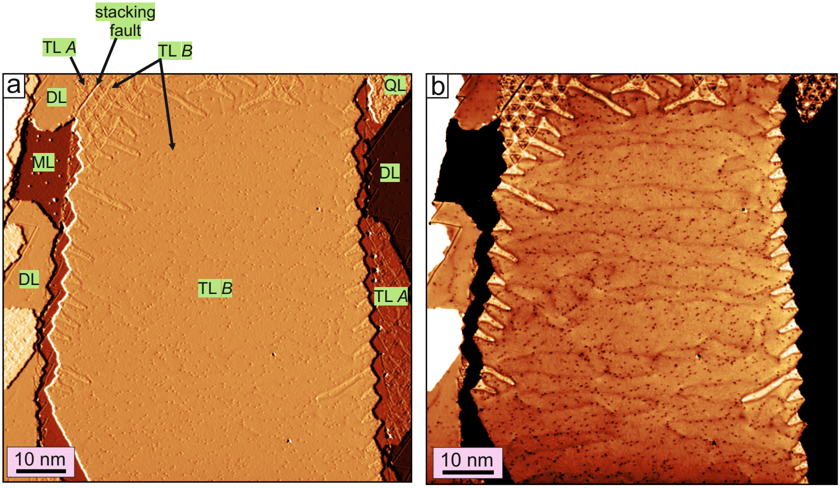

Figure 5.4: Overview of a large TL terrace in an annealed sample. **(a)** A partially differentiated STM image of a surface, enhancing the visibility of step edges and subtle structural variations across different regions. The two stacking variants (TL(A) and TL(B)) are observed separated by a stacking fault. However, the large TL terrace is of the stacking B type. **(b)** A topographical STM image of (a) helping the reader to see the height differences amongst the layers and the reconstruction lines. (Measurement parameters: a,b: $U = +100\,\mathrm{mV}$, $I = 1\,\mathrm{nA}$, $T = 4\,\mathrm{K}$).

Figs. 5.4 (a,b) show a large TL terrace with majority stacking of TL(B) in the partially differentiated topography and topography channels, respectively. The terrace is largely pseudomorphic and has the stripy reconstruction lines mostly at the edges of the terrace. A few reconstruction lines can be seen at the top of the terrace. A stacking fault line has been marked in Fig. 5.4 (a) where a transition from TL(A) to TL(B) can be seen. Interestingly, TL(A) shows a different reconstruction than the stripy one. This shows that the TL(A) stacked regions are probably more strained than TL(B). This looks similar to the reconstruction on the QL which will be discussed in detail in Chap. 6.

5.3 Magnetism of the TL of Mn on Ir(111)

5.3.1 Near room-temperature grown samples

Fig. 5.5 (a) presents an overview image in which regions of the DL, TL, and a small portion of the QL can be observed. In this image, both the DL and the majority of the TL(A) are pseudomorphic. A zoomed-in view of a pseudomorphic TL region is shown in Fig. 5.5 (c), where no visible domain walls are present, indicating that the area constitutes a single magnetic domain.

Fig. 5.5 (b) shows a TL region in the presence of a structural defect-specifically, a reconstruction line commonly found in the TL. Bright *U*-shaped features, interpreted as magnetic domain walls, appear to line the reconstruction. The inset shows the presence of a square like magnetic pattern near the magnetic domain wall distinct from the hexagonal pattern in the domain. This likely arises from the magnetic pattern from the domain wall. This will be discussed in more detail in the following sections.

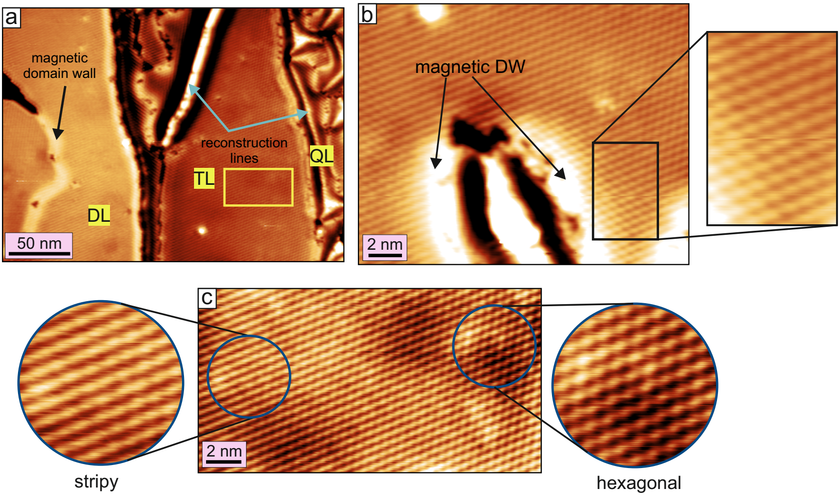

Figure 5.5: (a) A large-scale SP-STM image showing regions of the DL, TL(A) and QL coverage. A magnetic domain wall on the DL and dislocation lines on the TL and QL are labelled. **(b)** A higher magnification STM image focusing on a magnetic domain wall (magnetic DW) around a reconstruction line on the TL. The inset on the right shows a zoomed-in view revealing a square type magnetic pattern distinct from the surrounding extended domain. **(c)** A zoomed-in constant-current SP-STM image of an area from (a), marked by a yellow rectangle, shows a gradual change in magnetic pattern going from a stripy to a hexagonal pattern in a single domain. (Measurement parameters: all: $U = +5\,\mathrm{mV}$, $I = 2\,\mathrm{nA}$, $T = 4\,\mathrm{K}$).

In panel (c) of Fig. 5.5, a zoomed-in SP-STM image of the region marked by a yellow rectangle in panel (a) is shown. The magnified insets reveal a gradual transition in the magnetic contrast from a stripy to a hexagonal-like pattern within a single magnetic domain. This coexistence suggests that the magnetic structure in the TL is not rigidly locked to the atomic lattice and may exhibit local distortions even within an otherwise uniform domain. It is worth noting that the boundaries of this TL terrace could also influence the magnetic state: on the left, a buried step edge associated with the DL is present, while on the right, another buried step edge marks the transition toward the QL. Due to the lack of additional SP-STM measurements in such transitional regions, the precise influence of these step edges on the magnetic texture remains an open question.

Such behavior effectively rules out the row-wise antiferromagnetic (RW-AFM) state as the ground state in the TL, since the RW-AFM configuration should consistently exhibit a stripy appearance regardless of the tip magnetization direction. Regarding the possibility of the observed magnetic texture corresponding to the 2Q state, previous theoretical studies have shown that the 2Q configuration is not energetically favorable when only fourth-order higher-order interactions (HOIs) are considered [20]. However, inclusion of sixth-order terms in the spin Hamiltonian can stabilize the 2Q state as the ground state. Despite this, SP-STM simulations with varying tip magnetization directions reveal that the 2Q state maintains a visually similar appearance, with only contrast levels changing [20].

In contrast, distorted 3Q configurations, including the $3Q^2$ and $3Q^3$ states, exhibit markedly different magnetic contrasts depending on the orientation of the tip magnetization. Therefore, distinguishing between these 3Q variants in the TL requires a more comprehensive experimental approach. In particular, the application of a vector magnetic field would be necessary to resolve the full spin structure and unambiguously identify the underlying magnetic ground state.

Proceeding further, Fig. 5.6 (a) displays a high-resolution SP-STM topography image of the TL(A) having atomic and magnetic contrast. A three-armed, star-shaped structure is visible, attributed to hydrogen impurities forming structural features analogous to the island formations observed in the DL (see Sec. 4.4.3). The corresponding magnetic domain walls have been labelled in Fig. 5.6(a).

To resolve the atomic and magnetic features from the image, a two-dimensional fast Fourier transform (2D-FFT) was performed which is shown in Fig. 5.6(b). Panel(c) is the cropped out area from panel (a) upon which the 2D-FFT analysis is performed. To facilitate the interpretation, the atomic and magnetic components have been separately reconstructed in Figs. 5.6(d) and (e), respectively. The magnetic signal in Fig. 5.6(e) reveals the presence of rotational domains, thereby ruling out the $3Q^1$ state as a candidate ground state, as its inherent C_3 symmetry would not permit the existence of such rotational domains.

We now examine how the reconstruction lines influence the behavior of magnetic domain walls in the TL(A). Figs. 5.7(a) and (b) show a region spanning the TL(A) and QL across a buried step edge, imaged in the topographic and current channels, respectively. The reconstruction lines in this region exhibit a characteristic three-armed, star-like structure. Each arm of the dislocation line appears to preferentially stabilize a specific rotational domain. These three arms have been marked for one such star-shaped dislocation in Fig. 5.7(a) using pink dotted lines. In Fig. 5.7(b), the magnified inset shows the junction area of the star shaped reconstruction line. The three rotational domains are marked by numbers 1-3, corresponding to the arms of the reconstruction line marked in panel (a). The magnified inset shows stripe like patterns in rotational domains marked as 2 and 3 - which correspond to the magnetic state. There is no magnetic contrast in domain 1 likely due to the tip's magnetization being perpendicular to the domain's magnetization.

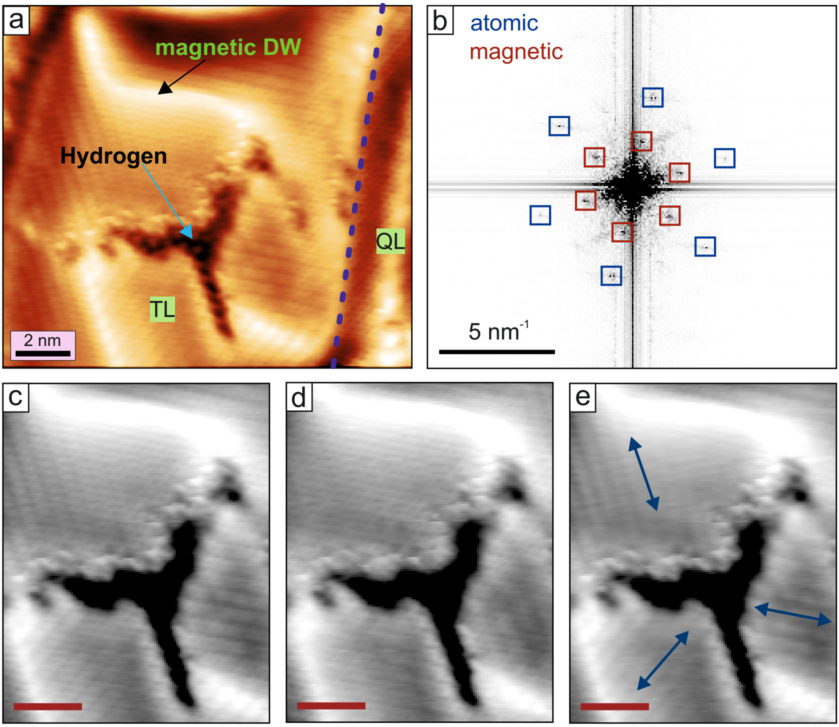

Figure 5.6: Atomic and Magnetic Structure near a Hydrogen-Induced Defect. **(a)** A constant-current topography STM image showing a hydrogen-induced defect (labeled "Hydrogen") on the TL. A buried step-edge to the QL is indicated by the dashed blue line, suggesting its interaction with the defect. **(b)** A 2D FFT of the area in (c) is shown in (b). Red squares correspond to the magnetic periodicity, while blue squares indicate the atomic lattice. The different frequencies reveal the coexistence of atomic and magnetic ordering. **(d,e)** The extracted pure atomic and magnetic resolution images are shown respectively. Rotational domains of the magnetic state can be seen in (e). (Measurement parameters: a: $U = -100\,\text{mV}$, $I = 6\,\text{nA}$, $T = 4\,\text{K}$).

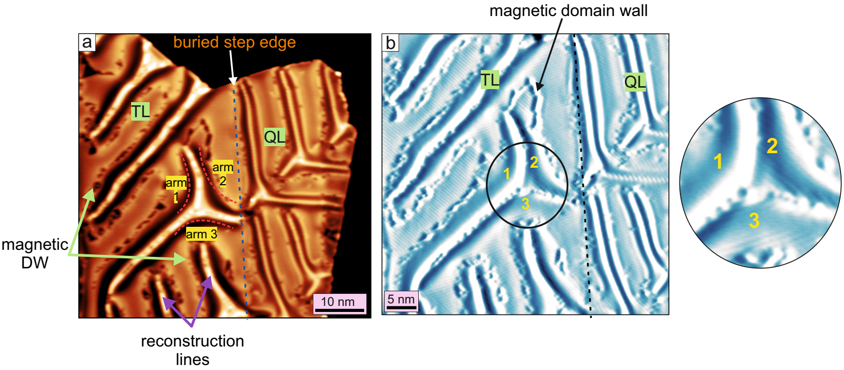

Figure 5.7: Influence of structural defects on the magnetic domain walls in the TL. (a) A constant-current topographical STM image showing regions of triple layer (TL) and quadruple (QL) coverage across a buried step edge indicated by a dashed line. The three arms of the star shaped reconstruction lines have been labelled in yellow as arm1, arm2 and arm3. **(b)** A current channel map, where the current sensitivity is enhanced to reveal the magnetic contrast. The magnified inset shows the junction of the star shaped reconstruction line, where a stripe like magnetic pattern can be seen for rotational domains marked by 2 and 3. (Measurement parameters: a,b: $U = +300\,\text{mV}$, $I = 1\,\text{nA}$, $T = 4\,\text{K}$).

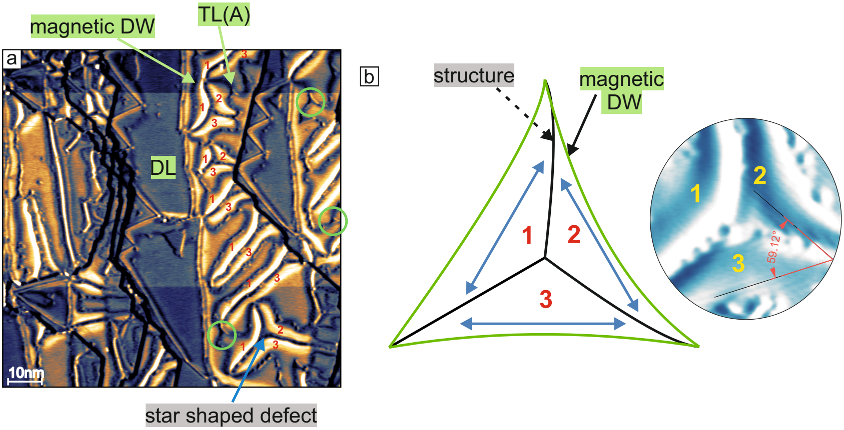

Figure 5.8: Mechanism of magnetic domain wall junction formation due to structural defects in the TL. (a) A dI/dU map revealing variations in the local electronic properties across a surface with regions of double layer (DL) and triple layer with stacking (TL(A)). The image shows many star shaped reconstruction lines on the TL areas with domain walls running around them (dark blue lines). **(b)** A schematic illustration depicting the proposed mechanism for magnetic domain wall formation at the structural defect shown in (a). The different arms of the structural defect (arm 1, arm 2, arm 3) require different rotational domains (labelled 1-3) of the magnetic state. The green lines represent magnetic domain walls that nucleate and propagate along these arms to allow for the different rotational domains. The double headed green arrows indicate the orientation of the rotational domains preferred by each arm. The rotational domains corresponding from the sketch have been marked in panel (a) for the TL terrace. (Measurement parameters: $U = 50\,\text{mV}$, $I = 1\,\text{nA}$, $T = 4\,\text{K}$).

From the images, it may appear that a magnetic domain wall lies along the center of each dislocation line. However, an alternative interpretation is also plausible: the dislocation lines may act solely as domain generators-defining the orientation of neighboring magnetic domains without hosting a magnetic domain wall themselves. Crucially, the *dI/dU* images do not provide conclusive evidence of electronic contrast that would distinguish a magnetic domain wall from a purely structural feature. Hence, this remains an open question.

To further interpret the role of reconstruction lines in dictating the magnetic domain wall trajectory, a schematic is presented in Fig. 5.8. The sketch in panel (b) features a single star-shaped reconstruction line. Magnetic domain walls, drawn in green, are seen to follow the curved arms of the reconstruction line, implying that each arm favors a specific orientational domain of the magnetic state. As illustrated in the *dI/dU* image in Fig. 5.8(a), the reconstruction lines occur frequently. The double headed green arrows shown in Fig. 5.8(b), indicate the orientation of the rotational domains preferred by each arm. The labelled rotational domains 1-3, have also been marked in the TL terrace in panel (a) in red. This repeating pattern of the same rotational domain being preferred by the same arm of the reconstruction line shows that there is a preference of the orientation of the rotational domain by the reconstruction lines. The magnified inset shows the resultant domain wall formation in the three arms of the star shaped reconstruction line. 60° domain walls as also measured for the stripes forming the domain wall across domains 2 and 3, are shown in the magnified inset.

Due to the frequent occurrence of such closely spaced reconstruction lines and the different orientational domain preferences of each arm, magnetic domain walls form around the reconstruction lines and occasionally form triple domain wall junctions - as marked in green circles. Supporting additional data is presented in the Appendix.

5.3.2 High temperature grown samples

We now move to samples grown at elevated temperatures with in-situ substrate annealing. In these samples, large pseudomorphic regions were successfully obtained, with reconstruction lines appearing only occasionally-either at terrace edges or, more rarely, within the central regions (see Fig. 5.9). The resulting surface mostly free of the reconstruction features provided an excellent opportunity to investigate the magnetic state of the triple layer in greater detail. In particular, this allowed for the observation of well-defined magnetic domain wall networks and the emergence of closed-loop magnetic structures.

Fig. 5.9(b) shows a dI/dU image in which the TL(B) region exhibits numerous isolated and interconnected loops as magnetic features. A particularly noteworthy feature is the alignment of the long axes of these elliptical loops. This directional preference is likely governed by the presence of dominant 120° domain walls, analogous to those observed in the DL system (see Fig. 4.20 in Chapter 4).

It is also evident that the TL surface in the annealed samples appears relatively contaminated. This contamination is most likely a result of resistive heating of the substrate holder, which was maintained at elevated temperatures (approximately 250–400 °C) during Mn deposition. The increased level of surface contamination in the TL may play a critical role in the formation of the isolated and interconnected loop structures observed. This aspect will be explored in the following section.

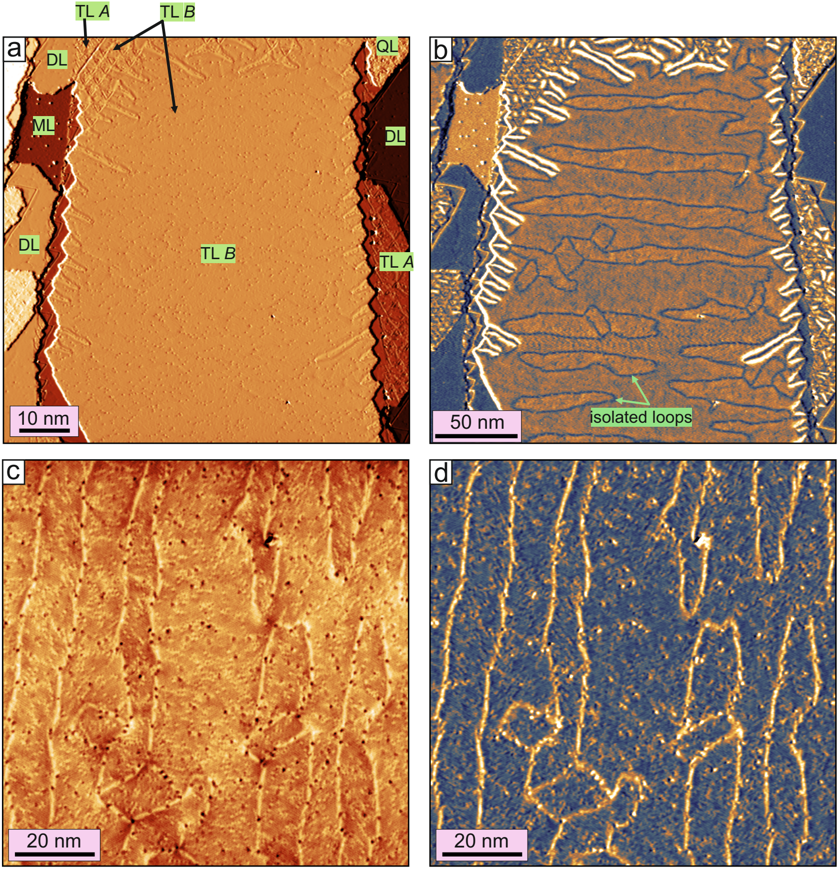

Figure 5.9: Existence of isolated and interconnected loops in the TL system grown at higher temperatures. (a) A partially differentiated topographical STM image showing a large triple layer terrace with the primary TL(B)) stacking. **(b)** A dI/dU map of the same surface area as in (a), showing the magnetic domain walls in isolated and interconnected loops. Also, the different layers with different electronic contrast can be seen. **(c)** A constant-current topographical overview SP-STM image showing a network of interconnected magnetic domain walls. **(d)** A dI/dU map of the same area as in (c), enhancing the contrast of the magnetic domain walls and revealing their intricate arrangement and branching patterns. (Measurement parameters: a,b: $U = +100\,\mathrm{mV}$, $I = 1\,\mathrm{nA}$; c,d: $U = +10\,\mathrm{mV}$, $I = 1\,\mathrm{nA}$; all: $T = 8\,\mathrm{K}$).

To investigate the magnetic domains in the TL, we refer to Fig. 5.10 grown at high temperature where a largely pseudomorphic TL is observed. Panel (b) presents a zoomed-in SP-STM topography image of the region highlighted by the yellow rectangle in panel (a). Three rotational domains are visible, along with a magnetic triple domain wall junction located at the center of the image. These stripe-like features have been previously shown in Fig. 5.5 and Fig. 5.6, where they were ruled out as being associated with the 1Q or 2Q states. Therefore, these stripes are attributed to the 3Q state, more specifically the $3Q^2$ configuration. However, since the tip magnetization is not characterized for any of the SP-STM images of the TL, the possibility of a distorted 3Q state or $3Q^3$ state cannot be conclusively excluded.

We now examine the characteristics of a magnetic domain wall in the TL. The SP-STM image shown in Fig. 5.11(a) captures a 120° magnetic domain wall. The left domain displays a dominant stripe-like magnetic contrast, while the right domain appears less clear due to the presence of surface defects. To gain deeper insight into the magnetic structure within the domain wall, a simulation of a 120° domain wall with rotational domains exhibiting the $3Q^2$ state is presented in Fig. 5.11(c). This simulation, performed for a monolayer by André Kubetzka in Monte-Crystal [21], incorporates a distortion of the $3Q^2$ state by tuning the magnetic anisotropy to favor the out-of-plane (OOP) direction. This adjustment was made to qualitatively reproduce the experimentally observed $3Q^2$ pattern. The simulation parameters are the following: J_1 (nearest neighbour exchange)= -15, J_2 (next-nearest neighbour exchange) = -5, ASE (anisotropic symmetric exchange) = -0.05, B (higher-order biquadratic exchange) = -0.6 and K (anisotropy) = -1 along the z direction. Fig. 5.11(d) shows a simulated SP-STM image with the above mentioned parameters and with a tip's magnetization being in plane, where θ (polar angle) and ϕ (within the xy-plane) are at 0°. Note that this pattern could most probably arise even for other distorted 3Q states with a canted tip

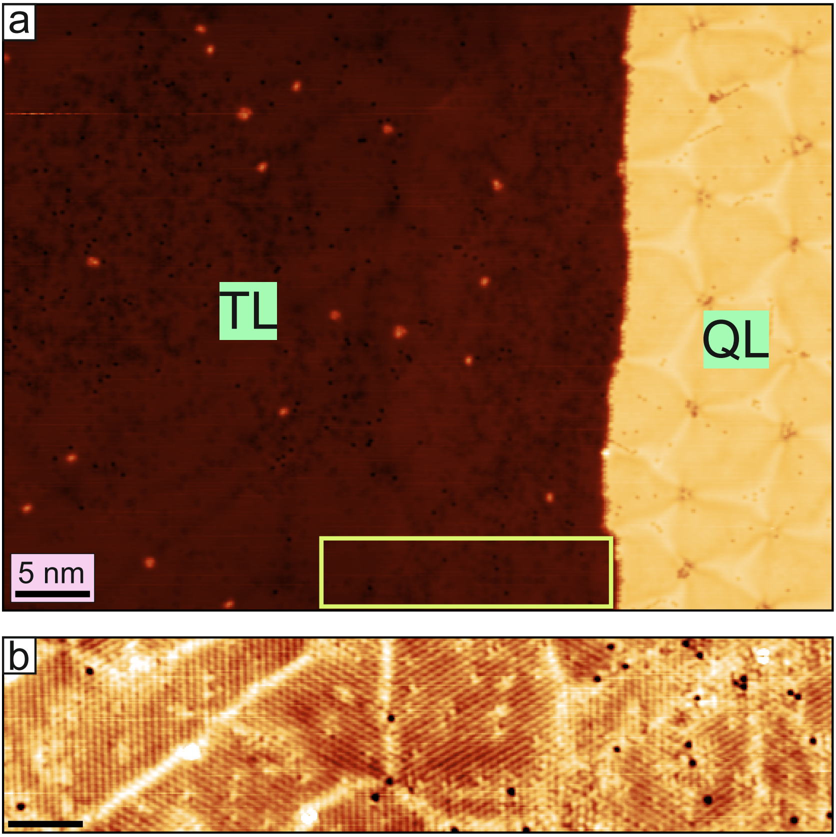

Figure 5.10: Magnetic imaging of rotational domains in the TL. (a) Constant-current STM topography image of a region containing the TL and QL terraces. The yellow rectangle indicates the image area of panel (b). **(b)** Zoom-in SP-STM topography image where the three rotational domains can be seen with domain walls (bright). A domain wall junction can be seen in the middle of the image where the three rotational domains with a stripy magnetic pattern meet. The scale bar in black corresponds to the one shown in panel (a). (Measurement parameters: (a): $U = 500\,\text{mV}$, $I = 800\,\text{pA}$; (b): $U = 10\,\text{mV}$, $I = 1\,\text{nA}$; all: $T = 4\,\text{K}$).

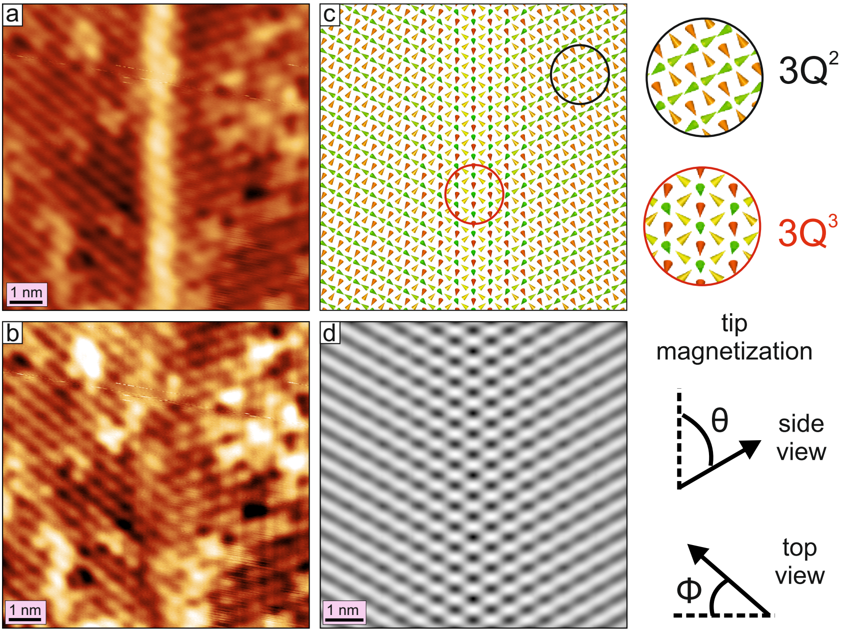

Figure 5.11: Simulation of a magnetic domain wall formed by two 3Q^2 domains. **(a)** Constant-current SP-STM topography image of a 120° magnetic domain wall in the TL with two adjacent 3Q^2 rotational domains. **(b)** To correct for line-wise height variations in the SP-STM data, the Gwyddion software's *Align Rows* feature was used in the vertical direction to see the domain wall magnetic pattern. **(c)** A spin model of a domain wall with two 3Q^2 domains shows the formation of a 3Q^3 magnetic state within the domain wall. **(d)** SP-STM simulation of (b) with a tip having θ (polar angle) and ϕ (within the xy-plane) angles of 0°corresponding to an in-plane sensitive tip. (Measurement parameters: $U = 10\,\text{mV}$, $I = 2\,\text{nA}$, $T = 8\,\text{K}$).

magnetization. Experimentally, one would need a vector magnetic field to verify the type of distorted 3Q state [20].

The simulated magnetic configuration within the domain wall in Fig. 5.11(c) reveals a hexagonal structure, characteristic of the $3Q^3$ state. This is particularly noteworthy, as a $3Q^3$ domain wall carries a non-zero topological charge, in contrast to the topologically trivial $2Q$ domain walls observed in the DL system.

To further analyze the magnetic texture of the domain wall, a correction for the line-wise height variations was performed for the image in panel (a). The alignment was performed along the vertical direction which effectively reduces scan line artifacts (in this case: domain wall) and enhances the visibility of surface features. Fig. 5.11(b) shows the resulting image, a hexagonal magnetic pattern is clearly visible within the domain wall, extending across several atomic distances into both adjacent domains.

Fig. 5.12 shows a few zoomed-in images of the magnetic domain walls and loops from the TL(B) terrace presented in Fig. 5.9(b).

In the domains, we can see at some places that there is an overlay of a hexagonal pattern on the dominant stripy pattern of the 3Q state. Especially in Figs. 5.12(b,d) the magnetic pattern is hexagonal in the loop and the domain respectively. This could be interesting with respect to topology. If the domain inside the loop has a slightly different magnetic structure, it is interesting to know how the spins wind or rotate from outside to inside the loop. This is also visible in zoomed-out images, where the dominant stripy magnetic pattern can be observed in Fig. 5.13. Figs. 5.13(a,b) show two nearby sample areas from the TL(B) stacked terrace presented in Fig. 5.9(b). An alternating pattern of the rotational domains can be seen in Fig. 5.13 with parallel domain walls. Magnified versions of selected areas are shown for Figs. 5.13(a,b) for clarity. Fig. 5.13(d) is a frequency filtered version of Fig. 5.13(c), where

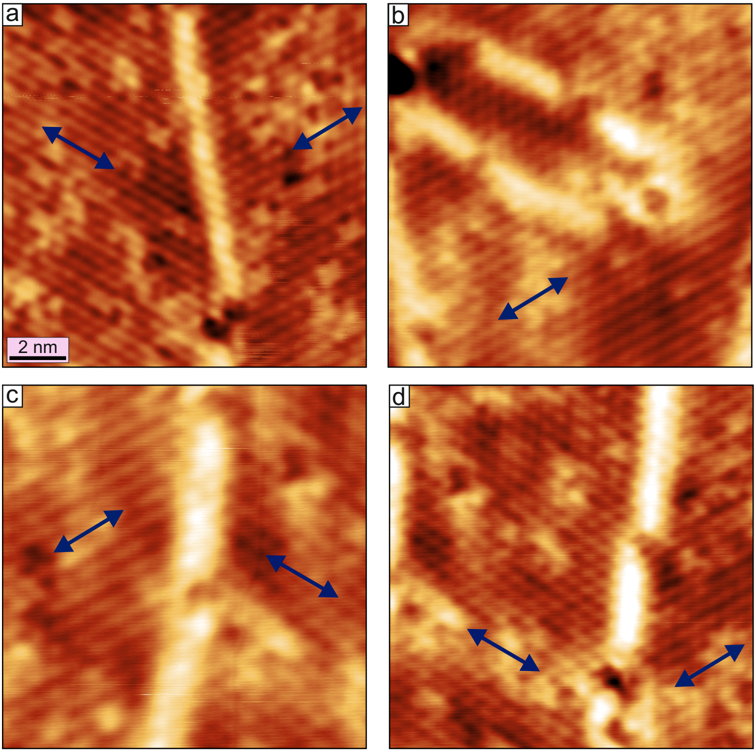

Figure 5.12: SP-STM imaging of magnetic domain walls in the TL. (a) Constant-current topographic SP-STM zoomed-in images showing the magnetic domain walls in different areas in the TL terrace from Fig. 5.9. The domains can be seen to have a majority stripy magnetic pattern along with the minority hexagonal pattern. Hence, the orientation of the rotational domains can be dictated by the stripy character, as shown by the double headed blue arrows. (Measurement parameters: all: $U = +10\,\mathrm{mV}$, $I = 2\,\mathrm{nA}$, $T = 8\,\mathrm{K}$).

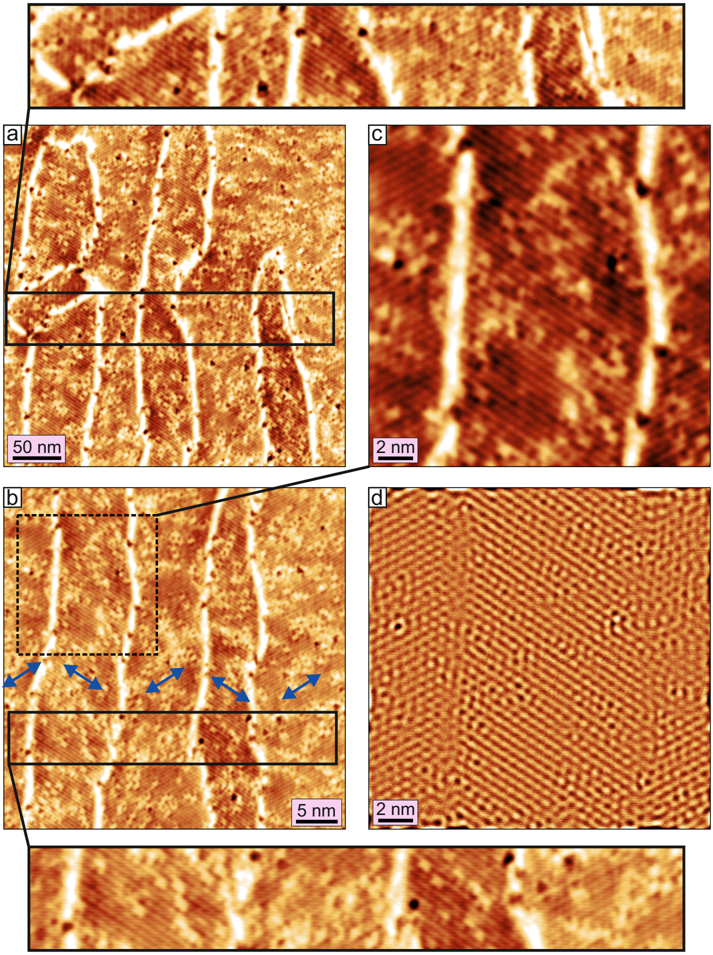

Figure 5.13: SP-STM imaging of the rotational domains in the TL. (a-c) Constant-current topographic SP-STM images of different sample areas showing the different rotational domains. Magnified insets are shown for better clarity of the magnetic contrast. **(d)** frequency filtered image of (c) to identify the magnetic pattern of the domain walls. The frequency split was carried out with a low-pass filter having a cutoff of 0.712 nm. (Measurement parameters: a: $U = +10\,\text{mV}$, $I = 4\,\text{nA}$; b,c: $U = +10\,\text{mV}$, $I = 3\,\text{nA}$; all: $T = 8\,\text{K}$).

the stripy pattern in the domains can be seen, but the magnetic structure in the domain wall is difficult to identify.

We have observed the presence of both isolated and interconnected magnetic loops in the TL system. However, a key question arises: are these two types of loops fundamentally the same? Based on current observations, it does not seem so.

Figures 5.14(a) and (c) illustrate representative examples of an interconnected loop and an isolated loop, respectively. The isolated loop corresponds to the structure marked at the bottom of Fig. 5.9(b). In contrast, the loop shown in Fig. 5.14(a) emerges as part of a larger domain wall network and exhibits corner features formed by triple junctions. At these junctions, the magnetic configuration is likely distinct from that within the domains or along the domain walls. This is consistent with previous observations in the DL, where only triple junctions within the domain wall network were found to host a localized 3*Q* state. In this case, the domains in the TL most likely have a distorted $3Q^2$ state, the domain walls have the $3Q^3$ state, and the magnetic state at the junctions is not known.

Following this reasoning, the loop in Fig. 5.14(a)-being part of a network and containing junction points-should be magnetically and potentially topologically different from the isolated loop shown in Fig. 5.14(b). This may also imply a difference in topological charge between the two cases. Verification of these hypotheses, however, requires further theoretical investigation, particularly simulations based on density functional theory (DFT) with system-specific parameters-analyses which remain to be performed.

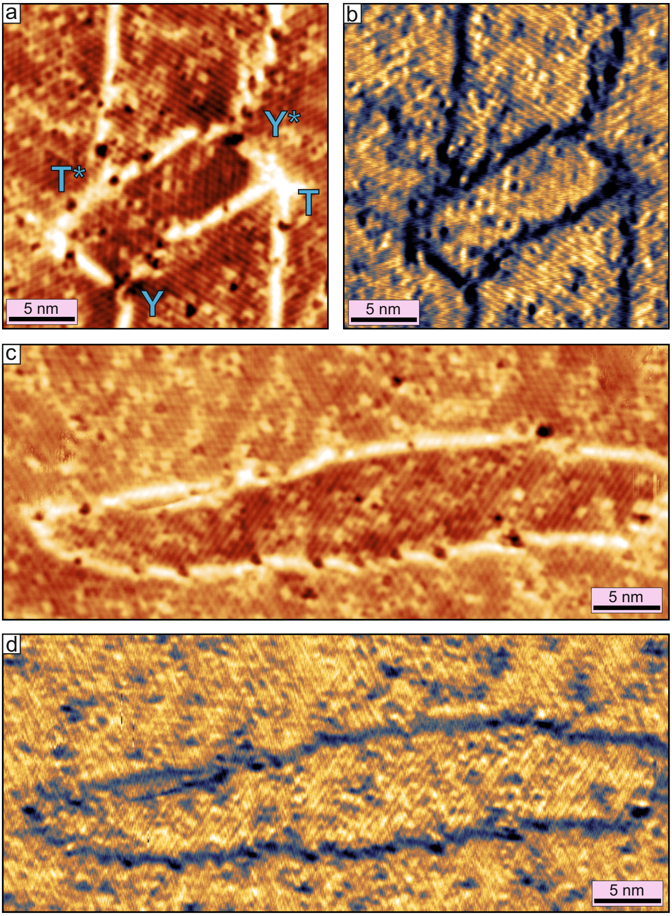

Figure 5.14: Differentiating between an interconnected and isolated magnetic loop. constant-current topography and dI/dU images showing an interconnected (**(a,b)**) and isolated loop (**(c,d)**) in the TL with magnetic contrast. The magnetic domain wall junction types have been marked in blue in (a). The magnetic state due to the junctions should in principle differentiate between the interconnected and the isolated loop in terms of the domain wall-magnetic and topological character. (Measurement parameters: all: $U = +10\,\mathrm{mV}$, $I = 4\,\mathrm{nA}$, $T = 8\,\mathrm{K}$).

5.4 Domain wall network in the TL Mn on Ir(111)

5.4.1 Without Ar bubble trapping

Now we move on to a more interesting domain wall behaviour, which we previously observed in the DL system too, but with the aid of trapping Argon bubbles in the Ir(111) crystal. In the TL system, as seen above, pseudomorphic areas exist grown by in-situ annealing. Fig. 5.15 shows an area of TL(A) free of reconstruction lines. This 60 x 60 nm image exhibits a domain wall network akin to the one seen in the DL. This DW network is visually identical to the DL except that here, no Argon has been trapped to generate this network.

An intriguing feature of the observed domain wall network in the TL is the presence of asymmetric triple junctions, which may indicate a structural shift within the TL. The asymmetry is particularly evident in the T-junctions, while it is less pronounced in the Y-junctions-mirroring the behavior observed in the DL system. A Y- and T-junction have been marked with lines spanning a triangle in the junction - thus showing the same chiral sense as in the DL.

This raises a fundamental question regarding the origin of the lateral shift in the TL. Two plausible scenarios exist: the shift may be intrinsic to the TL, or it may be a consequence of a pre-existing shift in the underlying DL.

A potential explanation can be proposed by considering the thermal history of the sample. After growth, the sample is transferred to the STM chamber, where it is cooled down to either 4.2 K or 10 K, depending on the specific setup. During this cooling process, the system passes through the Néel temperature (T_N), the precise value of which remains unknown. As the system cools through T_N, the TL, DL, and ML likely couple magnetically to stabilize a coherent magnetic ground state across

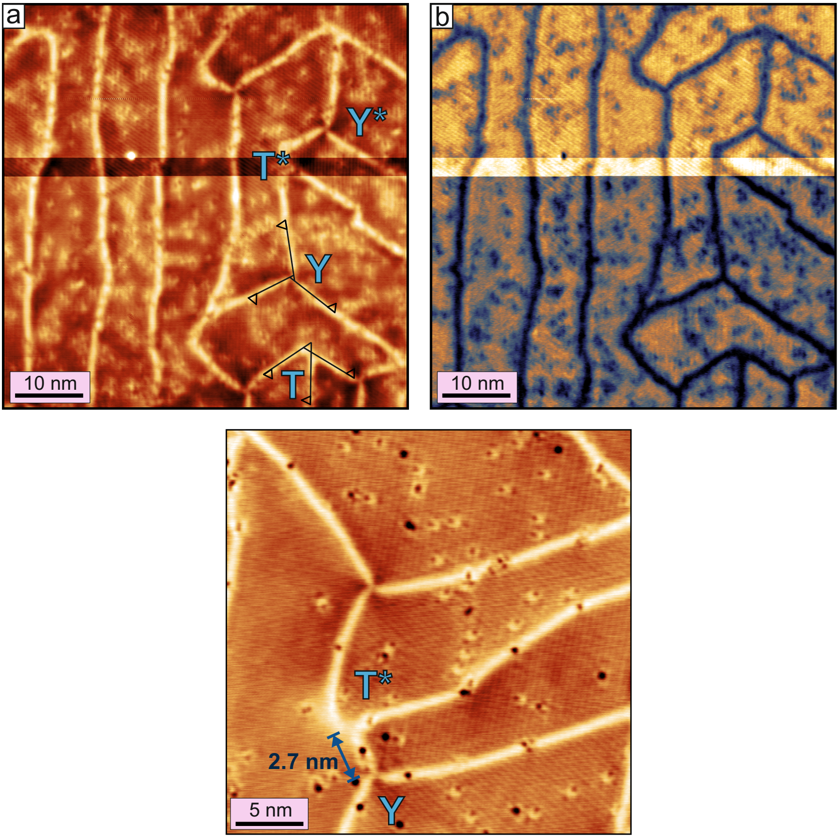

Figure 5.15: Domain wall network in the TL without Argon bubble implantation. constant-current SP-STM topography (**(a)**) and dI/dU (**(b)**) images showing a domain wall network in the TL without any Argon bubble implantation. The junctions appear to be asymmetric similar to the junctions in the DL. Also, a lot of defects on the TL surface can be seen which might play a similar role as the Argon bubbles for generating a domain wall network. (Measurement parameters: all: $U = +10\,\mathrm{mV}$, $I = 1\,\mathrm{nA}$, $T = 8\,\mathrm{K}$).

all layers. Assuming that all the layers have the same magnetic state, the structural shift observed in the TL could be native to it. However, the alternative-that the shift originates in the DL and propagates into the TL cannot be excluded. Definitive resolution of this question will require supporting evidence from DFT calculations.

The domain wall network in the TL is composed entirely of 120° domain walls and displays an alternating sequence of Y- and T-junctions, consistent with patterns seen in the DL domain wall network. A subtle, yet significant distinction, however, lies in the spatial arrangement of these junctions. In the TL, certain Y–T junction pairs are separated by very short distances-on the order of 2 nm-a feature not observed in the DL. The minimum distance permissible between Y- and T-junctions in such networks remains an open question. It may be governed by various factors, such as the magnetic configuration at the junctions, the topological orbital moment, or strain fields surrounding the junctions.

5.4.1.1 Comparing the network to the DL

Fig. 5.16 highlights a striking difference between the DL and TL systems in terms of magnetic domain wall density. The *dI/dU* images shown in panels (a) and (b) reveal that the TL(A) and TL(B) host a significantly higher density of magnetic domain walls compared to the DL. It is important to emphasize that these samples were grown without intentional trapping of Ar bubbles. Unfortunately, in these images, the measurements were not done at bias voltages that show a good contrast of the magnetic domain walls for both, the DL and TL simultaneously.

This observation prompts an important question: why does the TL tend to accommodate a higher density of domain walls than the DL? In Fig. 5.16(b), the TL exhibits a pronounced reconstruction pattern, which likely promotes the formation of domain walls. However, in

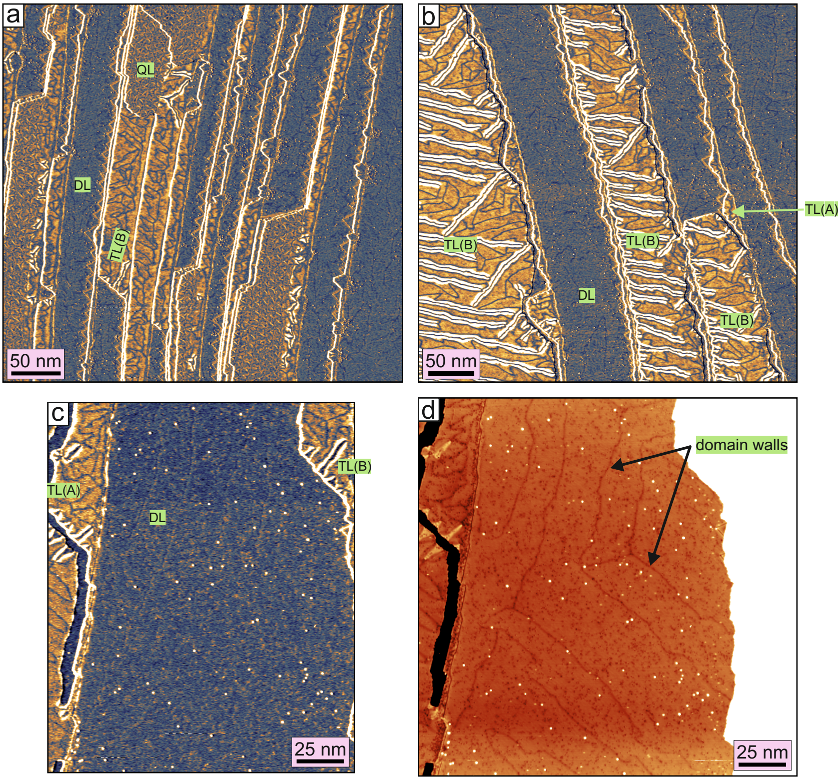

Figure 5.16: Comparing the domain wall network density in the DL and TL without Argon bubble implantation. **(a,b)** Constant-current dI/dU images showing sample areas with similar terrace widths of the DL and TL. A better visibility of the magnetic domain walls on a wide DL terrace (**(c)**) is given for the SP-STM topography image in **(d)**. (Measurement parameters: a,b: $U = +50\,\text{mV}$, $I = 1\,\text{nA}$, $T = 8\,\text{K}$; c,d: $U = +200\,\text{mV}$, $I = 1\,\text{nA}$, $T = 8\,\text{K}$).

Fig. 5.16(a), the TL is pseudomorphic-grown via in-situ annealing—and yet still shows a considerably higher domain wall density than the DL.

This leads us to revisit the role of surface contamination and defects in the TL. In both panels of Fig. 5.16, the TL surfaces appear defect-rich. Even in Fig. 5.16(a), where the DL also shows a relatively high defect density, a noticeable number of domain walls and triple junctions can be observed. This suggests that, beyond reconstruction, intrinsic or growth-induced disorder in the TL may be a key factor in facilitating dense domain wall formations. As discussed in the DL chapter, the Ar bubbles act as symmetry-breaking centers, locally modifying the magnetic environment and thereby determining the orientation of adjacent magnetic domains. It is reasonable to assume that the high density of intrinsic defects in the TL may serve a similar role, effectively acting as disorder-induced pinning centers that influence domain wall formation and propagation.

5.4.2 With Ar bubble trapping

We now turn to the sample in which Argon (Ar) bubbles were intentionally trapped within the Ir(111) crystal. As shown in Fig. 5.17, a large-scale magnetic domain wall network is observed in the TL region, reminiscent of the network structures previously reported for the DL system. The bright spots visible in these SP-STM images correspond to the enhanced signal arising from the trapped Ar bubbles.

These images, acquired with spin-polarized STM, reveal strong magnetic contrast within the rotational domains, particularly upon closer inspection. What distinguishes this domain wall network from the one shown in Fig. 5.15 is the presence of hexa-junctions which were not observed in the former case.

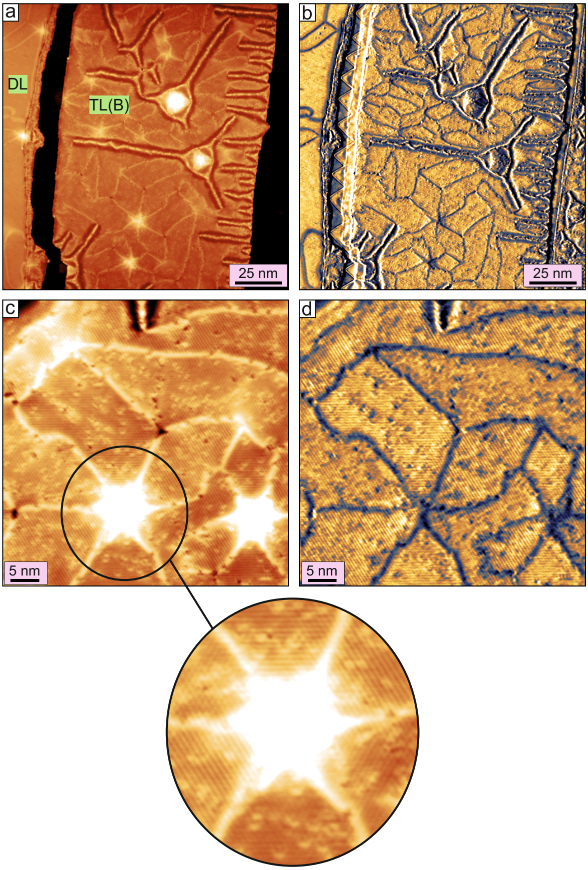

Figure 5.17: DW network in TL samples with Ar bubble implantation. (a,b) Constant-current SP-STM topography and dI/dU images showing the TL(B) stacked terrace with partly pseudomorphic areas exhibiting a domain wall network. A closer view of the domain wall network comprising triple and hexa-junctions is presented in the constant-current SP-STM topography and dI/dU images of (c,d). A magnified inset shows a better view of the magnetic contrast around the hexa-junction. (Measurement parameters: all: $U = +10\,\mathrm{mV}$, $I = 1\,\mathrm{nA}$, $T = 4\,\mathrm{K}$).

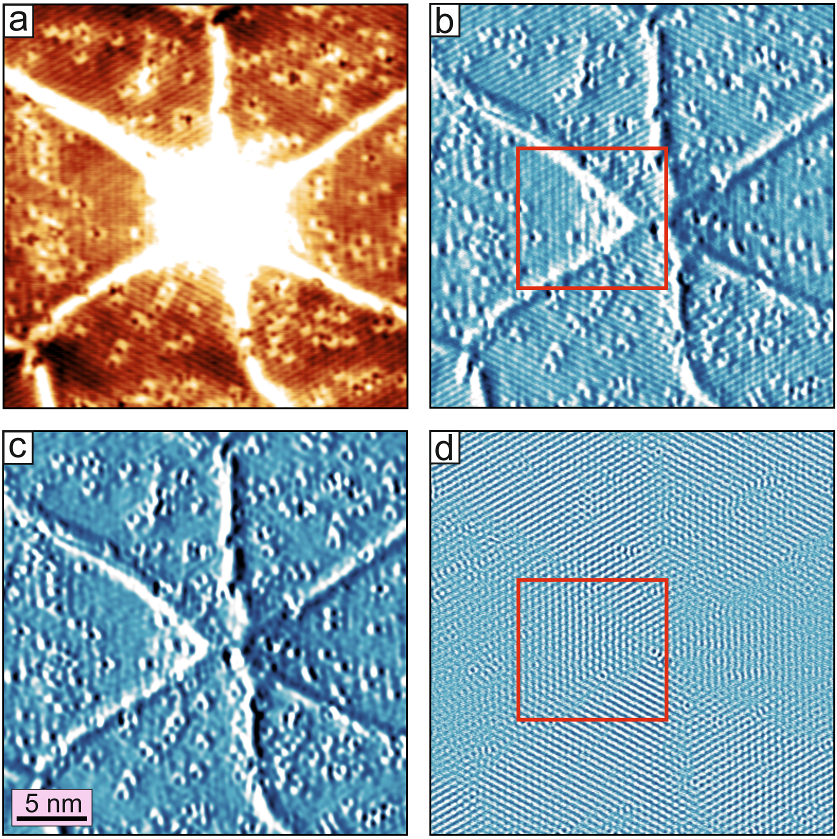

Figure 5.18: SP-STM imaging of a hexa-junction in the TL. (a) Constant-current SP-STM topography image of a hexa-junction seen in the TL. Opposite pairs of domains can be seen to have the same orientation of the $3Q^2$ state. The horizontal pairs of rotational domains show very weak magnetic contrast. To have a better look at the hexa-junction magnetic state, the current channel has been recorded in **(b)**. A frequency filtering of (b) was applied with a cutoff wavelength of 0.511 nm. The low-pass and high-pass filtered images are shown in **(c, d)**. A distinct magnetic pattern from the surrounding domains has been marked by a red square in (d). (Measurement parameters: $U = +10\,\mathrm{mV}$, $I = 1\,\mathrm{nA}$, $T = 4\,\mathrm{K}$).

We now examine the magnetic structure of a hexa-junction in the TL. Fig. 5.18 presents a SP-STM image highlighting such a junction. The current channel shown in Fig. 5.18(b) is used for visualizing the magnetic contrast, as it provides a better resolution of the magnetic features compared to the topographic channel.

To enhance the magnetic signal and separate it from structural contributions, the frequency split function in *Gwyddion* was employed. The result of this processing is shown in Fig. 5.18(c), where the low pass filtered image can be seen with the magnetic contrast isolated. The frequency filtering was performed using a cut-off wavelength of 0.511 nm and a PSDF edge width of 0. The high-pass filtered image shown in Fig. 5.18(d) reveals a distinct hexagonal magnetic pattern spreading outwards from the vicinity of the hexa-junction, marked with a red square. This pattern closely resembles the magnetic contrast observed near hexa-junctions in the DL system (see Fig. 4.33).

5.5 Summary

Beginning with the growth behavior, we observed that samples grown near room temperature exhibit stripe-like reconstruction patterns. These reconstruction lines do not fully disappear even when the sample is grown at higher temperatures, although larger pseudomorphic regions are obtained under such conditions. Two distinct stacking types are identified in the TL-denoted as TL(A) and TL(B). The reconstruction lines appear to influence the trajectory of magnetic domain walls, as exemplified by additional TL samples presented in the appendix.

Regarding magnetic properties, particularly for samples grown near room temperature, the ground state appears to be sensitive to nearby structural features such as reconstruction lines, and buried step edges formed at the interface with the DL and QL. Despite this sensitivity, the dominant magnetic texture remains stripy across the TL. This stripy contrast is especially prevalent in the pseudomorphic regions of samples grown at elevated temperatures, where three rotational domains were observed and attributed to a $3Q^2$ magnetic state. Simulations of domain walls separating such domains further suggest the possibility of a $3Q^3$ configuration, indicating the presence of topologically non-trivial magnetic states both within domains and along domain walls. However, definitive identification of the underlying magnetic ground state-whether it corresponds to the $3Q^2$ or a distorted 3Q state-requires further investigation with vector magnetic field control.

Additionally, asymmetric Y- and T-shaped junctions were observed in the TL domain wall network, potentially arising from a lateral shift in the system similar to that seen in the DL. The precise origin of this shift remains unclear, and it is not yet possible to determine whether it originates intrinsically from the TL or results from a proximity effect due to the underlying DL. Furthermore, domain wall networks were successfully nucleated using implanted argon bubbles, forming hexajunctions reminiscent of those previously observed in the DL.

Bibliography

1. Ferriani, P. *et al.* Atomic-Scale Spin Spiral with a Unique Rotational Sense: Mn Monolayer on W(001). *Phys. Rev. Lett.* **101,** 027201 (2 2008).
2. Meyer, S., Schmitt, M., Vogt, M., Bode, M. & Heinze, S. Dead magnetic layers at the interface: Moment quenching through hybridization and frustration. *Phys. Rev. Res.* **2,** 012075 (1 2020).
3. Weber, P. M., Drevelow, T., Qi, J., Bode, M. & Heinze, S. Evidence for a conical spin spiral state in the Mn triple layer on W (001): Spin-polarized scanning tunneling microscopy and first-principles calculations. *Physical Review B* **108,** 134419 (2023).
4. Finco, A., Hsu, P.-J., Kubetzka, A., von Bergmann, K. & Wiesendanger, R. Tailoring noncollinear magnetism by misfit dislocation lines. *Phys. Rev. B* **94,** 214402 (21 2016).
5. Hsu, P.-J. *et al.* Electric-field-driven switching of individual magnetic skyrmions. *Nature nanotechnology* **12,** 123–126 (2017).
6. Zhang, Y. *et al.* Promotion of superconductivity in magic-angle graphene multilayers. *Science* **377,** 1538–1543 (2022).
7. Andrei, E. Y. & MacDonald, A. H. Graphene bilayers with a twist. *Nature materials* **19,** 1265–1275 (2020).
8. Tanaka, M. *et al.* Superfluid stiffness of magic-angle twisted bilayer graphene. *Nature* **638,** 99–105 (2025).
9. Lu, Z. *et al.* Extended quantum anomalous Hall states in graphene/hBN moiré superlattices. *Nature,* 1–6 (2025).
10. Heinze, S. *et al.* Spontaneous atomic-scale magnetic skyrmion lattice in two dimensions. *nature physics* **7,** 713–718 (2011).

11. Spethmann, J., Grünebohm, M., Wiesendanger, R., von Bergmann, K. & Kubetzka, A. Discovery and characterization of a new type of domain wall in a row-wise antiferromagnet. *Nature Communications* **12,** 3488 (2021).
12. Spethmann, J. *et al.* Discovery of magnetic single-and triple-q states in Mn/Re (0001). *Physical review letters* **124,** 227203 (2020).
13. Li, P. & Ding, F. Origin of the herringbone reconstruction of Au (111) surface at the atomic scale. *Science advances* **8,** eabq2900 (2022).
14. Hamilton, J. C. & Foiles, S. M. Misfit Dislocation Structure for Close-Packed Metal-Metal Interfaces. *Phys. Rev. Lett.* **75,** 882–885 (5 1995).
15. Brune, H., Röder, H., Boragno, C. & Kern, K. Strain relief at hexagonal-close-packed interfaces. *Physical Review B* **49,** 2997 (1994).
16. Jankowski, M., Wormeester, H., Zandvliet, H. J. & Poelsema, B. Temperature-dependent formation and evolution of the interfacial dislocation network of Ag/Pt (111). *Physical Review B* **89,** 235402 (2014).
17. Aıt-Mansour, K. *et al.* C 60 on strain-relief patterns of Ag/ Pt (111): Film orientation governed by template superstructure. *Physical Review B—Condensed Matter and Materials Physics* **74,** 195418 (2006).
18. Takagi, H. *et al.* Spontaneous topological Hall effect induced by non-coplanar antiferromagnetic order in intercalated van der Waals materials. *Nature Physics* **19,** 961–968 (2023).
19. Nickel, F. *et al.* Coupling of the triple-q state to the atomic lattice by anisotropic symmetric exchange. *Physical Review B* **108,** L180411 (2023).
20. Haldar, S., Meyer, S., Kubetzka, A. & Heinze, S. Distorted 3 Q state driven by topological-chiral magnetic interactions. *Physical Review B* **104,** L180404 (2021).

21. See `https://github.com/JHagemeister/MonteCrystal`. Monte Crystal 3.2.0.

6 Quadruple layer of Mn/Ir(111)

Abstract

This chapter deals with the quadruple/fourth layer of Mn/Ir(111). This layer shows interesting aspects of growth and magnetism. The quadruple layer exhibits three different types of strain-relief reconstruction patterns with respect to temperature and coverage. At higher temperatures of growth, the QL generates a periodic reconstructed surface that is reminiscent of a Kagome - like lattice and different from the stripe-like pattern observed at lower growth temperatures. The magnetism is strongly influenced by the reconstruction, even more than the triple layer. The QL serves as a rich platform to learn about topology, chirality and strong magneto-structural coupling.

Introduction

Stress relief patterns have been discussed in the TL of Mn/Ir(111) chapter. A stripe-like reconstruction pattern was observed in the TL system upon growing the sample at higher than room temperature. A two stage growth process with respect to the annealing temperature will be discussed in this chapter. A transition from stripe-like to a network type stress relief pattern has been observed in the QL system with increasing annealing temperature. Moreover, the network type stress relief pattern exists in additional two kinds of reconstruction patterns not influenced by temperature, but by film coverage.

With respect to magnetism, the previous chapter showed that the TL of Mn/Ir(111) hosts a distorted $3Q^2$ state. This chapter reports on the further investigation of 3Q AFM magnetic states in the fourth layer of Mn/Ir(111). The existence of distorted $3Q^2$ rotational domains along with strong magneto-structural coupling will be discussed in this chapter.

6.1 Growth of the Mn QL on Ir(111)

6.1.1 Near room temperature growth

In Fig. 6.1(a, b) we see overview dI/dU and partially differentiated topography images of a sample having a coverage of around 2.4 MLs. In the dI/dU overview map, the QL can be seen in very small areas having the similar striped reconstruction phase as the TL. This image exhibits some multi-tip effects and hence some areas can be seen repeatedly and should be ignored as artifacts.

The only difference between the TL and the QL's growth is the thickness of the striped reconstruction lines in Fig. 6.1(c). Compared to the TL, the QL dislocation lines are a little thinner in appearance. This is better exemplified in the zoomed in image in Fig. 6.2 where the QL and the TL can be seen to coexist side by side across a buried step edge.

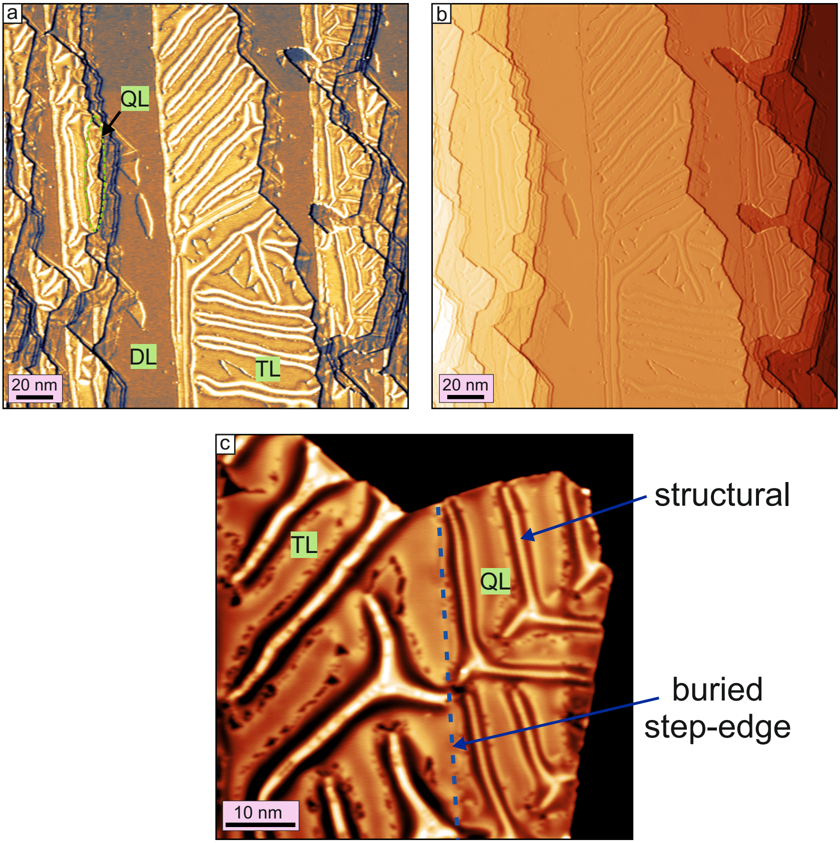

Figure 6.1: Overview of the QL in near room temperature grown samples. (a) A dI/dU map revealing electronic variations across a surface with regions of double layer (DL), triple layer (TL), and quadruple-layer (QL) coverage. **(b)** A partially differentiated STM topography image of (a). **(c)** A constant-current topographical STM image showing the surface morphology with regions of TL and QL across a buried step edge. The reconstruction lines on the QL appear thinner compared to the TL. (Measurement parameters: a,b: $U = +100\,\mathrm{mV}$, $I = 1\,\mathrm{nA}$; c: $U = +30\,\mathrm{mV}$, $I = 1\,\mathrm{nA}$; all: $T = 4\,\mathrm{K}$).

6.1.2 High temperature growth

The QL exhibits a change in the reconstruction pattern when grown beyond RT. Additionally, QL samples grown at higher temperatures, exhibit two types of reconstructions which we will discuss in detail. One is termed the Kagome-like reconstruction, and the other is called the triangular reconstruction.

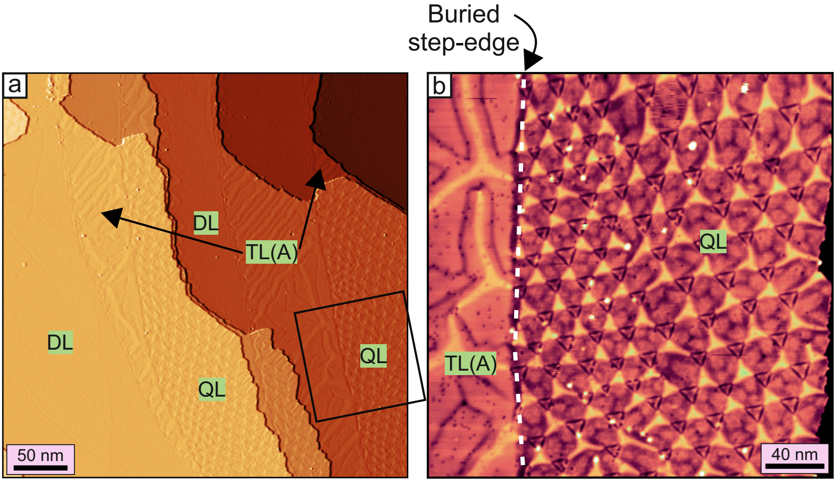

Figure 6.2: Effect of growth temperature on the QL reconstruction. The QL sample areas shown here were obtained by growing the sample at annealing temperatures of 250° . **(a)** A constant-current, partially differentiated STM topography image showing the DL, TL(A) and QL regions. The TL exhibits the striped reconstruction lines, whereas the QL exhibits the network type stress relief pattern reconstruction. **(b)** A zoom-in constant-current topography image of the area marked by a square in (a) shows the TL(A) besides the QL across a buried step edge with the striped and a network type stress relief pattern. (Measurement parameters: a: $U = +500\,\text{mV}$, $I = 1\,\text{nA}$; b: $U = -100\,\text{mV}$, $I = 1\,\text{nA}$; all: $T = 4\,\text{K}$).

Before delving into the details of the two types of reconstruction patterns, an illustrative image (Fig. 6.2) is presented to highlight the distinct growth behaviors of the triple-layer (TL) and quadruple-layer (QL) Mn/Ir(111) systems when grown at elevated temperatures. At this stage, the reader may disregard the magnetic domain walls (visible as dark lines) in both the TL and QL regions and instead focus on the structural features. It can be clearly observed that the TL terrace on the left exhibits a stripe-like reconstruction phase, whereas the adjacent QL terrace-separated by a buried step edge-displays a network type stress relief pattern.

The network type stress relief pattern in the Mn quadruple layer can manifest itself in two distinct configurations, as illustrated in Fig. 6.3. The specific reconstruction - either the *triangular* or the *Kagome-like* depends on the relative arrangement and connection geometry of three intersecting families of structural domain walls [1].

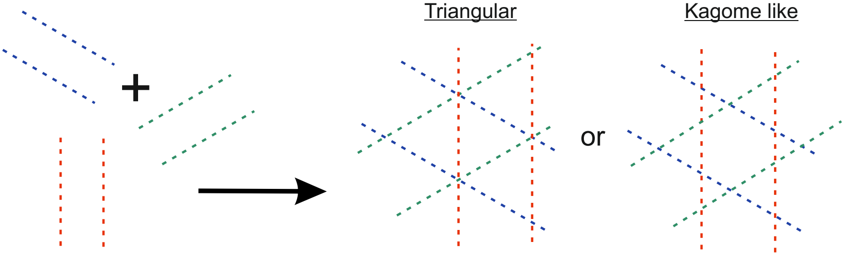

Figure 6.3: Formation of network motifs in the Mn quadruple layer (QL) from structural domain walls. The schematic illustrates how three families of structural domain walls (blue, green, and red dashed lines) intersect to form network type stress relief motifs. Depending on the intersection geometry, two distinct reconstruction patterns can arise: the *triangular* and the *Kagome-like* motifs. In the *triangular* reconstruction, all three domain wall families converge at a single point, whereas in the *Kagome-like* reconstruction, their intersections are offset, giving rise to a Kagome-like network.

The two distinct stress relief patterns observed in Fig. 6.3 occur in the QL. The decisive factor for the particular reconstruction pattern to occur is governed by the coverage of Mn. The characteristic reconstruction patterns corresponding to each case are displayed in Figs. 6.4(c) and (d), respectively. The sample with lower coverage ($\approx$ 3.3 monolayers) exhibits a triangular-type reconstruction, whereas the sample with higher coverage ($\approx$ 3.8 monolayers) displays a Kagome-like reconstruction pattern. A similar evolution of stress-induced surface reconstructions has been reported for the Ag/Pt(111) system, where triangular and Kagome-like patterns emerge with increasing film thickness at a constant annealing temperatures of 800 K [2, 3].

It is worth noting that a previous STM study on a similar network-type reconstruction in the bilayer system of Ag/Pt(111) revealed, through atomic-resolution imaging, that the reconstruction does not occur in the topmost layer but rather in the underlying Ag monolayer [4]. In the present case, atomically resolved images of the QL have not yet been obtained, and thus no direct structural evidence is available to confirm whether a similar scenario applies. However, indirect indications from magnetic imaging suggest that the reconstruction may reside within the TL rather than the QL. A detailed understanding of these magnetic contrast patterns, however, requires prior knowledge of the structural and magnetic properties of the QL. Therefore, this aspect will be revisited in the following section on the magnetism of the QL.

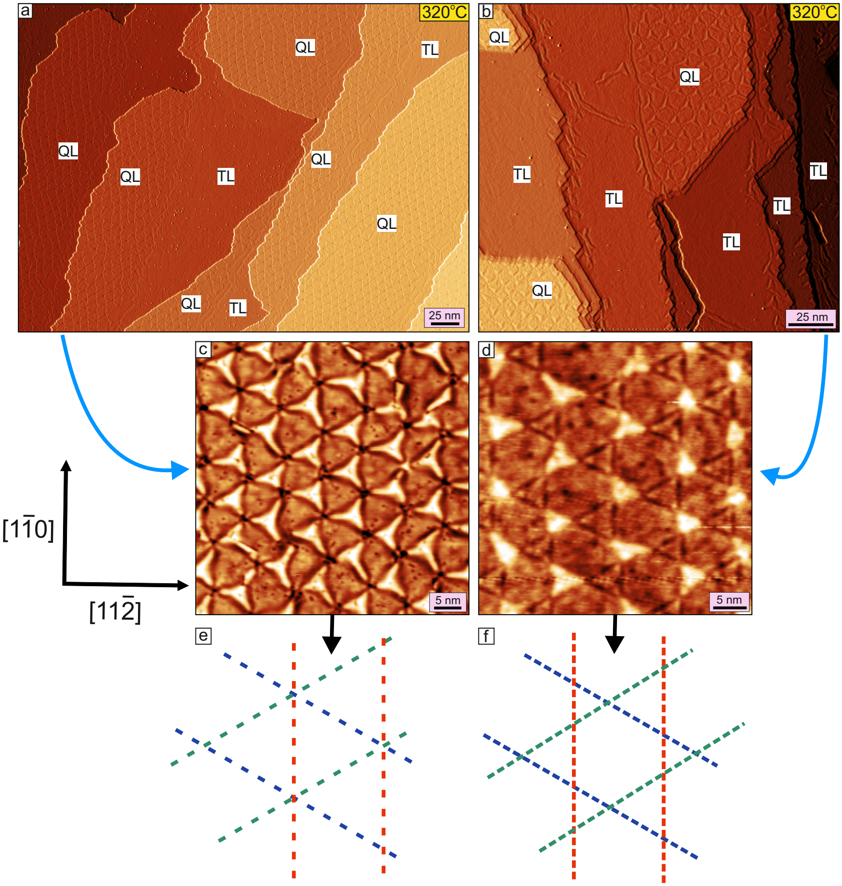

Figure 6.4: Coverage dependent stress relief patterns in the QL. (a,b) Partially differentiated constant-current topography STM images of different samples grown at the same annealing temperature of 320° . However, the coverage can be seen to differ in both cases: ≈ 3.8 MLs for (a) and ≈ 3.3 MLs for (b). **(c,d)** represent zoom-in constant-current topography STM images showcasing the *triangular* and *Kagome-like* reconstruction patterns, respectively. **(e,f)** The corresponding schematics are shown for (c,d) respectively. (Measurement parameters: a: $U = +500\,\text{mV}$, $I = 1\,\text{nA}$, $T = 4\,\text{K}$ b: $U = +20\,\text{mV}$, $I = 1\,\text{nA}$, $T = 8\,\text{K}$ c: $U = +100\,\text{mV}$, $I = 1\,\text{nA}$, $T = 4\,\text{K}$ d: $U = +200\,\text{mV}$, $I = 1\,\text{nA}$, $T = 8\,\text{K}$).

6.1.2.1 Type 1: Triangular reconstruction

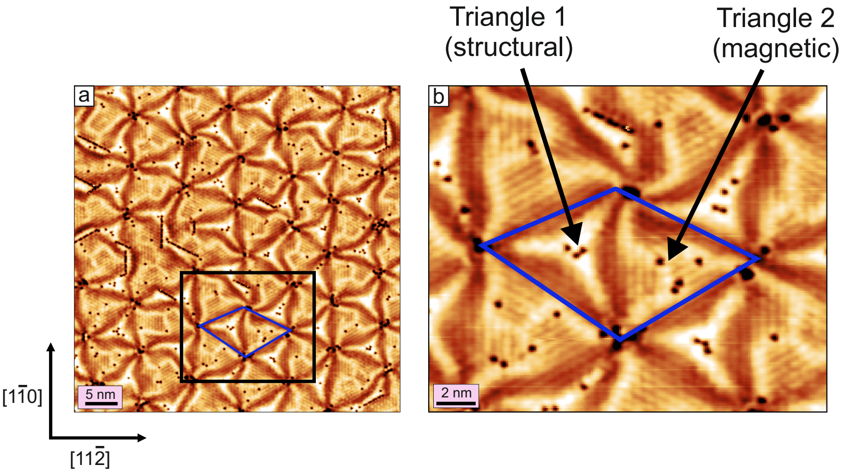

Figure 6.5: The triangular reconstruction phase of the QL. A constant-current SP-STM topography image shows a zoomed-in area of the QL exhibiting the triangular reconstruction. The blue rhombus outlines the unit cell, where one triangle corresponds to hosting a magnetic domain wall junction and the other to a star shaped structural feature. (Measurement parameters: $U = +10\,\mathrm{mV}$, $I = 1\,\mathrm{nA}$, $T = 4\,\mathrm{K}$).

In the STM image of Fig. 6.5, a sample area of the QL exhibiting the triangular type of reconstruction is shown. The unit cell is comprised of two triangles pointing in opposite directions. One triangle hosts a structural feature, whereas the other triangle has a magnetic domain wall junction.

Fig. 6.6 presents a proposed growth model for the triangular reconstruction pattern observed in the QL of Mn/Ir(111). The unit cell is diamond-shaped and consists of two oppositely stacked triangular domains. In the model, yellow atoms denote the stacking for the triangle hosting the magnetic domain wall junction (Triangle 2), while pink atoms constitute the triangle hosting the star shaped reconstruction line (Triangle 1).

This structural element resembles the Y-shaped reconstruction pattern observed in near-room-temperature-grown QL samples (see Fig. 6.1(c)).

The structure model shown in Fig. 6.6 suggests a transition from the pseudomorphic area stacking (pink atoms) to stacking B (dark blue atoms) along the Y-shaped line, with atomic relaxation occurring through intermediate bridge-site positions. The atoms labeled as "QL distorted" (refer to the legend in Fig. 6.6) are considered distorted because of their proximity to the stacking B atoms along the dislocation path. However, the precise nature of the relaxation of these atoms remains unclear due to limitations in the current experimental data.

It should be emphasized that this model is based on structural assumptions guided by STM observations, and minor deviations from the actual atomic configuration are possible. Further high-resolution experimental or theoretical input would be required to fully confirm the atomic structure of the reconstruction and associated dislocation lines.

I would like to emphasize here that the reconstruction in the model is occurring in the TL and not in the QL. The QL is assumed to grow pseudomorphic in a hexagonal layer with the underlying reconstruction from the TL influencing the magnetic properties, which will be discussed later.

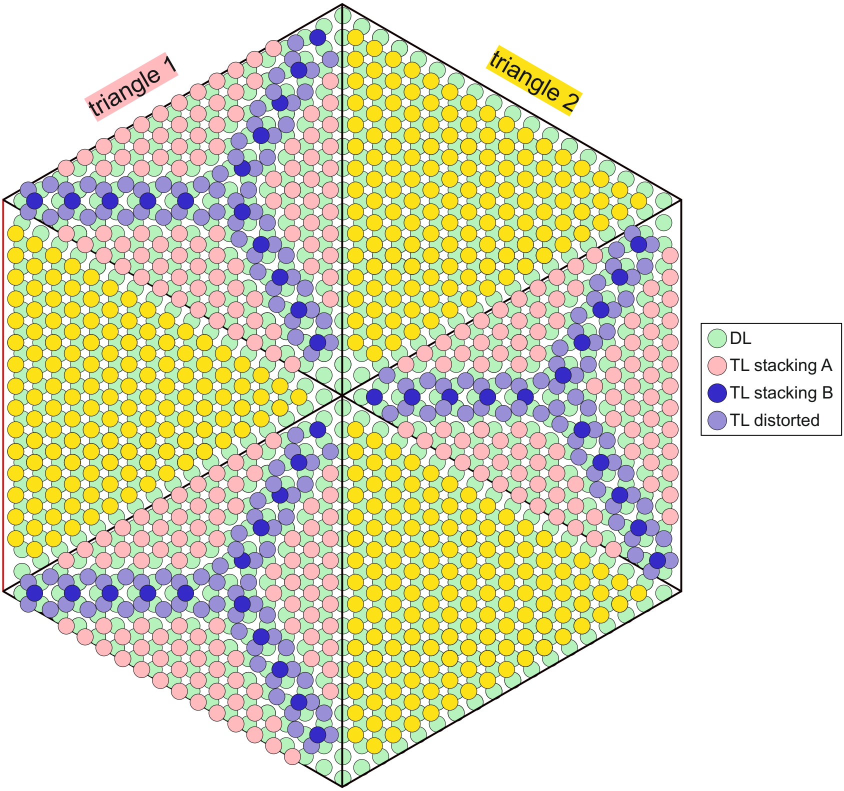

Figure 6.6: Structure model of the triangular reconstruction in the QL. The atomistic structure model of the triangular reconstruction shows the two triangles (labelled 1 and 2) in yellow and pink atoms respectively. Triangle 1 contains the star shaped reconstruction line. The reconstruction line is drawn in a way to accommodate for a differently stacked row of atoms (stacking B) compared to the surrounding area (stacking A). Please note that the reconstruction shown here is in the TL and the QL will be a pseudomorphic hexagonal layer - not shown.

6.1.2.2 Type 2: Kagome - like reconstruction

Fig. 6.7(a) presents an experimental STM image of the quadruple layer (QL) exhibiting a Kagome-like surface reconstruction pattern. A schematic representation of the pattern is shown in panel (b), with the various structural features labeled accordingly. Although the observed reconstruction closely resembles the well-known Kagome lattice, it is referred to here as Kagome-like. This distinction is made because, in true Kagome materials, the truncated hexagonal units contain only a single atom at their center, forming a distinct atomic arrangement characteristic of the Kagome unit cell. Kagome materials have recently garnered significant interest due to their relevance in exploring strongly correlated electronic phases and geometrically frustrated magnetism [5, 6].

Following the STM data presented in Fig. 6.7, a growth model for the Kagome-like reconstruction pattern is shown in Fig. 6.8. It is important to note that, throughout this thesis, the terms *Kagome-like reconstruction* and *truncated hexagon (TH) reconstruction* will be used interchangeably.

The unit cell of the Kagome-like reconstruction pattern is rhombus-shaped, as highlighted by the blue solid lines in Fig. 6.8. This unit cell comprises one truncated hexagon (TH) and two triangular regions of different sizes, denoted here as triangle 1 (hosting the star shaped dislocation line) and triangle 2 (pseudomorphic).

A comparable reconstruction pattern featuring both stripe-like and Kagome-like motifs has been reported in the bilayer Ag/Pt(111) system [1], which bears a close resemblance to the quadruple layer (QL) of Mn/Ir(111). Theoretical studies on the growth of Ag/Pt(111) have shown that fcc stacking is energetically more favorable than hcp stacking [7]. Consequently, during growth, the fcc-stacked regions tend to expand more, resulting in a greater area coverage. As no such theoretical calculations currently exist for the QL of Mn/Ir(111), it remains unclear

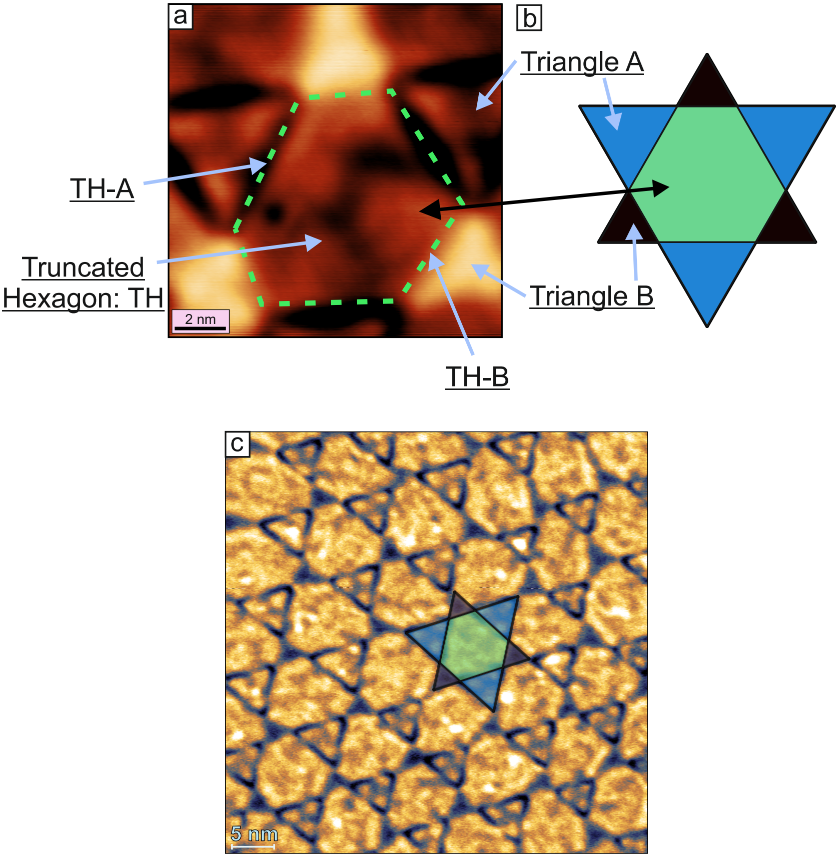

Figure 6.7: The Kagome - like reconstruction of the QL. (a) A constant-current STM topography image showing the unit cell of the Kagome - like reconstruction in the QL. The unit cell consists of a truncated hexagon (TH), and two kinds of triangular shaped regions - Triangle A and B. TH-A and TH-B refer to the transition areas between the TH and the A and B triangles. **(b)** Schematic of a Kagome unit cell. Different colors represent the different parts of the unit cell. **(c)** dI/dU image of the QL, where the Kagome-like reconstruction can be clearly seen. The schematic from (b) is overlaid on this image with a rotation. (Measurement parameters: (a): $U = +500\,\text{mV}$, $I = 2\,\text{nA}$, $T = 8\,\text{K}$; (b): $U = -500\,\text{mV}$, $I = 1\,\text{nA}$, $T = 8\,\text{K}$).

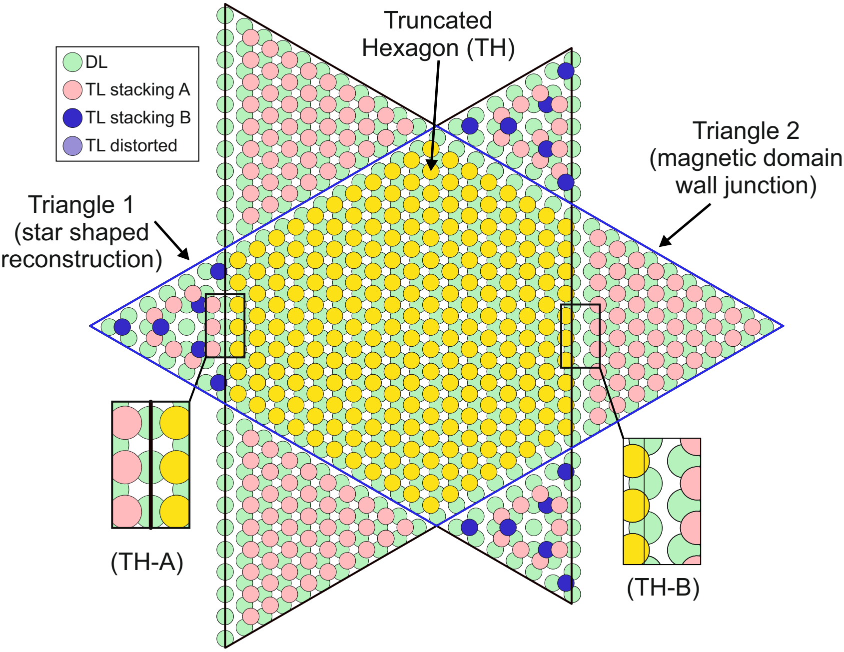

Figure 6.8: Structure model of the Kagome - like reconstruction in the QL. The atomistic structure model of the Kagome - like reconstruction is shown. Triangles 1, 2 are proposed to have a different stacking than the truncated hexagon (yellow atoms). Triangle 1 contains the star-shaped reconstruction line similar to the one observed in Fig. 6.6. The magnified insets enhance the TH-A and TH-B transition areas which appear to be different to each other. Please note that the reconstruction shown here is in the TL, while the QL will be a pseudomorphic hexagonal layer - (not shown).

whether a similar energetic preference applies in the present system.

An intriguing feature of this reconstruction is that the two triangles (1 and 2) differ in both size and edge morphology. As seen in the magnified insets of Fig. 6.8, the atomic spacing between the pink (triangular) and yellow (TH) atoms is larger in the case of TH-B than TH-A. Additionally, the edge geometry varies depending on direction: vertical edges exhibit narrower spacing between adjacent atomic rows, whereas diagonal edges display wider spacing. This observation is consistent with findings from the Ag/Pt(111) bilayer system, where similar anisotropic edge behavior has been reported [1].

I would like to emphasize here that the reconstruction in the model is drawn in the TL and not in the QL. The QL is assumed to grow pseudomorphically in a hexagonal layer with the underlying reconstruction from the TL influencing the magnetic properties, which will be discussed later.

Based on the established growth behavior of Mn on Ir(111), the monolayer (ML) and bilayer (DL) adopt an hcp stacking sequence relative to the fcc substrate [8, 9]. The structural evolution beyond the DL is less straightforward. Experimental observations hint that the reconstruction visible in the quadruple layer (QL) originates in the underlying triple layer (TL), while the QL itself appears pseudomorphic, showing no reconstruction features. This suggests that the TL undergoes stress relaxation, possibly by transitioning to an fcc stacking sequence, thereby relieving strain accumulated in the lower hcp-stacked layers. As a result, the QL grows pseudomorphic on this relaxed TL. Therefore, a stacking sequence where the QL returns to fcc stacking beyond the DL is the most plausible structural configuration. Continued hcp stacking in the TL and QL can be excluded, as it would not account for the observed reconstruction behavior.

6.1.3 Differentiating between structural and magnetic features

As the structure is strongly linked to the magnetism (Fig. 6.5 and Fig. 6.7), it is important to decipher the structural and magnetic features. One such feature is the three armed star that occurs in the reconstruction pattern, especially visible in the triangular reconstruction type of the QL. Here I am going to show data that helps to distinguish between the structural and magnetic features in the QL.

Fig. 6.9 shows different sample areas for two different samples grown similarly. In Fig. 6.9(a), the DL reconstruction line can be seen connecting the zig-zag dislocation lines in the DL to the dislocations lines in the TL. Magnetic domain walls have been labelled separately in (a).

The *dI/dU* image in Fig. 6.9(b) shows the DL, TL, and QL. The reconstruction lines observed in the TL and QL exhibit similar shape and contrast, differing only in their length. This qualitative similarity suggests that the reconstruction lines in these layers are of the same origin or nature.

Fig. 6.9(d) presents a zoomed-in constant-current topography image of the region marked by a blue square in Fig. 6.9(c). In this image, the dislocation line in the DL appears to connect to the dislocation line in the TL, as highlighted by the blue dotted ellipse. If this feature were a magnetic domain wall, similar connections would be expected to occur more frequently, or at least be observed for other dislocation lines as well. Additionally, the hydrogen visible in this image either forms an island on the DL or appears localized on magnetic domain walls in the TL region, where it is seen as dark contrast along the domain walls.

Hence, this analysis establishes a clear understanding of the structural and magnetic features present in the system.

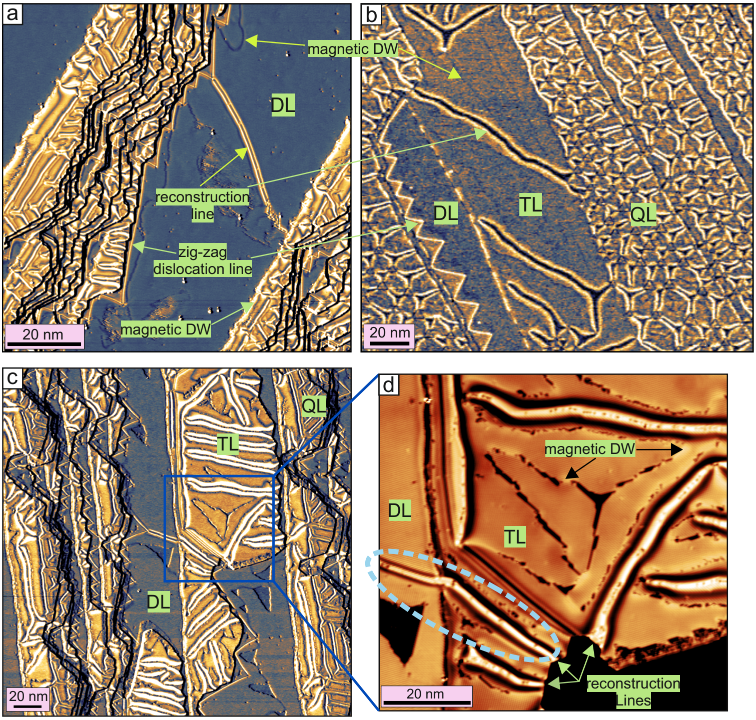

Figure 6.9: Differentiating between structural and magnetic features for the QL reconstructions. (a,b,c) *dI*/*dU* images revealing electronic variations associated with magnetic domain walls and reconstruction lines in the DL, TL and QL areas. **(d)** Zoomed-in constant-current SP-STM image of the DL and TL regions across a buried step edge. The reconstruction line in the DL can be seen to extend into the TL. The star shaped dislocation lines in the TL and QL can now be attributed to be the same feature also observed in the DL. (Measurement parameters: a: $U = +100\,\text{mV}$, $I = 1\,\text{nA}$; b: $U = +300\,\text{mV}$, $I = 0.2\,\text{nA}$; c,d: $U = +50\,\text{mV}$, $I = 1\,\text{nA}$; all: $T = 4\,\text{K}$).

6.1.4 Origin of the observed reconstructions

Stress relief in close-packed metal systems was a subject of significant interest during the 1990s. Isotropic stress relaxation was extensively studied in metal-on-metal systems such as Cu/Ru(0001) [10], Ag/Pt(111) [1], Au(111) [11], and Pt(111) [12, 13]. Notably, the Au(111) and Pt(111) surfaces were found to reconstruct even in the absence of an additional overlayer. For example, the Au(111) surface exhibits a well-known herringbone reconstruction, which arises due to a mismatch between the preferred lattice spacing of the surface atoms and that of the underlying bulk. In contrast, the Pt(111) surface undergoes reconstruction only under specific conditions, such as high-temperature annealing or upon the deposition of alkali metals.

To theoretically understand these stress relief mechanisms in Pt(111), Raghani et al. [13] employed a two-dimensional extension of the Frenkel–Kontorova (FK) model, mapping the surface system onto a one-dimensional FK framework. Within this model, they defined a dimensionless stability parameter R, which serves as a criterion for determining whether a surface is energetically favorable to undergo reconstruction. A critical value of R delineates the boundary between stable (unreconstructed) and unstable (reconstructed) surface configurations:

$$R = \frac{(\sqrt{3}\pi a)\left(\gamma - \frac{4}{3}\sigma\right)}{8\sqrt{kW}} \tag{6.1}$$

In the above equation, k is the spring constant for nearest neighbour bonds which stems from the nature of the 1D FK model. W is the amplitude of the sinusoidal potential connecting fcc and hcp atomic positions as we are dealing with a hexagonal close packed structure. σ and γ are the surface stress and surface energy constants, respectively, of the top layer. Now, upon inserting these values into the equation, if $|R| >/< 1$, the surface will not reconstruct. They find this value to be -1 for Pt(111) which indicates Pt to be in the borderline situation. Hence Pt(111) is easily prone to surface reconstruction upon annealing.

To date, no equivalent theoretical calculations have been reported for Ir(111). However, despite Ir(111) being a widely studied substrate for numerous material systems [14, 15], reconstruction phenomena have not been observed on its surface. In the present work, STM investigations of Mn/Ir(111) reveal that annealed samples in the double-layer (DL) regime do not exhibit any reconstruction, suggesting that the DL remains pseudomorphic. Reconstruction patterns begin to emerge only from the triple-layer (TL) onward. In the quadruple-layer (QL), a temperature-dependent reconstruction is observed-from a stripe-like pattern (RT) to a network type stress relief pattern (higher than RT).

Interestingly, several studies have shown that increasing coverage can drive the surface into a new reconstruction phase. This behavior has been reported for Cu/Ru(0001) [10], Pt(111) [2, 13], and for alkali-metal adsorption on Au(111) [16]. In the theoretical work by Raghani et al. [13], several factors contributing to the evolution of reconstruction patterns are discussed. One such factor is the parameter W, which depends on the annealing temperature, (see Eq. (6.1)). Additional variables include the surface chemical potential γ and the excess surface atom density $\Delta\rho$, defined relative to the unreconstructed phase-both of which have been shown to influence reconstruction stability.

6.2 Magnetism of the Mn QL on Ir(111)

Having discussed the growth characteristics and reconstruction behavior of the QL, we now turn our attention to its magnetic properties. This section focuses on identifying the magnetic ground state of the QL and examining how the underlying reconstruction patterns influence the observed magnetic domains and domain walls.

6.2.1 Near room temperature samples

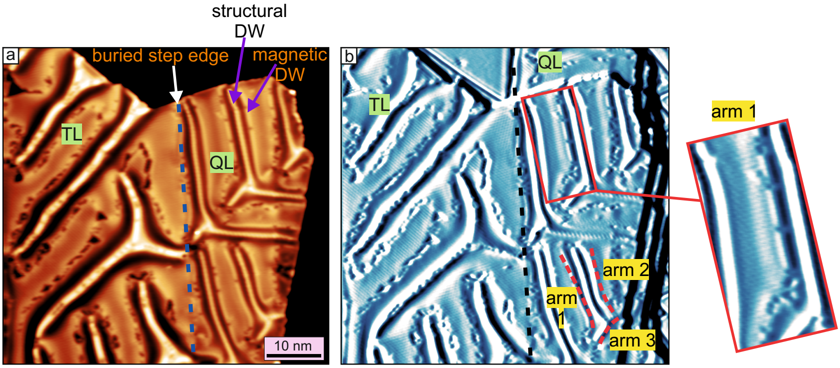

Figure 6.10: Magnetism in the QL of near room temperature grown samples. **(a)** constant-current SP-STM topography image showing regions of the TL and QL across a buried step edge. A buried step edge is indicated by a dashed blue line. Structural and magnetic domain walls are labeled. **(b)** A current channel map of the same area as in (a), where the magnetic contrast is better seen. A magnified inset shows the rotational domain preferred by arm1. For arm2 and arm3, the domains are not large enough to be magnified for better clarity. (Measurement parameters: a,b: $U = +100\,\text{mV}$, $I = 1\,\text{nA}$; all: $T = 4\,\text{K}$).

In samples grown near room temperature, the QL exhibits the stripe-like reconstruction phase, and the associated trajectory of magnetic domain walls closely resembles that observed in the TL (see Fig. 5.8). Fig. 6.10 presents SP-STM measurements, with the topography and current maps shown in panels (a) and (b), respectively. Apart from the slight difference in the width of the reconstruction lines, the domain wall behavior in the QL is similar to that in the TL region. Notably, no magnetic domain wall is observed at the buried step edge from the TL to the QL, in contrast to the distinct domain wall observed at the DL–TL interface (see Fig. 4.14). This observation suggests that the QL likely shares the same magnetic ground state as the TL. Nonetheless, a gradual transition from the likely $3Q^2$ or distorted 3Q state in the TL to another distorted 3Q variant in the QL cannot be excluded [17].

6.2.2 High temperature grown samples

As shown in Fig. 6.2, the QL undergoes a reconstruction phase transition upon annealing. In the following, we investigate how this newly formed reconstruction influences the local magnetic properties, with particular emphasis on the behavior of magnetic domain walls. This analysis is supported by a combination of schematic illustrations and experimental SP-STM data.

6.2.2.1 Triangular reconstruction

We now turn to the spin-polarized scanning tunneling microscopy (SP-STM) data obtained from the QL in the triangular reconstruction phase. As shown in Fig. 6.11, the SP-STM images reveal that each triangular unit consistently hosts a distinct triple junction feature, characterized by three adjoining rotational magnetic domains. Within the unit cell-outlined by a blue rhombus, two types of triangular motifs can be distinguished: the left triangle corresponds to a structurally defined Y-type feature, whereas the right triangle exhibits a magnetic Y-type domain wall triple junction.

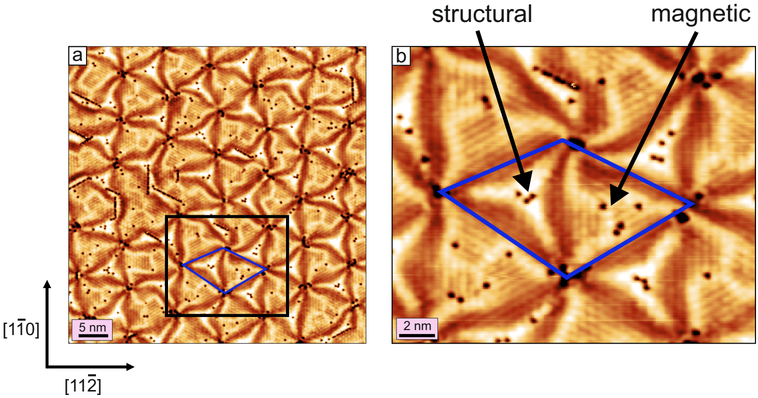

Figure 6.11: Magnetic imaging of the triangular reconstruction in the QL. (a) Constant-current SP-STM topography overview image showing an area of the triangular reconstruction in the QL. **(b)** A zoomed-in constant-current SP-STM image showing the magnetic rows in the structural and the magnetic triangles. A magnetic triple domain wall junction can be seen in the magnetic triangle. The magnetic domains can be seen to have a stripy contrast. (Measurement parameters: a,b: $U = +10\,\text{mV}$, $I = 1\,\text{nA}$, $T = 4\,\text{K}$).

Fig. 6.12 below, presents schematic representations of the triangular reconstruction pattern, overlaid with the associated magnetic domain walls. In these illustrations, red features denote structural domain walls, while blue and green indicate chiral magnetic domain walls, having a handedness. No consistent correlation has been identified between the chirality of the structural and magnetic domain walls in this reconstruction pattern. Therefore, a range of possible chiral combinations is depicted in Fig. 6.12 towards the right, to account for the observed variability. The possible options shown are drawn for a pair of triangles that correspond to the unit cell.

Based on the schematic and experimental data, the red structural lines depicted in the sketch are, in principle, expected to coincide with magnetic domain walls. However, in the experimental topography and differential conductance images, it is challenging to unambiguously distinguish the magnetic domain walls superimposed on these Y-shaped structural features. This difficulty arises due to the convolution of structural and magnetic contrast in the imaging data, which limits the ability to clearly resolve their spatial overlap.

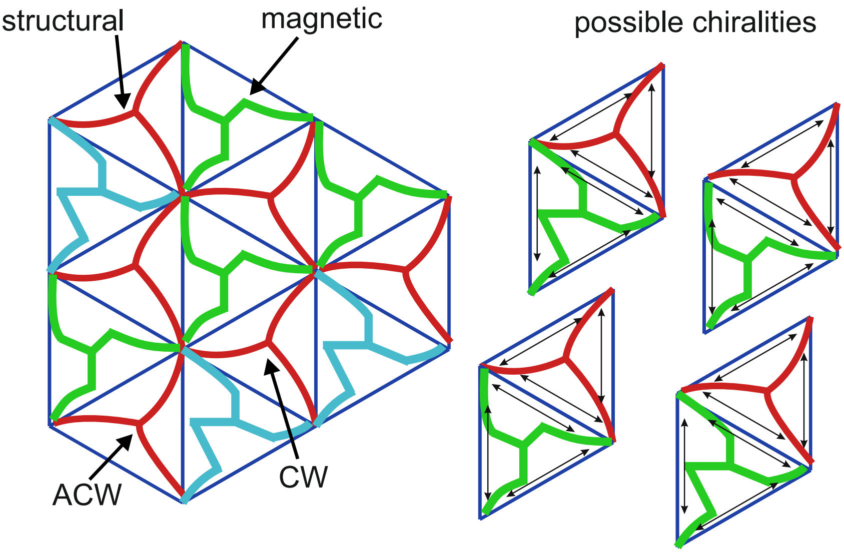

Figure 6.12: Differentiating the structural and magnetic counterparts in the triangular reconstructed QL. The left panel shows a schematic representation of the triangular reconstructed QL. Red lines indicate structural elements, while green lines represent the magnetic domain walls. The structural and magnetic domain walls occur in both chiralities. Green and blue magnetic DWs correspond to the clock-wise and anti-clockwise handedness. Dark blue lines highlight the underlying triangular lattice. Double headed arrows indicate the orientation of the rotational domains that have a majority stripy pattern. The right panel illustrates the possible chiralities that can arise in such a system, showcasing different arrangements of the structural (red) and magnetic (green) elements within the rhombus shaped unit cell.

6.2.2.2 Closer look at the magnetic triple domain wall junctions

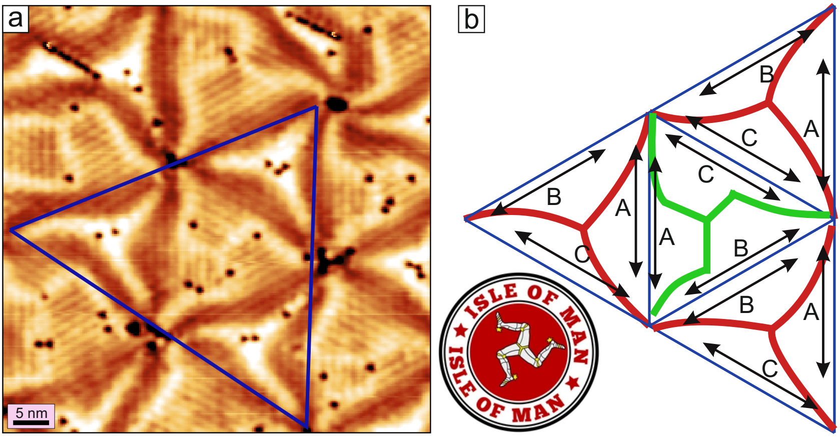

Figure 6.13: Understanding the magnetic domain wall junction generator mechanism. (a) Constant-current SP-STM topography image of an area having the triangular reconstruction on the QL. The triangle drawn in blue captures one magnetic triangle in the centre with three structural triangles at the vertices. **(b)** Schematic of the elements of the blue triangle in (a) comprising the three structural and one magnetic triangle. The different rotational domains have been labelled by A,B and C and their orientation is indicated by double headed arrows. The rotational domains emanating from the structural triangles propel towards the triangle in the centre forcing the creation of a magnetic triple domain wall junction. The magnetic triple domain wall junction is reminiscent of the logo of the Isle of Man flag shown in (b). (Measurement parameters: $U = +10\,\text{mV}$, $I = 1\,\text{nA}$, $T = 4\,\text{K}$).

In the above Fig. 6.13(a), a triangle in solid blue lines has been drawn that encompasses a single magnetic triangle in the centre which contains the magnetic triple domain wall junction. To understand the mechanism behind the formation of this junction, a sketch in Fig. 6.13(b) is presented.

In the sketch, the green coloured feature is the magnetic domain wall, while the red colour is for the structural features. The three rotational domains of the magnetic rows have been denoted by double-headed black arrows and are labelled as A,B and C for simplicity. The blue lines are the structural edges of the triangles that are part of the three pairs of dislocation lines running in the close packed row directions.

As illustrated in the schematic, the magnetic domains labeled A, B, and C extend from the three adjacent structural triangles, each of which hosts a structural Y-type feature (highlighted in red). This suggests that the formation of the magnetic triple junction can be interpreted as a consequence of magnetic domains A, B, and C propagating from their respective structural triangles towards the central magnetic triangle. To accommodate these three competing magnetic orientations, the system stabilizes through the formation of three magnetic domain walls that converge at a single junction point.

This mechanism implies a coupling between the orientation of structural features and the resulting magnetic domain arrangement. Notably, a similar requirement for specific rotational domain configurations along each arm of the structural features has also been observed in samples grown near room temperature, as shown in Fig. 5.8.

It is interesting to see that the domain walls mostly prefer this unique shape which is reminiscent of the flag of the country Isle of Man! To understand the geometry of the magnetic triple junction, we will now look at the magnetic domains and classify them based on the relative angles enclosed by them (see Fig. 6.14).

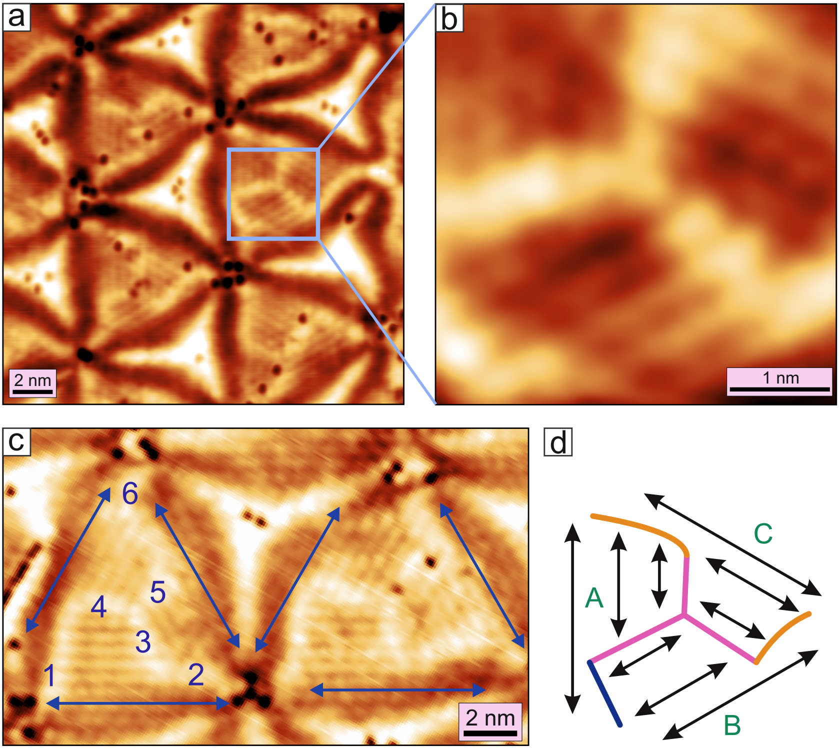

Figure 6.14: Closer look at the magnetic triple domain wall junction in the triangular reconstructed QL. (a) Constant-current SP-STM topography image of an area having the triangular reconstruction in the QL. **(b)** A zoomed-in SP-STM image showing a single magnetic triple domain wall junction with the three stripy rotational domains. **(c)** Two magnetic and one structural triangle. The magnetic domain walls, if seen in parts, mostly have one rotational domain aligned parallel to themselves and the other rotational domain at an angle of 120 degrees. **(d)** Sketch of a triple magnetic domain wall junction. The pink-colored parts of the domain wall correspond to regions where the orientation of one domain is parallel to the domain wall trajectory. The blue part of the domain wall corresponds to the A and B domains being at 30 and 90 degrees to the domain wall. The orange parts are areas where one domain is near to parallel. (Measurement parameters: all: $U = +10\,\mathrm{mV}$, $I = 4\,\mathrm{nA}$, $T = 4\,\mathrm{K}$).

The magnetic domain wall junction shown in Fig. 6.14(b) closely resembles the idealized configuration expected for this particular reconstruction phase. A detailed inspection of the magnetic contrast along the domain walls reveals a consistent trend: one of the two adjacent magnetic domains is typically aligned parallel to the local direction of the domain wall. This recurring alignment suggests that the domain wall tends to follow a trajectory that maintains parallel orientation with at least one neighboring domain. Such configurations are classified here as $(0^\circ, 120^\circ)$ domain wall types, where the angles denote the relative orientation of the adjacent domains with respect to the domain wall direction. The rationale for not labeling these as $(0^\circ, 60^\circ)$ configurations is clarified in the subsequent paragraph referring to Fig. 6.14(d).

For clarity, panel (c) provides a numbered annotation (1–6) highlighting regions at the domain wall junctions where this parallel alignment is evident. These configurations are most prominent in junctions that approximate the ideal geometry-resembling the triskelion-like motif, akin to the Isle of Man flag. Nevertheless, deviations from the ideal triskelion configuration are also observed, resulting in alternative domain wall types such as $(90^\circ, 30^\circ)$ or $(60^\circ, 60^\circ)$, depending on local structural irregularities.

The schematic in Fig. 6.14(d) is a representation of the domain wall junction shown in panel (b), where the magnetic domain orientations are depicted using double-headed arrows. Pink-colored segments of the domain wall correspond to regions where one domain is aligned nearly parallel to the domain wall trajectory. The blue segment represents a domain wall between A and B domains that are oriented at 30° and 90°, respectively, with respect to the wall—thus yielding a 120° domain wall type. Orange-colored segments indicate areas where one domain is approximately parallel to the wall. Since the domain wall contrast remains uniform across all parts of the triple domain wall junction, it can be concluded that the QL maintains a 120° domain wall type throughout.

Overall, the QL exhibits exclusively 120° magnetic domain walls, in contrast to the DL, where the 120° domain wall is dominant but coexists with less frequently observed 60° domain walls.

6.2.2.3 Kagome - like reconstruction

We now turn to the second type of reconstruction pattern observed in the QL: the Kagome-like reconstruction. Fig. 6.15(a) shows an SP-STM image of a representative unit cell exhibiting this reconstruction. A magnetic domain wall junction is clearly visible within the truncated hexagon and can also be faintly identified in the adjacent type A triangles. To aid interpretation, Fig. 6.15(b) presents a schematic overlay of the structural and magnetic features corresponding to panel (a). The blue and green colors indicate domain wall junctions of different handedness. It is worth noting that triangles A and B host a magnetic and structural domain wall respectively. Triangle B must have a magnetic domain wall coinciding with the structural domain wall, but it has been hard to resolve this experimentally.

Fig. 6.15(c) displays an SP-STM image of the same area shown in panel (a), but acquired at a different bias voltage to enhance the magnetic contrast. Regions exhibiting hexagonal and stripe-like magnetic patterns have been marked in the image. Among the three rotational magnetic domains, only one domain has a clear stripe-like contrast. The remaining two domains are less distinct and appear to partially exhibit hexagonal magnetic contrast.

To gain further insight into the magnetic ground state of the QL, we refer to Fig. 6.16, which presents a series of SP-STM measurements performed using a bulk Cr tip, spin-polarized in an arbitrary direction. Panels (a) and (c) show topographic images, while panels (b) and (d) display the corresponding dI/dU maps of the same area, acquired with a slightly

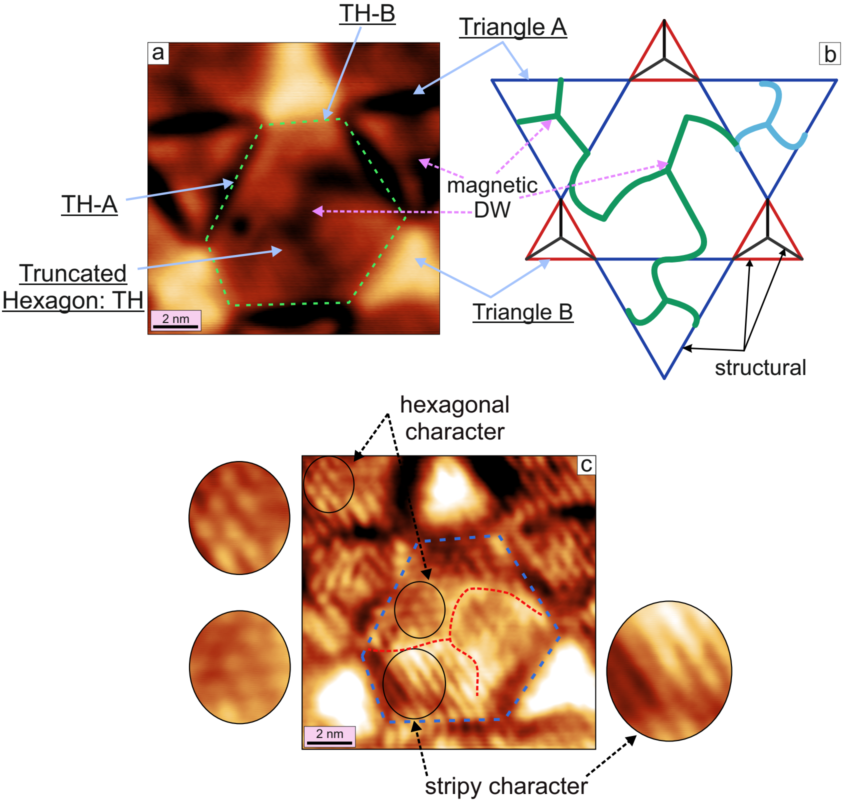

Figure 6.15: Magnetic imaging of the Kagome - like reconstruction in the QL. **(a)** Constant-current STM topography image of a unit cell of the Kagome - like reconstructed QL. The magnetic and structural domain walls have been labelled in the schematic in (b). **(c)** Spin resolved SP-STM topography image of (a) showing the magnetic triple domain wall junction in the truncated hexagon. The rotational domains around the magnetic domain wall show stripy and hexagonal patterns. (Measurement parameters: a: $U = +500\,\text{mV}$, $I = 2\,\text{nA}$; b: $U = +10\,\text{mV}$, $I = 2\,\text{nA}$; all: $T = 8\,\text{K}$).

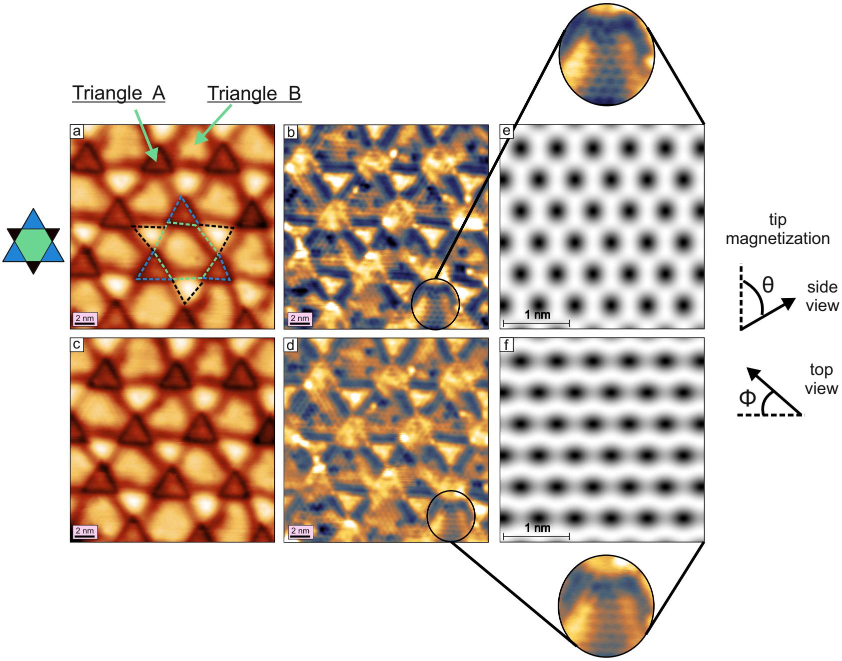

Figure 6.16: Spin-polarized STM measurement series of the Kagome - like reconstruction. Constant-current SP-STM topography and dI/dU images show an area of the QL having the Kagome - like reconstruction in **(a,b)**. The dI/dU magnified insets for (a,b) show different magnetic patterns for the same truncated hexagon which indicates a change in the tip's magnetization for these two images. **(e,f)** Simulated SP-STM images of the $3Q^2$ state with the tip's magnetization being defined by $\theta = 60°$ and $\phi = 90°$ in (e) and $\theta = 30°$ and $\phi = 90°$ for the simulation in (f). (Measurement parameters: all: $U = +2.5\,\text{V}$, $I = 4\,\text{nA}$, $T = 4\,\text{K}$).

altered tip condition.

In the top panel, the magnetic pattern within the truncated hexagon regions exhibits a hexagonal appearance, most clearly visible in the bottom right and top left hexagons. The bottom right truncated hexagon is shown with a 2× magnification for better visibility. In contrast, the magnetic pattern in the bottom panel appears to lie between a purely hexagonal and a purely stripe-like pattern.

To understand this observation, simulated SP-STM images of a $3Q^2$ domain with a canted tip magnetization are shown alongside the experimental data in panels (e,f). The hexagonal contrast (panel (e)) is reproduced for a tip magnetization orientation with polar and azimuthal angles of $\theta = 60^\circ$ and $\phi = 90^\circ$, respectively. The near-stripe contrast (panel (f)) is simulated for a tip with $\theta = 30^\circ$ and $\phi = 90^\circ$.

From the experimental SP-STM data presented in the above figures, it is observed that the rotational domains in the QL predominantly exhibit a stripy magnetic pattern, often accompanied by small regions of hexagonal contrast. A purely stripy magnetic configuration has never been observed across an entire rotational domain in the QL. Furthermore, the absence of a magnetic domain wall at the buried step edge between the TL and the QL suggests that the magnetic state of the QL is either identical to that of the TL or corresponds to a distorted 3Q variant that can continuously transform into the TL's 3Q configuration [17]. Definitive verification of this hypothesis would require SP-STM measurements in a vector magnetic field. However, the simulated SP-STM data shown in Fig. 6.16 for a $3Q^2$ state with a canted tip magnetization shows good agreement with the experimental observations, thereby supporting the $3Q^2$ state as a plausible candidate for the magnetic ground state of the QL.

We now examine a different region of the QL exhibiting the truncated hexagon reconstruction pattern, as shown in Fig. 6.17. This particular area appears largely free of defects, with the reconstruction pattern becoming more widely spaced from the top to the bottom of the terrace. While magnetic domain walls are not easily discernible in the topographic image, they appear with strong contrast in the corresponding dI/dU map. The sharp boundaries of the truncated hexagons are also well-resolved in the dI/dU image, particularly in the lower half of the terrace.

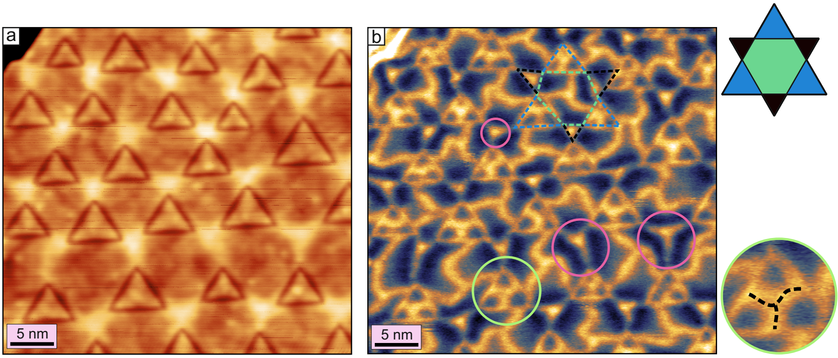

Figure 6.17: Electronic contrast of the structure and magnetism in the Kagome - like reconstructed QL. (a,b) constant-current SP-STM topography and dI/dU images of an area of the Kagome - like reconstructed QL. In the dI/dU image in (b), pink circles highlight the star shaped dislocation lines (structural DWs) and the green circle highlights the presence of a clear magnetic triple domain wall junction in triangle A. This is shown better in a magnified inset. (Measurement parameters: a,b: $U = 2\,\text{V}$, $I = 1\,\text{nA}$, $T = 8\,\text{K}$).

In addition to the domain walls present within the truncated hexagons, magnetic contrast is also visible in the medium-sized triangles associated with different stacking types (highlighted as blue triangles in the accompanying schematic). These regions also exhibit magnetic triple domain wall features, although the precise classification of the junctions-whether Y-type or T-type remains ambiguous. Only one triangle within this image displays a clearly resolved magnetic triple domain wall junction, marked by a bright green circle.

Besides magnetic information, the *dI/dU* image also contains structural contrast. Small Y-shaped structural features, marked by bright pink circles, are visible throughout the image. These features become slightly more pronounced in the lower region, where the reconstruction is more expanded, while their size is nearly negligible in the upper portion due to the tighter packing of the reconstruction pattern.

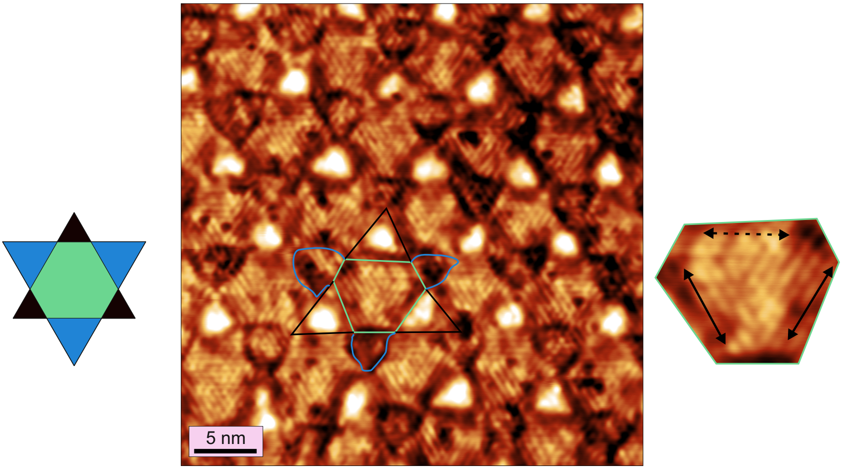

Figure 6.18: Identifying the orientational domains in the Kagome-like reconstructed QL. A SP-STM topography image is shown in the centre of the QL having the Kagome-like reconstruction. The truncated hexagon, triangle A and B have been outlined by hand in the image. The magnified inset on the right is the truncated hexagon marked in green. Stripes with different orientations have been marked by double headed arrows. In the top domain, it is hard to see the stripes, and so the expected orientation of the stripes has been marked with a dashed double headed arrow. This trend is seen for every truncated hexagon in the image.

To resolve the orientations of the rotational domains in the Kagome-like reconstruction, we can look at Fig. 6.18. The magnified inset on the right shows the truncated hexagon outlined in green in the SP-STM topography image in the centre. Two rotational domains can be seen with a stripy magnetic order marked by double headed arrows. The third rotational domain does not clearly show the orientation of the stripes and hence has been marked by a dashed double headed arrow. In essence, the stripes are parallel to the long edges of the truncated hexagon, which is visible for almost every truncated hexagon in the topography image. The orientation of the magnetic pattern in the blue triangles is hard to resolve experimentally.

One unresolved aspect of the magnetic structure in the Kagome-like reconstruction is the termination behavior of magnetic domain walls within the truncated hexagons and medium-sized triangles. In the earlier sketch (Fig. 6.15(b)), the domain walls were drawn to terminate in a connected manner. However, this type of connectivity is difficult to confirm experimentally. Therefore, a schematic shown in Fig. 6.19 illustrates an idealized version of the Kagome-like reconstruction, where magnetic domain walls of both chiralities are depicted terminating at arbitrary positions. It is important to note that the actual Kagome-like reconstruction observed in the QL is not perfectly periodic but exhibits local distortions and irregularities, making it a distorted variant of the idealized structure.

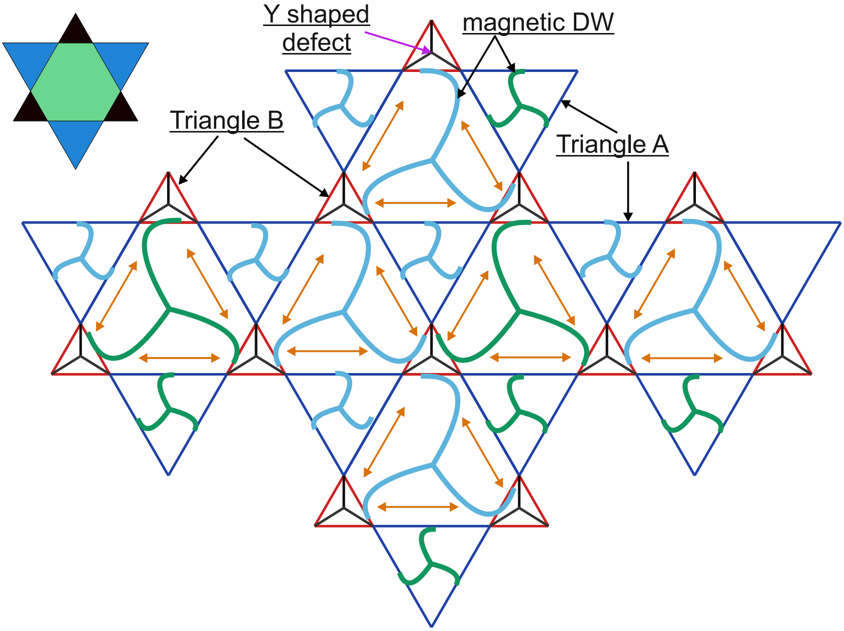

Figure 6.19: Ideal Kagome - like reconstruction pattern with the existence of chiral magnetic domain wall junctions. This schematic illustrates an ideal Kagome - like reconstruction pattern with chiral magnetic domain wall junctions in the truncated hexagon and the A type triangles. The blue and green magnetic domain walls refer to the opposite handedness. The orientation of the rotational domains has been marked by double headed arrows in orange for every truncated hexagon. The termination point of the magnetic domain walls is not known from the experiments and hence has not been clearly shown in this schematic. In experiments, the Kagome - like pattern has distorted structural features. The double headed orange arrows show the orientation of the rotational domains in each truncated hexagon.

6.2.3 Layer dependent reconstruction

6.2.3.1 Triangular reconstruction

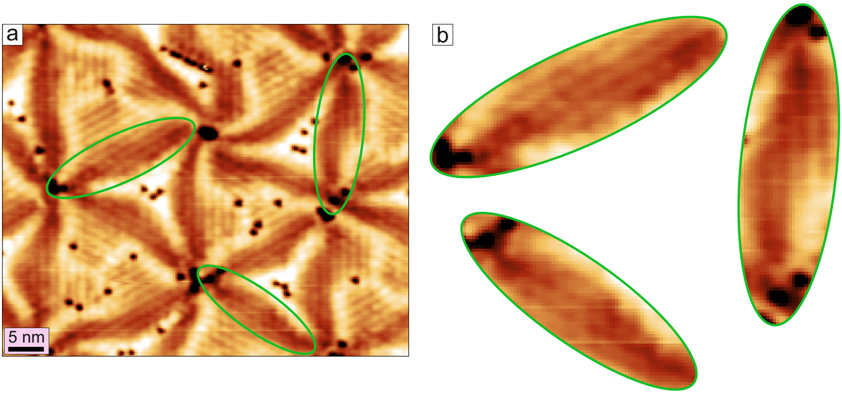

Figure 6.20: Seeing the magnetic rows in the dislocation lines in the triangular reconstructed QL. (a) constant-current STM topography image of an area of the Kagome - like reconstructed QL. **(b)** Magnified insets of areas circled in green in (a) which show the magnetic rows in the dislocation lines, i.e. the transition areas between the structural and magnetic triangles. (Measurement parameters: $U = +10\,\text{mV}$, $I = 1\,\text{nA}$, $T = 4\,\text{K}$).

For the structure models presented for the Kagome-like and the triangular reconstructions of the QL, the QL was assumed to grow pseudomorphically, while the reconstructions were assumed to be located in the TL. As we now have knowledge of the orientational magnetic domains in the QL, we will see hints supporting the argument that the reconstructions reside in the TL and not in the QL.

In Fig. 6.20(a) above, ellipses are drawn along the close-packed [111] directions to emphasize the magnetic patterns in the transitional regions between the structural and magnetic triangles - i.e., across the dislocation lines. These ellipses serve to highlight the continuity of the magnetic features across these structural boundaries.

Fig. 6.20(b) shows 2× magnified versions of these ellipses, revealing that the magnetic rows remain largely undistorted as they traverse the dislocation lines. This continuity suggests that the magnetic domains extend seamlessly from the structural triangles into the magnetic triangles. Such behavior may indicate that the observed reconstruction originates not at the surface of the QL, but rather from a sub-surface layer beneath it.

To confirm this hypothesis, atomic-resolution imaging would be essential. However, such high-resolution data has not yet been obtained for this particular system.

6.2.3.2 Kagome-like reconstruction

In Fig. 6.21 one can see that for certain areas (marked by rectangles) the magnetic features appear curved. These areas are the edges of the structural triangles and the truncated hexagon. The stripy magnetic pattern appears unperturbed in these regions - as if there was no dislocation line or structural boundary. Hence, this observation could provide a hint that the structural reconstruction might be in the underlying layer, i.e. the Mn TL on Ir(111) and only the magnetism in the top layer is dictated by the underlying layer's reconstruction. This would suggest a very strong inter-layer magneto-structural coupling. The similar reconstruction observed in the bilayer of Ag/Pt(111) [18] was also later found out to have the reconstruction in the underlying layer and not in the top layer which is rather surprising.

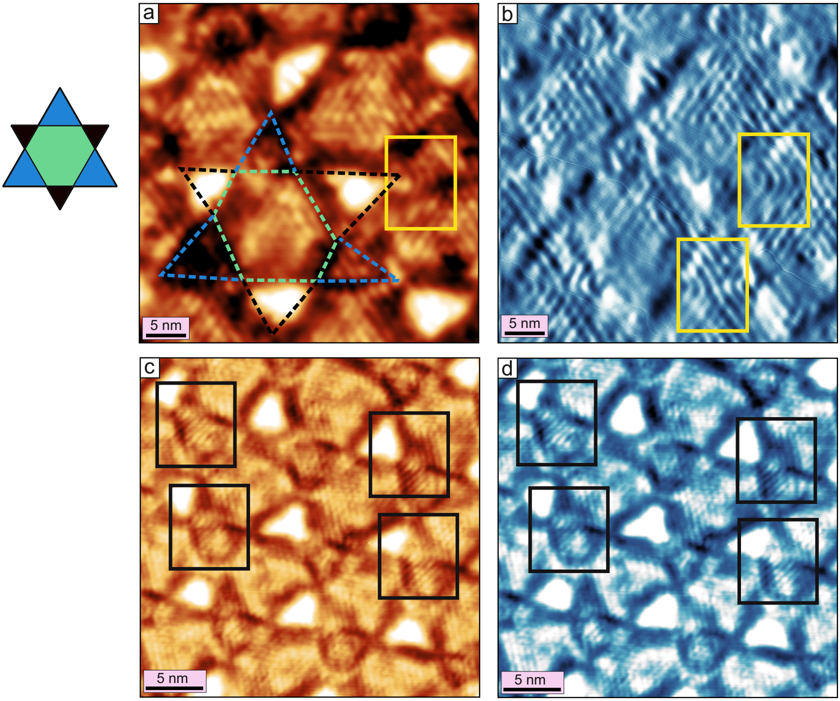

Figure 6.21: Magnetic contrast in the dislocation lines for the Kagome-like reconstructed QL. Constant-current STM topography and *current* images of two sample areas **(a,b)** and **(c,d)** respectively, with magnetic contrast. The rectangles drawn indicate the transition areas between the truncated hexagon and the different triangles. The magnetic patterns can be seen in these areas which might suggest that the reconstruction is not in the QL but in the layer below. (Measurement parameters: a: $U = +10\,\mathrm{mV}$, $I = 7\,\mathrm{nA}$; b: $U = +10\,\mathrm{mV}$, $I = 2\,\mathrm{nA}$; all: $T = 8\,\mathrm{K}$).

6.2.4 Bias dependence of the structure and magnetism

In Fig. 6.22, a strong bias dependence of the structure and magnetism is shown in the corresponding dI/dU and constant-current topographic images in the triangular reconstruction pattern. An interesting observation is the simultaneous presence and absence of the magnetic and structural junctions in the topography and dI/dU channels for the same bias voltage. The SP-STM image at 500 mV in Fig. 6.22(a) shows the magnetic domain wall junctions to be confined in every magnetic triangle. However it appears from the topography image at 1V shown in Fig. 6.22(c) that the magnetic domain wall junctions connect to each other.

In Fig. 6.23, I try to compare the two kinds of reconstruction phases of the QL imaged at the same bias voltage of 1V. Figs. 6.23(a) and (b) show the Kagome-like and the triangular types of reconstruction, respectively. Additionally, one can see that the magnetic domain wall junctions in the Kagome-like pattern are present as small and large junctions in the blue triangles and truncated hexagons, respectively. Whereas in the triangular reconstruction, the magnetic domain wall junctions have the same size on average in every triangle.

The magnetic domain wall junctions possess a handedness which has been denoted by coloured small circles in Fig. 6.23. The blue and green circles correspond to anti-clockwise and clockwise handedness of the junctions, respectively.

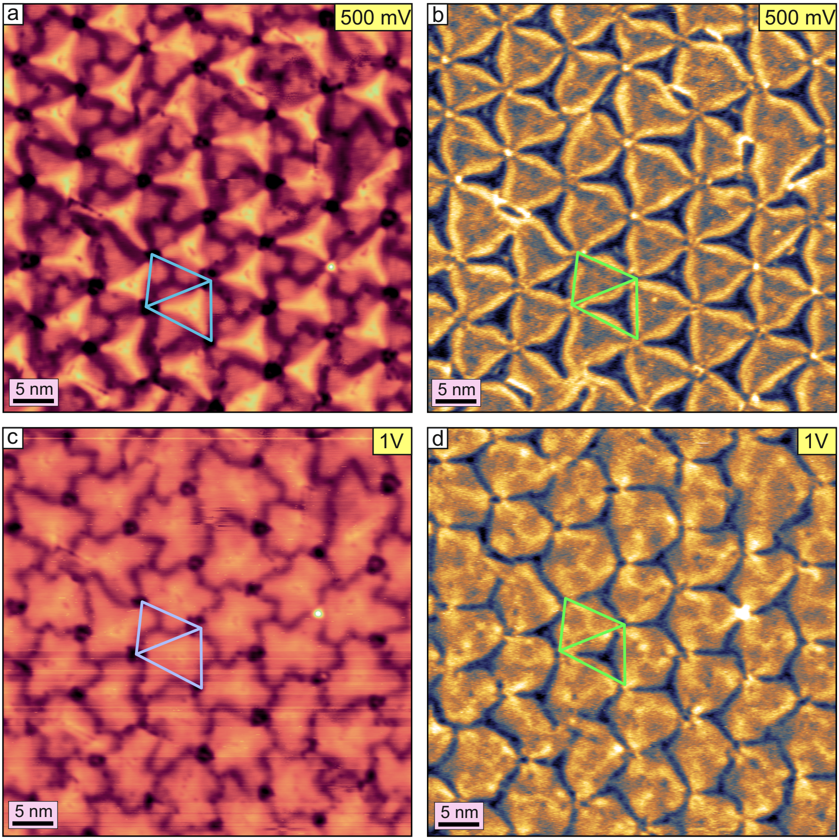

Figure 6.22: Bias dependence of the QL triangular reconstructed phase. Constant-current SP-STM topography and dI/dU images of the triangular reconstructed QL shown at 500 mV (**(a,b)**) and 1V (**(c,d)**). The unit cell is outlined in blue and green colours for the topography and dI/dU images, respectively. (Measurement parameters: a,b: $U = +500\,\mathrm{mV}$, $I = 1\,\mathrm{nA}$; c,d: $U = +1\,\mathrm{V}$, $I = 1\,\mathrm{nA}$; all: $T = 4\,\mathrm{K}$).

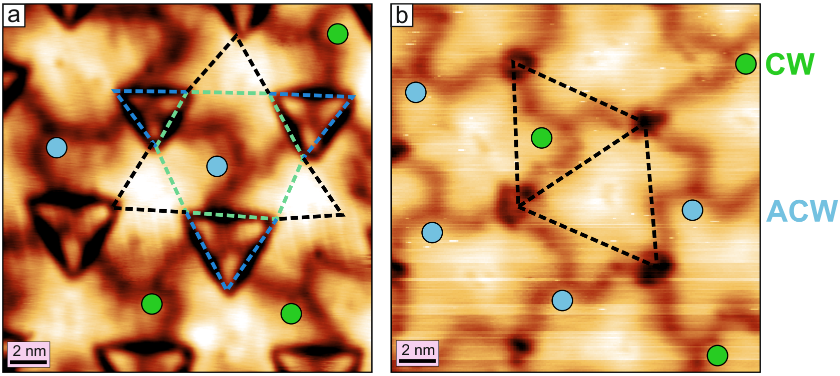

Figure 6.23: Bias dependence of the Kagome-like and triangular reconstructed phases - both measured at 1V (a,b) Constant-current SP-STM topography images measured at 1V for the Kagome - like and triangular reconstructed QL. Chiral magnetic domain wall junctions have been marked with blue and green circles corresponding to anti-clockwise and clock-wise handedness. (Measurement parameters: a: $U = +1\,\text{V}$, $I = 0.5\,\text{nA}$; b: $U = +1\,\text{V}$, $I = 1\,\text{nA}$; all: $T = 8\,\text{K}$).

6.2.5 Domain wall network properties

Now we revisit the domain wall patterns in the QL with the aim to understand their connectivity with respect to a domain wall network. While both the triangular and Kagome-like reconstructions exhibit chiral magnetic domain wall triple junctions, the magnetic features may not be just merely confined within individual structural units.

At a first glance, it may appear that the magnetic domain walls are locally restricted within each triangular unit of the triangular reconstruction, and within each truncated hexagon or medium-sized triangle in the Kagome-like phase. This interpretation suggests a scenario where each structural motif independently hosts a self-contained magnetic junction.

However, the SP-STM images presented in Fig. 6.24 offer a contrasting perspective. The magnetic domain wall junctions are not isolated but appear to be continuously connected across the surface, forming an extended domain wall network. Such connectivity may have profound implications for the topological and chiral nature of the system and opens up avenues for interpreting the magnetic structure in terms of extended magnetic domain wall networks rather than isolated magnetic domain wall junctions.

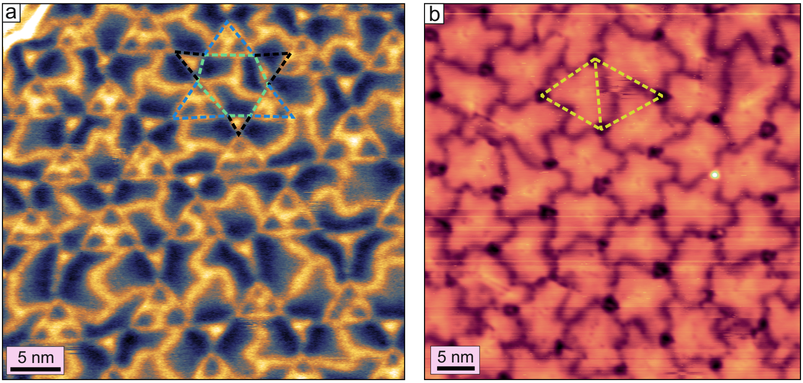

Figure 6.24: Revisiting the magnetic domain walls in the QL with a domain wall network perspective. (a,b) Magnetic domain wall network in the Kagome - like and triangular reconstruction seen in the dI/dU and topography STM images. In (a), the magnetic domain wall junctions in the truncated hexagons and the A type triangles might be connected and hence constitute a large network. In (b), the magnetic domain wall junctions in the different magnetic triangles, if connected, could also constitute a large network. (Measurement parameters: a: $U = 2\,\mathrm{V}$, $I = 1\,\mathrm{nA}$, $T = 8\,\mathrm{K}$; b: $U = +1\,\mathrm{V}$, $I = 1\,\mathrm{nA}$, $T = 4\,\mathrm{K}$).

Coming to the last aspect of the domain wall junctions in the QL, we will discuss briefly about hexa-junctions in this system. In Fig. 6.25(a), the marked elliptical areas are spots where six domain walls meet. As the structural domain walls should in principle have an overlaid magnetic domain wall, these hexa-junctions can be considered as the merging point meeting of six magnetic domain walls and three structural domain walls at the same time.

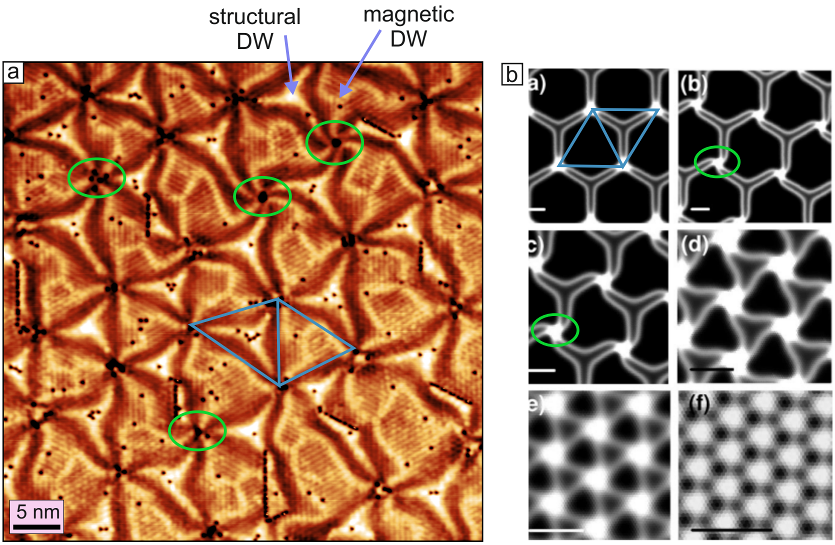

Figure 6.25: Hexa-junctions in the QL. (a) Constant-current STM topography image showing a large area of the triangular reconstructed QL. Green ellipses highlight hexa-junctions, where six domain walls (3 structural and 3 magnetic) meet. The spiraling of the hexa-junction might arise from the structural domain walls only. This spiraling nature of the hexa-junctions corresponds to the simulated STM images shown in **(b)**. The spiraling areas in the simulated STM images are encircled in green. This was calculated for Pt(111), where the spiraling nature is attributed to a slight misalignment of the top layer w.r.t. the bottom layer to release strain. Panel (b) is reprinted with permission from [7], copyright 2003 of the American Physical Society. The unit cell of (a) is drawn in (b) to identify the hexa-junction positions. (Measurement parameters of (a): $U = 10\,\mathrm{V}$, $I = 1\,\mathrm{nA}$, $T = 4\,\mathrm{K}$).

Additionally, a slight rotation of the domain walls at the hexa-junctions is visible leading to a spiral like appearance. This can be understood from the STM simulations shown in parts (b,c) of Fig. 6.25(b) from the work of Raghani et al. for Pt(111) [13]. The bright spots in the STM simulations are on-top positions and these positions rotate a little to release stress. The rotation in (b) is of 0.14° which causes a spiral like appearance. They are referred to as bright 'rotors' in their work. Hence, with this knowledge from the literature, it can be said that the QL hexa-junctions show the same behaviour to release stress in the surface. It is important to note that in the simulations shown in Fig. 6.25(b), the bright spots at the hexa-junctions are proposed to correspond to on-top atomic positions. However, this feature is not observed in the QL reconstruction shown in Fig. 6.25(a), where instead a dark contrast accompanied by apparent defects is visible at the hexa-junctions. This contrast difference can be attributed to local stress relaxation at these junctions, which may lead to the formation of atomic defects.

Interestingly, the spiraling behavior of the QL is absent for the hexa-junctions observed in the DL and TL of Mn/Ir(111). This absence may indicate a progressive increase in epitaxial strain with layer thickness, suggesting that the QL experiences a significantly higher degree of strain compared to the DL and TL.

Such spiraling behaviour has also been observed in twisted bilayer graphene as a stress releasing mechanism [19]. A similar pattern has also been simulated for the system of Cu(111)/Ni(111) [20].

6.2.6 Switching chiral magnetic junctions

We now turn to a particularly intriguing aspect of the QL. As demonstrated in the preceding sections, the QL hosts chiral triple domain wall junctions. From an application perspective, the ability to experimentally manipulate or switch the chirality of these junctions would be highly desirable. However, before pursuing such manipulation, it is essential to understand both the feasibility of chirality switching and the possible underlying mechanisms.

It is important to note that not all chiral entities can be switched experimentally. In the case of the QL, the junctions do not exhibit a global chirality preference; that is, there is no dominant chirality observed across the sample. The chirality appears random, suggesting that the clockwise (CW) and anticlockwise (ACW) configurations are energetically degenerate. It was shown in Fig.6.12, that the magnetic and structural domain walls can exist in both kinds of handedness. This degeneracy arises due to the magnetic domain walls being able to satisfy the requirement of the 120° type. Hence, there seems to be no reason for one type of handedness to exist.

To investigate the switching mechanism, voltage pulses were applied via the STM tip in an attempt to induce chirality reversal. Pulses were delivered both directly at the center of the junctions and by moving the STM tip around the junctions at high bias voltages. In addition to these methods, normal scanning at elevated bias voltages was also tested. Among these approaches, the most successful method was high bias scanning during normal imaging, which occasionally resulted in observable changes, which are described in detail below.

All images presented in this section are from the dI/dU channel, as magnetic domain walls are less distinctly visible in the topography data. The domain wall contrast in the dI/dU map can probably be attributed to the non-collinear magneto-resistance. In each figure, the junction of interest is marked with a green circle, and the images are shown in sequential scanning order to highlight the observed modifications over time.

In Fig. 6.26 (a), the SP-STM map acquired at a sample bias of 200 mV exhibits relatively weak magnetic domain wall contrast, making it somewhat challenging to clearly identify the domain walls. Nevertheless, their presence can still be inferred based on their characteristic shape. The chiral junction of interest, highlighted with a green circle, displays a configuration that closely resembles the schematic illustration shown above panel (a).

Panels (b) and (c) reveal a degree of fuzziness around the junction, which likely indicates local perturbations or interactions with the STM tip, suggesting that the domain wall junction may be undergoing manipulation. In panel (d), a clear reversal in chirality is observed: the junction now exhibits a right-handed (clockwise) configuration, in contrast to the left-handed (anticlockwise) arrangement seen in panel (a).

This instance represents the only observed event in which a chirality switch was successfully induced. In the next example, shown in Fig. 6.27, we examine a case where only partial modifications to the junction were observed, without a full reversal in handedness.

In the second example shown in Fig. 6.27, the sample area was scanned at 2.5 V and 3 V seen in (a) and (b) respectively. One can see that although the junction preserves its handedness, it get more symmetric in (d), i.e. almost equal length arms of the junction as opposed to unequal arm lengths in (a).

To understand whether the switching of the chiral junction influences the surrounding domains or domain walls, we can refer to the sketch in Fig. 6.28. Fig. 6.28(b) shows the switched state of the chiral magnetic triple domain wall junction in panel (a). Although the chirality has switched, there is no change in the orientation of the rotational do-

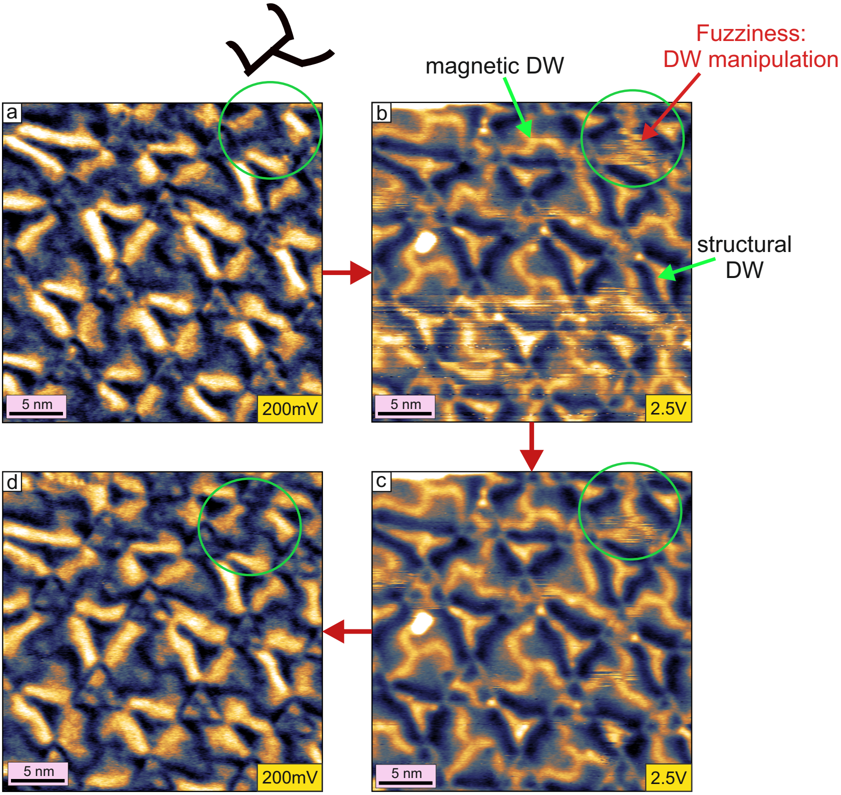

Figure 6.26: Switching of a chiral magnetic domain wall junction. (a-d) A measurement series showing spin-resolved dI/dU images, where a magnetic triple domain wall junction encircled in green in (a) has been observed to flip its handedness in (d). A scanning bias of 2.5 V was applied to the sample area in order to energetically perturb the domain wall junctions and promote their reconfiguration. (Measurement parameters: a,d: $U = +200\,\mathrm{mV}$; b,c: $U = +2.5\,\mathrm{V}$; all: $I = 1\,\mathrm{nA}$, $T = 4\,\mathrm{K}$).

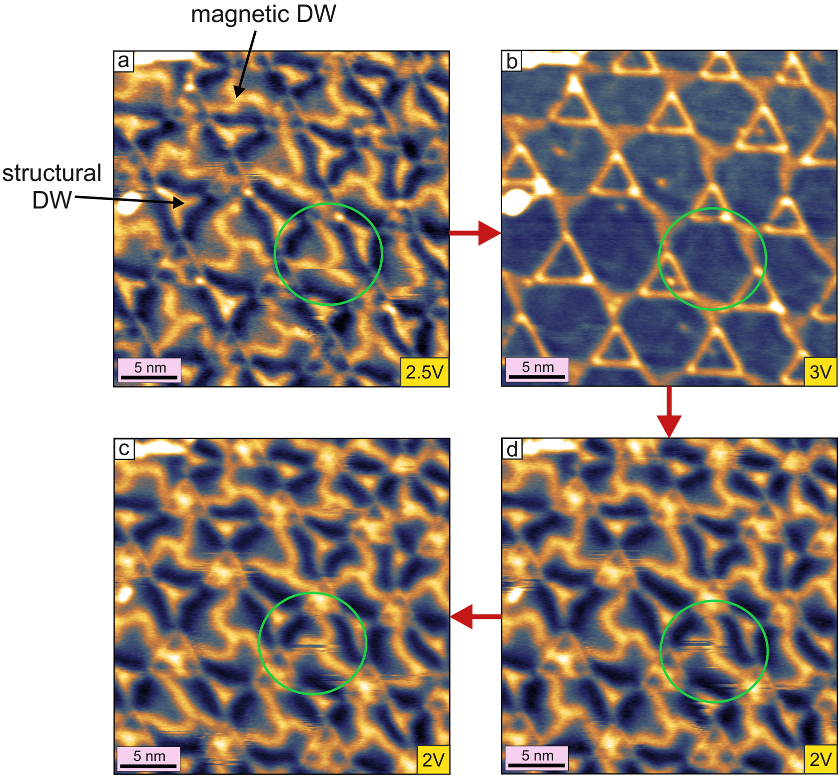

Figure 6.27: Partial perturbation of a chiral magnetic domain wall junction. (a-d) A measurement series showing spin-resolved dI/dU images, where a magnetic triple domain wall junction encircled in green in (a) has been partially reconfigured in (d). The sample area was scanned at 2, 2.5, and 2V in an attempt to energetically perturb the domain wall junctions and promote their reconfiguration. (Measurement parameters: a: $U = +2.5\,\mathrm{V}$; b: $U = +3\,\mathrm{V}$; c,d: $U = +2\,\mathrm{V}$; all: $I = 1\,\mathrm{nA}$, $T = 4\,\mathrm{K}$).

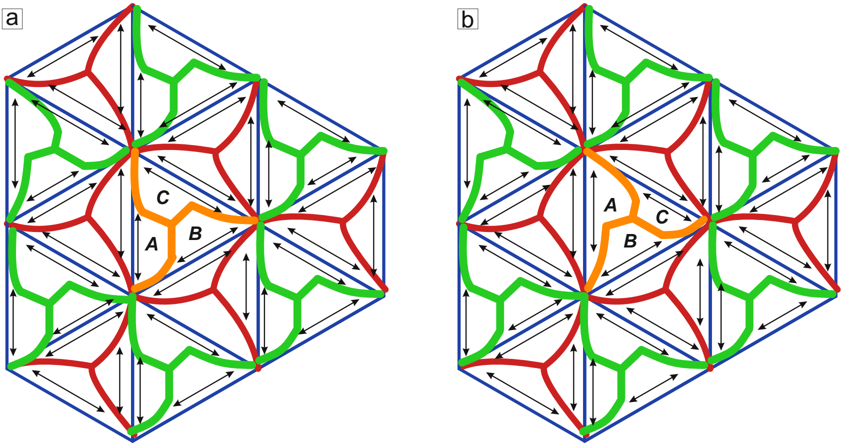

Figure 6.28: Schematic of the switching of a magnetic domain wall junction. **(a)** and **(b)** show sketches of how the triple domain wall junction (in orange), has been switched from clockwise to anti-clockwise handedness, respectively. The three rotational domains have been marked by double headed arrows and labelled as A, B and C. It can be seen in (b), that although the handedness has been inverted compared to (a), the rotational domains remain the same. This shows that switching the handedness of a single or multiple junctions does not impact the local or surrounding areas with respect to the orientation of the rotational domains.

mains - *A*, *B*, or *C* surrounding the orange domain wall junction. Hence, the sketch shows us that switching a single or multiple junction's handedness will not affect the domains and the domain wall network.

Besides the data shown in the above two examples, there is no other scanning series where a considerable change in the junction has been observed. Samples of the QL that have been tried for switching events have been measured at 4 K, 8 K and 80 K. Surprisingly, the only switching event that was observed (see Fig. 6.26) was measured at 4 K. At higher temperatures like 8 K and 80 K, one would expect the switching to happen more easily due to higher thermal energy, but this was not the case.

The examples presented above indicate that temperature alone may not be the primary factor governing the switching of chirality at domain wall junctions. This conclusion is supported by the fact that switching was observed only at 4 K, while no such events occurred at higher temperatures of 10 K and 80 K-an outcome that is counterintuitive if temperature were the dominant parameter. Instead, the pinning potential of domain walls due to surface or sub-surface defects might play a more decisive role for inhibiting the switching.

Another plausible explanation is that the inability to switch some junctions stems from a strong magnetic or structural coupling to the adjacent structural Y-type feature, effectively anchoring the magnetic configuration and preventing chirality reversal.

Obviously, open questions remain which are currently the subject of ongoing investigation. Future studies, potentially involving measurements at temperatures above 80 K using a variable-temperature STM, may provide further insight and possibly enable more frequent observations of chirality switching events.

6.3 Summary

In the QL, a transition from a stripe-like reconstruction pattern to a network-like stress relief configuration was observed upon increasing the growth temperature to approximately 250 °C. This network reconstruction comprises two distinct types: Kagome-like and triangular patterns-both arising from differences in adatom coverage. These reconstructions exhibit a strong dependence on the applied bias voltage during SP-STM imaging, underscoring the influence of local electronic structure.

Magnetically, the QL appears to share a similar ground state with the TL, likely corresponding to either a distorted 3Q state or a $3Q^2$ configuration. The current experimental data does not allow for an unambiguous distinction between these possibilities. Chiral magnetic triple domain wall junctions, with a triskelion-like geometry reminiscent of the Isle of Man motif, were observed in both Kagome-like and triangular reconstruction areas. One such junction was observed to undergo full switching, while several others exhibited partial switching. These features suggest that the QL supports a robust, possibly topological, magnetic state.

The persistence of uniform domain wall contrast throughout triple junctions implies a consistent 120° domain wall type, indicating a level of magnetic order that accommodates both structural complexity and rotational symmetry. In contrast to the DL–TL interface, where a magnetic domain wall reliably appears at the buried step edge, the absence of such a feature at the TL–QL interface suggests magnetic continuity between these layers-possibly facilitated by strain relaxation.

The QL thus provides a compelling example of magnetism emerging in a strain-engineered environment, where local structural modifications strongly influence the stability and texture of non-collinear magnetic states. The coexistence of complex reconstructions and topologically rich domain wall networks highlights the potential of this system to host emergent orbital magnetism. Future experiments should focus on resolving the magnetic ground state through SP-STM under vector magnetic fields, quantifying the topological orbital moment in the QL, and probing the detailed spin structure at the triple and hexa-junctions.

Bibliography

1. Brune, H., Röder, H., Boragno, C. & Kern, K. Strain relief at hexagonal-close-packed interfaces. *Physical Review B* **49,** 2997 (1994).
2. Jankowski, M., Wormeester, H., Zandvliet, H. J. & Poelsema, B. Temperature-dependent formation and evolution of the interfacial dislocation network of Ag/Pt (111). *Physical Review B* **89,** 235402 (2014).
3. Röder, H. *Microscopic processes in heteroepitaxial growth: nucleation, growth and alloying of silver on the (111) surface of platinium* tech. rep. (EPFL, 1994).
4. Aıt-Mansour, K. *et al.* Interface-confined mixing and buried partial dislocations for Ag bilayer on Pt (111). *Physical Review B—Condensed Matter and Materials Physics* **86,** 085404 (2012).
5. Meschke, V., Gorai, P., Stevanovic, V. & Toberer, E. S. Search and structural featurization of magnetically frustrated kagome lattices. *Chemistry of Materials* **33,** 4373–4381 (2021).
6. Wang, Q., Lei, H., Qi, Y. & Felser, C. Topological quantum materials with kagome lattice. *Accounts of Materials Research* **5,** 786–796 (2024).
7. Pushpa, R., Rodríguez-Laguna, J. & Santalla, S. N. Reconstruction of the second layer of Ag on Pt (111): Extended Frenkel-Kontorova model. *Physical Review B—Condensed Matter and Materials Physics* **79,** 085409 (2009).
8. Rodríguez-Sota, A. *et al.* Phase Coexistence of Mn Trimer Clusters and Antiferromagnetic Mn Islands on Ir (111). *ACS nano* **18,** 3699–3706 (2024).
9. Saxena, V. *et al.* Strain-driven domain wall network with chiral junctions in an antiferromagnet. *arXiv preprint arXiv:2408.12580* (2024).

10. Hamilton, J. C. & Foiles, S. M. Misfit Dislocation Structure for Close-Packed Metal-Metal Interfaces. *Phys. Rev. Lett.* **75,** 882–885 (5 1995).

11. Li, P. & Ding, F. Origin of the herringbone reconstruction of Au (111) surface at the atomic scale. *Science advances* **8,** eabq2900 (2022).

12. Bott, M., Hohage, M., Michely, T. & Comsa, G. Pt(111) reconstruction induced by enhanced Pt gas-phase chemical potential. *Phys. Rev. Lett.* **70,** 1489–1492 (10 1993).

13. Pushpa, R. & Narasimhan, S. Reconstruction of Pt(111) and domain patterns on close-packed metal surfaces. *Phys. Rev. B* **67,** 205418 (20 2003).

14. Finco, A., Hsu, P.-J., Kubetzka, A., von Bergmann, K. & Wiesendanger, R. Tailoring noncollinear magnetism by misfit dislocation lines. *Phys. Rev. B* **94,** 214402 (21 2016).

15. Von Bergmann, K. *et al.* Complex magnetism of the Fe monolayer on Ir (111). *New Journal of Physics* **9,** 396 (2007).

16. Barth, J., Behm, R. & Ertl, G. Mesoscopic structural transformations of the Au(111) surface induced by alkali metal adsorption. *Surface Science* **302,** L319–L324 (1994).

17. Haldar, S., Meyer, S., Kubetzka, A. & Heinze, S. Distorted 3 Q state driven by topological-chiral magnetic interactions. *Physical Review B* **104,** L180404 (2021).

18. Aıt-Mansour, K., Ruffieux, P., Gröning, P., Fasel, R. & Gröning, O. Positional and orientational templating of C60 molecules on the Ag/Pt (111) strain-relief pattern. *The Journal of Physical Chemistry C* **113,** 5292–5299 (2009).

19. Mesple, F. *et al.* Giant atomic swirl in graphene bilayers with biaxial heterostrain. *Advanced Materials* **35,** 2306312 (2023).

20. Shao, S., Wang, J., Misra, A. & Hoagland, R. G. Spiral patterns of dislocations at nodes in (111) semi-coherent FCC interfaces. *Scientific reports* **3,** 2448 (2013).

7 Summary and Outlook

Abstract

Here, I will be revisiting some common aspects of magnetism and growth that were seen across the DL, TL and QL.

7.1 Summary

7.1.1 Growth

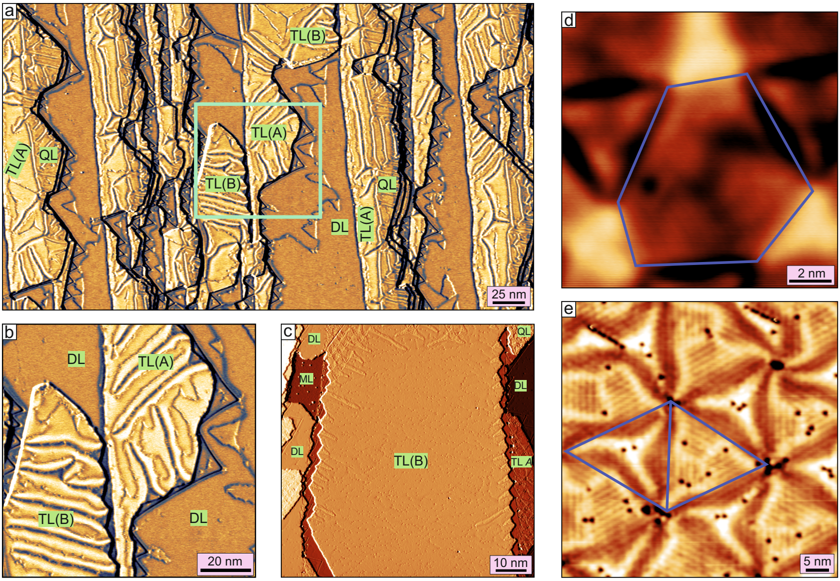

Figure 7.1: An overview of the growth of Mn multilayers on Ir(111). Pseudomorphic areas of the DL can be seen in **(a)**. The different types of TL stackings can be seen in **(a,b,c)**. **(d,e)** show the Kagome like and triangular reconstructions in the QL. (Measurement parameters: a: $U = -100\,\mathrm{mV}$, $I = 1\,\mathrm{nA}$, $T = 4\,\mathrm{K}$; b: $U = -100\,\mathrm{mV}$, $I = 1\,\mathrm{nA}$, $T = 4\,\mathrm{K}$; c: $U = +100\,\mathrm{mV}$, $I = 1\,\mathrm{nA}$, $T = 4\,\mathrm{K}$; d: $U = +500\,\mathrm{mV}$, $I = 2\,\mathrm{nA}$, $T = 8\,\mathrm{K}$; e: $U = +10\,\mathrm{mV}$, $I = 4\,\mathrm{nA}$, $T = 4\,\mathrm{K}$).

Fig. 7.1 shows the different growth types of the DL, TL and QL. An overview image in (a) shows the different layers that were grown at near room temperature. The DL is mostly pseudomorphic with the exception of a few reconstruction lines, the zig-zag dislocation lines, and the hydrogen impurity islands. The TL and QL have the striped reconstruction phase - also shown in a zoom-in in (b). When grown at higher temperatures, the TL gets mostly pseudomorphic as shown in panel (c). The QL undergoes a change in the reconstruction pattern from stripy to a triangular like network at higher growth temperatures and additionally hosts two kinds of reconstruction patterns, which depend on the coverage/surface adatom density as discussed before in Section 6.1.2. The Kagome-like and the triangular reconstruction patterns can be seen in (d-e) respectively.

Hence, in summary we observe different kinds of reconstructions on the TL and QL based on temperature and adatom surface density. The findings are in good agreement with previous independent calculations done for Pt(111) motivated by the first imaging of such reconstruction patters in a bilayer of Ag on Pt(111). The strong interaction of the magnetism with the growth of different layers of the same material is fascinating and complements the studies of Pt(111), Au(111) and Cu/Ru(0001) sample systems for the non-magnetic case.

7.1.1.1 Reconstruction lines

The star-shaped reconstruction line appears as a periodic feature in the QL and occurs frequently in the TL. As shown in the respective chapters, the orientation of the rotational domains of the 3Q state has been analyzed in the vicinity of these features. While the correlation is clearly established in the case of the QL, the situation is less straightforward for the TL due to the limited availability of experimental SP-STM data. However, in Fig. 7.2, a comparison between the TL and QL demonstrates that the star-shaped features appear structurally similar and exhibit a comparable preference for the orientation of the 3Q rotational domains. This correspondence is further illustrated schematically in panel (c).

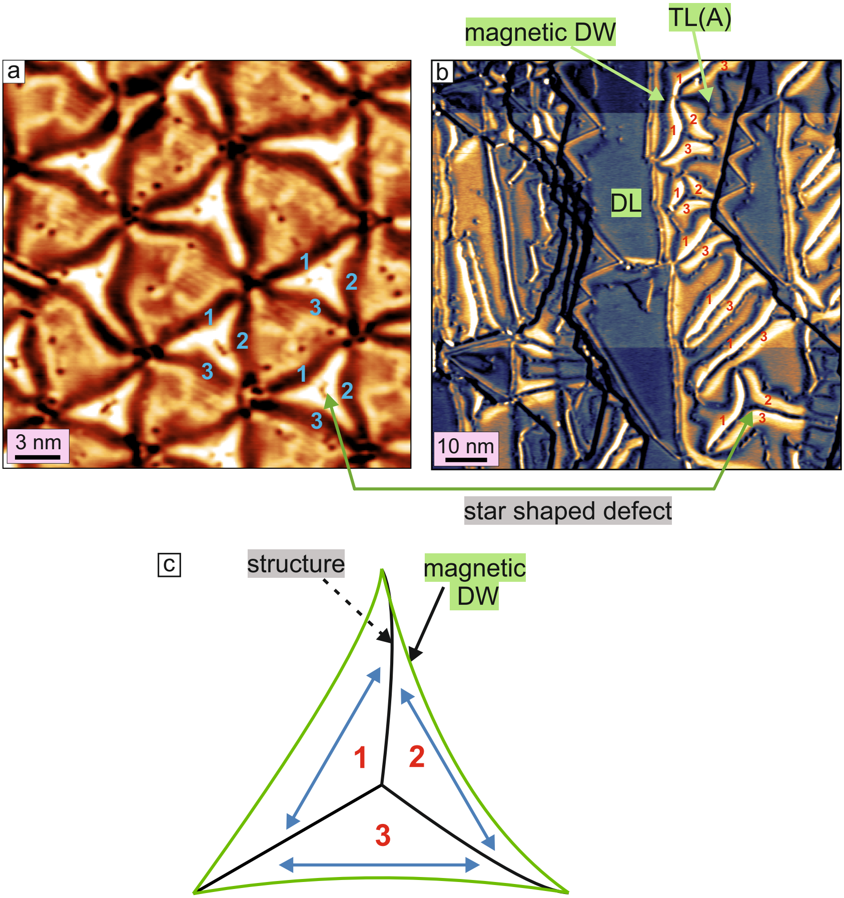

Figure 7.2: A comparison of the orientational domain preference of the reconstruction in the TL and QL. (a) A SP-STM topography image showing a region of the QL with the triangular reconstruction and the different orientational domains marked from 1-3. A similar preference of the orientational domains can be seen for the star shaped reconstruction in the TL where the orientational domains have been marked in red from 1-3. **(c)** A sketch showing the preference of the orientational domain by each arm of the star shaped reconstruction feature.(Measurement parameters: (a): $U = 10\,\text{mV}$, $I = 1\,\text{nA}$, (b): $U = 50\,\text{mV}$, $I = 1\,\text{nA}$; (all): $T = 4\,\text{K}$)..

7.1.2 Domains and domain walls

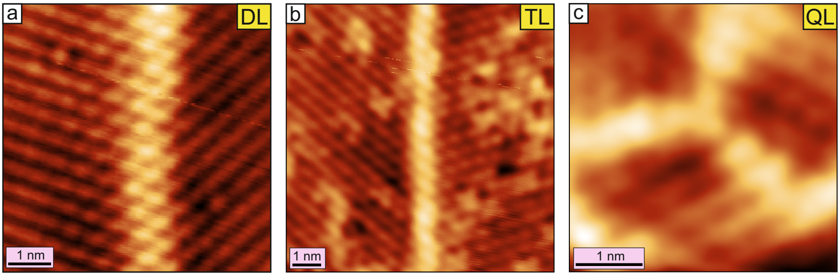

Figure 7.3: An overview of domain walls across all the layers of Mn/Ir(111). The magnetic domain walls are shown with magnetic contrast for the DL (**(a)**), TL (**(b)**) and QL (**(c)**) of Mn/Ir(111). (Measurement parameters: a: $U = +10\,\text{mV}$, $I = 3\,\text{nA}$, $T = 4\,\text{K}$; b: $U = 10\,\text{mV}$, $I = 2\,\text{nA}$, $T = 8\,\text{K}$; c: $U = +10\,\text{mV}$, $I = 4\,\text{nA}$, $T = 4\,\text{K}$).

With respect to the magnetic ground state, the DL hosts the row-wise antiferromagnetic state, while the TL and the QL host the distorted $3Q^2$ state that has a dominant stripy character with some areas showcasing a hexagonal magnetic pattern.

Fig. 7.4 shows the characteristic domain walls for the DL, TL and QL. As discussed in the respective chapters, the DL domain wall is a coplanar 2Q state domain wall which was also observed in the fcc-stacked Mn/Re(0001). The TL has distorted $3Q_2$ rotational domains which are most likely separated by $3Q^3$ domain walls as seen in the simulation for such a case (see Fig. 5.11), but in the monolayer limit. The QL has the unique Isle of Man reminiscent triskelion shaped domain wall junction. The domain wall's magnetic structure has not been determined so far, but as the rotational domains around it are very similar to the TL case, a possible candidate could be the $3Q^3$ state.

Hence, in summary, the TL and QL have topologically non-trivial domain walls and magnetic domains, whereas the DL has the collinear

RW-AFM state with coplanar non-collinear magnetic domain walls and localized non-coplanar 3Q state hosting junctions.

7.1.3 Domain wall network

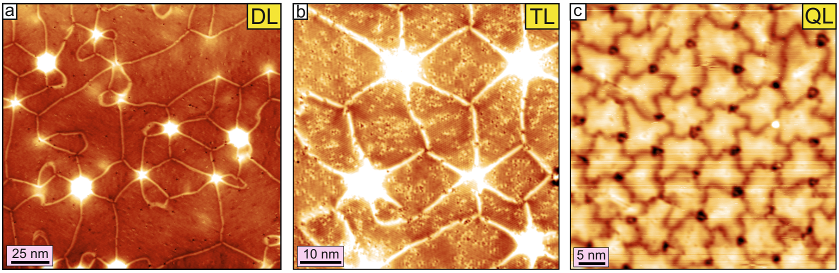

Figure 7.4: An overview of the DW network across all the layers of Mn/Ir(111). The magnetic domain wall network shown for the DL (**(a)**), TL (**(b)**), and QL (**(c)**) of Mn/Ir(111). (Measurement parameters: a: $U = +10\,\mathrm{mV}$, $I = 5\,\mathrm{nA}$; b: $U = 10\,\mathrm{mV}$, $I = 1\,\mathrm{nA}$; c: $U = +1\,\mathrm{V}$, $I = 1\,\mathrm{nA}$; all: $T = 4\,\mathrm{K}$).

Fig. 7.4 presents an overview of the domain wall network in the DL, TL and QL. The difference here is that the DW network in the QL is not induced by the Argon bubbles, but rather by the strong structural reconstruction. The network connectivity in the DL and TL is the same i.e., it includes the Y, Y*, T, T* and the hexa-junctions, whereas in the QL, every junction appears to be the same - triskelion shaped. Additionally, it is not clear yet if the domain wall network in the QL can really be called a network or if there are isolated junctions confined in every triangle.

Nevertheless, being able to demonstrate the generation of large domain wall networks in different atomic layers of Mn/Ir(111) is an advancement in the field of antiferromagnetism.

7.2 Outlook

7.2.1 Growth

Based on the work reported in [1] where the diffusion of adatoms is shown to be influenced by the spatial anisotropy of the magnetic ground state, it would be interesting to observe the diffusion of adatoms and the formation of islands or chains across different rotational domains. As the DL system exhibits a lateral shift differently for the different rotational domains, a strong influence could be expected for the growth and diffusion of adatoms.

For the TL of Mn/Ir(111), a clear transition from the striped reconstruction to the network type stress relief pattern was not observed as opposed to the QL. Only in one instance did the TL show the network type stress relief pattern in small patches (Fig. 5.4). Hence, it would be interesting to investigate the transition temperature for the TL system to convert into the network type stress relief pattern.

7.2.2 Transport experiments

The domain configurations observed in the different layers of Mn/Ir(111), such as the magnetic triple and hexa-junctions, closed loops and the domain wall networks, are attractive spin textures to be studied at least computationally.

The triple and hexa-junctions in the DL host the 3Q state which is topologically non-trivial. Hence, if an independent Y- or T-junction is subjected to a lateral charge current, potential Hall effects can arise due to the presence of the 3Q state in the junction as shown in Fig. 7.5.

However, the interaction of the conduction electrons with an indepen-

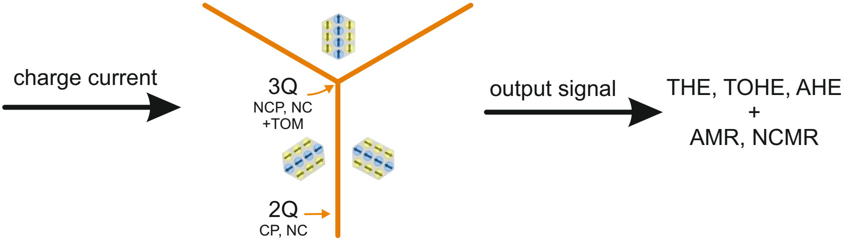

Figure 7.5: Schematic of a Y junction subjected to lateral charge currents. A Y junction is subjected to a charge current and the expected Hall signals along with the expected types of magneto-resistance are shown. The junction has the non-coplanar (NC) 3Q state with an associated topological orbital moment (TOM) - which can give rise to the Hall effects. The domain walls have the non-collinear (NC) and coplanar (CP) 2Q state which can give rise to some magneto-resistance signals in transport experiments.

dent Y- or T- junction will be complicated due to the presence of coplanar (domain wall) and non-coplanar (junctions) entities, both additionally being non-collinear. The domains and domain walls should likely exhibit the anisotropic magneto-resistance (AMR) and the non-collinear magneto-resistance (NCMR). The 3Q state in the junction is likely to exhibit signatures of the anomalous and topological Hall effects owing to the non-coplanarity and the presence of a topological orbital moment [2]. Moreover, the THE signal might also include contributions from the topological orbital Hall effect which can originate via the accumulation of an orbital angular momentum due to the possible cycloidal trajectory of the conduction electrons when interacting with the 3Q state, as proposed for skyrmions in [3].

Additionally, the magnetic domain walls in the TL and QL will be interesting to study as they most probably are topologically non-trivial.

7.2.3 Topological orbital moment

The topological orbital moment (TOM) has not been experimentally detected, but has been proposed to be probed via the technique of X-ray magnetic circular dichroism (XMCD) leveraging the interaction of circularly polarized light with orbital currents [4]. By (SP)-STM, it might be possible to observe the contribution of a sizable TOM (meV) in the local density of states, via scanning tunneling spectroscopy (STS) that can be verified by DFT band structure calculations. The value of the TOM reported for the Mn DL on Ir(111) is in the μeV range and hence could be difficult to probe via STS.

7.2.4 Domain wall network

A very peculiar application of the antiferromagnetic domain wall network could be its use as a potential reservoir for reservoir computing. It has been reported in the theoretical work by D. Pinna et al. [5], that random skyrmions pinned artificially qualify as a potential reservoir for reservoir computing. The domain wall network realized in the DL and TL has the T-junctions pinned by the Argon bubbles. Moreover, the spin textures of the domain walls and junctions are likely to exhibit a non-linear magneto-resistance response to an applied input voltage. Materials or spin textures that provide non-linear responses to applied external stimuli such as voltage, magnetic field, or temperature are attractive candidates for neuromorphic and reservoir computing. In addition, the antiferromagnetic nature of the domain walls and junctions provides a platform for computing applications in the THz range compared to ferromagnetic skyrmions reported in [5].

7.3 Afterword

Overall, the different layers of Mn/Ir(111) prove to be a rich platform offering insights into complex growth, interplay of strain and magnetism, antiferromagnetic and frustrated spin textures, topology, orbital moments and higher-order interactions. The use of localized strain through the entrapment of Argon bubbles to generate domain wall networks most likely will open doors to realize and study the domain wall dynamics in other antiferromagnetic materials close to applications. Fundamentally, this system serves as a platform to be explored further for improving the knowledge in higher-order interactions and orbital moments arising from topology.

Bibliography

1. Zahner, F. *et al.* Kicking Co and Rh atoms on a row-wise antiferromagnet. *arXiv preprint arXiv:2405.20472* (2024).
2. Takagi, H. *et al.* Spontaneous topological Hall effect induced by non-coplanar antiferromagnetic order in intercalated van der Waals materials. *Nature Physics* **19,** 961–968 (2023).
3. Göbel, B., Schimpf, L. & Mertig, I. Topological orbital Hall effect caused by skyrmions and antiferromagnetic skyrmions. *Communications Physics* **8,** 17 (2025).
4. Dos Santos Dias, M., Bouaziz, J., Bouhassoune, M., Blügel, S. & Lounis, S. Chirality-driven orbital magnetic moments as a new probe for topological magnetic structures. *Nature Communications* **7,** 13613 (2016).
5. Pinna, D., Bourianoff, G. & Everschor-Sitte, K. Reservoir computing with random skyrmion textures. *Physical Review Applied* **14,** 054020 (2020).

8 Appendix

In this chapter, I will present additional data related to the growth, in particular for the DL and the TL systems.

8.1 Néel temperature of the DL system

Fig. 8.1 (a) shows a partially differentiated STM topography image of a sample with regions of the ML, DL, and TL, measured at room temperature (RT). The zig-zag dislocation lines are marked in panels (a) and (c), and can be seen on the DL near the buried step edge of the ML-DL transition. The TL terrace on the left exhibits reconstruction lines oriented along the $[11\bar{2}]$ direction, rotated by 120°. In Fig. 4.10, it was assumed that the ML pins part of the adjacent DL with respect to the stacking. If this assumption holds, then the observation of zig-zag dislocation lines in the current figure suggests that the Néel temperature (T_N) of at least the DL system lies above RT.

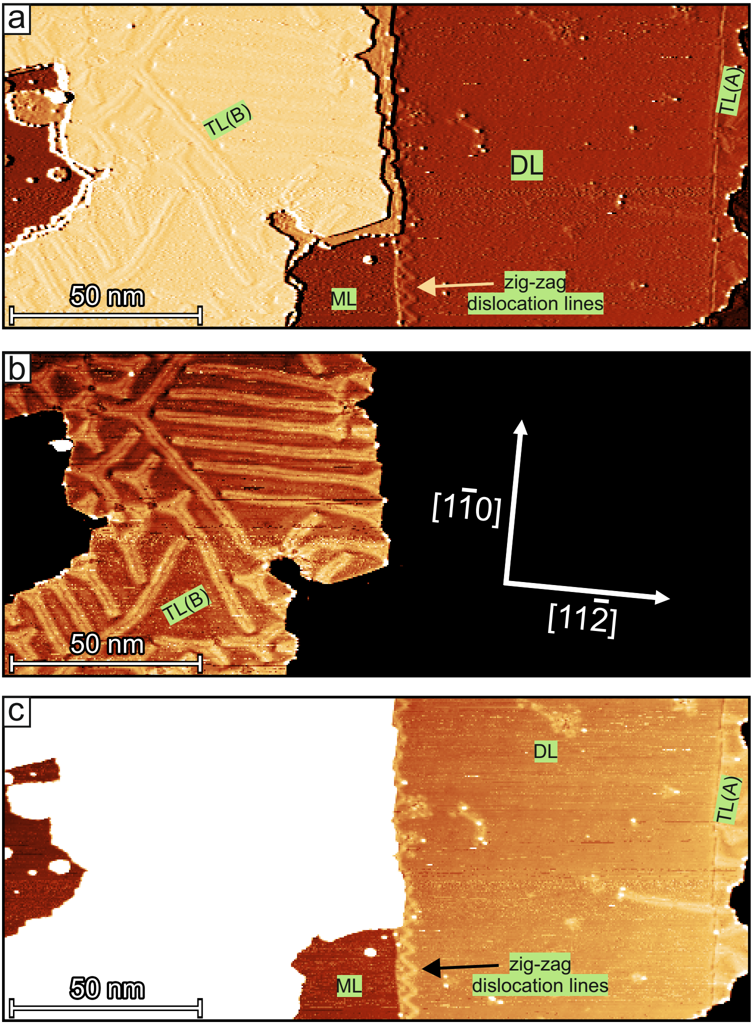

Figure 8.1: Zig-zag dislocation line in the DL observed at RT. (a) Partially differentiated STM topography image showing regions of the ML, DL, and the TL. **(b, c)** Constant-current STM topography images with adjusted height contrast to show the TL and DL regions clearly. The zig-zag dislocation lines have been marked in panels (a, c). (Measurement parameters: $U = 800\,\text{mV}$, $I = 1\,\text{nA}$, $T = 300\,\text{K}$).

8.2 Preference of the orientational domains by the reconstruction lines in the TL

Figs. 8.2(a) and (b) show a large terrace of the TL(B) in the constant-current topography and *dI/dU* channels, respectively. Long reconstruction lines are clearly visible in both panels and are consistently surrounded by magnetic domain walls. This behavior was previously discussed in the TL chapter (Fig. 5.7), where the preferential alignment of orientational domains along the reconstruction lines was addressed. In Fig. 8.2, all reconstruction lines are surrounded by magnetic domain walls, supporting the claim that each arm of a reconstruction line favors a specific orientation of the rotational domain of the $3Q$ state. Figure 8.2(c) shows a sample containing both TL(B) and TL(A) regions, with the orientational domains around the reconstruction lines labeled to highlight their preference for specific orientations. This has been exemplified in the magnified inset.

Fig. 8.3 presents partially differentiated constant-current SP-STM topography and *dI/dU* images of a TL(B) terrace grown at elevated temperature (470 K) with Argon ion implantation. Reconstruction lines are observed along the three equivalent directions separated by 120°, corresponding to the high-symmetry $[11\bar{2}]$ orientations. As in previous observations, magnetic domain walls-marked in the figure-are seen encircling the reconstruction lines, with each arm associated with a specific orientational domain. This domain selection behavior is further clarified in the following figure.

Fig. 8.4 shows a region of the TL(B), located near the sample area depicted in Fig. 8.3. A star-shaped reconstruction line is visible, featuring an additional triangular reconstruction at its center, which appears to coexist with an Argon bubble. This central reconstruction has not been investigated in detail. The focus here is on the consistent appearance of

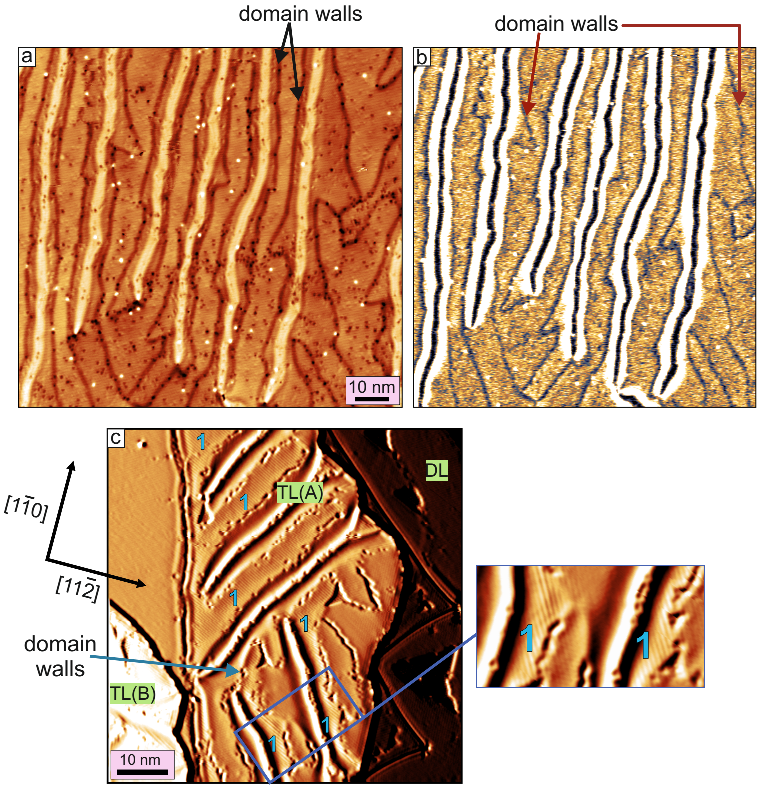

Figure 8.2: Magnetic domain walls surrounding reconstruction lines in TL(B). **(a)** Constant current STM topography and **(b)** corresponding dI/dU image showing a large terrace of TL(B) with long reconstruction lines that are consistently surrounded by magnetic domain walls. This supports the observation discussed earlier (Fig. 5.7) that each arm of the reconstruction line prefers a specific orientational domain of the 3Q state. **(c)** A wider view of the sample containing both TL(B) and TL(A) regions, with labeled orientational domains highlighting the domain selection behavior. The preference is further illustrated in the magnified inset. (Measurement parameters: (a) $U = 200\,\text{mV}$, $I = 1\,\text{nA}$, $T = 10\,\text{K}$; (c) $U = 30\,\text{mV}$, $I = 1\,\text{nA}$, $T = 4\,\text{K}$).

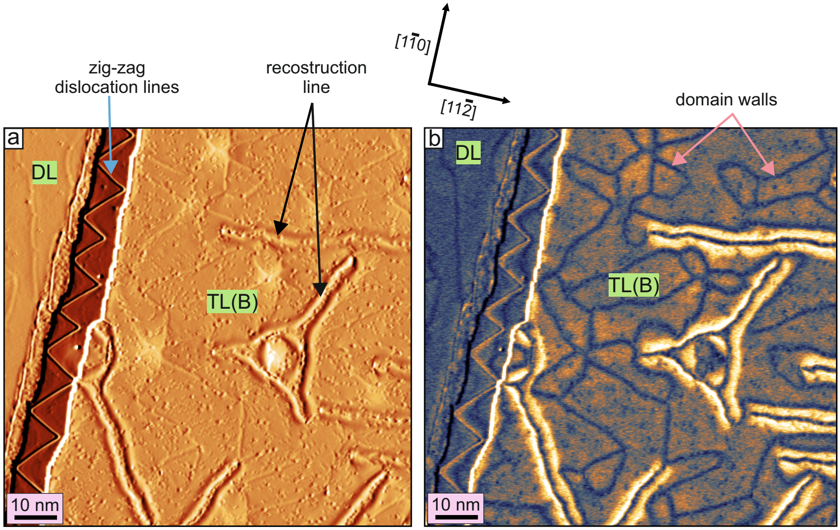

Figure 8.3: Domain wall arrangement around reconstruction lines in TL(B) grown at elevated temperature with Argon ion implantation. (a) Partially differentiated constant current STM topography and **(b)** dI/dU image of a TL(B) terrace grown at 470 K with Argon ion implantation. Reconstruction lines are observed along three equivalent directions separated by 120°, corresponding to the high-symmetry $[11\bar{2}]$ orientations. Magnetic domain walls, marked in the figure, are seen surrounding the reconstruction lines, with each arm favoring a specific orientational domain of the $3Q$ state. This domain selection behavior is further illustrated in the subsequent figure. (Measurement parameters: $U = 50\,\text{mV}$, $I = 400\,\text{pA}$, $T = 4\,\text{K}$).

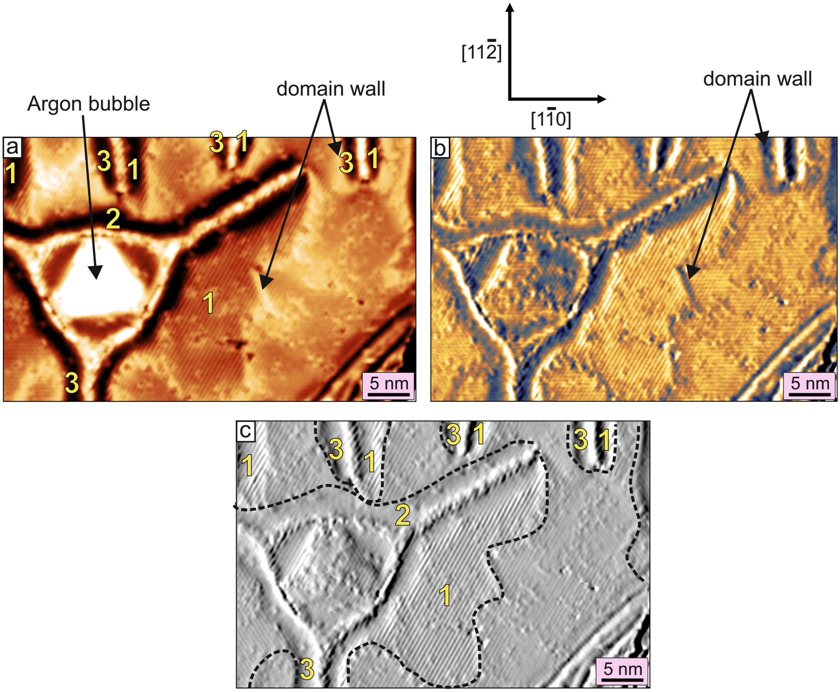

Figure 8.4: Star-shaped reconstruction line and associated domain selection in TL(B). (a), (b) Constant-current SP-STM topography and *dI*/*dU* images of a TL(B) region located near the area shown in Fig. 8.3. A star-shaped reconstruction line is visible, with an additional triangular reconstruction at its center coexisting with an Argon bubble. While the central reconstruction has not been studied in detail, magnetic domain walls can be seen surrounding each arm of the star-shaped reconstruction line, as well as the lines near the top of the image. **(c)** The domain walls are indicated by dotted lines in the current channel, and the rotational domains are labeled to highlight the preference of each arm for a specific orientational domain of the 3Q state. (Measurement parameters: $U = 10\,\text{mV}$, $I = 1\,\text{nA}$, $T = 4\,\text{K}$).

magnetic domain walls surrounding each arm of the star-shaped reconstruction line. Similar behavior is also observed for the reconstruction lines at the top of the image. The domain walls are marked in panels (a) and (b), and indicated by dotted lines in the current channel image shown in panel (c). The rotational domains in panel (c) are labeled to illustrate the preference of each arm of the reconstruction line for a specific orientational domain of the $3Q$ state.

Fig. 8.5 shows another region of the TL(B) terrace as shown in Fig. 8.3. Here, in the constant-current SP-STM topography image, a hexa-junction can be seen near two reconstruction lines. The stripy pattern for all the domains can be seen which has been marked by double headed arrows. If the reader follows the horizontal orientational domain below the hexa-junction, it can be seen that the reconstruction line selects the orientational domains such that it has a 60° domain wall in its centre. This was also the case for the DL reconstruction line as shown in Fig. 4.7.

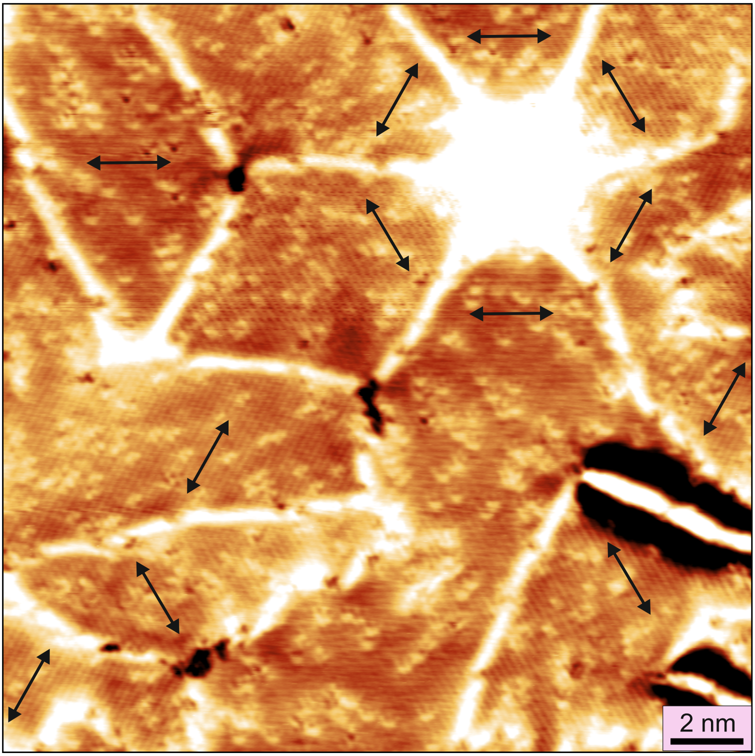

Figure 8.5: Hexa-junction and domain selection by reconstruction lines in TL(B). (a) Constant-current SP-STM topography image of a TL(B) terrace region, similar to that shown in Fig. 8.3, featuring a hexa-junction located near two reconstruction lines. A distinct stripy contrast is observed for all domains and is marked by double-headed arrows. Notably, the horizontal orientational domain located below the hexa-junction shows that the reconstruction line selects neighboring orientational domains such that a 60° domain wall is stabilized at its center. This behavior mirrors the domain selection mechanism seen in the DL reconstruction line shown in Fig. 4.7. (Measurement parameters: $U = 10\,\mathrm{mV}$, $I = 1\,\mathrm{nA}$, $T = 4\,\mathrm{K}$).

List of publications

Articles

Phase co-existence of Mn trimer clusters and antiferromagnetic Mn islands on Ir(111) [*Not included in this thesis*]
Arturo Rodríguez-Sota, Vishesh Saxena, Jonas Spethmann, Roland Wiesendanger, Roberto Lo Conte, André Kubetzka, and Kirsten von Bergmann
ACS Nano **18**, 3699–3706 (2024)
doi: 10.1021/acsnano.3c11459

Strain-driven domain wall network with chiral junctions in an antiferromagnet
Vishesh Saxena, Mara Gutzeit, Arturo Rodríguez-Sota, Soumyajyoti Haldar, Felix Zahner, Roland Wiesendanger, André Kubetzka, Stefan Heinze and Kirsten von Bergmann
under review in Nature Communications
doi: 10.48550/arXiv.2408.12580

Invited talks

Visualizing strain, topology and chirality in an antiferromagnet at the atomic scale
Vishesh Saxena, Mara Gutzeit, Arturo Rodríguez-Sota, Soumyajyoti Haldar, Felix Zahner, Roland Wiesendanger, André Kubetzka, Stefan Heinze and Kirsten von Bergmann
SPEAR conference on Spin-Orbitronics and 3rd Orbitronics Workshop, San Sebastian, Spain
Date: 31.03.2025

Imaging a strain driven domain wall network with chiral junctions in an antiferromagnet
Vishesh Saxena, Mara Gutzeit, Arturo Rodríguez-Sota, Soumyajyoti Haldar, Felix Zahner, Roland Wiesendanger, André Kubetzka, Stefan Heinze and Kirsten von Bergmann
Tata Institute of Fundamental Research Hyderabad, India
Date: 04.10.2024

Exploring the antiferromagnetic ground states and domain walls of Mn on Ir(111) by SP-STM
Vishesh Saxena, Arturo Rodríguez-Sota, Jonas Spethmann, Roland Wiesendanger, and Kirsten von Bergmann
Indian Institute of Science, Bangalore
Date: 14.11.2023

Exploring the antiferromagnetic ground states and domain walls of Mn on Ir(111)
Vishesh Saxena, Arturo Rodríguez-Sota, Jonas Spethmann, Roland Wiesendanger, and Kirsten von Bergmann
The Max Planck Institute of Microstructure Physics, Halle, Germany
Date: 26.10.2022

Contributed talks

Strain-driven domain wall network with chiral junctions in an antiferromagnet
Vishesh Saxena, Mara Gutzeit, Arturo Rodríguez-Sota, Soumyajyoti Haldar, Felix Zahner, Roland Wiesendanger, André Kubetzka, Stefan Heinze and Kirsten von Bergmann
Dutch SPM Day, Groningen, the Netherlands
Date: 08.11.2024

Local strain-induced complex antiferromagnetic spin textures on a bilayer of Mn on Ir(111) investigated via spin-polarized scanning tunnelling microscopy
Vishesh Saxena, Mara Gutzeit, Arturo Rodríguez-Sota, Soumyajyoti Haldar, Felix Zahner, Roland Wiesendanger, André Kubetzka, Stefan Heinze and Kirsten von Bergmann
International conference on Magnetism, Bologna, Italy
Date: 04.07.2024

Exploring the magnetic ground states in different layers of Mn on Ir(111) by SP-STM
Vishesh Saxena, Arturo Rodríguez-Sota, Jonas Spethmann, Roland Wiesendanger, and Kirsten von Bergmann *DPG Spring Meeting, Regensburg, Germany*
Date: 08.09.2022

Posters

Scanning tunneling microscopy: The tool to enter the atomic world
Vishesh Saxena, Khai That Ton, Arturo Rodríguez Sota, Felix Zahner, Andre Kubetzka, Roland Wiesendanger, Jens Wiebe and Kirsten von Bergmann
Science City Day, DESY Campus, Universiity of Hamburg, Germany
Date: 01.06.2024

Exploring the antiferromagnetic ground states and domain walls of Mn bi- and trilayers on Ir(111) by SP-STM
Vishesh Saxena, Arturo Rodríguez-Sota, Jonas Spethmann, Roland Wiesendanger, and Kirsten von Bergmann
20 years of Nanoscience at the University of Groningen, the Netherlands
Date: 12.04.2024

Exploring the antiferromagnetic ground states and domain walls of Mn bi- and trilayers on Ir(111) by SP-STM
Vishesh Saxena, Arturo Rodríguez-Sota, Jonas Spethmann, Roland Wiesendanger, and Kirsten von Bergmann
European school of Magnetism (ESM) 2022, Saarbrücken, Germany
3rd best poster nominator award

Exploring the antiferromagnetic ground states and domain walls of Mn on Ir(111) by SP-STM
Vishesh Saxena, Arturo Rodríguez-Sota, Jonas Spethmann, Roland Wiesendanger, and Kirsten von Bergmann
JEMS 2022, Warsaw, Poland
Best poster award
Date: 27.07.2022

Acknowledgments

I would like to start the acknowledgments by thanking **Professor Wiesendanger** for providing the opportunity to do my PhD in your esteemed research group. I remember the time when I had interviewed for the position and had got some good questions from you on my talk. I enjoyed the Christmas party days organized by you as a traditional event of the group. Also, it was nice to see some invited speakers talk about different fields of research in the group seminar and I was glad to be a part of it and invite some of my friends who gave talks in interesting topics outside of STM.

Kirsten, thank you very much for giving me a chance to work in your group despite having no experience in STM or topology. I still remember your teachings of the tricks to do SP-STM when I was new in the lab and hope to never forget it. I enjoyed my time under your supervision and learnt really a lot with regards to the analysis of structural and magnetic STM data. Whenever I thought I had a full understanding of some aspect of the data, you always came up with something new and interesting. I enjoyed the group's traditional Glühwein meetings at the Gänsemarkt Christmas Market where I increased the stamina of my legs by standing for 5 hours at sub zero degree Celcius temperatures. Jokes aside, I wish you many more beautiful STM discoveries! **Andre**, your out of the box ideas in magnetism have inspired me along the way. You have a nice way of teaching stuff in the lab and I had a nice time assisting you with the magnetic tip preparations. Also, when times got tough in the lab, it was fun to go on movie outings with you and see the immense lack of knowledge I had about Hollywood actors. I saved a good amount of time during my thesis writing due to your quick feedback and nice spin simulations. I wish you good luck with your career and bike adventures. **Stefan**, although we have not interacted a lot, but I have enjoyed our scientific discussions and our collaboration for the nice

DL paper. Thank you for your support and I hope we can collaborate in the future.

This PhD would be incomplete without my STM twin, **Arturo**. Thanks for being there bro at all times, especially for measuring in the VT lab for me when I was tired from my early morning workout sessions. Also, thanks for saving me from doing stupid mistakes in the lab. I will miss our random silly conversations; muffin breaks at Café Jungiusstrasse and doing the endless paper-work for SPEAR. I hope to keep seeing you time to time in life. Good luck for your postdoc and future jobs! **Jonas**, you were the first PhD student I interacted with and learnt some stuff from during my initial days in Hamburg. Thanks for removing time to correct my poster for the JEMS conference on a Sunday, which was the last day for submitting the poster! I will miss our Gnosa cake outings. **Khai**, would have been great if we became friends even earlier in my PhD. Times were super fun with you where we talked about physics, gossips and shared a great sense of humor. I will miss our random dinner plans at the Bunker Döner! Thank you **Dhaval** for your help and support during my accident and covid phase in Hamburg. Aapse to milna hota rhega. Aapke jo khana banane ke vaadein hain, use poora karo mujhe khilake. **Felix**, thanks for all your help in the lab with the transfers and helping me with the sample preparations! I did the most number of He and N2 fillings with you in the morning! I wish you good luck with your bright future! Also, thank you **Mara**, for sharing your DFT insights with me and also showing me around in Kiel. And thanks to **Felix** and **Soum** for helping me out with some complicated physics I had to go through.

Harim, **Eva**, **Elena**, **Jinkyung**, **Jens**, **Bianca**, **Christian** and **Arved** - it was really relaxing to have the coffee breaks with you people after lunch in 9A and I also enjoyed the Christmas party with you guys in the group last year. **Tim**, sorry that I could never attend your concerts, but I am sure you are a professional musician! I wish you good luck with the music and your passion in physics.

I would like to thank **Michael Langer** for all your spontaneous help that I received in a few instances. Also, thank you **Hajo** for your friendliness with the liquid He fillings. I would finally like to thank the remaining group members with whom I could not spend much time, but it was nice meeting them.

Coming to great friends I made from the SPEAR network! **Zhewen** (the Berry physics expert), **Ismael** (the neuromorphic expert), **Sergio** (numerical QM expert), **Maha** (SHNOs expert) - I really hope that we keep meeting each other time to time. I had amazing times with all of you and always wished we worked in the same group! Thank you **Eli** for managing the never ending reports in SPEAR with your sweet patience. And thanks **Sofi** for your extra soft skills sessions and lovely chats during our SPEAR meetings. I would also like to thank **Ingrid**, **Börge** and **Robin** for their insightful and passionate discussions on my research as well as theirs during my secondment time in MLU Halle.

Roberto, I am glad I came across you in my PhD. I learnt a lot of from you during these years ranging from the basics of surface science to advanced magnetism. I enjoyed our discussions about science and life at the Mensa lunch times. It is great that we still keep meeting each other in Groningen and Hamburg and I hope to stay in close contact with you!

Lastly I would like to thank my parents who always are there in my life as pillars of support. And of course to all my friends outside academia without whom life would not be as it is. Especially **Nawal** and **Azminul** whom I visited frequently in Groningen! Azmin bhai, ghar pe rukne dene ke liye shukriya. Aur aapke saath scooty wale scenes mazedaar the Groningen mai mixed with science, nature, philosophy and movies. It is nice to see you **Alida** working with STM! Also, thanks **Dennis** for your friendship and support during my last days in Groningen and early days in Hamburg. I wish you best of luck for your new job. **Mi-**

hir, PhD ke time zyada to nhi mil paye apan kyuki tu gaav mai rehta hai. But milte rahenge aur masti rukegi nhi. Finally, thanks to **DB** and the **Deutschland ticket**, that made it possible for me to explore many lovely towns and cities nearby Hamburg. And ofcourse, I cannot forget to thank **Savoy**, the best cinema in Hamburg for acting as a stress relief tool in my PhD by screening movies in English, which I recommend everyone to attend at-least once in their life!

Eidesstattliche Versicherung

I hereby declare and affirm that this doctoral dissertation is my own work and that I have not used any aids and sources other than those indicated. If electronic resources based on generative artificial intelligence (gAI) were used in the course of writing this dissertation, I confirm that my own work was the main and value-adding contribution and that complete documentation of all resources used is available in accordance with good scientific practice. I am responsible for any erroneous or distorted content, incorrect references, violations of data protection and copyright law or plagiarism that may have been generated by the gAI.

Hamburg, den 19.06.2025

VSaxena

Vishesh Saxena